**UNIVERSITY OF SOUTHAMPTON**

FACULTY OF ENGINEERING AND THE ENVIRONMENT

Aerodynamics and Flight Mechanics

# Boundary-Layer Receptivity and Breakdown Mechanisms for Hypersonic Flow over Blunt Leading-Edge Configurations

by

**Adriano Cerminara**

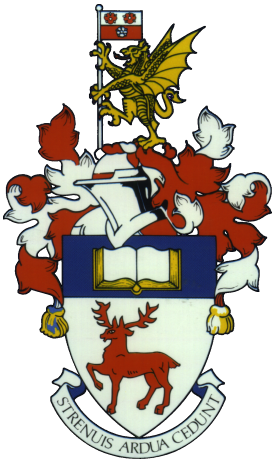


Thesis for the Degree of Doctor of Philosophy

June 2017

UNIVERSITY OF SOUTHAMPTON

ABSTRACT

FACULTY OF ENGINEERING AND THE ENVIRONMENT
Aerodynamics and Flight Mechanics

Doctor of Philosophy

# BOUNDARY-LAYER RECEPTIVITY AND BREAKDOWN MECHANISMS FOR HYPERSONIC FLOW OVER BLUNT LEADING-EDGE CONFIGURATIONS

by Adriano Cerminara

Direct numerical simulations have been performed to study receptivity and breakdown mechanisms for hypersonic flow over blunt leading-edge configurations with imposed freestream acoustic disturbances. Both two-dimensional (2D) and three-dimensional (3D) fast and slow acoustic wave models have been used. The former has been adopted for 2D simulations over a blunt-nose wedge probe designed to measure freestream noise levels in hypersonic wind tunnels; the latter has been used to perform 3D simulations for a span-periodic blunt wedge in unswept and swept configurations, and for a three-dimensional generic forebody model. In the 2D wedge simulations, an analysis of the post-shock wave structure shows that fast acoustic waves are efficiently transmitted across the shock as refracted waves, while slow acoustic waves generate convected waves. The wall response to the fast mode highlights a resonance-modulation behaviour in the nose region. An estimation of the freestream noise levels in the DLR high-enthalpy (HEG) and low-enthalpy (RWG) hypersonic wind tunnels has been performed, showing higher noise levels for the HEG wind tunnel at high Mach numbers. The 3D wedge simulations have been used to study the characteristics of the receptivity and breakdown mechanisms associated with different wave types (fast/slow), disturbance amplitudes, and sweep angles. The fast-mode induced transition has been observed to be a much more rapid and powerful process than the slow-wave related transition, because of the role played by the fast-mode resonance mechanism at the leading edge. Finally, the numerical simulations performed for a generic forebody geometry have enabled comparison with a recent transition experiment carried out in the Mach 6 Purdue hypersonic wind tunnel in noisy conditions. In this case, slow acoustic waves show the most similar transition patterns to the experimental case, and, in particular, are more efficient than fast waves in triggering nonlinear growth of streamwise streaks, related to crossflow inflectional instabilities located in the off-centerline leading-edge region.

# Contents

# List of Figures

# List of Tables

# Declaration of Authorship

I, Adriano Cerminara , declare that the thesis entitled *Boundary-Layer Receptivity and Breakdown Mechanisms for Hypersonic Flow over Blunt Leading-Edge Configurations* and the work presented in the thesis are both my own, and have been generated by me as the result of my own original research. I confirm that:

- this work was done wholly or mainly while in candidature for a research degree at this University;
- where any part of this thesis has previously been submitted for a degree or any other qualification at this University or any other institution, this has been clearly stated;
- where I have consulted the published work of others, this is always clearly attributed;
- where I have quoted from the work of others, the source is always given. With the exception of such quotations, this thesis is entirely my own work;
- I have acknowledged all main sources of help;
- where the thesis is based on work done by myself jointly with others, I have made clear exactly what was done by others and what I have contributed myself;
- parts of this work have been published as:
  - Adriano Cerminara and Neil D. Sandham, *Leading-Edge Receptivity to Acoustic Waves for High-Speed Flows over a Blunt Wedge*, ESA/TRP Project Deliverable, TN 9000, 2015
  - Adriano Cerminara and Neil D. Sandham, *Leading-Edge Receptivity to Acoustic Waves for High-Speed Flows over a Blunt Wedge*, AIAA Paper 2015-3078, 45th AIAA Fluid Dynamics Conference, Dallas, TX, 2015
  - Adriano Cerminara and Neil D. Sandham, *Boundary-layer receptivity and breakdown in hypersonic flow over a swept blunt wedge with three-dimensional freestream acoustic disturbances*, AIAA Paper 2016-4247, 8th AIAA Flow Control Conference, Washington, D.C., 2016

Signed:.....

Date:.....

# Acknowledgements

I would like to express my gratitude to Prof. Neil Sandham, for giving me the possibility to undertake this research project, for inspiring me the enthusiasm with regard to my work, for both his patience and confidence relative to my achievements, and for leading me in an efficient and constructive way towards the path of becoming a professional researcher. I would like to thank Dr. Nigel J. Taylor, who supervised my work giving me very useful advice and inputs for further improvement, which was particularly important for my professional growth. Thanks also to Dr. András Sóbester and Konstantinos Kontogiannis, who contributed to make our periodic progress meetings very productive and interesting, and for their patience during my (long) talks.

I would like to thank my great office colleagues, Kuti, Stefan, Robert, Jacob, Alex, Francesco, Daniel, Markus, Guangda, Anas, for making my PhD period at the University of Southampton very enjoyable. Thanks to all the other colleagues of the Aerodynamics and Flight Mechanics research group of the University of Southampton, including Javi, Jacques, Angeliki, Jeroen, Rammah, Patrick, Richard, and many others, with which I spent a great time. I would like to thank also Dr. Nico De Tullio and Dr. S.P. Jammy for very fruitful technical discussions. Thanks in general to all the staff of the AFM group of the University of Southampton. A special and warm thank goes to Dr. Andrea Sansica, for his greatly appreciated personal and technical support, for plenty of advice and exchange of ideas, which were really helpful to me through my PhD.

I would like to acknowledge MBDA UK Limited for supporting this PhD project. Part of the work reported here formed part of an ESA/TRP project (22793/09/NL/CP). Computer time on the UK National Supercomputing Service (ARCHER) was provided by the UK Turbulence Consortium (UKTC) under EPSRC (Engineering and Physical Sciences Research Council) Grant No. EP/L000261/1. Support is gratefully acknowledged from EPSRC under the Grant No. EP/J016381/2 'Thermal and Reactive Flow Simulation on High-End Computers' for additional computer time.

I would like to thank my mother and my father, who always believed in me, and let me free to discover my path by myself, sure that whatever way I had gone would have been the correct one. To my father, in particular, I feel to dedicate this work, knowing that his happiness for my achievement would have compensated for the time we could not spend together. I thank all my family, my brother, Giuseppe, for transmitting me his passion for the aerospace science, which strongly motivated me through my whole academic career, and my sisters, Alessandra and Anna, for their love and individual support. Finally, I would like to thank Susanna, for always being next to me and helping me enhance my strengths and self-confidence in every situation, and for accompanying me with her invaluable love through my life journey.

# List of Acronyms

| | |
|---|---|
| **1D** | One-dimensional |
| **2D** | Two-dimensional |
| **3D** | Three-dimensional |
| **CFL** | Courant-Friedrichs-Lewy |
| **DNS** | Direct Numerical Simulation |
| **FFT** | Fast Fourier Transform |
| **LES** | Large Eddy Simulation |
| **LST** | Linear Stability Theory |
| **MTS** | Mixed Time Scale |
| **NoSTRANA** | Nonlocal Stability and Transitional Analysis |
| **PSE** | Parabolised Stability Equations |
| **SBLI** | Shock-Boundary-Layer Interaction |
| **SGS** | Sub Grid Scale |
| **TVD** | Total Variation Diminishing |

# Nomenclature

| | | |
|---|---|---|
| $A$ | = | amplitude of the freestream acoustic waves |
| $a$ | = | speed of sound/parameter in the analytic hyperbola function/parameter of the stretching function $S$ |
| $a^l_{i+\frac{1}{2}}$ | = | $l$-th characteristic speed at the interface $i+\frac{1}{2}$ |
| $b$ | = | parameter of the stretching function $S$ |
| $C$ | = | ratio of Sutherland's constant to reference temperature |
| $C_{MTS}$, $C_T$ | = | constants of the MTS approach |
| $c$ | = | disturbance phase speed/parameter of the stretching function $S$ |
| $c_{ph}$ | = | standard definition of the phase speed |
| $c_p$, $c_v$ | = | specific heats at constant pressure and volume |
| $c_f$ | = | skin-friction coefficient |
| $d$ | = | number between 0 and 1 |
| $E$ | = | total energy |
| $\mathbf{F}$ | = | flux vector |
| $\tilde{\mathbf{F}}_{i+\frac{1}{2}}$ | = | flux vector at the interface $i+\frac{1}{2}$ |
| $f$ | = | frequency |
| $f_0$ | = | base frequency of the system of acoustic waves |
| $f_s$ | = | $j$-dependent function of the stretching function $S$ |
| $F_s$ | = | standard definition of the dimensionless frequency |
| $G$ | = | filter convolution kernel in the LES approach |
| $g$ | = | $x$ coordinate of the analytic hyperbola centre/ periodic function of the wave solution in the LST method |
| $g^l_i$ | = | limiter function of the second-order upwind TVD scheme |
| $h$ | = | $x$ coordinate of the analytic hyperbola centre/damping function of the 3D acoustic wave model |
| $i$, $j$, $k$ | = | grid coordinates |
| $J$ | = | Jacobian determinant of the coordinate transformation matrix |
| $\mathbf{K}$, $\mathbf{L}$ | = | right and left hand side coefficient matrices of the eigenvalue problem in the LST method |
| $\mathbf{k}$ | = | wave vector |

| | | |
|---|---|---|
| $k$ | = | scalar wavenumber/parameter of the nonlinear numerical dissipation |
| $k_{es}$ | = | SGS turbulent kinetic energy |
| $L$ | = | domain length |
| $M$, $M_n$ | = | freestream Mach number, Mach number in the shock normal direction |
| $N$ | = | total number of frequencies/points in each grid direction |
| $n$ | = | integer number of frequencies/time index |
| $\hat{n}$ | = | shock normal direction |
| $p$ | = | static pressure |
| $Pr$ | = | Prandtl number |
| $Pr_t$ | = | SGS turbulent Prandtl number |
| $\mathbf{Q}$ | = | vector of the conservative variables |
| $\mathbf{q}$ | = | vector of the primitive variables |
| $q^l$ | = | generic conservative variable |
| $R$ | = | nose radius |
| $\mathbf{R}^{-1}_{i+\frac{1}{2}}$, $\mathbf{R}_{i+\frac{1}{2}}$ | = | left and right eigenvector matrices of the Jacobian matrix in the system of governing equations at the interface $i+\frac{1}{2}$ |
| $Re$, $Re_m$ | = | Reynolds number based on the nose radius and unit Reynolds number (1/m) |
| $S$ | = | grid stretching function in the wall-normal direction/ parameter in the damping function $h$ |
| $S_{ij}$, $S^*_{ij}$ | = | strain-rate tensor and deviatoric part of the strain-rate tensor |
| $s^l_{i+\frac{1}{2}}$ | = | limiter function of the second-order symmetric TVD scheme |
| $T$, $T_0$ | = | static temperature, stagnation temperature |
| $T_S$ | = | Mixed Time Scale |
| T | = | base period of the acoustic waves |
| $t$ | = | time |
| $U$ | = | magnitude of the velocity vector |
| $u$, $v$, $w$ | = | velocity components in the $x$, $y$, and $z$ directions respectively |
| $u_{cross}$ | = | velocity component in the crossflow direction |
| $u_I$ | = | crossflow velocity at the inflection point of the crossflow boundary-layer profile |
| $u_t$ | = | wall-tangential streamwise velocity component |
| $v_n$ | = | wall-normal velocity component |
| $w_t$ | = | generic wave front at the time $t$ |
| $w_I$ | = | crossflow velocity at the inflection point of the crossflow boundary-layer profile |
| $x$, $y$, $z$ | = | Cartesian coordinates |
| $y_n$ | = | wall-normal distance |
| $\alpha$ | = | angle of attack/streamwise wavenumber |

| | | |
|---|---|---|
| $\alpha_r$, $\alpha_i$ | = | real part and imaginary part (spatial growth-rate) of the streamwise wavenumber |
| $\alpha_x$ | = | inclination angle of a wave front with respect to the $x$-axis |
| $\alpha^l_{i+\frac{1}{2}}$ | = | $l$-th element in the vector of the characteristic jumps at the interface $i+\frac{1}{2}$ |
| $\beta$ | = | spanwise wavenumber/wave-front inclination angle with the wall direction |
| $\gamma$ | = | ratio of the specific heats |
| $\gamma^l_{i+\frac{1}{2}}$ | = | wave speed term in the second-order upwind TVD scheme |
| $\Delta$ | = | cutoff length scale of the filter convolution kernel in the LES approach |
| $\delta$ | = | half-wedge angle/boundary-layer thickness |
| $\delta_{st}$ | = | stand-off distance along the stagnation line |
| $\delta_{ij}$ | = | Kronecker delta |
| $\delta_1$, $\tilde{\delta}$ | = | threeshold parameters of the entropy correction term |
| $\Delta x$, $\delta t$ | = | $x$-wise distance and time increment |
| $\Delta\tilde{\mathbf{F}}^-_{i+\frac{1}{2}}$, $\Delta\tilde{\mathbf{F}}^+_{i+\frac{1}{2}}$ | = | flux jumps at the interface $i+\frac{1}{2}$ from the left and the right state |
| $\epsilon$ | = | relative error |
| $\Theta_i$ | = | SGS heat flux |
| $\theta$ | = | incidence angle of the acoustic wave vector with respect to the $x$-axis/angle between asymptotes of the shock-adapted analytic hyperbola and the $x$-axis |
| $\theta^l_{i+\frac{1}{2}}$ | = | $l$-th component of the Harten switch at the interface $i+\frac{1}{2}$ |
| $\hat{\theta}^l_i$ | = | characteristic-jump based function of the Harten switch $\theta^l_{i+\frac{1}{2}}$ |
| $\Lambda$ | = | sweep angle |
| $\lambda$ | = | incidence angle of the acoustic wave vector with respect to the shock normal direction/disturbance wavelength |
| $\mu$ | = | dynamic viscosity |
| $\nu_t$ | = | turbulent eddy viscosity |
| $\xi$, $\eta$, $\zeta$ | = | curvilinear coordinates |
| $\rho$ | = | density |
| $\sigma$ | = | oblique shock angle |
| $\sigma_{ij}$ | = | SGS stress tensor |
| $\tau$ | = | direction tangential to the $k$-grid lines in the 3D generic forebody model |
| $\tau_{ij}$ | = | viscous stresses |
| $\hat{\tau}$ | = | shock tangential direction |
| $\phi$ | = | phase angle of the acoustic waves in the spanwise direction/ |

| | | |
|---|---|---|
| | | generic physical quantity in the Favre filter |
| $\Phi_{i+\frac{1}{2}}$ | = | vector containing the characteristic speeds in the nonlinear dissipation term at the interface $i+\frac{1}{2}$ |
| $\phi^l_{i+\frac{1}{2}}$ | = | $l$-th element of the vector $\Phi_{i+\frac{1}{2}}$ |
| $\phi^{l*}_{i+\frac{1}{2}}$ | = | $l$-th element of the vector $\Phi_{i+\frac{1}{2}}$ pre-multiplied by the Harten switch |
| $\psi$ | = | phase angle of the acoustic waves in the streamwise direction/ entropy correction term |
| $\omega$ | = | angular frequency |
| $\omega_r$, $\omega_i$ | = | real part and imaginary part (temporal growth rate) of the frequency |
| $\omega_x$ | = | streamwise vorticity |

*Subscripts*

| | | |
|---|---|---|
| $ac$ | = | acoustic wave |
| $a$, $b$ | = | mode $a$, mode $b$ |
| $ev$ | = | entropy/vorticity wave |
| $F$ | = | fast acoustic waves |
| $i$, $j$, $k$ | = | $i$, $j$, $k$ directions |
| $n$ | = | $n^{th}$ frequency/shock-normal direction/wall-normal direction |
| $max$, $min$ | = | maximum and minimum value |
| $ps$ | = | post-shock value |
| $S$ | = | slow acoustic waves |
| $t$, $t+\delta t$ | = | instants of time |
| $w$ | = | value at the wall |
| $x$, $y$, $z$ | = | $x$, $y$ and $z$ directions |
| $\tau$ | = | shock tangential direction |
| $\infty$ | = | freestream value |

*Superscripts*

| | | |
|---|---|---|
| $*$ | = | dimensional value |
| $'$ | = | fluctuating value |
| $\bar{}$ | = | mean value/filtered quantity in the LES method |
| $\hat{}$ | = | eigenvector/eigenfunctions of the eigenvalue problem in the LST method |
| $\tilde{}$ | = | Favre filtered quantity in the LES method |

# Chapter 1

# Introduction

The aim of the research described in this thesis is to further increase understanding of transition in high-speed flows, using high-resolution numerical simulations to help understand all the stages of transition, from receptivity to breakdown. In this chapter the challenges are explained and previous literature is reviewed, so that specific objectives of the present study can be formulated.

## 1.1 Motivation

Laminar-turbulent transition plays a fundamental role in the aerodynamic performance of flying vehicles, due to its impact on the skin friction coefficient and on the boundary-layer capability to stay attached to the body surface. However, at hypersonic speeds (i.e. conventionally at Mach numbers above 5, Anderson[1]) it assumes an even more critical role, as it also determines the structural integrity of the vehicle itself due to the effect on the wall heat-transfer rate. The hypersonic flow environment is, in fact, characterised by very high values of heat transfer, which comes from the large amount of kinetic energy gradually dissipated within the boundary layer through viscous effects, and converted into thermal energy. This high amount of internal energy produces high temperature peaks inside the boundary layer at small normal distances from the wall, which provide, in turn, high temperature gradients at the wall, namely high values of the surface heat flux. In order to reduce the heating effects, the hypersonic vehicles need an appropriate thermal protection system (TPS) capable of storing, or radiating/dissipating outwards, the high heat load coming from the boundary-layer flow, thus keeping the surface temperature of the internal structure within tolerable values. Boundary-layer transition causes a dramatic increase of the wall heat-transfer rates, as a result of the turbulent mixing enhancing the mass and energy transport between different flow layers inside a turbulent boundary layer. As a consequence, an unpredicted transition to turbulence in regions of particularly high heat-transfer rates (e.g. the nose region) might result in a

failure of the structure. In particular, the slender leading-edge geometries are the most exposed to this risk, as they are characterised by the highest heat-transfer rates, since the heat flux at the stagnation point ($q_{sp}$) is inversely proportional to the square root of the leading-edge nose radius (i.e. $q_{sp} \propto \sqrt{1/R}$, Anderson[1]). Thus, an appropriate aero-thermal design is necessary for any hypersonic vehicle, which involves the design of a suitable geometry in accordance with the mission-dependent requirements of aerodynamic efficiency and wall heat-flux reduction, along with the choice of the materials and structures used for the thermal protection system. In this context, the prediction of the transition point is a requirement of crucial importance. Indeed, the knowledge of the point (or the region) where the flow becomes turbulent allows the prediction of surface heating and skin friction coefficient along the wall, and, hence, the optimisation of the vehicle geometry and thickness of the TPS, aimed at reducing weights and costs. Unfortunately, the prediction of transition at hypersonic speeds is not straightforward, but, on the contrary, is a very challenging problem, on which the research community has been working for several decades, accumulating a certain amount of experimental data as well as numerical results, which, however, do not yet clarify unambiguously critical aspects of the problem. The main aspects that make transition at high Mach numbers so difficult to understand and control are the complexity of the hypersonic flow in the leading-edge region, and the multiple poorly controlled factors that strongly influence transition in the experimental ground tests, including noise, the presence of small undetected angles of attack, surface roughness, etc. (Schneider[2]).

Hypersonic flow adds a further degree of complexity with respect to subsonic/low-supersonic flows. The different physical phenomena (Anderson[1], Park[3]), which can be considered as the principal features of a generic hypersonic flow, can be summarised as follows: (i) an entropy-vorticity layer downstream of the bow shock in front of a blunt-nosed body, (ii) a thin shock layer due to the high Mach number, (iii) a thick boundary layer, due to the usually very low freestream density values (corresponding to low Reynolds numbers) characterising this flow regime and to the high temperature levels reached inside a hypersonic boundary layer (which in turn provide low density levels), with the possibility at very high Mach numbers of a merging of the shock wave itself with the boundary layer, (iv) the viscous interaction phenomenon on the leading-edge region of a slender body, and (v) the chemical reactions happening inside the shock layer for very high Mach numbers. Although the intensity of these phenomena depends on the particular case, i.e. on the specific Mach number, Reynolds number, total enthalpy of the freestream, and the particular shape of the body, the presence of each one of them increases the complexity of the flow, making it less predictable with respect to the lower-speed flows. Consequently, the complexity of the mathematical models used to describe this types of flow increases as well. Additional complexity of hypersonic flows influences transition, resulting in the growth mechanism of the boundary layer instabilities being different and more complicated than the transition mechanism for subsonic/low-supersonic flows.

In the past decades, several efforts by the scientific community have been made in order to describe the transition mechanism in hypersonic boundary layers, through theoretical models coming from the linear stability theory (LST)(Fedorov[4]), direct numerical simulations (DNS) (Balakumar and Owens[5], Ma and Zhong[6, 7, 16], Zhong and Ma[17], Balakumar and Kegerise[18]) and by means of flight and experimental data (Schneider[2, 19, 20]). In some cases (e.g. Zhong and Ma[17]), the DNS results agree well with the results of the linear stability theory, especially when it is possible to neglect most of the physical phenomena listed above; but a certain discrepancy with experimental data still remains. The lack of correlation between numerical, theoretical and experimental results lead us to discuss other aspects, in addition to those quoted above, that make transition at hypersonic speeds so difficult to describe. This includes the poor reliability of the ground test experimental results. It is well known that the acoustic noise generated in the freestream by the turbulent boundary layer on the nozzle walls of a wind tunnel strongly affects the transition mechanism on the body wall, as it determines the initial conditions of the receptivity process inside the boundary layer (namely amplitude, frequencies and wavenumbers of the disturbances internalised inside the boundary layer). Any small change in the initial conditions will result in a change in the whole transition mechanism, and in a shift of the transition point (Schneider[2]). This is actually due to the nature of turbulence itself, that makes it a phenomenon strongly dependent on the initial and boundary conditions. For example, two apparently equal initial data sets for the flow into a wind tunnel will produce in general two different flowfields at the same point in the space, at each instant of time. It is for this reason that the mathematical description of turbulence requires a stochastic approach. However, the onset of turbulence is linked to the presence in the initial conditions of small undetected factors, like roughness, geometrical imperfections, etc., that strongly influence the flowfield everywhere. The noise generated in the wind tunnel is one of these poorly controlled factors, as it is generated by the transition process on the walls of the nozzle, which is in turn affected by surface roughness, geometrical imperfections, or unexpected variations in the operation conditions of the wind tunnel. Moreover, any change in the tunnel configuration or test conditions will change the tunnel noise, resulting in uncertainties in the comparison of experimental data from two different facilities (Schneider[2]). Besides the wind tunnel noise, there are other local factors influencing transition, that are relative to the body, such as the roughness of the body surface, small angles of attack, shape imperfections, and so on; all of them are potentially poorly controlled. Taking also into account the fact that any wind tunnel cannot simulate exactly the atmospheric environment, it is not sensible to rely on the ground-test measurements in order to make transition predictions relevant to flight, even in the case of low-noise wind tunnels. The only way to develop a reliable method to predict transition is to understand the whole mechanism that leads to transition, and how it is influenced by the external disturbances.

In this scenario, direct numerical simulation is a very useful tool to study, for controlled

external disturbances, the leading-edge mechanism of generation of the boundary-layer modes and their downstream evolution until transition is induced, thus overcoming the limit imposed by the experimental measurements of only detecting the transition point. Also, DNS makes it possible to extend the study of the transition mechanism to high-disturbance environments, thus overcoming the limit of the LST, which gives reliable results only for small environmental disturbances. A typical limit of any numerical simulation is represented by the need to impose a freestream disturbance field, which cannot reproduce exactly the unknown real-world environmental noise of a hypersonic wind tunnel, since it is, in general, very difficult or impossible to measure completely (Schneider[21]). For this reason, a cross-validation study with reproducible experimental measurements is needed in order to appropriately calibrate the freestream disturbance field. A different approach, already used in some numerical studies (e.g. Duan *et al.*[12]), consists of computing the freestream disturbance field through a separate numerical simulation, aimed, for example, at reproducing the acoustic noise generated by the turbulent boundary layer over the nozzle walls. However, this approach is limited too, primarily by the fact of not accounting for the noise generated elsewhere in the wind tunnel (for example the noise coming from the reservoir), and secondly due to the difficulty in reproducing the three-dimensional effects of a real wind-tunnel environment as well as the morphology of the nozzle surface, i.e. isolated and distributed roughness, and other geometrical discontinuities, which can differently affect the characteristics of the radiated noise. Another limit, specific to the direct numerical simulations, is represented by their high computational cost, which has led most of the DNS studies so far to mainly consider two-dimensional (2D) mean flows or very simple three-dimensional (3D) flows (e.g. the flow over a sphere-cone, or a flat plate with 3D disturbances, etc.). However, in order to obtain results of more practical interest for flying vehicles, complex 3D mean-flow effects and their related instabilities should be taken into account.

The main aim of the present research is to contribute to the development of a reliable method to predict transition at hypersonic speeds, by studying the physical breakdown-transition mechanism corresponding to a certain receptivity mechanism in the leading-edge region, and its link with the characteristics of the freestream disturbance field (in terms of type of wave, frequencies and wavenumbers), as well as with the propagation features of the waves induced downstream of the shock and interacting with the boundary layer. To achieve this goal, the challenges concerning the above mentioned limits of the direct numerical simulations are tackled by i) designing a 2D/3D multi-frequency model of the acoustic noise (which is the most relevant type of disturbance in a hypersonic wind tunnel), to which random phases in both the longitudinal and the spanwise directions are applied, in order to simulate the random nature of the real-world noise, as well as different freestream disturbance amplitude levels, in order to study the amplitude effect on the transition mechanism for different types of the acoustic waves (namely fast and slow waves); ii) setting up a computational tool, consisting of an appropriate

shock-capturing scheme, showing a good compromise between numerical stability, solution accuracy and convergence rate, in conjunction with an adaptive shock-aligned grid, allowing good solution quality in each particular numerical case; and iii) performing a parametric study for different flow conditions, characteristics of the freestream disturbances, and geometrical configurations with gradually increasing degree of complexity (i.e. a 2D cylinder-wedge with 2D disturbances, a planar span-periodic cylinder-wedge with 3D disturbances in unswept and swept configurations, and the 3D geometry of a generic forebody model), in order to map the different receptivity characteristics and transition scenarios observed in the different cases. Thus, the present thesis provides a set of computational receptivity-transition data useful for realistic hypersonic vehicle shapes, with different geometrical configurations, that can be used for the validation of both ground-test and flight-test results. Moreover, a combined numerical-experimental study is shown, aimed at estimating the freestream noise levels in different hypersonic wind tunnels, which represents a basis for the gradual path towards a full characterisation of the environmental noise, and for a more accurate calibration of the wave-field model for future numerical investigations.

## 1.2 General aspects of boundary-layer transition

Boundary layer transition is the process through which the boundary layer evolves from an initial laminar state to a final turbulent state, by means of the generation of boundary layer instabilities and their downstream growth and amplification. External disturbances leading to the generation of the boundary layer instabilities include atmospheric turbulence, acoustic waves, entropy spottiness, particulates, etc. In the case of small amplitude disturbances, which is the case of most practical importance for the atmospheric flight, the path to turbulence consists of three stages (Kachanov[22], Zhong and Wang[23]): receptivity, linear eigenmode growth, and nonlinear breakdown to turbulence.

Receptivity is the process by which the external disturbances enter the boundary layer and are converted into internal boundary layer waves travelling downstream. Initial amplitudes, frequencies and phase velocities of these waves depend, in general, on the properties of the disturbances interacting with the boundary layer and on the characteristics of the receptivity process itself (e.g. leading-edge receptivity, roughness receptivity, etc.), and represent the initial conditions for the downstream growth mechanism of the boundary-layer instabilities up to the nonlinear breakdown (Saric *et al.*[24]). Indeed, the whole process leading to breakdown depends on the initial conditions established by the receptivity mechanism. The receptivity process is, in turn, affected by parameters related to the flow conditions, such as the Mach and Reynolds numbers, by the type of the external forcing, including frequencies, wavenumbers, and amplitudes of the environmental disturbances, and by local-flow patterns, including nose bluntness, surface roughness and waviness, and non-parallel effects. The way in which these factors

influence receptivity has led to the division of the receptivity theory into two main classes, on the basis of the wavenumber spectrum of the forcing mechanism: 'forced receptivity', and 'natural receptivity'. In forced receptivity, the forcing mechanism is a localised source of vibrations, such as a vibrating ribbon or wall suction/blowing. In this case, the wavenumber spectrum of the forcing disturbance is broad enough to include the wavenumber of the instability waves, thus leading to the direct excitation of a boundary-layer wave (Saric *et al.*[24]). In contrast, in the natural receptivity process the wavenumbers of the freestream forcing mechanism, consisting of acoustic, vortical, or entropy waves, are in general significantly different to the instability wavenumbers. Therefore, in the latter case, a process of energy transfer from the wavelength of the freestream disturbances to that of the internal wave is needed in order to generate an instability wave in the boundary layer (this process can be defined as a wavelength conversion process). The transfer of energy between the different wavelengths is, in turn, allowed in regions where short-scale streamwise variations of the mean flow occur, as was shown by Goldstein [25], i.e. in regions where small-scale non-parallel effects are important. Such regions are the body leading edge, localised zones of short-scale variation in surface geometry, due for example to curvature discontinuities, roughness and wall humps, or locations of shock/boundary-layer interaction.

The study of the leading-edge effects on the boundary-layer receptivity has been a subject of several investigations. Lin *et al.*[26], for example, performed a numerical study of the leading-edge receptivity to freestream sound for an incompressible flow over a flat plate with an elliptic and a polynomial-smoothed elliptic leading edge, for different aspect ratios of the ellipse, and found that a sharper leading edge is less receptive, and that the effect of smoothing the curvature discontinuity at the ellipse-flat-plate junction is to significantly reduce the receptivity. Schrader *et al.*[27] investigated numerically the receptivity to vortical disturbances for an incompressible flow over a flat plate with elliptic leading edge, and showed that the leading-edge bluntness enhances a non-modal instability mechanism, which consists in the generation of stramwise vorticity through the interaction of vertical freestream vortices with the boundary layer at the leading edge. A similar mechanism had been observed by Nagarajan *et al.*[28] in the numerical simulations of a compressible flow over a flat plate with a super-ellipse leading-edge, for the case of bypass transition induced by strong freestream vortices and enhanced by increasing bluntness. Ma and Zhong [7], and Malik and Balakumar [29] performed numerical simulations of the receptivity to acoustic waves in a Mach 4.5 flow over a flat plate with sharp and blunt (super-ellipse) leading edge respectively, for the same freestream conditions and frequency of the acoustic waves. From an analysis of their results, the response in the early nose region is about three times higher for the blunt leading-edge case, compared to the sharp flat plate, suggesting that a blunt leading edge enhances the receptivity mechanism to acoustic disturbances at high Mach numbers (which will be described later in this chapter). Both leading-edge receptivity theory and localised receptivity theory were reviewed in detail by Saric *et al.*[24].

The second stage consists in the downstream propagation of the small-amplitude instability waves, which can be either amplified, in the case of unstable boundary layer, or attenuated. The amplification or attenuation of the instability waves corresponds to the boundary-layer linear stability problem (Mack[30]). The linear growth of instabilities occurs over relatively long streamwise length scales. It is, in general, modulated by local flow conditions (Saric *et al.*[24]), like pressure gradients, temperature gradients, surface mass transfer, the presence of an entropy layer beyond the boundary-layer thickness (and consequently the generation of inflection points in the profile of the streamwise velocity along the wall-normal direction outside of the boundary layer), and non-parallel effects, resulting either in a stabilising or destabilising effect. For example, the presence of inflection points in the boundary-layer velocity profile always provides a destabilising effect (Kachanov[22], Zhong and Ma[17]). A study of the non-parallel stability can be found in the work of Fasel and Konzelmann [31]. LST, in which the linear growth of instabilities is studied by solving the eigenvalue problem of the homogeneous linearised stability equations, is helpful in identifying the unstable modes and predicting their downstream amplification, and hence is used as a method to predict transition. In the context of LST, the $e^n$ method, which integrates the normal-mode growth rates, is commonly used for boundary-layer transition predictions (Zhong and Ma[17]). Besides the absence of nonlinear effects, a limitation of the $e^n$ method is the fact that it does not consider the initial generation of the instability modes, which is the receptivity mechanism. However, for the subsonic/low-supersonic regime, the $e^n$ method provides in general satisfactory results, due to the presence of a relatively simple receptivity mechanism, which satisfies the assumption of negligible interactions between the different wave modes generated in the nose region (Fedorov[4]). Instead, in the hypersonic flow regime, the receptivity mechanism is significantly more complex (Fedorov[4], Zhong and Wang[23], Fedorov and Khokhlov[32]), so that the interactions between the different modes generated in the leading-edge region need to be taken into account. Hence, any transition prediction by the $e^n$ method is in general not reliable at hypersonic speeds.

When the amplitudes of the instability waves reach significant values, the flow enters the last stage of the path to transition, where three-dimensional and nonlinear effects take place, for example as secondary instabilities. These effects cause a very rapid growth of disturbances, and lead to nonlinear breakdown, randomisation, and a final transition into a turbulent state. Nonlinear breakdown has been studied for nearly sixty years, but some aspects of the final transition to a fully developed turbulent state remain still unsolved. Two fundamental experimental studies for low speeds, conducted by Klebanoff *et al.*[33] and by Kachanov *et al.*[34], showed the existence of two main regimes of nonlinear breakdown: the K-regime and the N-regime (according to Kachanov's terminology, Kachanov[22]). The K-regime, corresponding to the transition mechanism observed in the experiment by Klebanoff *et al.*[33], consists of a strong downstream amplification of the weak natural uncontrolled spanwise modulation of the mean flow (thinking for example of the flow over a flat plate), along with the appearance, at the points where the

streamwise velocity fluctuations are maximum (*peaks*), of high-frequency disturbances (*spikes*), whose nonlinear amplification quickly leads to breakdown and randomisation. In contrast, the N-breakdown (Kachanov[34]) starts with the appearance of a broad spectrum of low-frequency 3D oscillations of the fundamental wave (including subharmonics of the fundamental wave), which are amplified further downstream until three-dimensional randomisation is reached. In particular, the key-mechanism that leads to the generation and amplification of these 3D low-frequency fluctuations (and hence to the N-breakdown mechanism) is a subharmonic resonant interaction between the quasi-subharmonic 3D disturbances and the 2D fundamental wave. Moreover, the N-regime of transition is usually observed for small values of the initial fundamental-wave amplitude. So, the K and N regimes are essentially different in terms of the frequencies of the nonlinear disturbances leading to breakdown, but both types of transition clearly show the three-dimensional nature of breakdown. Kachanov[22] illustrated in details the N-breakdown mechanism, highlighting the decisive role played by resonant wave interactions in the transition process.

The three stages described above represent the path to transition in the case of weak environmental disturbances. As disturbance amplitudes increase, the nonlinear effects become increasingly important, until, for sufficiently high disturbance levels, the linear growth stage is bypassed completely, and the initial receptivity stage is followed by direct nonlinear breakdown and transition to turbulence. A characteristic feature of this direct mechanism is the formation of turbulent spots (Emmons[35]). The spot is a arrow-head fluid structure with a turbulent core, and with a constant lateral growth rate. An important characteristic of these structures is that they grow even in a surrounding stable laminar flow. Indeed, the boundary layer downstream the breakdown can show, within a region of a certain length, an intermittent turbulent behaviour, with a sequence of turbulent spots, interspersed among laminar regions, as shown in the work of Schneider[2] in a Mach 4.3 transition experiment. Intermittent turbulence of this type precedes the final fully turbulent state, but, as it occurs over an extended region, contributes to making detailed prediction difficult. In this context, Redford *et al.*[36] carried out an investigation of the sensitivity of the growth rates of turbulent spots to Mach number and wall temperature, along with a detailed study of the fundamental mechanisms of the spot growth. In particular, they found two different mechanisms of spot growth: one involving the advection of turbulent structures from the spot core outwards along lateral jets; the other consisting in the creation of new structures by destabilisation of the surrounding flow. Increasing Mach number and wall cooling were found to play an important stabilising role in the spot growth rate, especially in relation to the latter mechanism.

Hence, different types of transition exist, depending on the amplitude of the environmental disturbances. On the basis of what has been said above, it is clear that a key

factor determining the mechanism of transition is the way the instability waves are generated in the boundary layer. The presence of either the K-regime or the N-regime in the nonlinear breakdown phase, and the evolution of the instabilities in the linear growth phase are strongly dependent on initial conditions. Thus, it is neceessary to understand how the freestream disturbances are entrained into the boundary layer, and create the initial amplitude and spectral characteristics of the instability waves.

## 1.3 Characteristics of the environmental noise in hypersonic wind tunnels

The environmental noise of a hypersonic wind tunnel can be considered as composed of all the types of waves, namely acoustic waves, entropy waves, and vorticity waves. The acoustic waves represent adiabatic compression and expansion waves, which produce perturbations of pressure and density with the same sign (namely in phase), and velocity disturbances with the same or opposite sign, dependent on the acoustic waves being of the type of *fast* or *slow* respectively. In particular, in a supersonic flow, the fast acoustic waves are acoustic disturbances moving at the speed of sound relative to the flow and propagating in the direction of the flow, so that their phase speed is the sum of the streamwise mean velocity of the flow ($U$) and the speed of sound ($a$), namely $U + a$. In contrast, the slow acoustic waves are oriented in the opposite direction of the mean flow, thus their phase speed is the difference between the flow velocity and the speed of sound, i.e. $U - a$. The entropy waves, instead, are related to temperature spottiness at constant pressure, which provide density perturbations, accordingly to the equation of state (which will be presented in Chapter 2), with no velocity disturbances; while the vorticity waves are linked to perturbations in the velocity components transverse to the mean flow direction, with no disturbances of the thermodynamic variables. Moreover, the entropy and vorticity waves are convected by the flow, so their propagation speed is coincident with the flow velocity ($U$).

The intrinsic inhomogeneity of the environmental noise in hypersonic wind tunnels makes the disturbance field itself very difficult to measure with the current experimental techniques (Schneider [8]). The degree of complexity of the freestream disturbance field is further increased by the inhomogeneity of the amplitude and orientation of the different types of waves, dependent on the particular section of the wind tunnel from which the waves are generated. For example, waves coming from the reservoir and waves radiated from the nozzle walls will have, in general, different amplitude and orientation, aside from pertaining to a different class of waves. Entropy and vorticity waves contribute to the noise coming from the upstream section of the wind tunnel, while acoustic waves are the dominant disturbances radiated by the turbulent boundary layer on the nozzle walls (e.g. Schneider [9, 10], Masutti *et al.*[11]). Moreover, the natural three-dimensionality

and irregularity in the structure of the disturbance field makes it substantially unpredictable.

Despite its high complexity, some simplifications of the disturbance field can be made, according to numerical and theoretical studies available in the literature. For example, in a recent numerical study, Duan *et al.*[12] showed that the noise generated by a fully turbulent boundary layer in a flow at Mach 2.5 over a flat plate is mainly characterised by acoustic disturbances with wavefront orientation and phase speed belonging to the class of slow acoustic waves. This is an indication that slow acoustic modes are efficiently produced by turbulent boundary layers on the wind tunnel walls. On the other hand, considering the effect of the non-acoustic type of disturbances, it was shown by the theoretical study of McKenzie and Westphal [13] on the interaction of freestream disturbances with an oblique shock, which was then extended to the case of a shock attached to a wedge by Duck *et al.*[14, 15], that incident entropy/vorticity waves can generate intense acoustic waves behind the oblique shock. This was proved by Ma and Zhong [16] from a numerical study of the receptivity for a Mach 4.5 flow over a flat plate to different types of freestream disturbances, in which it was observed that, in the case of freestream entropy and vorticity waves, the boundary-layer disturbances are mainly induced by fast acoustic waves generated behind the shock by the freestream forcing waves.

In the light of these considerations, the acoustic disturbances, pertaining to both the classes of fast and slow acoustic waves, have been considered as the main forcing disturbances in the present numerical study.

## 1.4 Receptivity to freestream disturbances at hypersonic speeds

As we have seen, the whole process leading to breakdown depends on the initial conditions established by the receptivity mechanism. This is why receptivity plays a role of primary importance in the study of the growth mechanism of the boundary-layer instability modes, and hence in the prediction of the transition point. The receptivity process is, in turn, affected by mean-flow parameters (e.g. Mach number, Reynolds number, angle of attack, etc.), properties of the external forcing (type, amplitude, frequency, phase speed and orientation), local-flow patterns and geometrical factors. The Mach number, in particular, plays an crucial role in the main characteristics of the receptivity process, meaning that the generation mechanism of the internal modes by external small-amplitude disturbances shows some fundamental differences depending on the particular flow regime. These differences can be summarised as follows:
a) In subsonic/low-supersonic boundary layers, the receptivity mechanism consists essentially in the excitation, by the freestream disturbances, of the Tollmien-Schlichting

waves, which represent the first instability mode. This is the characteristic unstable mode of this flow regime; all the other modes generated in the boundary layer are stable, and their interaction with the first mode can be neglected. In contrast, in the hypersonic regime, besides the first mode, there is the presence of other higher-frequency instability modes, so-called *Mack* modes, that can coexist in the boundary layer, as shown by Mack[30], making the internal instability spectrum significantly more complex than at moderate Mach numbers. Stetson *et al.*[37] observed the second-mode instability in a Mach 8 transition experiment over a cone, which showed that the second (Mack) mode plays a major role in the transition process.
b) In the low-subsonic flow regime, as the wavenumber spectrum of the external disturbances is very different to that of the boundary-layer instability modes, the excitation of waves inside the boundary layer always happens by means of a wavelength matching mechanism, as explained above in the context of the natural receptivity. In contrast, at supersonic Mach numbers the wavelength conversion mechanism is no longer needed, as the excitation of the boundary-layer modes in this flow regime is essentially due to a direct resonant-interaction mechanism between the internal waves and the freestream disturbances, as shown in several theoretical and numerical studies (Fedorov and Khokhlov[32], Fedorov[4], Balakumar[38], Zhong and Ma[17], Zhong and Wang[23]).

These different phenomena result in the receptivity mechanism at hypersonic speeds being significantly more complicated than at lower Mach numbers. In particular, the resonance/synchronisation mechanism is a key-aspect of the receptivity of hypersonic boundary layers to environmental disturbances, as it determines the generation of the instability modes, by synchronisation of these, either with the external modes or with other stable internal modes, dependent on the external disturbances (for example fast or slow acoustic waves). This means that another distinction about the receptivity mechanism has to be made, concerning the type of environmental disturbances. In this context, considering the case of a blunt body in a hypersonic flow, the shock - freestream-wave interaction plays a major role for the establishment of the disturbances generated behind the curved shock and interacting with the boundary layer. Ma and Zhong [16] numerically studied the receptivity for a Mach 4.5 flow over a flat plate to different types of freestream disturbances, and observed that, in the case of freestream entropy and vorticity waves, the boundary-layer disturbances are mainly induced by fast acoustic waves generated behind the shock by the freestream forcing waves. The theoretical studies by Fedorov and Khokhlov[32], and Fedorov[4] showed that freestream fast acoustic, entropy and vorticity waves produce a similar receptivity mechanism, while slow acoustic waves interact with the boundary layer in a different way. In particular, if the waves interacting with the boundary layer are of the type of fast acoustic, entropy or vorticity waves, a stable internal mode (mode F, or fast mode) is generated at the leading edge through a resonance mechanism, namely due to the synchronisation between mode F and the forcing waves. This mode then leads, in a region further downstream along the wall, to the excitation of a lower phase-speed mode (mode S, or slow mode), representing

the class of the instability modes, including both the first instability mode and the Mack modes. The excitation of mode S is due to another synchronisation mechanism, which now involves mode F, whose phase speed gradually decreases downstream, and mode S. Further downstream, mode S becomes unstable and grows very rapidly, corresponding to the excitation of the second instability mode. On the other hand, if the waves interacting with the boundary layer are slow acoustic waves, the resonance mechanism at the leading edge with the external waves leads directly to the generation of mode S, which becomes unstable and grows further downstream.

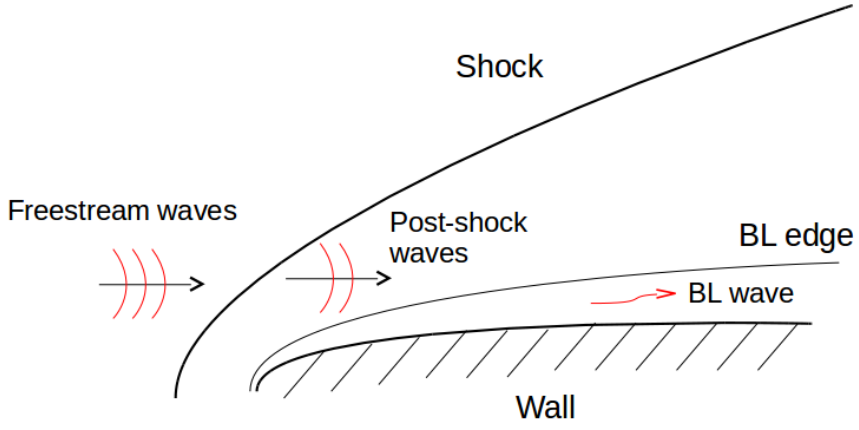


Figure 1.1: Sketch of a blunt body in a hypersonic flow with freestream disturbances

This mechanism has been numerically investigated through DNS computations by different authors, e.g. Zhong and Ma[17] (for the case of the flow over a cone with fast acoustic waves), Balakumar[38] (for the interaction of 3D fast and slow acoustic waves with a blunted flat plate), and Kara *et al.*[39] (for the flows over a cone and a wedge with both fast and slow acoustic waves). Tumin *et al.*[40] performed a joint numerical-theoretical study of the receptivity to 2D perturbations in a Mach 8 flow over a sharp wedge, in which a multimode decomposition technique was used to decompose the numerical perturbation field into normal modes and identify the discrete modes F and S. Malik and Balakumar[29] also studied numerically the bluntness effect on the receptivity to fast and slow acoustic waves over a blunted flat plate with three different leading-edge thicknesses. Moreover, the angle of incidence of the acoustic waves can play an important role in the features of the perturbation field near the leading edge, as shown in the numerical work of Egorov *et al.*[41] for the case of the boundary-layer receptivity over a flat plate. The following figure shows an illustrative scheme of the mode S excitation mechanism for different freestream disturbance types. The resonance/synchronisation causes the generation of mode F and mode S at the leading edge, dependent on the type of freestream disturbance, and is also the leading mechanism of the intermodal exchange

from mode F to mode S further downstream (for the case of fast acoustic, entropy or vorticity waves), where mode S is excited.

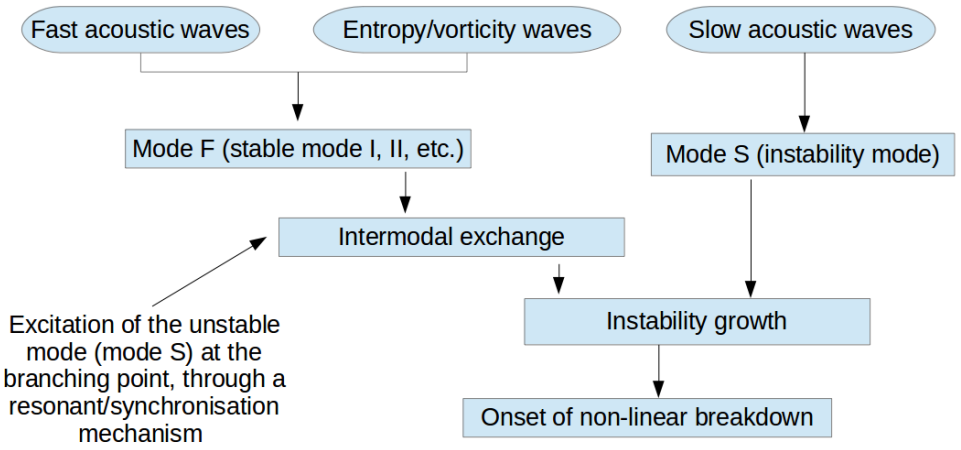


Figure 1.2: Scheme of mode S excitation mechanism

Mode F is always stable and is characterised, as shown in the works of Ma and Zhong [16] and Zhong and Wang [23], by the appearance in sequence of multiple modes of increasing frequencies (mode I, II, III, etc., using Ma and Zhong's [16] notation). Each of these modes is first amplified (due to the above mentioned resonance mechanism), and then decays, with a decreasing phase speed, until approaching the phase speed of mode S (synchronisation with mode S). Mode S is, in contrast, characterised by the appearance in sequence of a first mode (corresponding to the Tollmien-Schlichting waves) in the leading-edge region, and by multiple higher-frequency Mack modes ($2^{nd}$ mode, $3^{rd}$ mode, etc., according to their appearance order), excited after the decay of each of the above mentioned series of fast modes. This receptivity process will be discussed in more detail in the next chapters of the present thesis, for the results of the numerical cases with freestream fast acoustic waves. In the case of slow acoustic waves, mode S follows the same evolution cycle described above (with the appearance in sequence of the first mode, the second mode, etc.) without the presence of mode F, because mode S is directly excited at the leading edge through the resonance mechanism with the slow acoustic waves. Among the instability modes pertaining to mode S, the dominant mode in hypersonic boundary layers is the second mode, whose amplitude and growth rate determine the position of the transition point. However, the second-mode amplitude and growth rate depend on the interaction mechanisms preceding the point where it is excited (the first mode F - mode S synchronisation point). This means that the field can be divided into two regions: *upstream* of the first mode F - mode S synchronisation point, namely in the leading-edge region, where the initial resonance mechanism between external disturbances and internal modes takes place, and *downstream*, where the second mode gets in and is amplified (Fedorov[32]). Therefore, in order to be able to predict

the amplitude of the instability waves inside a hypersonic boundary layer, and make some transition predictions, we need to study the upstream region, which is the early part of the receptivity process. At the same time, the downstream region needs to be treated without any particular simplifying assumptions, in order to include possible further interactions between forcing disturbances and boundary-layer waves, that can lead to a strong modulation of the internal modes. These needs lead us towards the use of the DNS as an appropriate tool to accurately simulate the evolution of the instabilities inside the boundary layer of hypersonic vehicles, and to predict transition, as well as a method to validate LST results.

The receptivity process for hypersonic vehicles is, in general, influenced also by other effects, such as the nose bluntness, entropy layer, wall temperature and chemical nonequilibrium effects. Nose bluntness and entropy-layer effects were studied in the experiment by Stetson *et al.*[37]; the results showed that increasing bluntness, below a certain limit value, delays transition, but this trend is reversed above this limit. DNS studies of the hypersonic flow over blunt cones with nose bluntness effects and wall temperature effects were conducted by Kara *et al.*[39, 42]. Hornung *et al.* [43] carried out experiments on hypersonic transition with chemical nonequilibrium effects, that become relevant at very high Mach numbers. Theoretical, numerical and/or joint computational-experimental investigations of chemical and/or vibrational nonequilibrium effects on the boundary-layer receptivity and transition in hypersonic flow are represented by, e.g., the works of Stuckert and Reed [44], Ma and Zhong [45], Stemmer [46], Parsons *et al.*[47], Jewell *et al.*[48] and Mortensen and Zhong [49]. In particular, the DNS study of Ma and Zhong [45], concerning the receptivity to freestream disturbances in a Mach 10 oxygen flow, showed that the second mode is destabilised by real gas effects, thus confirming the theoretical predictions of Stuckert and Reed [44] for the linear stability of a Mach 25 flow over a sharp cone. In the computational-experimental study of Jewell *et al.*[48] the presence of carbon dioxide in a hypersonic flow over a cone was shown to delay significantly transition, compared to a pure air flow, while, more recently, the theoretical study of Mortensen and Zhong [49] for a Mach 15.99 hypersonic flow over a blunt cone, including thermochemical nonequilibrium and surface graphite ablation, showed that blowing destabilises a real-gas flow, and the second mode is slightly stabilised by the carbon species. Although several other authors have conducted DNS studies in these areas, the problem of the receptivity of hypersonic nonequilibrium flows, along with the transition reversal problem due to entropy-layer effects, are still unresolved, and are beyond the scope of the present investigation.

## 1.5 Effect of oblique disturbances

The resonance mechanism, upon which the receptivity to freestream disturbances in hypersonic flows is based, is strongly influenced by the orientation of the incident waves, with important consequences on the transition process. Fasel *et al.*[50] performed a DNS of the complete transition to turbulence through oblique breakdown for a flat plate at Mach 3 , introducing a pair of oblique waves in the boundary layer. In their work it is shown that the oblique instability waves are strongly amplified until oblique breakdown is triggered, which can then lead to a fully developed turbulent boundary layer. In the works of Berlin *et al.*[51] and Berlin and Henningson[52], the response to oblique freestream waves in combination with a nonlinear mechanism was found to be a powerful process leading to a different transition scenario, namely oblique transition, which is characterised by nonmodal growth of the disturbances and requires lower initial amplitudes compared to the case of transition caused by two-dimensional instabilities. Ma and Zhong[7] also studied the receptivity to freestream fast acoustic waves on a flat plate at different angles of incidence, and obtained the highest amplitude response for an incidence angle of about 26°. Egorov *et al.*[41] studied the response to fast and slow acoustic waves over a 2D flat plate for different angles of incidence of the wave vector with respect to the streamwise direction. The receptivity to three-dimensional acoustic waves with assigned inclination angles and wavenumbers in the spanwise direction was studied numerically by Balakumar[38] for a blunt flat plate at Mach number 3.5 in the linear regime. In his work, the amplification of the instability waves downstream of the neutral point agrees very well with PSE (Parabolized Stability Equations) predictions.

## 1.6 Effect of a sweep angle

In the case of a swept leading edge, the receptivity to external acoustic disturbances, and the resulting transition process, can be strongly affected by the presence of the crossflow instability, which is related to the generation, due to the inflectional instability of the crossflow boundary-layer profiles, of streamwise-oriented co-rotating vortices. In particular, the inflection of the boundary-layer crossflow profile originates in regions of pressure gradients (e.g. the leading edge), and is essentially due, as described by Saric *et al.* [53], to an imbalance, occurring inside the boundary layer, between the centripetal acceleration, linked to the curvilinear trajectory of the streamlines in a flow over a swept body, which decreases inside the boundary layer due to the gradual reduction of the streamwise velocity up to the zero value at the wall, and the pressure gradient, which, in contrast, remains unchanged in the boundary layer. This imbalance generates a boundary-layer velocity component perpendicular to the streamwise and the wall-normal directions (namely the crossflow), which reaches a peak at a certain wall-normal distance, before going to zero at the wall, thus causing an inflection point.

The crossflow instability in swept leading edges has been investigated both experimentally and numerically by several authors. A review of the three-dimensional boundary-layer stability and transition with a focus on the effects of the crossflow instability on swept wings and rotating disks is presented in the work of Saric *et al.* [53]. Experimental studies showing the role of the crossflow instabilities on the transition process in three-dimensional boundary layers can be found in the works of White and Saric [54], Bippes [55], Cattafesta *et al.* [56] and Creel *et al.* [57]. Tokugawa *et al.* [58] conducted a transition experiment on an axisymmetric body at Mach 1.2 and incidence angles of 1° and 2°, and detected stationary crossflow vortices in the region where the foremost transition occurred. An eigenvalue analysis was used by Li and Choudhari [59] to study the spatial instabilities in crossflow dominated swept-wing boundary layers, while a linear stability analysis was performed by Nomura [60] to study the effects of crossflow instabilities on the spatial growth of first-mode waves for the three-dimensional supersonic boundary layer over an infinite swept wing. Paredes and Theofilis [61] and Paredes *et al.*[62] performed spatial BiGlobal linear stability analyses in hypersonic flow over an elliptic cone model, showing the importance of instability modes localised along the centerline of the body (so called centerline modes), and classified as shear-layer instabilities, as a result of a mushroom-like fluid structure formed along the centerline. Finally, DNS studies were performed by Balakumar and King [63], Pruett *et al.* [64] and Speer *et al.* [65], to investigate the effects of the crossflow instabilities in supersonic flows over swept wings at Mach 3, 3.5 and 5.1 respectively.

## 1.7 Objectives of the present study

The objective of the present work is to perform direct numerical simulations of the full transition process from imposed freestream disturbances over blunt leading-edge geometries, and use the results to clarify mechanisms of hypersonic transition. This is of fundamental importance to link the final breakdown mechanism to the characteristics of the freestream disturbances, without any arbitrary intermediate simplification. The freestream disturbances are introduced as an inflow boundary condition in the computational domain, through an acoustic-wave model that will be described later. This direct approach, along with a cross-validation with available data from transition experiments, can also play an important role in calibrating the model to reliably reproduce the main characteristics of the wind-tunnel noise.

A better interpretation of the several physical mechanisms leading to transition in the experimental facilities is needed, i.e. an understanding of how the receptivity and breakdown mechanisms are affected by key factors that influence transition in the ground-test experiments, including Mach number, Reynolds number, angle of attack, sweep angle, amplitude and orientation of the incident waves, shock-disturbance interaction, leading-edge shape, etc. For this reason, the present work has been carried out in three main

stages, considering different geometries and disturbance models for the study of i) the receptivity mechanism for a 2D wedge-shaped geometry, representative of a measurement probe used in recent experimental investigations, with 2D acoustic waves, ii) the receptivity and breakdown mechanisms for a 2D wedge-shaped geometry with 3D acoustic disturbances in both unswept and swept configurations, iii) the receptivity and breakdown mechanisms for the 3D geometry of a generic forebody model, recently tested in a hypersonic wind tunnel, with 3D acoustic disturbances.

In the first stage, two-dimensional numerical simulations are performed for a cylinder-wedge geometry inserting planar fast and slow acoustic waves with multiple frequencies as freestream disturbances. These numerical cases cover a set of non-transitional experiments carried out at DLR on a probe (Wagner *et al.* [84]) designed to measure the disturbance levels in high and low enthalpy hypersonic wind tunnels. The main objectives of these numerical simulations are the following:

- to determine the characteristics of the transmitted waves (i.e. the wave structure) behind of the shock,
- to determine the characteristics of the response along the wall,
- to assess the sensitivity of the leading-edge receptivity to the angle of attack and the angle of incidence of the acoustic waves,
- to estimate the freestream noise levels in the different wind tunnels and flow conditions relative to the DLR experiments, through a combination of the numerically obtained transfer functions (i.e. freestream-to-wall disturbance level) and the experimental data for the disturbance levels on the wall.

In the second stage, another cylinder-wedge geometry is considered, with half-wedge angle equal to that of the generic forebody shape used in the third stage, but three-dimensional simulations are performed in this case, with a 3D acoustic-wave model accounting for multiple spanwise wavenumbers. The simulations are carried out at the same Mach number (Mach 6) for fast and slow acoustic waves with different freestream disturbance amplitude levels, in order to consider both linear and nonlinear cases, and for both unswept and swept leading-edge configurations. In this case, the main goal is to analyse the different transition scenarios reached for different wave-type - amplitude-level - leading-edge-configuration (i.e. swept/unswept) combinations, with the following objectives:

- to deduce the different receptivity mechanisms to freestream fast and slow acoustic waves, with and without nonlinearities,

- to determine the resonance mechanism at the leading edge between the internal modes and the external forcing, including an assessment of the relevance of previous theoretical approaches (Fedorov and Khokhlov[32]),
- to determine the extent of influence of crossflow instabilities generated at the leading edge due to the presence of a sweep angle.

Finally, in the third stage, a full three-dimensional geometry is considered, representative of a generic forebody model that was used in recent transition experiments performed by MBDA in the Purdue hypersonic wind tunnel at Mach 6 (Durant *et al.* [89]). For this case, direct numerical simulations are performed making use of the same three-dimensional acoustic-wave model used in the second stage, for both fast and slow acoustic waves, with the following objectives:

- to compare the simulations with the experimental results, thus assessing the suitability of the acoustic-wave model, and the dominant disturbances in the Purdue hypersonic wind tunnel,
- to determine the main transition mechanism on the geometry of a generic forebody.

The results obtained in this work serve as an assessment of the freestream disturbance levels and of the dominant type of disturbances characterising the environmental noise in hypersonic wind tunnels, providing at the same time a further understanding of the main physical mechanisms leading to transition in the hypersonic wind tunnels for different flow conditions, disturbance characteristics and geometrical configurations. This can shed light on the ambiguity still present in transition experiments (Schneider [8]), and help to set-up a transition prediction method.

# Chapter 2

# Numerical method

## 2.1 Governing equations

We consider numerical solutions of the three-dimensional Navier-Stokes equations for compressible flows, written in conservation form, under the assumption of perfect gas. The set of non-dimensional conservation equations in Cartesian coordinates can be written as

$$\frac{\partial \mathbf{Q}}{\partial t} + \frac{\partial \mathbf{F}_j}{\partial x_j} = 0 \,, \tag{2.1}$$

In the equation above, $\mathbf{Q}$ is the vector of the conservative variables, while $\mathbf{F}_j$ is the vector of the fluxes in Cartesian coordinates. The components of the vectors of the system in conservative form are

$$\mathbf{Q} = \begin{bmatrix} \rho \\ \rho u \\ \rho v \\ \rho w \\ \rho E \end{bmatrix} , \tag{2.2}$$

$$\mathbf{F}_j = \begin{bmatrix} \rho u_j \\ \rho u u_j + \delta_{1j} p - \frac{1}{Re}\tau_{1j} \\ \rho v u_j + \delta_{2j} p - \frac{1}{Re}\tau_{2j} \\ \rho w u_j + \delta_{3j} p - \frac{1}{Re}\tau_{3j} \\ \rho \left(E + \frac{p}{\rho}\right) u_j - \frac{1}{Re}\left(u\tau_{1j} + v\tau_{2j} + w\tau_{3j} + \frac{\mu}{(\gamma-1)PrM^2}\frac{\partial T}{\partial x_j}\right) \end{bmatrix} \tag{2.3}$$

The terms $\rho$, $\rho u$, $\rho v$, $\rho w$ and $\rho E$ are the conservative variables of the system of equations, where $\rho$ is the density, $u$, $v$ and $w$ are the velocity components respectively in the $x$, $y$ and $z$ directions, and $E$ is the total energy per unit mass. In the flux vectors, the terms $p$, $T$, $\tau_{ij}$, and $\mu$ are respectively the pressure, the temperature, the components

of the viscous stress tensor, and the dynamic viscosity of the flow. The non-dimensional quantities are obtained through normalisation of the dimensional variables with their freestream reference values: the velocity components are normalised with the freestream main velocity ($U^*_\infty$), the density is normalised with the freestream density ($\rho^*_\infty$), the viscosity is normalised with the freestream dynamic viscosity ($\mu^*_\infty$), the temperature is normalised with the freestream temperature ($T^*_\infty$), the total energy is normalised with the square of the freestream main velocity ($U^{*2}_\infty$), while the pressure and viscous stresses are normalised with the term $\rho^*_\infty U^{*2}_\infty$, related to the freestream dynamic pressure ($\frac{1}{2}\rho^*_\infty U^{*2}_\infty$). Note that the superscript ($^*$) is used to denote dimensional values. The nose radius ($R^*$) is chosen as the characteristic length to normalise the length scales, while the time scales are normalised with respect to the fluid-dynamic characteristic time ($R^*/U^*_\infty$), based on the velocity of the undisturbed flow and on the characteristic length. The terms $Re$, $Pr$, $M$, and $\gamma$ are respectively the Reynolds, Prandtl and Mach numbers, and the constant-pressure to constant-volume specific heat ratio ($\gamma = c^*_p/c^*_v$), i.e. the dimensionless parameters of the flow. The Reynolds number is defined with respect to the nose radius, as $Re = (\rho^*_\infty U^*_\infty R^*)/\mu^*_\infty$; the Prandtl number is set to 0.72 for air, and $\gamma$ is equal to 1.4, as we are considering a perfect gas model. The dynamic viscosity is, in turn, expressed in terms of temperature by Sutherland's law

$$\mu = T^{3/2}\frac{1+C}{T+C} \ , \tag{2.4}$$

where the constant C represents the ratio between the Sutherland's constant (set to 110.4 K) and the freestream reference temperature ($T^*_\infty$). The viscous stresses are defined in terms of the velocity derivatives, under the assumption of a Newtonian fluid, as

$$\tau_{ij} = \mu\left[\frac{\partial u_i}{\partial x_j} + \frac{\partial u_j}{\partial x_i} - \frac{2}{3}\delta_{ij}\frac{\partial u_k}{\partial x_k}\right] \ . \tag{2.5}$$

We also need a relation linking the total energy to the temperature, which in non-dimensional form can be expressed as

$$E = \frac{T}{\gamma(\gamma-1)M^2} + \frac{1}{2}\left(u^2+v^2+w^2\right) \ . \tag{2.6}$$

Finally, the system of equations is closed by the equation of state for a perfect gas

$$p = \frac{1}{\gamma M^2}\rho T \ . \tag{2.7}$$

The system of equations in Cartesian coordinates is transformed into a system of equations in curvilinear coordinates ($\xi$, $\eta$, $\zeta$) as

$$\frac{\partial \bar{\mathbf{Q}}}{\partial t} + \frac{\partial \bar{\mathbf{F}}_j}{\partial \xi_j} = 0 \ . \tag{2.8}$$

The relations between the vectors in curvilinear and Cartesian coordinates are expressed by

$$\bar{\mathbf{Q}} = J\mathbf{Q}, \quad \bar{\mathbf{F}}_j = J\mathbf{F}_i \frac{\partial \xi_j}{\partial x_i} \ , \tag{2.9}$$

with $J = \det ||\partial(x, y, z)/\partial(\xi, \eta, \zeta)||$ being the Jacobian of the transformation matrix.

## 2.2 Two-dimensional acoustic-wave model

Figure 2.1 shows a sketch of the planar acoustic waves travelling in the direction of the wave vector $\mathbf{k}$, with an inclination angle $\theta_{xy}$ in the $xy$-plane with respect to the positive $x$-axis of the Cartesian reference system. The freestream perturbations of the physical quantities are expressed relative to the freestream density perturbation ($\rho'$) by means of the following relations, derived from the linearised dimensionless Euler equations under the assumption of small perturbations,

$$u'_\infty = \pm \frac{1}{M} \rho'_\infty \cos\theta_{xy} \ , \ v'_\infty = \pm \frac{1}{M} \rho'_\infty \sin\theta_{xy} \ , \ p'_\infty = \frac{1}{M^2} \rho'_\infty \ , \tag{2.10}$$

$$E'_\infty = \frac{1}{M} \rho'_\infty \left( \frac{1}{\gamma M} + \cos\alpha \cos\theta_{xy} + \sin\alpha \sin\theta_{xy} \right) \ , \tag{2.11}$$

where $\alpha$ denotes the angle of attack. The inclination angle of the acoustic waves ($\theta_{xy}$) is considered positive for waves impinging from below (as represented in the sketch of figure 2.1). In the relations for the velocity component perturbations, the '+' sign is used for fast acoustic waves, while the '−' sign applies to slow acoustic waves, as fast waves would be oriented in the same sense indicated by the wave vector in figure 2.1, while slow waves would be oriented in the opposite sense, thus producing an opposite-sign perturbation (with respect to the sign of $\rho'_\infty$) for both the velocity components. The relations for the fluctuations of the velocity components and pressure are consistent with the relations used by Egorov *et al.*[41] for their 2D acoustic-wave model (with the exception of the inclination angle being considered positive for waves coming from above in their work), while the derivation of the total energy perturbation is shown in Section 2.3.

The freestream density perturbation as a function of time and Cartesian coordinates, for the case of multiple frequencies, is expressed as

$$\rho'_\infty(x, y, t) = A \sum_{n=1}^{N} \cos\left(k_{nx} x + k_{ny} y - \omega_n t + \psi_n\right) \ , \tag{2.12}$$

where $A$ is the assigned amplitude, $k_{nx}$ and $k_{ny}$ are the wavenumbers respectively in the $x$ and $y$ directions, $\omega_n$ is the angular frequency, $\psi_n$ is the phase angle, $N$ represents the

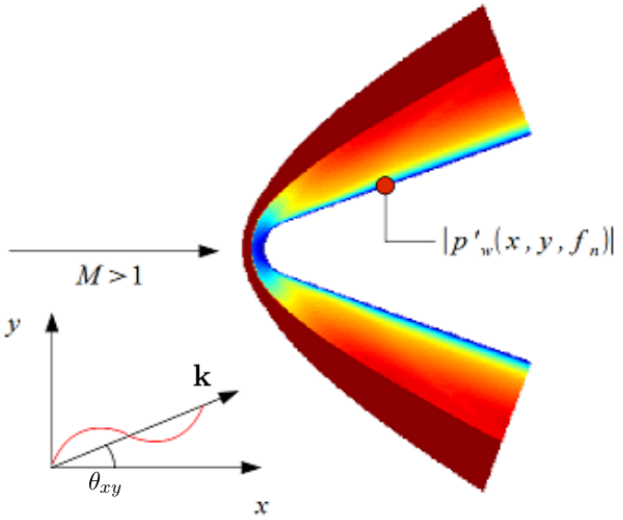


Figure 2.1: Sketch of the planar acoustic waves and of the computational domain near the nose region. The solution shown here, for illustration purposes, is the $u$ velocity field

total number of frequencies of the wave spectrum, and the subscript '$n$' indicates the $n^{th}$ frequency. The wavenumbers and the angular frequency are, in turn, expressed by

$$k_{nx} = |k_n| \cos\theta_{xy} \;;\; k_{ny} = |k_n| \sin\theta_{xy} \;;\; |k_n| = \frac{\omega_n}{\cos\theta_{xy} \pm 1/M} \;;\; \omega_n = n\omega_1 = 2\pi n f_1 \;. \tag{2.13}$$

Here, $|k_n|$ is the magnitude of the wave vector for the $n^{th}$ frequency, which depends on the angle $\theta_{xy}$, since the convection velocity of the acoustic waves is the projection of the mean freestream velocity along the wave propagation direction, while $f_1$ is the smallest frequency of the complete spectrum. From the relation for the angular frequency it is evident that each frequency is a multiple of the lowest frequency. Again, the plus sign in the denominator of $|k_n|$ indicates fast acoustic waves, while the minus sign is for slow acoustic waves.

In the unsteady computations, the acoustic waves are, then, inserted into the computational domain by imposing, at each point along the inflow boundary and at each instant of time, the following form of the vector of the conservative variables,

$$\mathbf{Q}^U = \begin{bmatrix} \rho_\infty + \rho'_\infty \\ (\rho_\infty + \rho'_\infty)(u_\infty + u'_\infty) \\ (\rho_\infty + \rho'_\infty)(v_\infty + v'_\infty) \\ (\rho_\infty + \rho'_\infty)(E_\infty + E'_\infty) \end{bmatrix} , \tag{2.14}$$

in which each physical quantity in the freestream is expressed as a sum of a steady base flow and a fluctuation term, for which equations 2.10, 2.11, 2.12, and 2.13 apply.

## 2.3 Equation for the total energy perturbation

Let us consider the relation for the dimensionless total energy in the freestream,

$$E_\infty = \frac{T_\infty}{\gamma(\gamma-1)M^2} + \frac{1}{2}\left(u_\infty^2 + v_\infty^2\right) \ . \tag{2.15}$$

By applying the Reynolds decomposition we get

$$E_\infty + E'_\infty = \frac{T_\infty + T'_\infty}{\gamma(\gamma-1)M^2} + \frac{1}{2}\left[(u_\infty + u'_\infty)^2 + (v_\infty + v'_\infty)^2\right] \ , \tag{2.16}$$

from which, by expanding the terms, and neglecting higher-order terms (on the assumption of small perturbations), we obtain

$$E_\infty + E'_\infty = \frac{T_\infty}{\gamma(\gamma-1)M^2} + \frac{1}{2}\left(u_\infty^2 + v_\infty^2\right) + \frac{T'_\infty}{\gamma(\gamma-1)M^2} + u_\infty u'_\infty + v_\infty v'_\infty \ . \tag{2.17}$$

The sum of the first two terms of the right hand side is, by definition, the freestream mean total energy. Hence, the fluctuation of the total energy is given by

$$E'_\infty = \frac{T'_\infty}{\gamma(\gamma-1)M^2} + u_\infty u'_\infty + v_\infty v'_\infty \ . \tag{2.18}$$

The mean velocity components in the $x$ and $y$ directions can be expressed as a function of the angle of attack ($\alpha$) as $u_\infty = \cos\alpha$ and $v_\infty = \sin\alpha$ (considering that the magnitude of the dimensionless freestream mean velocity, $U_\infty$, is 1). The velocity perturbation components, induced by the acoustic wave travelling in the direction of the wave vector, are given by $u'_\infty = U'_\infty \cos\theta_{xy}$ and $v'_\infty = U'_\infty \sin\theta_{xy}$, where $\theta_{xy}$ is the inclination angle of the acoustic waves with respect to the $x$-axis, and $U'_\infty$ is the magnitude of the velocity fluctuation in the wave-vector direction, which is, in turn, related to the density perturbation by

$$U'_\infty = \frac{1}{M}\rho'_\infty \ . \tag{2.19}$$

By substituting the above relations for the velocity components into the formula for the total energy, we get

$$E'_\infty = \frac{T'_\infty}{\gamma(\gamma-1)M^2} + \frac{1}{M}\rho'_\infty\left(\cos\alpha\cos\theta_{xy} + \sin\alpha\sin\theta_{xy}\right) \ . \tag{2.20}$$

At this point, in order to express the temperature perturbation as a function of the density perturbation, we consider the equation of state for a perfect gas, in which the Reynolds decomposition has been applied,

$$p_\infty + p'_\infty = \frac{1}{\gamma M^2}\left(\rho_\infty + \rho'_\infty\right)\left(T_\infty + T'_\infty\right) \ . \tag{2.21}$$

In the above equation the pressure terms are normalised with the term $\rho_\infty U_\infty^2$. By expanding the right hand side, neglecting higher-order terms, and subtracting the freestream mean pressure, we obtain

$$p'_\infty = \frac{1}{\gamma M^2}\left(\rho_\infty T'_\infty + T_\infty \rho'_\infty\right) \ . \tag{2.22}$$

In terms of the temperature fluctuation, and considering that $\rho_\infty$ and $T_\infty$ (dimensionless freestream mean density and temperature respectively) are equal to 1, we obtain

$$T'_\infty = \gamma M^2 p'_\infty - \rho'_\infty \ . \tag{2.23}$$

Substituting, in the above relation, the equation (2.10) relating the freestream pressure fluctuation to the density fluctuation, $p'_\infty = \rho'_\infty / M^2$, we obtain

$$T'_\infty = (\gamma - 1)\rho'_\infty \ . \tag{2.24}$$

Finally, by substituting this relation into the formula of the total energy, we obtain the total energy fluctuation amplitude as a function of the density fluctuation amplitude, the angle of attack and the angle of incidence of the acoustic waves, as

$$E'_\infty = \frac{1}{M}\rho'_\infty \left(\frac{1}{\gamma M} + \cos\alpha\cos\theta_{xy} + \sin\alpha\sin\theta_{xy}\right) \ . \tag{2.25}$$

## 2.4 Three-dimensional acoustic-wave model

The three-dimensional wave system consists of a main two-dimensional wave and pairs of opposite-angle oblique waves of lower amplitude. The oblique acoustic waves are considered as planar waves travelling with an angle $\theta_{xz}$ in the $xz$-plane. The freestream perturbations of $x$- and $z$-velocity components, pressure and total energy in terms of the freestream density fluctuation are still expressed by equations 2.10 and 2.11, provided we replace $\theta_{xy}$ with $\theta_{xz}$, and $v'_\infty$ with $w'_\infty$. Note that, in this case, we do not consider an inclination angle in the $xy$-plane, i.e. $\theta_{xy} = 0$, and, as a consequence, the freestream velocity component in the vertical direction is $v'_\infty = 0$. Also, as the oblique waves have an opposite angle in the $xz$-plane, their added contribution to the spanwise velocity is zero.

The freestream perturbation of the density as a function of time and Cartesian coordinates, for the case of multiple frequencies, is expressed as

$$\rho'(x,z,t) = \sum_{m=0}^{M}\sum_{n=1}^{N} A_m \cos\left(\beta_m z + \phi_m\right)\cos\left(\alpha_n x - \omega_n t + \psi_n\right) \ , \ (\beta_0 = \phi_0 = 0) \ , \tag{2.26}$$

where $\alpha_n$ and $\beta_m$ are the wavenumbers, respectively, in the $x$ and $z$ directions, $\omega_n$ is the angular frequency, $A_m$ is the amplitude of each wave mode, $\phi_m$ and $\psi_n$ are random phase angles (an exception has to be made for $m = 0$, for which $\phi_m$ is fixed to zero), $N$ and $M$ represent the total number of frequencies and (non-zero) spanwise wavenumbers respectively, while the subscripts '$m$' and '$n$' indicate the $m^{th}$ spanwise wave mode and the $n^{th}$ frequency respectively. In the present study $N = 10$, indicating a spectrum of 10 different frequencies, and $M = 2$, thus giving 2 multiple spanwise wavenumbers for the oblique waves, according to the relation $\beta_m = 2\pi m/L_z$ (with $L_z$ being the length of the domain in the $z$ direction). Note that $m = 0$ provides a 2D wave in the body reference system, as $\beta_0 = 0$ and $\phi_0 = 0$, namely a wave whose wave vector is aligned with the $x$-axis of the body reference system. However, as $x$ is perpendicular to the leading edge, for swept cases such a wave mode ($m = 0$) represents an oblique wave with respect to the streamwise direction, with an inclination angle equal to the sweep angle ($\Lambda$) of the leading edge. An illustrative example of an infinite swept leading edge and of our domain geometry (in the $xz$-plane) is shown in figure 2.2.

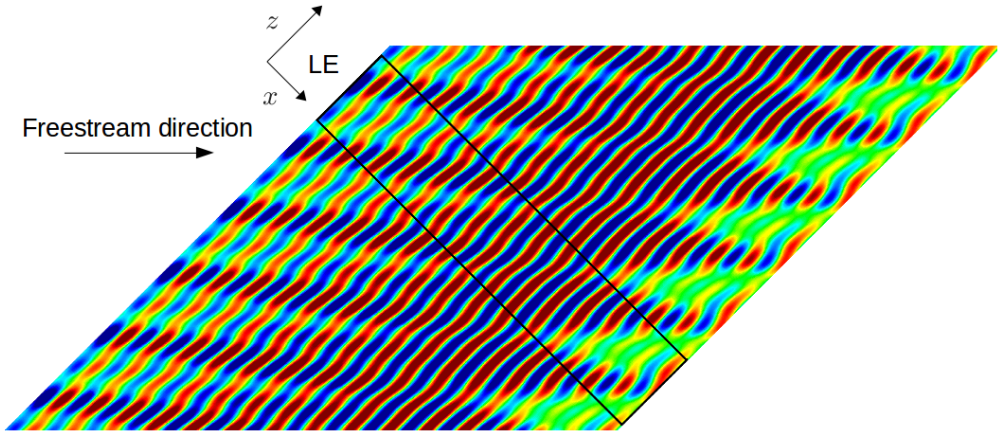


Figure 2.2: Illustrative example of an infinite swept leading edge ($\Lambda = 45°$). The black lines indicate the edges of our computational domain on the body surface in the $xz$-plane. The contours are relative to a solution for the wall pressure fluctuations

The wavenumber in the $x$-direction $\alpha_n$ is linked to the angular frequency $\omega_n$ through the relation $\alpha_n = \omega_n/(1 \pm 1/M)$, with $\omega_n = 2\pi f_n$, being $f_n$ the $n^{th}$ frequency of the forcing spectrum. The term $1 \pm 1/M$ represents the dimensionless phase speed along the $x$-axis of the freestream waves, where the plus sign indicates fast acoustic waves, while the minus sign stands for slow acoustic waves. Hence, an oblique acoustic wave travelling with an inclination angle $\theta_{xz}$ with respect to the $x$-axis has a wavenumber $\alpha$ in the $x$ direction equal to the corresponding wavenumber of the dominant 2D fast or slow acoustic wave. The value of $A_0$ determines the amplitude of the main 2D wave, while the amplitude of each pair of oblique waves for $m = 1, 2$ is linked to that of the 2D wave through the relation $A_1 = A_2 = \frac{1}{2}A_0$. For each non-zero spanwise wavenumber two

oblique acoustic waves with equal and opposite angles $\theta_{xz}$ are forced, and the amplitude $A_m$ (for $m = 1, 2$) represents the sum of the amplitudes of the two opposite-angle waves, such that each single oblique wave has an amplitude equal to $\frac{1}{4}A_0$.

Summarising, the system of forced waves consists of a superposition of a dominant 2D wave ($m = 0$) and two ($m = 1, 2$) pairs of equal and opposite angle ($\theta_{xz}$ and $-\theta_{xz}$) oblique waves, each wave having an amplitude of one fourth of the main 2D wave amplitude. The value of the inclination angle of the forced oblique waves in the $xz$-plane for each spanwise wavenumber ($m$) and for each frequency ($n$) is given by

$$\theta_{xz}^{m,n} = \pm \arctan\left(\frac{\beta_m}{\alpha_n}\right) . \tag{2.27}$$

Finally, the vector of the conservative variables at the inflow boundary in the unsteady 3D computations is

$$\mathbf{Q}^U = \begin{bmatrix} \rho_\infty + \rho'_\infty \\ (\rho_\infty + \rho'_\infty)(u_\infty + u'_\infty) \\ (\rho_\infty + \rho'_\infty)(v_\infty + v'_\infty) \\ (\rho_\infty + \rho'_\infty)(w_\infty + w'_\infty) \\ (\rho_\infty + \rho'_\infty)(E_\infty + E'_\infty) \end{bmatrix} . \tag{2.28}$$

It is reminded that (as already said above) in the considered problem, as the two opposite-angle waves travel in opposite directions along the $z$-axis, their freestream $z$-velocity perturbation cancels, so that $w'_\infty = 0$ identically. Also, the freestream perturbation of the $y$-velocity component $v'_\infty$ is fixed to zero, as all the waves are travelling in the direction parallel to the $xz$-plane.

## 2.5 Code features

The code we use to carry out our DNS computations is the SBLI (Shock-Boundary-Layer-Interaction) code, developed over a number of years at the University of Southampton. In order to perform the computations for compressible flows in the presence of shock waves, the SBLI code uses a shock-capturing method, which is applied as a filter step to the solution obtained through the base scheme at the end of each time integration step. The base scheme is, in turn, based on a fourth-order central finite difference scheme for space discretization, and makes use of an entropy-splitting method (Yee *et al.*[66]) to improve the nonlinear stability of the high-order central scheme, thus requiring less numerical dissipation than the un-split approach. At the wall either a fourth order Carpenter boundary scheme (Carpenter *et al.*[67]) or a lower-order scheme can be chosen. For time integration, a third-order Runge-Kutta scheme is used. The shock-capturing

scheme consists of a second-order TVD (total variation diminishing)-type algorithm, with a particular compression method (Yee *et al.*[68]), which restricts the artificial dissipation to the shock region, thus providing minimum dissipation in the smooth regions. Furthermore, the scheme is supplemented with the Ducros sensor (Ducros *et al.*[69]), which turns off the artificial dissipation in the vortical region (i.e. the boundary layer). A favourable feature of this sensor is that it does not require any a-priori knowledge of the shock position. The code works using MPI libraries, and has been set up to run in parallel, by dividing the domain into a number of sub-domains, and assigning each of them to a particular processor. A validation of the code can be found in the work of De Tullio *et al.*[82], where DNS results are compared with PSE (Parabolized Stability Equations) results for the case of transition induced by a discrete roughness element in a boundary layer at Mach 2.5.

## 2.6 Shock-capturing scheme

A characteristic filter (Yee *et al.*[68]), activated at the final step of each Runge-Kutta time integration cycle, allows the shock to be captured with minimum numerical dissipation. The characteristic filter consists of a second-order Harten-Yee TVD-type shock-capturing scheme, with imposed *flux limiters* that limit the anti-diffusive terms of the flux derivatives in order to satisfy the TVD stabilising condition in each direction, whilst minimising the numerical dissipation. In particular, the TVD condition in a certain direction requires that the total variation of a discrete solution in that direction, i.e. $\sum_i |q_{i+1} - q_i|$, where $q$ denotes a generic conservative variable, cannot increase with time. In order to describe the algorithm used in the filter step, we consider for simplicity the one-dimensional governing equations,

$$\frac{\partial \mathbf{Q}}{\partial t} + \frac{\partial \mathbf{F}}{\partial x} = 0 \, . \tag{2.29}$$

Using a finite-volume concept, we denote with $i-1$, $i$, $i+1$ three consecutive points of the one-dimensional computational domain, and with $i-\frac{1}{2}$, $i+\frac{1}{2}$ the points at the interface between points $i-1$, $i$, and points $i$, $i+1$, respectively. In the finite volume approach, the time variation of a generic conservative variable $q^l$ (with $l = 1, ..3$, for a one-dimensional system of conservation equations) is equal to the net-flux of the physical quantity through the interfaces $i-\frac{1}{2}$ and $i+\frac{1}{2}$ (i.e. the edges of the control volume of the fluid particle centred on the point $i$). Following this approach, and using a $1^{st}$-order forward differencing discretization for the time derivatives, we obtain the vector of conservative variables at the point $i$ and at the time $n+1$, as

$$\mathbf{Q}_i^{n+1} = \mathbf{Q}_i^n + \frac{\Delta t}{\Delta x}\left(\tilde{\mathbf{F}}_{i-\frac{1}{2}} - \tilde{\mathbf{F}}_{i+\frac{1}{2}}\right), \tag{2.30}$$

where $\Delta t$ and $\Delta x$ are the time step and the spacing between $i-\frac{1}{2}$ and $i+\frac{1}{2}$, while the terms $\tilde{\mathbf{F}}_{i-\frac{1}{2}}$ and $\tilde{\mathbf{F}}_{i+\frac{1}{2}}$ denote the numerical fluxes at the interfaces of the control volume. The numerical flux vector $\tilde{\mathbf{F}}_{i+\frac{1}{2}}$ is cast in the form

$$\tilde{\mathbf{F}}_{i+\frac{1}{2}} = \frac{1}{2}\left(\mathbf{F}_{i+1} + \mathbf{F}_i + \mathbf{R}_{i+\frac{1}{2}}\Phi_{i+\frac{1}{2}}\right), \tag{2.31}$$

where $\frac{1}{2}\left(\mathbf{F}_{i+1} + \mathbf{F}_i\right)$ represents the central differencing portion of the numerical flux, and $\frac{1}{2}\left(\mathbf{R}_{i+\frac{1}{2}}\Phi_{i+\frac{1}{2}}\right)$ is the *nonlinear dissipation* term, with $\mathbf{R}_{i+\frac{1}{2}}$ being, for characteristic-based methods, the right eigenvector matrix of the matrix $\frac{\partial F}{\partial Q}$ evaluated using a symmetric average between $\mathbf{Q}_i$ and $\mathbf{Q}_{i+1}$ (i.e. Roe's approximate average state, described by Roe[70]). The term $\Phi_{i+\frac{1}{2}}$ will be described in detail later. The numerical flux expressed in equation 2.31 represents an average between states $i$ and $i+1$, as the flux at the interface can be derived both from the flux at point $i$ through the form

$$\tilde{\mathbf{F}}_{i+\frac{1}{2}} = \mathbf{F}_i + \Delta\tilde{\mathbf{F}}^{-}_{i+\frac{1}{2}}, \tag{2.32}$$

and from the flux at point $i+1$ through the form

$$\tilde{\mathbf{F}}_{i+\frac{1}{2}} = \mathbf{F}_{i+1} - \Delta\tilde{\mathbf{F}}^{+}_{i+\frac{1}{2}}, \tag{2.33}$$

where $\Delta\tilde{\mathbf{F}}^{-}_{i+\frac{1}{2}}$ and $\Delta\tilde{\mathbf{F}}^{+}_{i+\frac{1}{2}}$ are the flux jumps respectively from the left state $(i)$ and from the right state $(i+1)$ to the internal (or intermediate) state $(i+\frac{1}{2})$ across the system of waves generated in a Riemann problem at the intermediate point. Performing the arithmetic average between equations 2.32 and 2.33, equation 2.31 is obtained. Following this approach, the nonlinear dissipation term can be expressed as

$$\Delta\tilde{\mathbf{F}}_{i+\frac{1}{2}} = \frac{1}{2}\left(\Delta\tilde{\mathbf{F}}^{-}_{i+\frac{1}{2}} - \Delta\tilde{\mathbf{F}}^{+}_{i+\frac{1}{2}}\right) = \frac{1}{2}\left(\mathbf{R}_{i+\frac{1}{2}}\Phi_{i+\frac{1}{2}}\right), \tag{2.34}$$

where, for characteristic-based methods, the term $\Phi_{i+\frac{1}{2}}$ contains the characteristic speeds (the elements of the diagonal matrix of the system of governing equations in characteristic form) of the waves travelling both leftwards and rightwards in the Riemann problem originated at $i+\frac{1}{2}$, each one multiplied with the jump (between point $i+1$ and $i$) of the corresponding characteristic variable (elements of the variable vector of the diagonalised system of equations in characteristic form).

If Roe's first-order upwind scheme (in a modified version, as in Yee *et al.*[68]) is used for the dissipation term, the elements of the vector $\Phi_{i+\frac{1}{2}}$ can be expressed as

$$\phi^l_{i+\frac{1}{2}} = -\psi(a^l_{i+\frac{1}{2}})\alpha^l_{i+\frac{1}{2}}, \tag{2.35}$$

where $a^l_{i+\frac{1}{2}}(\mathbf{Q}_i, \mathbf{Q}_{i+1})$ (that should not be confused with the unsubscripted variable denoting the speed of sound) are the elements of the diagonal matrix of the system in characteristic form (i.e. the characteristic speeds), computed through Roe's approximate

average state, and $\alpha^l_{i+\frac{1}{2}}$ are the elements of the vector of characteristic jumps, given by

$$\alpha_{i+\frac{1}{2}} = \mathbf{R}^{-1}_{i+\frac{1}{2}} \left( \mathbf{Q}_{i+1} - \mathbf{Q}_i \right), \tag{2.36}$$

with $\mathbf{R}^{-1}_{i+\frac{1}{2}}$ the left eigenvector matrix of $\frac{\partial F}{\partial Q}$, evaluated through Roe's approximate average state. In some regions of the flowfield (e.g. the sonic regions) some wave speeds can approach zero, thus providing close-to-zero values for the numerical dissipation, with the possibility of numerical instabilities and non-physical solutions. For this reason, a correction to the characteristic speeds is used (the so called *entropy correction*), in order to prevent the wave speeds from reaching too small values, and can be expressed as

$$\psi(a^l_{i+\frac{1}{2}}) = \begin{cases} |a^l_{i+\frac{1}{2}}| & |a^l_{i+\frac{1}{2}}| \geq \delta_1 \\ \frac{(a^l_{i+\frac{1}{2}})^2 + \delta_1^2}{2\delta_1} & |a^l_{i+\frac{1}{2}}| < \delta_1. \end{cases} \tag{2.37}$$

Here, $\delta_1$ is a parameter whose numerical value is problem dependent, and typical values are in the range $0.05 - 0.25$. For the simulations in the present work a more suitable form of $\delta_1$ for hypersonic blunt-body flows has been chosen, which is the form suggested by Yee *et al.*[71]

$$(\delta_1)_{i+\frac{1}{2}} = \tilde{\delta} \left( |u_{i+\frac{1}{2}}| + |v_{i+\frac{1}{2}}| + c_{i+\frac{1}{2}} \right), \tag{2.38}$$

where we remind that $c$ denotes the speed of sound in this section, and that the subscript $i + \frac{1}{2}$ denotes quantities computed on the intermediate point through Roe's average intermediate state (Roe[70]). The term $\tilde{\delta}$ is a constant set to 0.25 in all our simulations.

The scheme in equation 2.35 is first-order accurate, which means that it produces diffusive solutions that smear the high gradients. For this reason, many extensions have been made over the decades in order to make the shock-capturing schemes second-order accurate. The way to achieve high resolution consists of introducing perturbation terms in the first-order scheme, which increase the overall accuracy of the scheme. These terms can be described as *anti-diffusive* terms, as their effect is to reduce the amount of numerical dissipation added by the scheme. An example of higher-order shock-capturing scheme, which is the scheme used in our numerical simulations, is the following

$$\phi^l_{i+\frac{1}{2}} = -\psi \left( a^l_{i+\frac{1}{2}} \right) \left( \alpha^l_{i+\frac{1}{2}} - s^l_{i+\frac{1}{2}} \right), \tag{2.39}$$

where $s^l_{i+\frac{1}{2}}$ is, in general, a function of the characteristic jumps at $i + \frac{1}{2}$ and at the neighbouring interface points (i.e. $s^l_{i+\frac{1}{2}} = s^l_{i+\frac{1}{2}}(\alpha^l_{i-\frac{1}{2}}, \alpha^l_{i+\frac{1}{2}}, \alpha^l_{i+\frac{3}{2}})$). The term $s^l_{i+\frac{1}{2}}$ represents an anti-diffusive function, as it reduces the numerical dissipation. However, in order to prevent the scheme from generating spurious oscillations, it is necessary that the amount of dissipation added is sufficient for the scheme to satisfy the TVD condition; hence, the anti-diffusive term has to be limited by means of *limiter* functions (Piperno and Depeyre[72], Toro and Billett[73]). Thus, the flux-limiter approach sets in

general the accuracy of the scheme at a middle point between a low-order scheme and a high-order scheme, namely it increases the accuracy of a first-order scheme, decreasing the amount of added numerical dissipation, and limits, at the same time, the anti-diffusive terms in order to constrain the scheme to stay inside the valid region of the TVD condition. In practice, with reference to equation 2.39, the term $s^l_{i+\frac{1}{2}}$ contains the limiter in the form of a minmod function, which is equal, for a list of arguments, to the smallest number in absolute value if the arguments are of the same sign, or is equal to zero if any arguments are of opposite sign. Examples of limiter functions are (Yee *et al.*[71])

$$s^l_{i+\frac{1}{2}} = \text{minmod}\left(\alpha^l_{i-\frac{1}{2}}, \alpha^l_{i+\frac{1}{2}}\right) + \text{minmod}\left(\alpha^l_{i+\frac{1}{2}}, \alpha^l_{i+\frac{3}{2}}\right) - \alpha^l_{i-\frac{1}{2}} \tag{2.40}$$

$$s^l_{i+\frac{1}{2}} = \text{minmod}\left(\alpha^l_{i-\frac{1}{2}}, \alpha^l_{i+\frac{1}{2}}, \alpha^l_{i+\frac{3}{2}}\right) \tag{2.41}$$

$$s^l_{i+\frac{1}{2}} = \text{minmod}\left[2\alpha^l_{i-\frac{1}{2}}, 2\alpha^l_{i+\frac{1}{2}}, 2\alpha^l_{i+\frac{3}{2}}, \frac{1}{2}\left(\alpha^l_{i-\frac{1}{2}} + \alpha^l_{i+\frac{3}{2}}\right)\right] \tag{2.42}$$

Limiter functions 2.40, 2.41 and 2.42 are listed in order of decreasing diffusivity and increasing accuracy. However, as the less diffusive limiters are also the less stable, and have a lower convergence rate, limiter 2.41 is chosen for our computations, which provides a good trade-off between accuracy and stability.

The scheme in equation 2.39, together with one of the three limiter forms 2.40, 2.41, and 2.42, represents the Harten-Yee second-order *symmetric* TVD-type scheme (Yee *et al.*[71]), and has been implemented by the author of the present thesis in the version of the SBLI code used for our numerical simulations, showing good results in terms of both resolution and stability. The implementation of the Harten-Yee symmetric scheme was motivated by the need of solving numerical issues related to the original version of the TVD filter applied to our numerical case. In particular, the previous version of the SBLI code was equipped with a different type of Harten-Yee scheme, namely the second-order *upwind* TVD-type scheme (Yee *et al.*[68]), which showed very good results in several DNS studies (e.g. Sansica [79] and Van Den Eynde [77]) based on flat-plate-like computational boxes (with or without roughness elements), but which proved to be unsuitable for our cylinder-wedge geometry, as it produced asymmetric solutions (between the upper and the lower side of the wedge) in preliminary 2D test cases (set up with zero angle of attack and without freestream disturbances). The above mentioned upwind scheme, in its original implementation, is reported here, as follows

$$\phi^l_{i+\frac{1}{2}} = \frac{1}{2}\psi\left(a^l_{i+\frac{1}{2}}\right)\left(g^l_{i+1} + g^l_i\right) - \psi\left(a^l_{i+\frac{1}{2}} + \gamma^l_{i+\frac{1}{2}}\right)\alpha^l_{i+\frac{1}{2}}, \tag{2.43}$$

$$\gamma^l_{i+\frac{1}{2}} = \frac{1}{2}\psi(a^l_{i+\frac{1}{2}}) \begin{cases} \left(g^l_{i+1} - g^l_i\right)/\alpha^l_{i+\frac{1}{2}} & \alpha^l_{i+\frac{1}{2}} \neq 0 \\ 0 & \alpha^l_{i+\frac{1}{2}} = 0, \end{cases} \tag{2.44}$$

where $g^l_i$ and $g^l_{i+1}$ are the anti-diffusive terms, and need to be limited. An example of limiter function $g^l_i$ is (Yee *et al.*[68])

$$g^l_i = \text{minmod}\left[2\alpha^l_{i-\frac{1}{2}}, 2\alpha^l_{i+\frac{1}{2}}, \frac{1}{2}\left(\alpha^l_{i+\frac{1}{2}} + \alpha^l_{i-\frac{1}{2}}\right)\right]; \tag{2.45}$$

other possible forms for $g^l_i$ can be found in the work of Yee *et al.*[68]. The upwind scheme 2.43 is, in general, more accurate than the symmetric scheme 2.39, however, while the symmetric scheme is independent from the sign of the characteristic speeds, in the upwind scheme the numerical dissipation terms depend on the wave-speed sign, due to the second entropy correction term in equation 2.43, which involves the sum of the wave speed $a^l_{i+\frac{1}{2}}$ and the wave speed $\gamma^l_{i+\frac{1}{2}}$, related to the jump of the added function $g$ between points $i$ and $i+1$. This is indeed, the source of the asymmetric patterns observed in the solution of our preliminary 2D test cases.

Apart from implementing in the SBLI code the symmetric scheme, which provides symmetric solutions due its property of independence from the wave-speed sign, a modification of the upwind scheme has been proposed by the author of the present thesis, concerning the entropy correction term for the two different wave speeds. The idea consists in removing the dependence from the wave-speed sign by applying the entropy correction, in the form expressed by equation 2.37, separately for each wave speed, rather than on their sum. Following this approach, the upwind scheme has been recast in the following form

$$\phi^l_{i+\frac{1}{2}} = \frac{1}{2}\psi\left(a^l_{i+\frac{1}{2}}\right)\left(g^l_{i+1} + g^l_i\right) - \left[\psi\left(a^l_{i+\frac{1}{2}}\right) + \psi\left(\gamma^l_{i+\frac{1}{2}}\right)\right]\alpha^l_{i+\frac{1}{2}}. \tag{2.46}$$

This modified version of the upwind scheme has shown the capability of providing symmetric solutions for our cylinder-wedge geometry, with a resolution comparable to that of the original upwind scheme 2.43. However, the symmetric scheme, expressed by equations 2.39 and 2.41, has been preferred because of its higher robustness and convergence rate, and is used for all the calculations in the present thesis.

The form expressed by equation 2.39 is not actually the final form of the TVD scheme used for the computations. The numerical dissipation term $\phi^l_{i+\frac{1}{2}}$ is, in fact, pre-multiplied by another term, so called *Harten switch* (Yee *et al.*[68]), which distributes the dissipation in the flowfield in an efficient way, minimising it in the smooth regions. Thus, the numerical dissipation assumes the following form

$$\phi^{l*}_{i+\frac{1}{2}} = k\theta^{l}_{i+\frac{1}{2}}\phi^{l}_{i+\frac{1}{2}}, \tag{2.47}$$

where $k$ is a problem-dependent parameter, and $\theta^{l}_{i+\frac{1}{2}}$ is the Harten switch. For smooth flows $k$ can be very small, while in the presence of strong shock waves it has to assume higher values. The common range of $k$, considering different problems, is $0.03 \leq k \leq 2$ (Yee *et al.*[68]). In our numerical simulations, the value of $k$ is set in the range between 1.5 and 2, in which the higher values are used for the higher Mach number flows. The function $\theta^{l}_{i+\frac{1}{2}}$ is the key-mechanism for distributing the dissipation in a efficient way, achieving high accuracy in regions where minimum numerical dissipation is needed (e.g. the boundary layer), and can be expressed as

$$\theta^{l}_{i+\frac{1}{2}} = \max\left(\hat{\theta}^{\mathrm{l}}_{\mathrm{i}}, \hat{\theta}^{\mathrm{l}}_{\mathrm{i+1}}\right), \tag{2.48}$$

$$\hat{\theta}^{l}_{i} = \frac{\left|\left|\alpha^{l}_{i+\frac{1}{2}}\right| - \left|\alpha^{l}_{i-\frac{1}{2}}\right|\right|}{\left|\alpha^{l}_{i+\frac{1}{2}}\right| + \left|\alpha^{l}_{i-\frac{1}{2}}\right|}. \tag{2.49}$$

In conclusion, the shock-capturing algorithm used for our numerical simulations consists of the second-order symmetric Harten-Yee TVD-type scheme 2.39, in conjunction with the limiter function 2.41 and the Harten switch, expressed by equations 2.47, 2.48 and 2.49. The shock-capturing algorithm, which has been described for a one-dimensional case here, has to be solved in all the other directions for 2D and 3D problems.

## 2.7 LES approach: Mixed-Time Scale Model

The main feature of the DNS is the capability of resolving all the length scales of the flow, but it requires very fine grids to resolve the smallest length scales. The basic idea of the Large Eddy Simulation (LES) approach, instead, is to resolve only the largest length scales of the flow, and to remove the smallest ones, by applying a low-pass filter to the governing equations 2.2, which reduces the computational cost of the numerical simulation. However, the unresolved smallest length scales have an important effect on the flowfield, which needs to be modelled. A detailed description of the LES methodology is given by Sagaut [78].

As a first step, the governing equations are filtered by means of a low-pass convolution filter applied onto the variable vector $\mathbf{Q}$, as

$$\overline{\mathbf{Q}}(x,y,z,t) = \int_{-\infty}^{\infty}\int_{-\infty}^{\infty}\int_{-\infty}^{\infty}\mathbf{Q}(\tilde{x},\tilde{y},\tilde{z},t)G(\tilde{x}-x,\tilde{y}-y,\tilde{z}-z)d\tilde{x}d\tilde{y}d\tilde{z} \tag{2.50}$$

where $\overline{\mathbf{Q}}$ is the filtered variable vector, and $G$ is the filter convolution kernel, which has a cutoff length scale (or characteristic length scale) $\Delta$. All the length scales smaller than $\Delta$ are not resolved, and are called sub-grid scales (SGS). From the above definition of the low-pass filter, the flowfield $\mathbf{Q}$ can be considered as a sum between the filtered field ($\overline{\mathbf{Q}}$) and a sub-filtered field ($\mathbf{Q}'$, i.e. the unresolved portion).

The use of the spatial filter 2.50 leads to the filtered conservative governing equations, to which another filter, i.e. the Favre filter, is applied. The Favre filter is defined as

$$\tilde{\phi} = \frac{\overline{\rho\phi}}{\overline{\rho}} \ , \tag{2.51}$$

where $\phi$ is any physical quantity. For example, the continuity equation with the filters 2.50 and 2.51 is

$$\frac{\partial \overline{\rho}}{\partial t} + \frac{\partial \overline{\rho}\tilde{u}_i}{\partial x_i} = 0 \ , \tag{2.52}$$

in which the filter 2.51 has been applied to the term $\overline{\rho u_i}$. The derivation of the complete set of the Favre-filtered equations is beyond the scope of the present thesis, and can be found in the work of Sansica [79].

The second step is to model the SGS terms that are present in the Favre-filtered equations. Some of these terms can be neglected, as shown in the work of Touber and Sandham [80], and the remaining SGS terms that need to be modelled are the SGS stress tensor,

$$\sigma_{ij} = \overline{\rho}(\widetilde{u_i u_j} - \tilde{u}_i \tilde{u}_j) \ , \tag{2.53}$$

and the SGS heat flux,

$$\Theta_i = \widetilde{T u_i} - \tilde{T}\tilde{u}_i \ . \tag{2.54}$$

The SGS stress tensor is modelled as

$$\sigma_{ij} - \frac{1}{3}\delta_{ij}\sigma_{kk} = -2\overline{\rho}\nu_t \widetilde{S}^*_{ij} \ , \tag{2.55}$$

while the SGS heat flux is modelled as

$$\Theta_i = -\frac{\nu_t}{Pr_t}\frac{\partial \tilde{T}}{\partial x_i} \ . \tag{2.56}$$

In equations 2.55 and 2.56, $\nu_t$ represents the eddy viscosity, $Pr_t$ the turbulent Prandtl number, which is assumed constant and equal to 1, while the term $\widetilde{S}^*_{ij}$ is the deviatoric part of the strain-rate tensor, which is given by

$$\widetilde{S}^*_{ij} = \widetilde{S}_{ij} - \frac{1}{3}\delta_{ij}\widetilde{S}_{kk} \ , \tag{2.57}$$

and

$$\widetilde{S}_{ij} = \frac{1}{2}\left(\frac{\partial \tilde{u}_i}{\partial x_j} + \frac{\partial \tilde{u}_j}{\partial x_i}\right) \ . \tag{2.58}$$

The eddy viscosity $\nu_t$ is, then, obtained through the mixed-time scale (MTS) model (Inagiki *et al.* [81]) as

$$\nu_t = C_{MTS} k_{es} T_S \ , \tag{2.59}$$

in which $k_{es}$ is the SGS turbulent kinetic energy, given by

$$k_{es} = \left[\tilde{u}_i - \tilde{\bar{u}}_i\right]\left[\tilde{u}_i - \tilde{\bar{u}}_i\right] \ , \ \tilde{\bar{u}}_i = \frac{\overline{\bar{\rho}\tilde{u}_i}}{\bar{\bar{\rho}}} \ , \tag{2.60}$$

$T_S$ is the mixed-time scale, defined as

$$T_S = \left(\frac{\Delta}{\sqrt{k_{es}}}\right)^{-1} + \left(\frac{C_T}{|\tilde{S}^*|}\right)^{-1} \ , \tag{2.61}$$

while $C_{MTS}$ and $C_T$ are two constants, which in our simulations have been set to 0.03 and 10 respectively (as in Touber and Sandham [80]).

The main advantages of the MTS model are that it does not need a wall-damping function, as the eddy viscosity decreases near the wall, and that the eddy viscosity vanishes in the laminar regions of the flow, as the turbulent kinetic energy ($k_{es}$) approaches zero here.

Finally, it should be mentioned that the spatial filter (equation 2.50) used in the SBLI code has a characteristic length scale (or width), $\Delta$, equal to the grid spacing, and is applied only in the streamwise and spanwise directions.

# Chapter 3

# Grid features and numerical noise reduction

In this Chapter we will describe the main properties of the grids used in our simulations, as well as numerical issues related to the grid quality and concerning the production of spurious oscillations. The effect of this numerical noise on the physical solution and its sensitivity to the grid refinement will be shown through a grid resolution study applied to one of the 2D cases relative to the DLR experiments. A grid-adaptation methodology, along with a local shock refinement technique, aimed at reducing the numerical noise, which have been used for some of our simulations (including the 3D cases), will be presented here and tested on 2D cases. All the results shown in this Chapter, which are relative to the set of 2D numerical cases simulating the DLR experiments, serve to illustrate and validate the above mentioned grid properties and techniques. For the complete set of results of our 2D simulations, and a more detailed discussion about their physical relevance, the reader should refer to Chapter 4.

## 3.1 Computational domain and source of numerical oscillations

Figure 3.1 shows an example of a typical grid used for the numerical simulations, in non-dimensional coordinates.

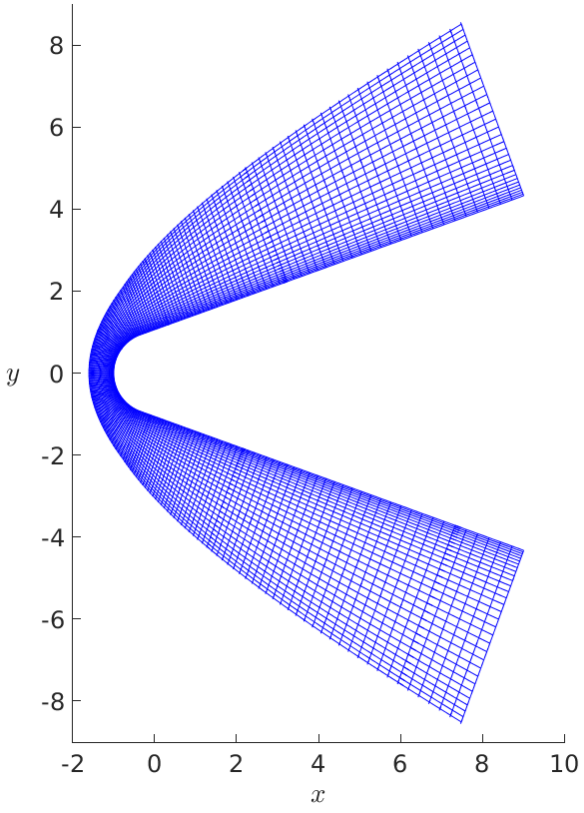


Figure 3.1: Example of mesh used for preliminary numerical simulations. Size = 360 × 150, grid plotted every 5 and 2 points in the wall-normal and wall-tangential directions respectively

The length of the domain in figure 3.1 is about 10 nose radii, which is the dimension used for our preliminary 2D simulations, and corresponds to the nose region of the 20° half-wedge angle cylinder-wedge domain considered in Chapter 4 to reproduce the geometry of the measurement probe used in the DLR experiments. Figure 3.2 shows the details of the mesh in the nose region close to the stagnation point. As can be seen, the computational domain is made of two families of curves, one in the direction tangential to the wall (which is denoted by the index $j$), and the other in the wall-normal direction (denoted by the index $i$). The grid generation method, based on the approach adopted by Bianchi *et al.*[83], adapts the computational domain to the shape of the approximated shock resulting, for a given Mach number, from Billing's correlations (Anderson[1]). A stretching function increases the density of points towards the wall in the $i$ direction, so that to resolve the boundary-layer region. Stretching is also provided towards the outer edge of the domain, in order to provide higher resolution near the bow shock wave.

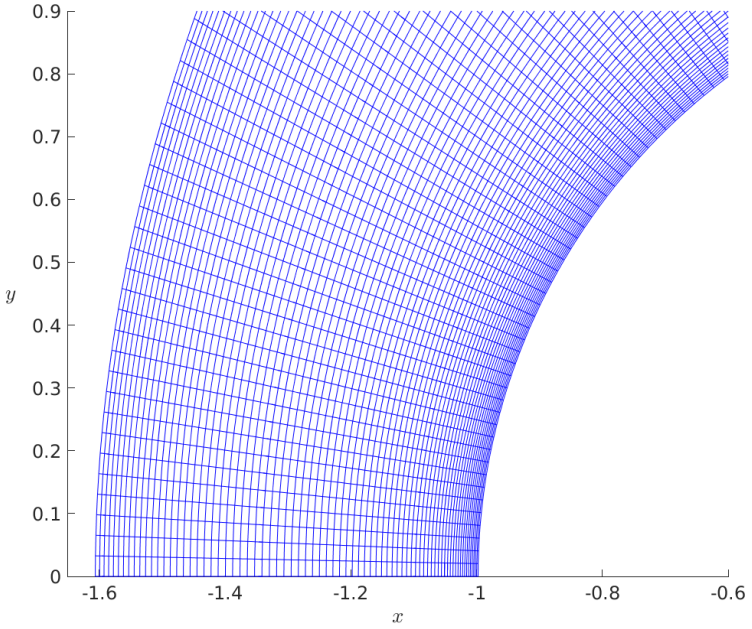


Figure 3.2: Details of the mesh in the nose region. Size = $360 \times 150$, grid plotted every 2 points in the wall-normal direction

Figure 3.3 shows an example of the grid (of size $2240 \times 150$) used for the numerical cases simulating the DLR wind-tunnel experiments. The domain extends up to about 400 nose radii downstream, thus covering the length within which a series of pressure transducers have been placed on the wall of the measurement probe (only the upper half of the domain is shown in the figure, due to the symmetry).

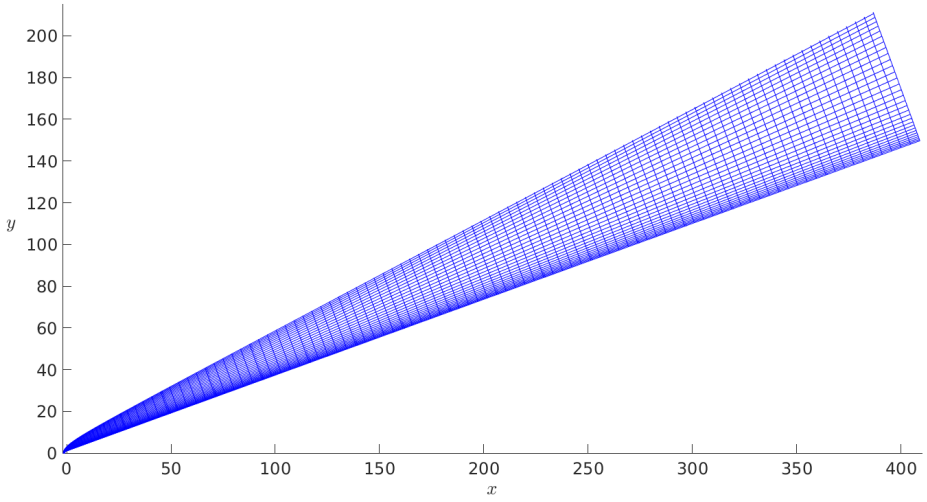


Figure 3.3: Example of computational domain used in the six numerical cases concerning the DLR wind-tunnel experiments, in non-dimensional coordinates. Only half of the domain is shown due to the symmetry of the geometry. Size = $2240 \times 150$, grid plotted every 5 and 10 points in the wall-normal and wall-tangential directions respectively

Preliminary unsteady simulations contained high levels of numerical noise affecting the solution both behind the shock and on the wall. In particular, the results showed that if the amplitude of the freestream acoustic waves (in terms of the density fluctuation amplitude) was below a certain order of magnitude ($1 \times 10^{-2}$) the fluctuation levels downstream of the shock were strongly affected by numerical noise that seemed to come from the nose region. As a consequence, the solution of the fluctuation quantities inside the boundary layer was not reliable, and this imposed the need to find the source of the numerical noise as well as an affordable way to suppress, or at least reduce, it to an acceptable level. The cause of the numerical noise was found to be in shock-grid misalignment, which is a known problem in the literature (Lee and Zhong[74]). In particular, the $j$-curves in proximity to the shock should be closely aligned with the curved shock in order not to generate spurious numerical oscillations of the physical quantities behind the shock (theoretically, the best situation would be that of a unique grid line following the shock shape). The problem is illustrated in figure 3.4, where the density fluctuation field (obtained by inserting fast acoustic waves with a density fluctuation amplitude of $1 \times 10^{-4}$ in the freestream) in the nose region is shown for one of the six numerical cases relative to the DLR experiments ($M = 6$, $Re = 630$, $\alpha = 0°$, the conditions for all the cases are given in Chapter 4). As can be seen, density spikes are formed just behind the shock curve (corresponding to the blue region), giving rise to oscillations in the density field that are convected downstream and along the wall. Figure 3.5 shows a close up on the points where the problem originates.

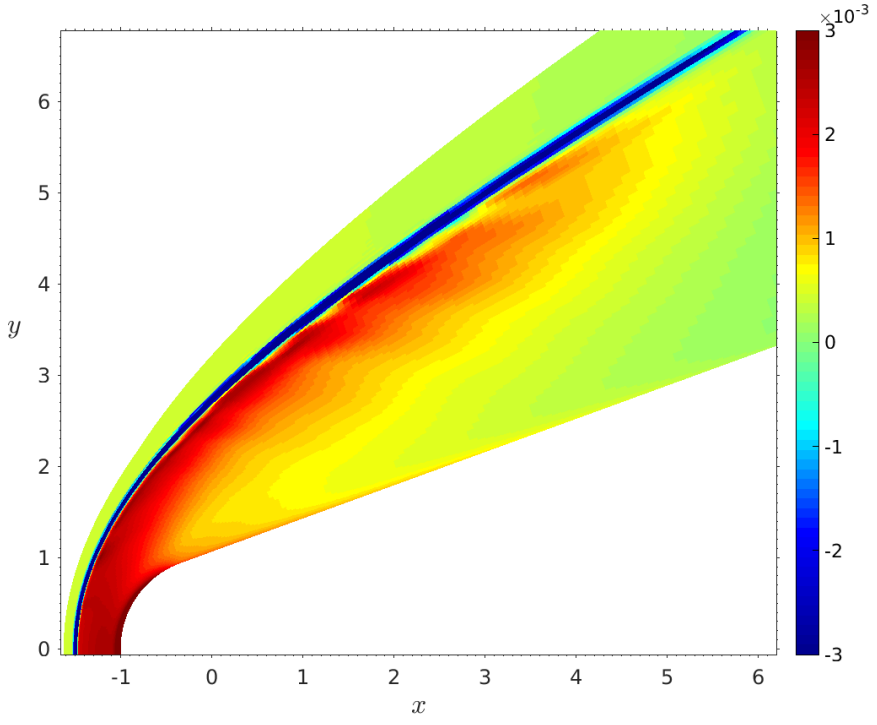


Figure 3.4: Example of numerical oscillations in the density fluctuation field. Mach 6 case

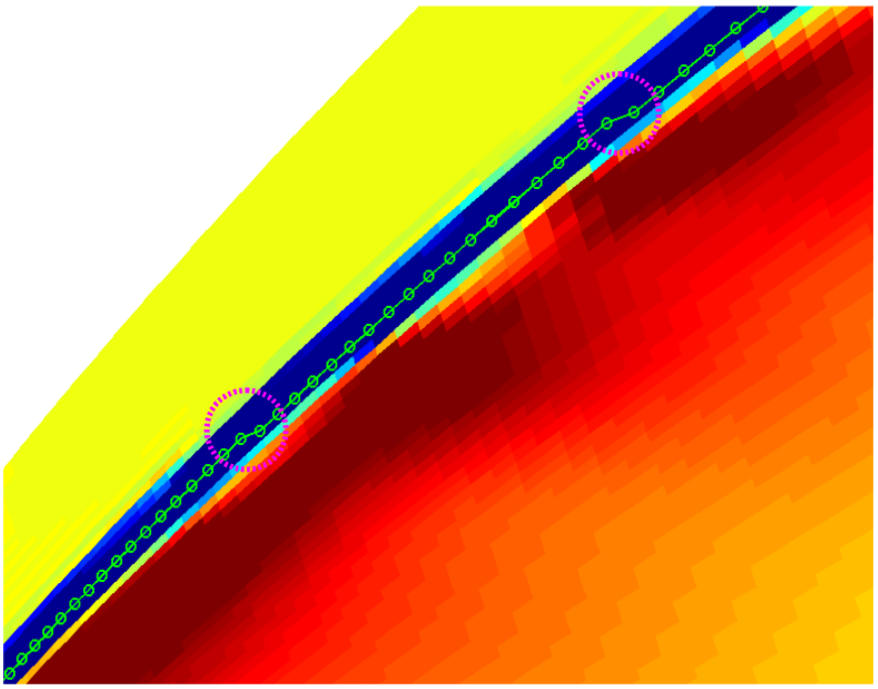

Figure 3.5: Example of numerical oscillations in the density fluctuation field. Close up on the shock-grid misalignment points. Mach 6 case

The green line with circular markers, in figure 3.5, is the locus of the grid points (markers) where the shock is located (corresponding to the points where the pressure gradient, computed through a fourth-order central finite difference scheme, is maximum). It can be seen from the figure how, at some points (those shown with purple circles), the shock jumps from one $j$-grid line to another, and in correspondence of these points a density oscillation is released into the flowfield. This demonstrates that the problem of the numerical oscillations (or spikes) is correlated to a shock-grid misalignment problem. The poorer is the alignment, the higher are the density spikes and the oscillations affecting the solution on the wall.

Another example of misalignment problem is shown in figure 3.6, for a case at $M = 7.3$, and $Re = 440$. In this figure it is evident a strong spike of density fluctuations is seen at a point just behind the shock, at $x \approx 205$. Figure 3.7 shows a close up of the point of interest, where it is evident that the shock jumps from a grid line to another, due to the misalignment, and a density spike is formed.

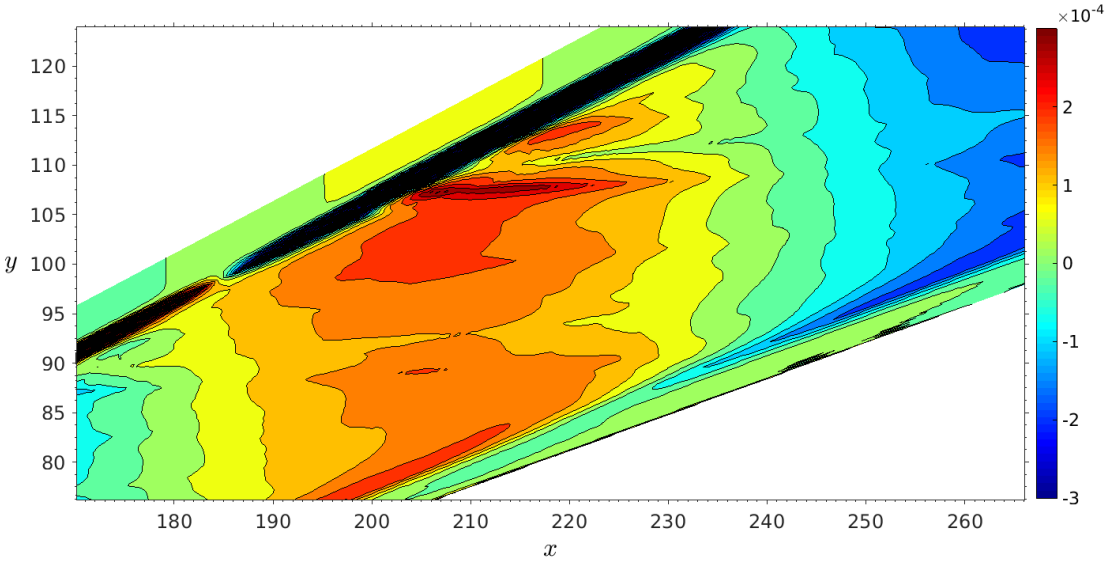


Figure 3.6: Example of numerical oscillations in the density fluctuation field. Mach 7.3 case

The problem of the shock-grid misalignment and the origin of post-shock oscillations was examined by Lee and Zhong[74], who also considered the effect of the grid resolution on the numerical noise generation. In particular, they showed that the intensity of the post-shock oscillations was more significantly influenced by the shock-grid alignment than the grid resolution, which, in contrast, affects the wavelength of the oscillations (which increases for coarser grids). A grid resolution study shown in the next Section of the present Chapter will demonstrate a very good agreement with the results of Lee and Zhong[74] concerning the role of the grid resolution on the numerical noise.

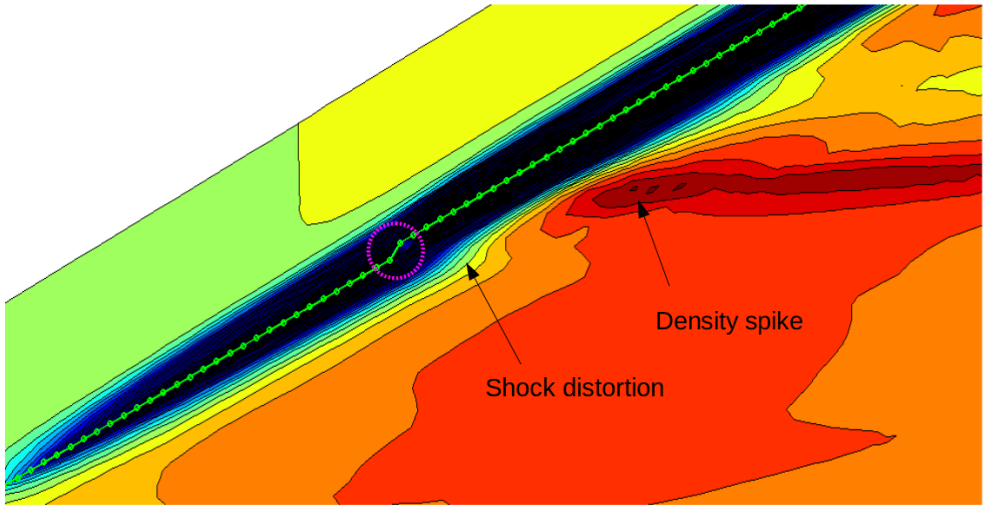


Figure 3.7: Example of numerical oscillations in the density fluctuation field. Close up on the misalignment point. Mach 7.3 case

The problem of the post-shock oscillations generated by shock-capturing schemes was also studied from a mathematical point of view by Arora and Roe[75], and Zaide and Roe[76], who addressed the cause of the spurious numerical oscillations in the case of slowly moving shocks (which is relevant to our case, as the shock oscillates slightly due to the interaction with the acoustic waves) to the nonlinearity of the Rankine-Hugoniot jump conditions, and to the presence in the numerical solution of intermediate shock states (states in the middle between the left state and the right state of a shock), which results in an ambiguity of the shock position. The ambiguity in the shock position consists in the fact that, depending on whether we apply the conservation of the density or the conservation of the energy to estimate the shock position, we will obtain two different estimates (Zaide and Roe[76]). Moreover, this ambiguity seems to be Mach-number dependent, increasing for higher Mach numbers. The main consequence of this problem appears to be the generation of a spike of the momentum behind the shock, giving rise to numerical oscillations of the physical variables.

On the basis of the observations above, there are two practical ways to reduce the post-shock numerical noise: (i) adding more numerical dissipation by the shock-capturing scheme, (ii) aligning as much as possible the grid with the shock shape. The first target can be achieved by simply imposing a higher value for the coefficient $k$ that multiplies the numerical dissipation term in equation 2.47. This is indeed the approach we used in all our numerical simulations, by setting, as already said in Chapter 2, the value of $k$ in the range between 1.5 and 2, which represents the maximum value suggested by Yee *et al.*[68]. This method has allowed us to obtain good solutions for the receptivity of the fluctuation quantities along the body wall for the 2D numerical cases with zero angle of attack, although, as will be shown in Section 3.2, numerical oscillations of limited amplitude are still present, in particular in the nose region, which, however, do not affect the physical solution (this applies in general to all the results shown in Chapter 4). In contrast, when an asymmetric case (with an angle of attack equal to 10°) is considered, adding more numerical dissipation was not enough to reduce the numerical noise up to an acceptable level. Thus, in this case, as will be shown in Section 3.3, a grid-alignment technique on both the wedge sides was necessary in order to obtain sensible results. A discussion about the application of the shock-grid alignment methodology in our 3D cases (considered in Chapters 5 and 6) will be given as well in Section 3.3 of the present Chapter.

## 3.2 Grid resolution study for the case $M = 6$, $Re = 630$ and $\alpha = 0°$, for the wedge with two-dimensional acoustic waves

In this Section, we present a resolution study for one of the six numerical test cases ($M = 6$, $Re = 630$ and $\alpha = 0°$), in which we compare the pressure fluctuation amplitude distributions along the wall at different frequencies (obtained through a Fast Fourier Transform approach) between two different grid levels. Among these, one is the same grid size we have used for the results that will be shown in Chapter 4 (2244×150), which we refer to as the fine grid, and the other is a coarser grid, whose size is lowered by 1/3 in both directions with respect to the fine grid. For time saving purposes, the domain for the coarse grid is half of the domain used for the results shown Chapter 4, and corresponds to a length in the streamwise direction of approximately 200 nose radii, so that the coarse grid size is 908×100 (1496×100 would be the size for the full 400 nose radii length domain; while 908 points in the wall-tangential direction correspond to half of the domain length with the point distribution being denser in the nose region). The simulations have been run with freestream fast acoustic waves, at an amplitude of $10^{-4}$ (relative to the freestream density disturbance), and for 10 multiple frequencies (from 50 kHz to 500 kHz).

Figure 3.8 shows the wall response for the two grid levels, while figure 3.9 shows a close-up in the nose region. The wall pressure fluctuation amplitudes ($p'_w$) are normalised with the pressure fluctuation amplitude imposed in the freestream ($p'_\infty$). Note that, to simplify the notation, from now on we will refer to the fluctuation amplitudes omitting the absolute value symbols (| |). A good agreement of the results between the two grid levels is shown at all the frequencies, indicating that the overall trend of the response along the wall can be considered, within a certain tolerance, as grid independent. However, the results show the presence of numerical oscillations, pertaining to the noise coming from the shock and affecting the solution at the wall, especially in the nose region. Furthermore, these oscillations are grid dependent at all the frequencies. In particular, it can be seen that the grid resolution has a strong influence on the phase and the wavelength of such oscillations, with the wavelength decreasing as the grid size is increased. This is evident by looking closely at the oscillations in the nose region shown in figure 3.9, and by comparing the distance between two consecutive peaks for the solution obtained with the coarse and the fine mesh. The amplitude is affected as well by the grid resolution, but, while in the nose region it is decreased by refining the grid, as expected, further downstream this effect is lost, and the oscillation amplitude seems no longer be reduced by a higher grid resolution (figure 3.8).

These results for the numerical oscillations agree qualitatively very well with the results shown by Lee and Zhong[74] on the post-shock spurious numerical oscillations using shock-capturing schemes. In particular, in their work it is highlighted that a higher

grid resolution decreases the wavelength of such oscillations, but provides only a slight reduction of their amplitude, which, in turn, seems to be much more sensible to the shock-grid alignment, as will be shown in Section 3.4.

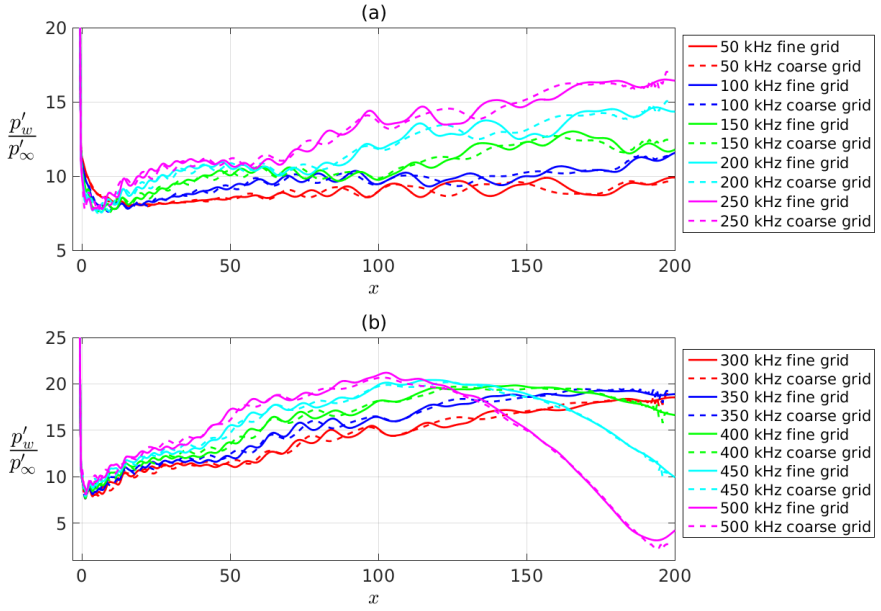


Figure 3.8: Pressure fluctuation distribution along the wall at the lower frequencies (a), and the higher frequencies (b), for two different grid levels

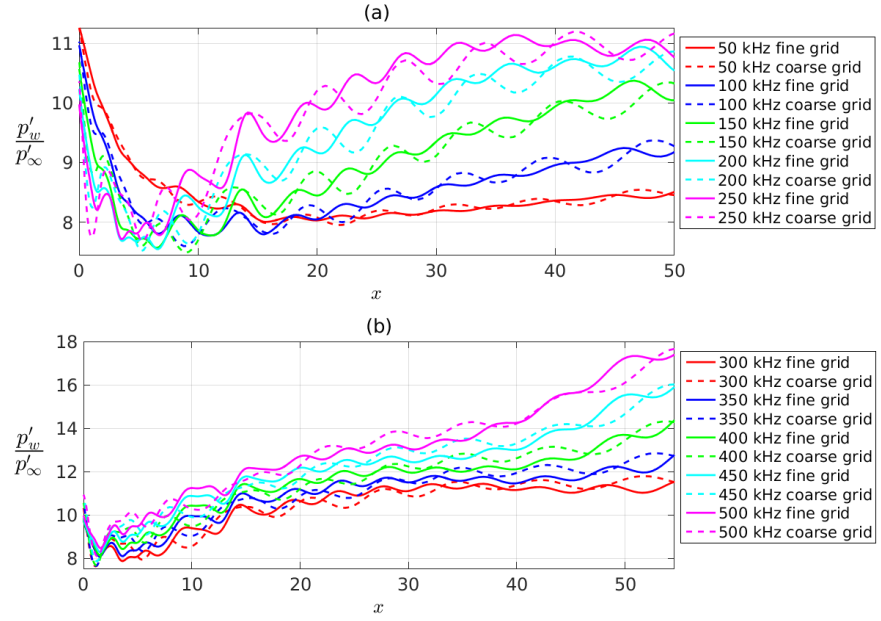


Figure 3.9: Close-up in the nose region of the wall pressure fluctuation distribution at the lower frequencies (a), and the higher frequencies (b), for two different grid levels

In conclusion, in the light of our grid resolution study, it emerges that the overall response along the wall agrees very well between the two different grid levels, thus confirming a good grid independence of the physical information provided by our numerical results. The numerical oscillations are, in contrast, significantly sensitive to the grid resolution, in terms of their phase and wavelength, and slightly grid dependent relative to their amplitude.

## 3.3 Shock-adapted grid methodology

In this Section a new method to obtain grids aligned with the computational shock is presented. Our default grid generation method (Bianchi *et al.*[83]) consists of adapting the shape of the internal grid lines in proximity of the domain outer edge with the shock shape estimated by Billing's correlations (Anderson[1]) in function of the Mach number and the radius of the circle for a cylinder-wedge geometry. However, although Billing's correlations provide a good approximation of the shock shape, there will be in general a difference between the estimated shock shape by Billing's correlations and the shape obtained by the direct numerical simulations. This means that adapting the domain to the shock shape estimated by Billing's correlations will in general result in a certain level of misalignment between the shock and the grid. For this reason, in order to suppress or at least reduce in amplitude the grid-dependent post-shock oscillations, a new method based on adapting the grid to the shape of the shock obtained in a previous numerical simulation has been developed. The method consists of three steps: (i) first, computing the baseflow of a particular numerical case by means of a grid obtained by Billing's correlations; (ii) then, computing the shock shape by identifying the points of maximum spatial pressure gradient in the wall-normal direction, and finding a numerical fit to the computed shock shape; (iii) finally, obtaining a new grid adapted to the shock shape, and repeating the simulation from the previously computed solution. The final steady-state solution contains a shock that is well aligned with the grid. This solution will then be the starting solution for the unsteady simulations. As a first test of the methodology, the equation used to fit the shock shape is the analytic equation of an east-west opening hyperbola centred at the point $(h,\, g)$ in a Cartesian coordinate system,

$$\frac{(x-h)^2}{a^2} - \frac{(y-g)^2}{b^2} = 1 \ , \tag{3.1}$$

where $h = -a - \delta_{st}$ (with $\delta_{st}$ being the shock stand-off distance along the stagnation line), $g = 0$, $a$ is the distance between the centre of the hyperbola (intersection point between its two asymptotes) and the vertex of each branch, and $b$ is linked to $a$ through the relation $b = a \tan\theta$, with $\theta$ being the inclination angle of the asymptotes with the hyperbola transverse axis (which is the $x$-axis in our case). Figure 3.10 shows, for illustration purposes, the example of an east-west opening hyperbola centred at the

origin of the Cartesian coordinate system. Among the two branches (blue curves) of the hyperbola shown in figure 3.10, we take the one on the right hand side, along the positive $x$-semi-axis. The value of $h$ translates the hyperbola vertex (the intersection with the $x$-axis) to the point on the negative $x$-semi-axis where the shock is located along the stagnation line. In fact, in our non-dimensional Cartesian reference system the centre of the circular leading edge is at the origin of the axes and the stagnation point is located at (-1,0) (as evident in figure 3.2).

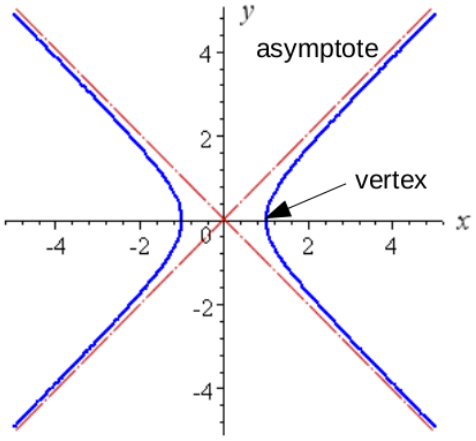


Figure 3.10: Illustration of an east-west opening hyperbola centred at the origin of the coordinate system

From the first baseflow solution, the stand-off distance ($\delta_{st}$) along the stagnation line and the inclination angle ($\theta$) of the shock shape at a large distance from the nose (at a theoretically infinite distance it is equal to the inclination angle of the oblique weak shock formed on a ramp with the same inclination angle as the half-wedge angle) can be evaluated. Finally, the parameter $a$ is varied until the value that provides the best fit between the hyperbola and the shock shape is found. Once all the coefficients in equation 3.1 are known, they are used in the grid generation process. The resulting adapted grid will then contain a $j$-line exactly following the analytical hyperbola fitting the computational shock. This method has proved good capabilities of noise reduction, which make it suitable for the purposes of our 2D simulations, namely the laminar wall-response analysis to freestream disturbances. In particular, the effectiveness of this shock-grid alignment technique, applied to a 2D Mach 6 case with an angle of attack, will be shown in Section 3.4.

The shock-adapted grid obtained through the method of the analytical hyperbola described above provides, in general, a good overall shock-grid alignment through the whole length of the shock curve, but can still allow the presence of small local misalignments, in particular in the curvilinear part of the bow shock. This happens, for example, in cases where the numerical solution is affected by some oscillations or 'bump' along the shock curve, which may be due to the presence of a small background numerical noise,

unsteadiness of the solution, a poor initial grid resolution, or geometrical imperfections of the wall, as in the case of localised roughness (which is not treated in the present study). In all these cases, it is more practical to use a method that does not force the grid to follow a regular shape according to an analytical formula. For this reason, a method based on a spline interpolation has also been developed. This method fits a spline curve, computed over all the $x$ points of our grid resolution, through some selected points along the computational shock, in order to obtain a smooth curve with $y$ coordinates adjusted to guarantee a local shock-grid alignment also in the irregular regions of the numerical shock. Then, through an iterative procedure (after each computation a spline-based shock-adapted grid is obtained, which will be the grid of a successive simulation, and so on), a smoother computational shock is obtained. The smoother is the shock, the more regular will be the next-step adapted grid. The final result will be a properly smooth highly shock-aligned grid, along with a high-quality baseflow to be used as restart solution of the unsteady simulations. Figure 3.11 shows an example of one application of the spline-based method (for a symmetric Mach 6 case). As can be seen, a very good alignment is obtained everywhere along the shock.

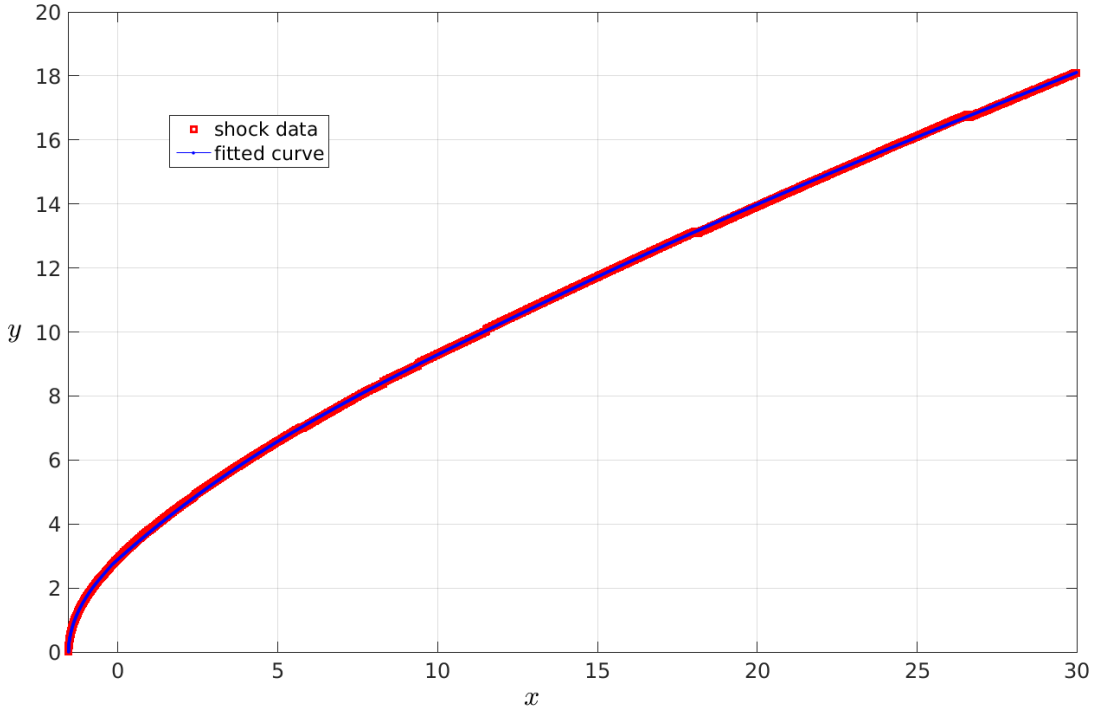


Figure 3.11: Example of shock-adapted $j$- grid line in the curvilinear part of the shock, obtained through a spline interpolation

Due to the above mentioned multi-step procedure, this method requires, in general, more computational efforts compared to the analytic-hyperbola-based method, which, in contrast, provides a regular grid straight from the beginning. For this reason, the spline-based method is used only for the 3D span-periodic wedge simulations (that will be treated in Chapter 5), in which the analysis of the breakdown-transition process,

especially at the low freestream disturbance amplitudes, requires very low levels of numerical-noise contamination. In particular, for these cases, the shock-grid alignment is achieved through 2D simulation of the corresponding baseflow (the geometry is a planar span-periodic wedge), in both swept and unswept cases. The 2D shock-adapted grid is then extruded in the third dimension, and unsteady simulations with 3D freestream disturbances are carried out. For the 3D simulations relative to the Mach 6 generic forebody geometry (Chapter 6), instead, none of the above described method is used, as the shock-grid alignment methodology was not extended to a generic 3D geometry. However, for the 3D generic forebody case, an excellent shock-grid alignment is not required, as, due to a small half-wedge angle (4°) and to very high values of the sweep angle reached by the leading edge in the off-centerline region (see geometry details in Chapter 6), a relatively weak shock is formed in front of the body, which producing very small noise levels not affecting the physical solution. For this reason, and as the unsteady simulations have been performed only at high freestream amplitude levels, the effect of post-shock numerical oscillations on the boundary-layer solution is negligible in this case. Hence, the standard method, based on Billing's correlations, has been used to generate the 3D grid in the generic forebody case.

## 3.4 Effect of the shock-grid alignment. Application to the case $M = 6$, $Re = 630$ and $\alpha = 10°$, for the wedge with two-dimensional acoustic waves

In this Section we show an application of the shock-adapted grid method based on the analytic hyperbola to a case with an angle of attack of 10°, whose solution is affected by the shock-grid misalignment problem, particularly on the windward side (the bottom side of the wedge). The problem of the numerical noise generated behind the shock is seen in figure 3.12, which shows the density fluctuation field obtained by inserting fast acoustic waves in the flow direction with an amplitude of $10^{-4}$. As can be seen, on the windward side (where the shock is stronger) there are strong post-shock oscillations (or density spikes) originating from the shock and travelling downstream. This numerical noise corrupts the solution of the wall pressure fluctuation distribution along the bottom side of the body for each acoustic frequency (a set of 10 frequencies from 50 kHz to 500 kHz with different phase), as shown in figure 3.13 (the wall pressure fluctuations $p'_w$ are normalised with the freestream pressure fluctuation $p'_\infty$).

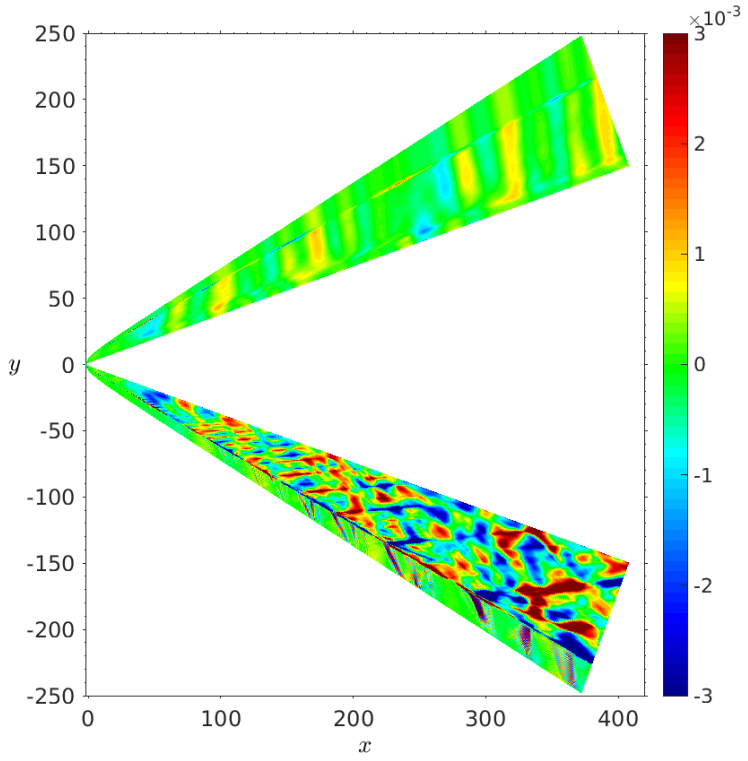


Figure 3.12: Density fluctuation field with the initial non-adapted grid

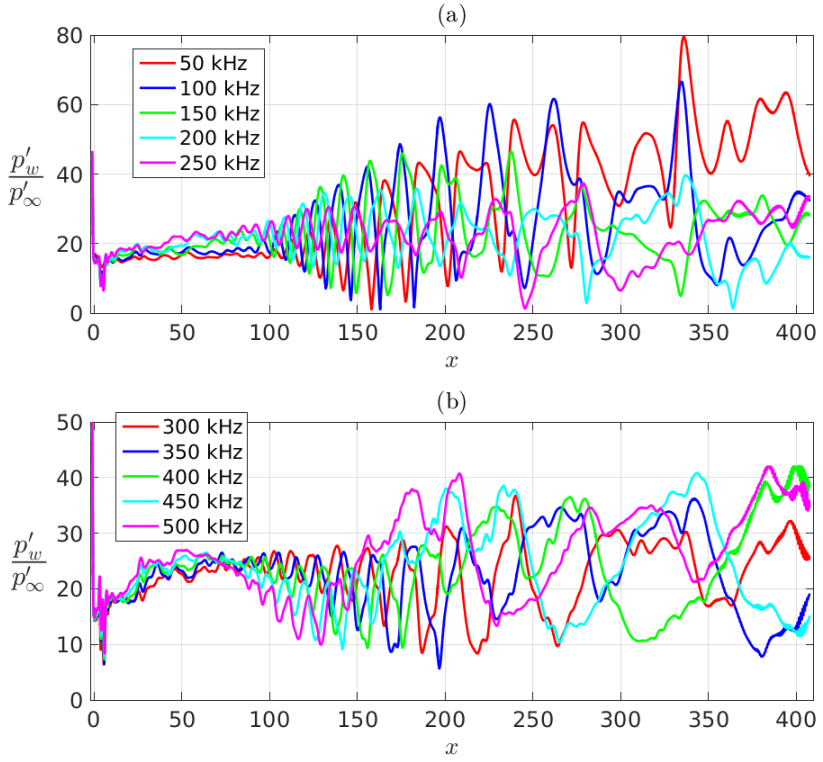


Figure 3.13: Pressure fluctuation distribution along the wall at different frequencies on the windward side, with the initial non-adapted grid, for the lower frequencies (a) and the higher frequencies (b)

Figure 3.14 shows the comparison between the computed shock shape, the shape of the initial grid and that of the shock-adapted grid obtained through the analytic-hyperbola method described in Section 3.3. The shape of the initial grid corresponds to the grid line that follows the shock shape estimated by Billing's correlations (for zero angle of attack), while the one concerning the adapted grid corresponds to the grid line following the analytical hyperbola used in this example to fit the computed shock. Clearly, there is a significant misalignment issue on the lower side with the initial grid, while the new method provides a very good fitting both on the upper and the lower side.

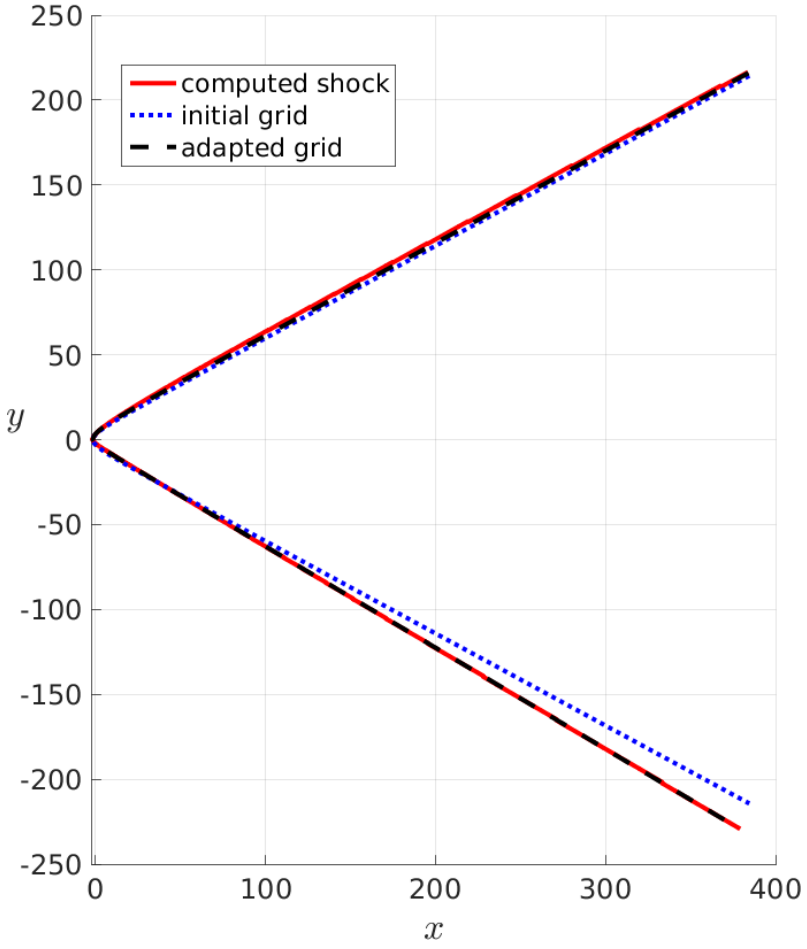


Figure 3.14: Shock shape computed with the initial grid, compared to both the initial and the new adapted grid shapes

Due to the asymmetry of this particular case, two different hyperbolic functions (with different angle $\theta$ and parameter $a$) have been used separately to fit the shock shapes on the upper and the bottom sides of the body. The result is a asymmetric shock-adapted grid, as shown by figure 3.15 in the nose region. Figure 3.16 shows the details of the new adapted grid along the lower side of the wedge, and the alignment with the shock curve (red line) computed with the initial grid.

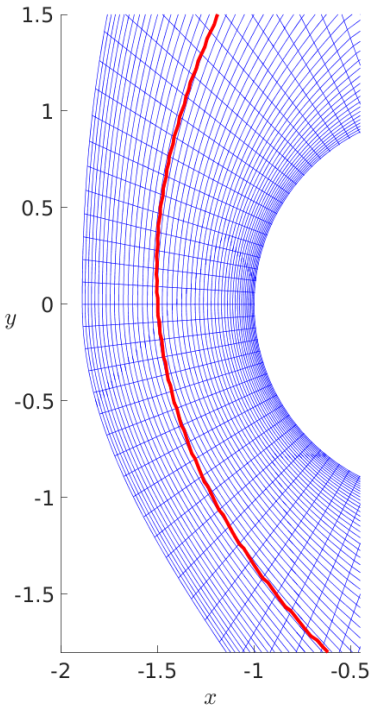


Figure 3.15: Details of the asymmetric shock-adapted grid in the nose region. The red line indicates the curve of the shock computed with the initial grid. Size = 2240 × 200, grid plotted every 4 and 3 points in the wall-normal and wall-tangential directions respectively

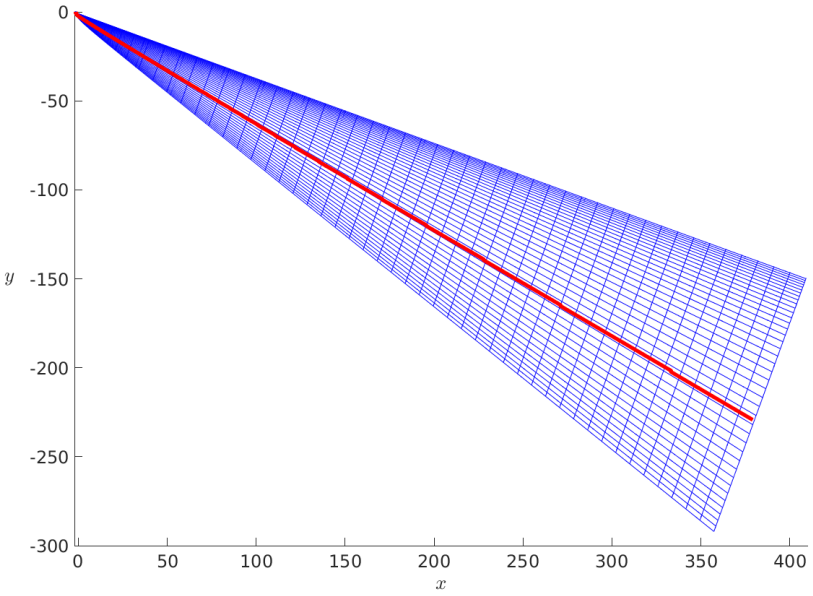


Figure 3.16: Asymmetric shock-adapted grid along the lower side of the wedge. The red line indicates the curve of the shock computed with the initial grid. Size = 2240 × 200, grid plotted every 5 and 20 points in the wall-normal and wall-tangential directions respectively

Figure 3.17 shows the effect of the grid alignment on the shock shape on a certain portion of the shock along the bottom wedge. In particular, a comparison between the locations of the points on the shock computed with the initial grid and those on the shock computed with the new aligned grid is shown. The shape of the analytic hyperbola used to generate the adapted grid is plotted as well. It is evident that the alignment has a significant beneficial effect on the shock shape, which now follows very well the curve corresponding to the hyperbola.

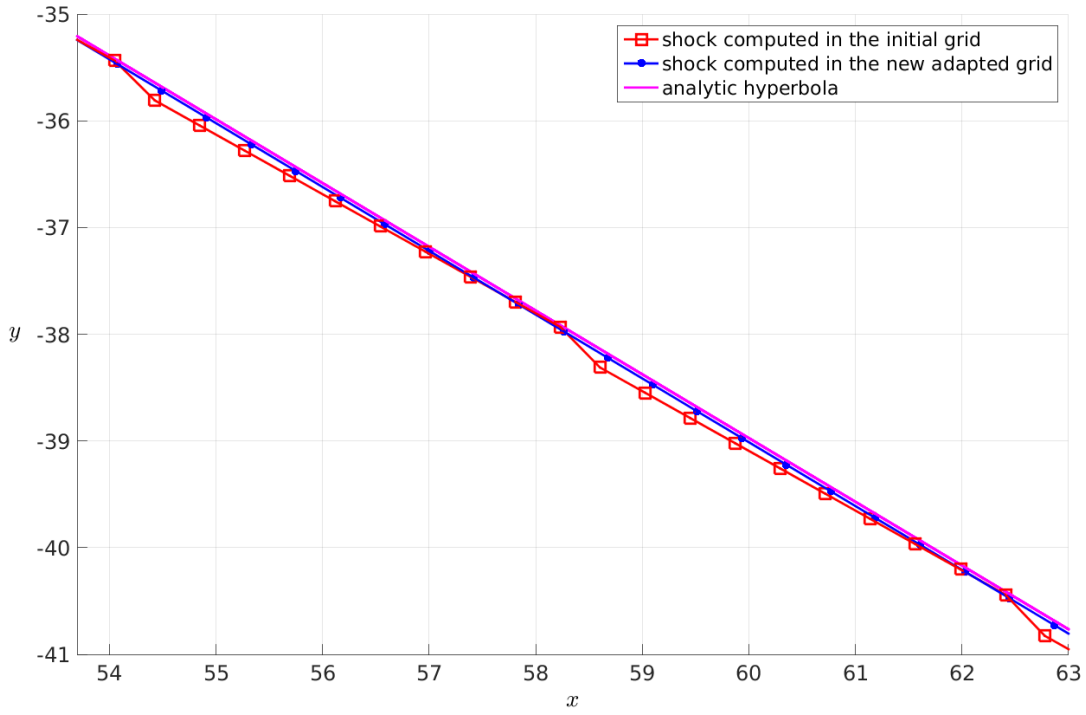


Figure 3.17: Effect of the grid alignment on the shock jumps, over a particular portion of the shock along the bottom wedge

The new aligned grid provides much better solutions both for the density fluctuation field and for the wall pressure distribution along the bottom side of the wedge, as shown by figures 3.18 and 3.19. It is, finally, important to mention that the regular high-wavelength oscillations shown for the higher frequencies in figure 3.19 represent a physical behaviour that will be explained in detail in the Chapter dedicated to the results of each numerical simulation (Chapter 4).

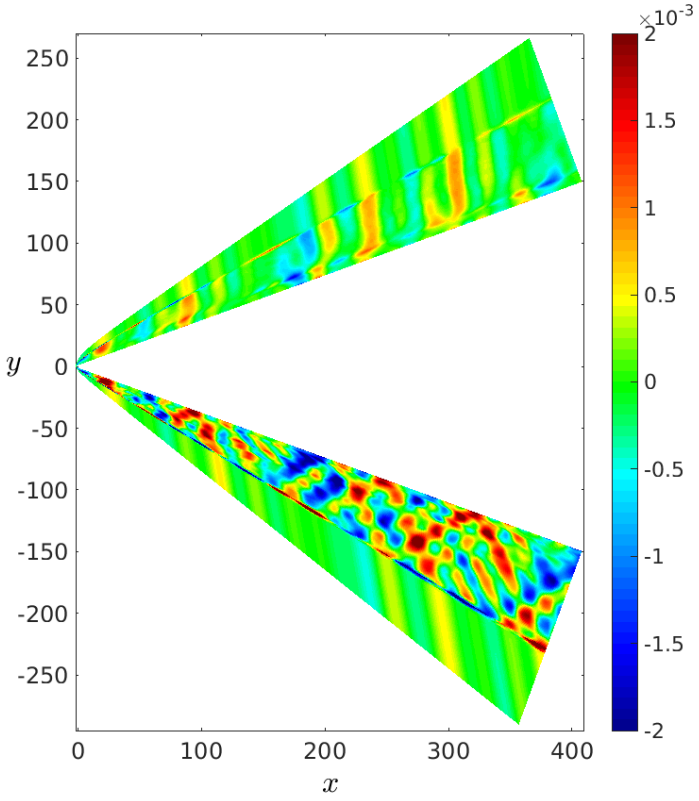


Figure 3.18: Density fluctuation field with the new shock-adapted grid

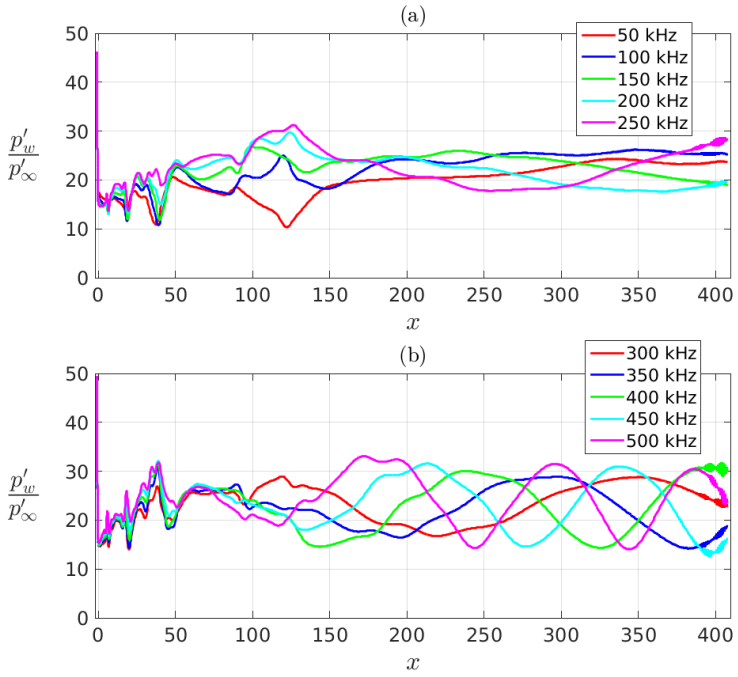


Figure 3.19: Pressure fluctuation distribution along the wall at different frequencies on the windward side, with the new shock-adapted grid, for the lower frequencies (a) and the higher frequencies (b)

## 3.5 Local grid refinement on the shock

In addition to the shock-grid alignment, a method to redistribute the grid points inside the computational domain to increase the point density locally on the shock has been developed. This method is based on a new stretching function, different to the one used by default in the grid generation procedure (described in Section 3.1, look for example at figure 3.1), which is able to smoothly distribute the points along the wall-normal direction increasing their density both in the boundary-layer region and near the shock. The stretching function is a function of the variable $j$ (grid point number) along the direction normal to the wall, which multiplies the distance of the outer edge of the domain from the wall for each value of $i$ (i.e. for each wall-normal grid line), thus assigning the position of each grid point along the $j$ (normal) direction between the wall and the outer edge. For example, when the stretching function is equal to 0 the points are assigned on the wall, when it is 1 the points are assigned on the outer edge, while when it is $1/(1+d)$ (where $d$ is a number between 0 and 1 that represents the percentage of the shock stand-off distance by which the domain outer edge has to be shifted outwards from the shock, e.g. 0.2 stands for the 20 % of the stand-off distance) it is the shock position.

The above mentioned stretching function is of the form

$$S(j) = \frac{f_s(j)}{f_s(N_y)} \ , \tag{3.2}$$

with

$$\begin{aligned} f_s(j) = 2\left(\eta^2 + a\eta\right) - \frac{\tanh(b(\eta - c)) + \tanh(bc)}{\tanh(b(1-c)) + \tanh(bc)} \\ + \frac{4b\eta e^{2bc}}{\left[\tanh(b(1-c)) + \tanh(bc)\right](1+e^{2bc})^2} \ , \end{aligned} \tag{3.3}$$

in which $a$ is the control parameter of the gradient at the wall (which is set to 0.2 in our simulations), $b$ is the stretching coefficient (a usual value is, e.g., $b = 4$), $c$ is a control parameter (between 0 and 1) for the position (along the $j$ direction) of the local refinement region, whose value needs to be appropriately assigned in order to centre the refinement zone on the $j$ location of the shock computed in a previous simulation, and $N_y$ is the total number of grid points in the normal direction. The function $\eta$ is defined as

$$\eta = \frac{j-1}{N_y - 1} \ , \ j = 1, .., N_y \ . \tag{3.4}$$

The stretching function $S(j)$ distributes the points following the trend shown in figure 3.20.

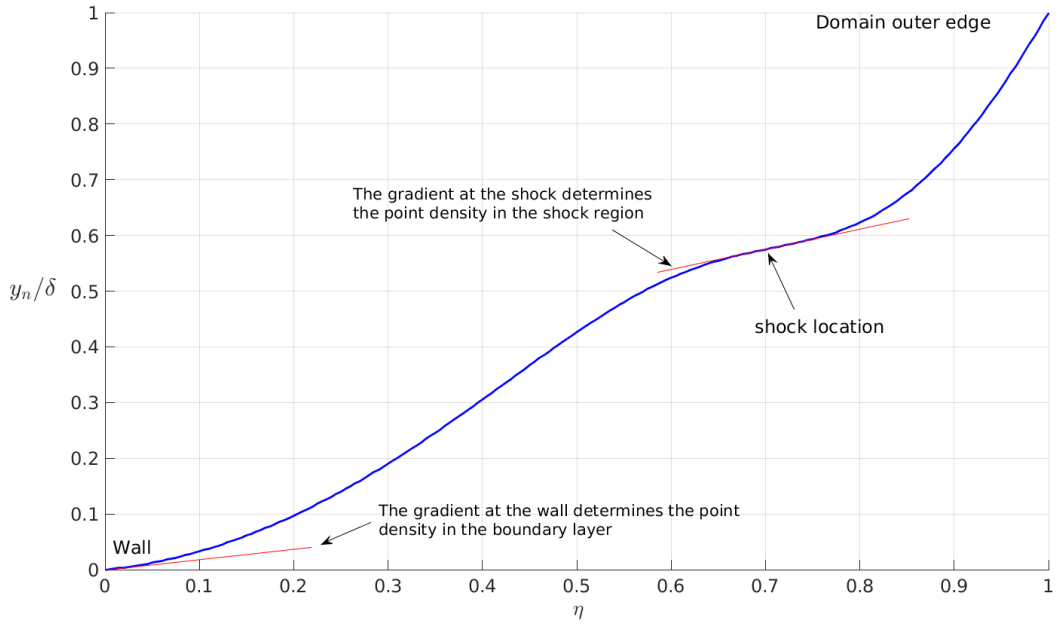


Figure 3.20: Example of point distribution (or stretching) function along the wall-normal ($j$) direction

In figure Figure 3.20, $y_n$ is the distance from the wall for each point $j$, and $\delta$ denotes the distance of the outer edge of the domain from the wall. In this example the shock is located at 0.58 times the outer-edge distance, which means that the domain outer edge is shifted outwards from the shock by a factor of 0.72 times the shock stand-off distance. As is evident from the figure, the local refinement in the boundary layer and in the shock region is obtained by smoothly varying the function gradient in the $j$ direction, so that to reduce it when crossing the boundary layer and the shock regions and increase it elsewhere. In particular, the lowest values of the gradient are reached at the wall and at the shock location; these, in turn, represent two parameters that can be tuned in order to control the stretching intensity (or density of points) towards the wall and on the shock. This method gives a sharper shock, thus increasing the quality of the solution, for a limited number of grid points in the wall-normal direction.

In figure 3.21 an example of a shock-aligned grid (with the method of the analytical hyperbola), with local refinement on the shock obtained by the stretching function describe above, is shown.

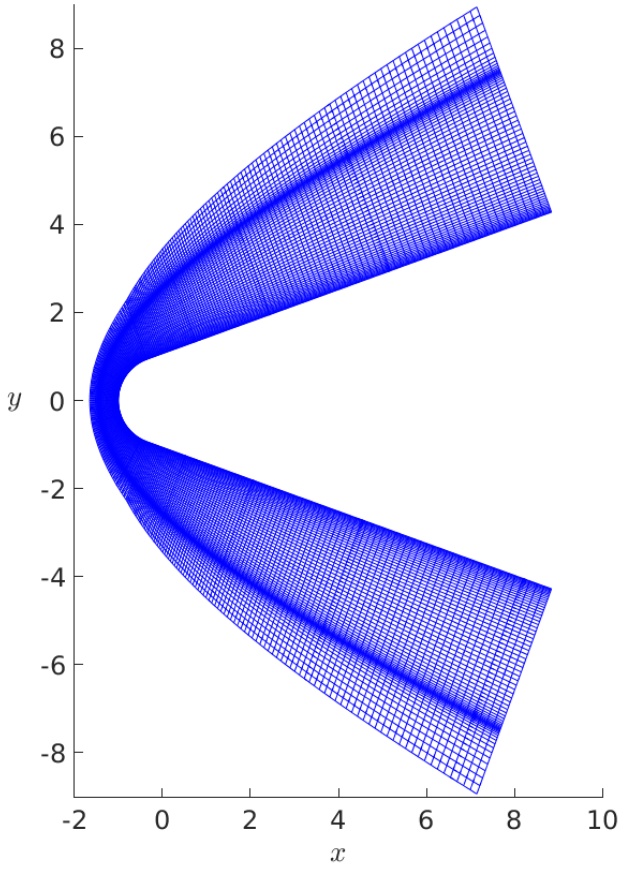


Figure 3.21: Example of shock-adapted mesh with refinement on the shock. Size = 560 × 200, grid plotted every 3 and 2 points in the wall-normal and wall-tangential directions respectively

This mesh has been tested for the case (among those considered in Chapter 4) with $M = 6$, $Re = 630$, and $\alpha = 0°$ (which is the same considered in the resolution study in Section 3.2), inserting fast acoustic waves with a set of 10 frequencies (from 50 to 500 kHz) and a freestream disturbance amplitude (for the density) of $1 \times 10^{-4}$. Figures 3.22 and 3.23 show respectively the results of the mean pressure field and the mean Mach number field, highlighting the shock sharpness and the smooth solution downstream of the shock.

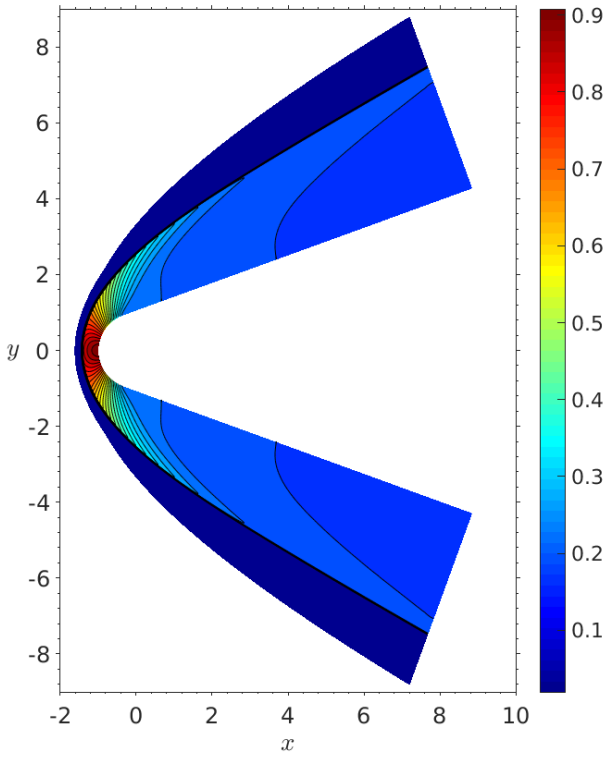


Figure 3.22: Mean pressure field. $M = 6$, $Re = 630$, $\alpha = 0°$

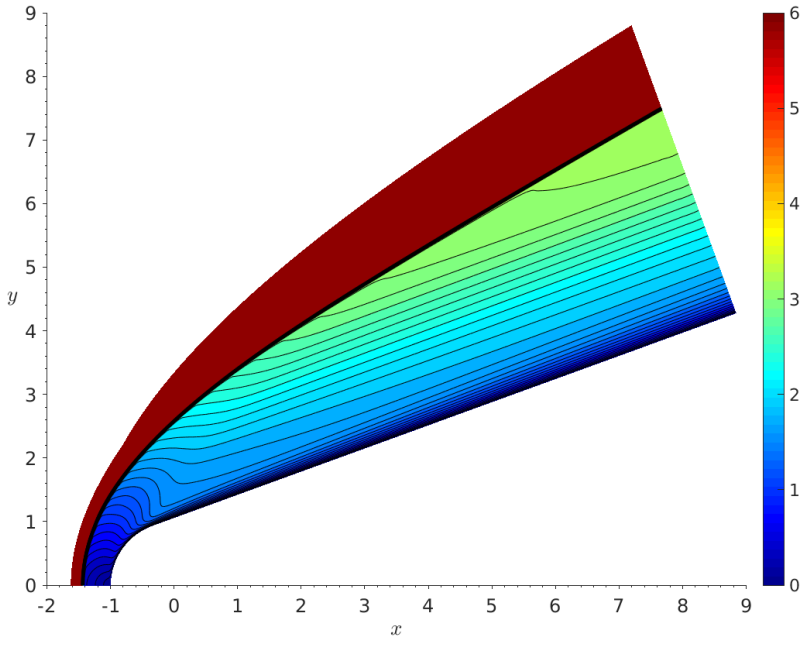


Figure 3.23: Mean Mach number field. $M = 6$, $Re = 630$, $\alpha = 0°$. Only half domain is shown, due to the symmetry of the solution

Figure 3.24 shows a comparison between the wall pressure fluctuation distributions (along the wedge) obtained with the shock-adapted locally-refined grid (with grid size

$560 \times 200$) and those obtained with the original grid (e.g. without local refinement on the shock, and based on Billing's correlations for the shock shape). In particular, the result for the original grid is the same result shown in the resolution study in Section 3.2 for the finer grid (with grid size $2244 \times 150$). Hence, the considered test represents a further grid resolution study of the same numerical case, but focused on the early leading-edge region and involving both the effects of shock-grid alignment and local refinement on the wall-response solution.

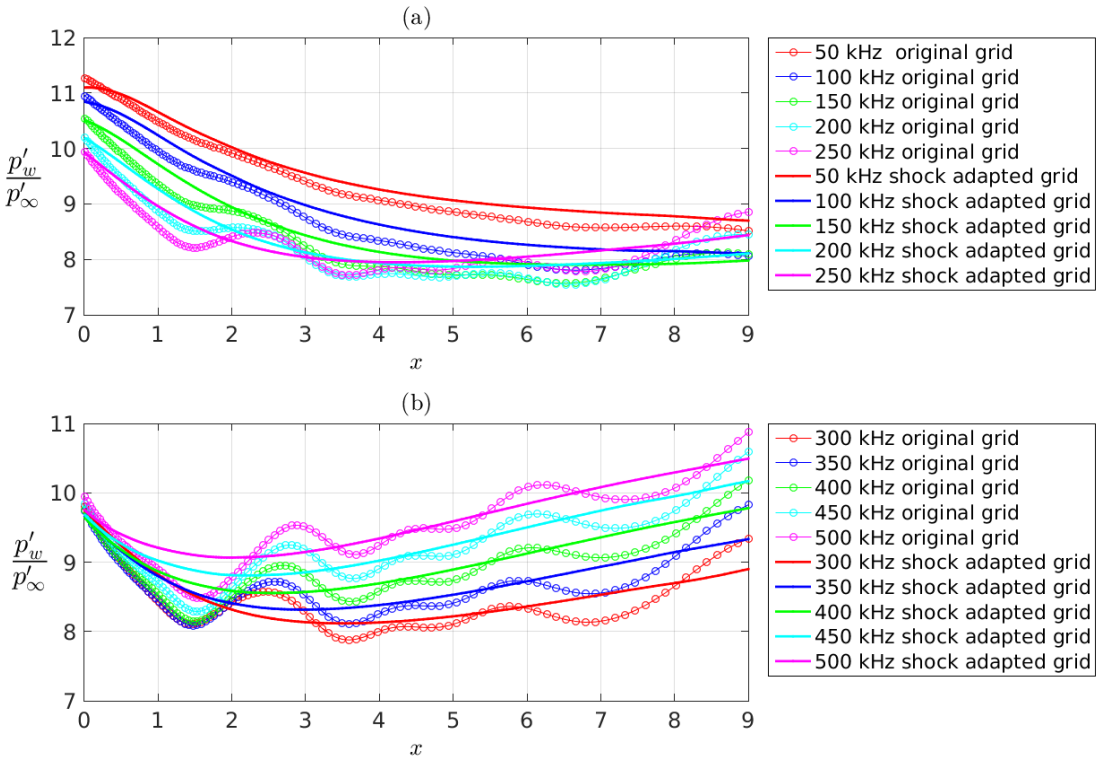


Figure 3.24: Wall pressure fluctuation distribution for the lower frequencies (a) and the higher frequencies (b). $M = 7.3$, $Re = 440$, $\alpha = 0°$

It is evident from figure 3.24 that the shock-grid alignment along with the local refinement on the shock provide a significantly smoother solution along the wall in the nose region for all frequencies, without the presence of the numerical oscillations which affect the solution on the original mesh.

The method of the local refinement on the shock imposes strict limits on the effective time needed to perform a simulation run. In particular, the minimum $\Delta x$ in the shock region along the stagnation line can significantly reduce the minimum allowable time step of the simulation (even of one or two orders of magnitude), if the point density on the shock is too high. This means that the stretching on the shock has to be controlled properly, so that to impose a gradient of the point distribution function on the shock (see figure 3.20) that is not lower than a certain threshold value, which, in turn, is problem dependent. This clearly increases the complexity of the grid generation process. Another limit of

this method is represented by the fact that changing significantly, through the shock refinement, the internal morphology of the grid, with respect to an initial mesh with a different point distribution, will result in the shock assuming a slightly different position in the new simulation with respect to the initial solution. As a consequence, a multi-step procedure is required for the shock-grid alignment method to allow convergence of the adapted grid to the final computed shock shape.

Due to above described challenges, the local shock refinement method has been used, in conjunction with the spline-based shock-grid alignment method described in Section 3.3, only in our 3D simulations for the span-periodic wedge (whose results will be shown in Chapter 5), in which, as already mentioned in Section 3.3, the analysis of the full receptivity-breakdown-transition process in the presence of small-amplitude freestream disturbances requires the solution inside the boundary layer to have minimal levels of numerical noise.

# Chapter 4

# Results for the wedge probe with two-dimensional acoustic waves

In this Chapter we will present the results obtained for the set of 2D numerical simulations concerning the DLR experiments on the wedge probe. Six different freestream conditions have been considered overall, with Mach number ranging from 3 to 7.3. As already mentioned in Chapter 3, for all the cases with a symmetric mean flow (5 out of 6 cases) the standard grid generation method based on Billing's correlations has been used, while for an asymmetric case (the case with 10° angle of attack), shock-grid alignment has been provided through the method based on the analytical hyperbola.

## 4.1 Flow conditions for the 2D numerical cases

Table 4.1 shows the flow conditions for the numerical cases studied, namely freestream Mach number ($M$), unit Reynolds number ($Re_m$), stagnation temperature ($T_0^*$), freestream temperature ($T_\infty^*$), freestream pressure ($p_\infty^*$), wall temperature ratio ($T_w^*/T_\infty^*$), angle of attack ($\alpha$), and angle of incidence of the acoustic waves ($\theta$). These represent the same flow conditions as a set of experiments carried out at DLR on a probe (Wagner *et al.* [84]) designed to measure the disturbance levels in a high and low enthalpy hypersonic wind tunnels. The nose radius is $R^* = 0.1$ mm, and the half-wedge angle is set to 20°. In particular, cases 1 to 3 are relative to the tests in the Göttingen High Enthalpy Shock Tunnel (HEG), and cases 4 to 6 are relative to the tests performed in the DNW Ludwieg Tube (RWG).

Each of the six cases in table 4.1 has been simulated with both fast and slow acoustic waves as freestream disturbances, giving a total of 12 numerical simulations.

Table 4.1: Flow conditions of the six numerical simulations

| Case | $M$ | $Re_m$ (1/m) | $T_0^*$ (K) | $T_\infty^*$ (K) | $p_\infty^*$ (Pa) | $T_w^*/T_\infty^*$ | $\alpha$ (°) | $\theta$ (°) |
|---|---|---|---|---|---|---|---|---|
| 1 | 7.3 | $4.4\times10^6$ | 2740 | 234.034 | 2004.301 | 1.273 | 0 | 0 |
| 2 | 7.3 | $1.4\times10^6$ | 2680 | 228.909 | 619.337 | 1.302 | 0 | 0 |
| 3 | 7.3 | $1.4\times10^6$ | 2680 | 228.909 | 619.337 | 1.302 | 0 | 10 |
| 4 | 6.0 | $6.3\times10^6$ | 559 | 68.571 | 588.852 | 4.346 | 0 | 0 |
| 5 | 6.0 | $6.3\times10^6$ | 559 | 68.571 | 588.852 | 4.346 | 10 | 0 |
| 6 | 3.0 | $12.0\times10^6$ | 258 | 92.538 | 3588.5 | 3.22 | 0 | 0 |

Preliminary simulations were carried out for case 1 with fast acoustic waves, over a small domain (grid size $360 \times 150$) with streamwise length equal to 10 nose radii, and geometry presented in figure 4.1, in order to check the linearity of the pressure response along the wall, with disturbance amplitudes ranging from $10^{-1}$ to $10^{-4}$. The imposed single frequency in the preliminary simulations is high enough to provide a wavelength comparable with the size of the domain.

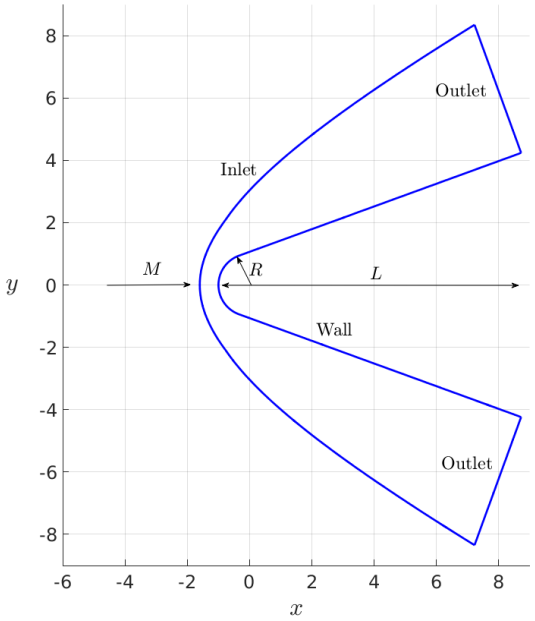


Figure 4.1: Computational domain

Figure 4.2 shows the amplitude of the pressure fluctuations at different points along the wall versus the amplitude of the imposed density fluctuations in the freestream. An excellent linearity trend of the wall pressure response between the different freestream amplitudes at all the different points along the wall is shown. In figure 4.3 the instantaneous density fluctuation field for the amplitude $1.0\times10^{-2}$ is presented. Here, the results show that the waves travelling along the wedge form two detached wave peaks of the same sign, one located in the boundary layer, the other behind the shock. This pattern

is qualitatively in good agreement with results found in literature (e.g. Kara *et al.*[39]), and indicates the presence of boundary-layer perturbations developing downstream.

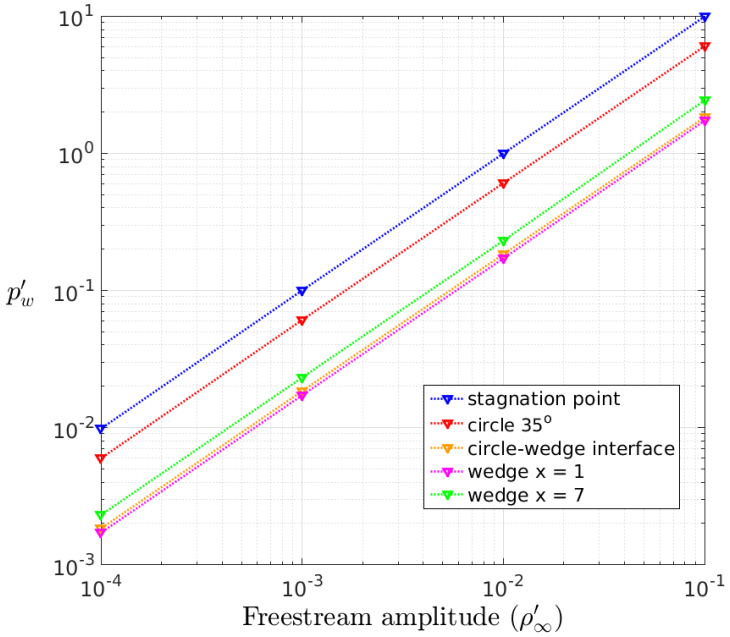


Figure 4.2: Pressure fluctuation amplitude at different points along the wall, from the stagnation point to the position $x = 7$ (with the outlet at $x = 9$), for increasing freestream amplitudes of the acoustic waves

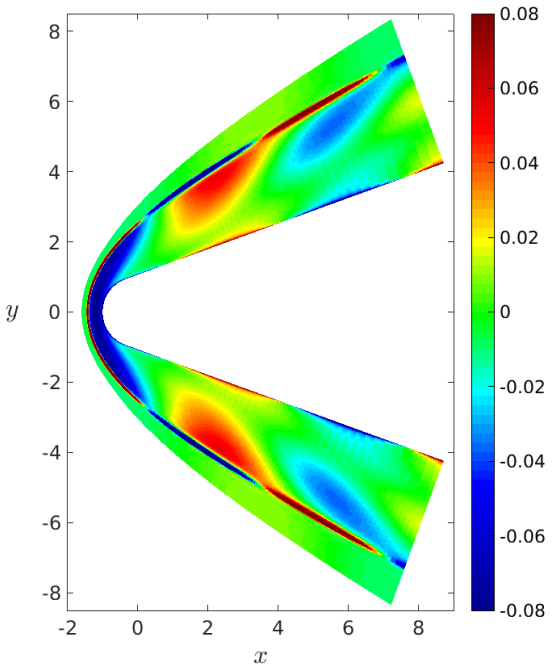


Figure 4.3: Instantaneous density fluctuation field

The boundary conditions applied to all the cases listed in table 4.1 are the following:

- fixed inflow boundary condition, with all the physical quantities set to their freestream values, applied until convergence to the steady state is reached;
- time periodic inflow condition corresponding to the 2D acoustic-wave inflow described in Section 2.2, applied to the steady base flow solution, in the unsteady computations, until periodic convergence is reached everywhere in the flowfield;
- no-slip and isothermal boundary conditions at the wall, with values of the wall temperature ratio listed in table 4.1;
- zero-gradient outflow boundary condition (at both the outflow boundaries) applied along the direction of the $j$-grid lines.

Finally, it should be mentioned that the initial state of the steady-state simulations corresponds to a uniform freestream flow at all the points inside the domain.

## 4.2 Preliminary validation of the code

Another preliminary simulation was performed in order to validate our results for the unsteady quantities with those numerically obtained at Langley Research Centre by Balakumar (private communication) for case 1 ($M = 7.3$, $Re = 440$), with slow acoustic waves as freestream forcing. For the present validation test case, only one frequency (150 kHz) of the slow planar acoustic waves was considered. The length of the domain is, in this case, 400 nose radii. The results of this validation test case are presented in figure 4.4, which shows a comparison of the results for the instantaneous wall pressure fluctuation distribution (here both positive and negative values are shown, not the amplitude) obtained by Balakumar and those obtained through our computations. In both cases, the wall pressure fluctuations have been normalised with the corresponding pressure amplitude imposed in the freestream. Our numerical results are shown for both a non-aligned grid (red solid curve), namely a grid obtained through the standard method based on Billing's correlations, and a shock-aligned grid (black dotted line) obtained through the spline-based method, already discussed in Section 3.3.

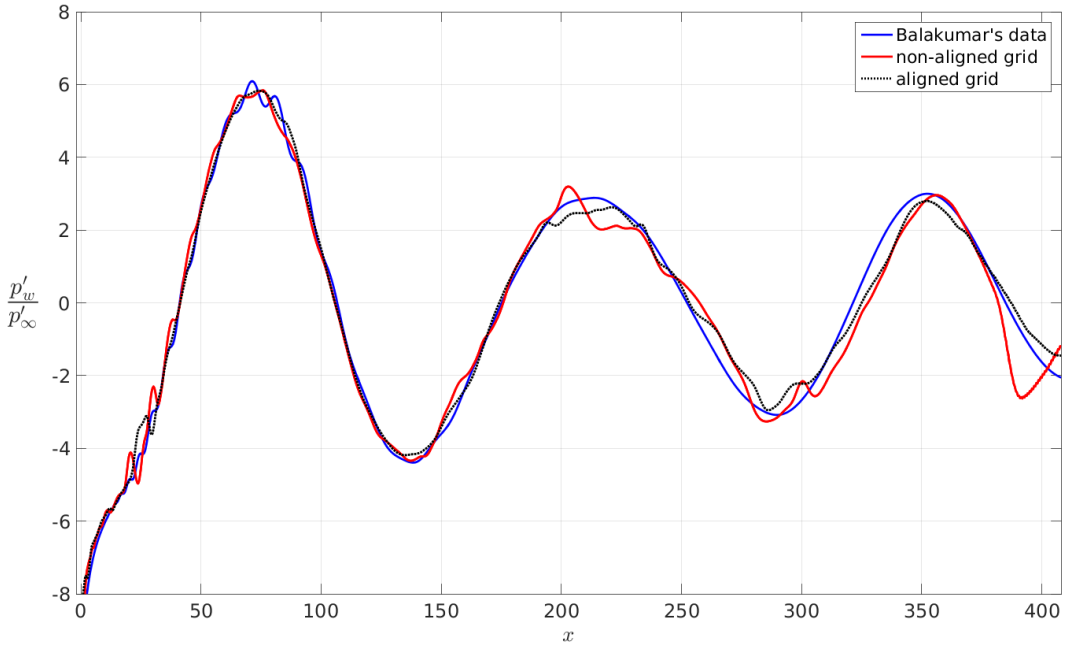


Figure 4.4: Wall pressure fluctuations for the frequency 150 kHz with freestream slow acoustic waves. Case1, $M = 7.3$, $Re = 440$

As can be seen, there is a very good agreement in the wall response between Balakumar's data and our numerical results, for both the aligned and non-aligned grids. This demonstrates the capability of the SBLI code, as well as the suitability of both grid types, to provide physical results for the considered numerical simulations. The aligned grid shows in general a slightly smoother profile compared to the non-aligned grid, especially in the nose region ($x = 0 - 150$), but is still affected by a small numerical noise further downstream. This is mainly due to the fact that, although a high shock-grid alignment level is achieved for the mean flow, in the unsteady simulations the physical oscillations of the shock wave, induced from the interaction with the freestream acoustic waves, result in the alignment being lost locally and numerical oscillations being released downstream of the shock, which are higher in the coarser part of the domain (namely the downstream region). Also, in this case, the presence of a relatively strong shock, due to the high values of the Mach number (7.3) and the half-wedge angle (20°), makes the unsteady solution very sensitive to the misalignment effects. The standard (i.e. non-aligned) grid, in contrast, provides slightly more pronounced numerical oscillations everywhere in the wall response, which, however, do not influence the physical solution, as was already shown in the resolution study in Section 3.2.

In the light of these results, the noise level produced by the standard grid can be considered acceptable for the purposes of the present set of 2D simulations, thus motivating the use of the standard (and less numerically expensive) grid generation method based on Billing's correlations for all the cases with symmetric mean flow (in which a fairly good approximation of the shock shape is obtained through the standard method).

As already said in Chapter 3, the spline-based shock-grid alignment method is used for all our 3D numerical cases in Chapter 5 (for the span-periodic wedge), where the downstream propagation of small numerical oscillations present in the wall response might affect significantly the transition mechanism. Moreover, in order to suppress the residual oscillations present in the solution obtained through the adapted (i.e. aligned) grid (as shown in figure 4.4), a local grid refinement on the shock is used as well for the 3D cases in Chapter 5, which provides a further improvement of the solution quality, as shown in Section 3.5.

## 4.3 Results for the 2D unsteady simulations

In this section we present numerical results for the cases listed in table 4.1 with planar fast and slow acoustic waves in the flowfield, with multiple frequencies and a density perturbation amplitude of $1 \times 10^{-4}$ at each frequency. The dimensionless frequency is normalised with the nose radius and the freestream velocity as $f = f^* R^*/U^*_\infty$. For all the cases with fast acoustic waves, a set of 10 multiple frequencies ranging from 50 kHz to 500 kHz has been imposed; while, for slow acoustic waves, the frequency range is case dependent. In particular, considering the numerical simulations with slow acoustic waves, 10 frequencies have been inserted from 20 kHz to 200 kHz for case 1, from 25 kHz to 250 kHz for cases 2 and 3, and from 50 kHz to 500 kHz for cases 4, 5 and 6. These ranges were chosen in order to increase the frequency resolution at lower frequencies for the HEG cases (namely cases 1 to 3) with slow acoustic waves. The phases $\phi_n$ in equation 2.12 are chosen as fixed random numbers in the range 0 to $2\pi$. The overall amplitude level (rms of $\rho'_\infty$) of the multi-frequency signal imposed in the freestream is $2.24 \times 10^{-2}$ for each case.

The domain length is $400R$ and the grid size for cases 1, 2, 3 and 4 in table 4.1 is 2244×150, while the grid size for cases 5 and 6 is 2244×200. As already said before, the grids for cases 1 to 4, and 6 were obtained through the standard (based on Billing's correlations) method, while for case 5 the analytical-hyperbola-based method has been used to provide shock-grid alignment. Numerical results are presented for the instantaneous density fluctuation field, and for the pressure fluctuation amplitude distribution along the wall at different frequencies, the latter having been computed through a Fast Fourier Transform approach. The wall pressure fluctuation amplitude is normalised with respect to the freestream pressure fluctuation amplitude at each frequency (i.e. $p'_w/p'_\infty$). For the symmetric cases (case 1, 2, 4, 6), the results are presented on the top side of the wedge, while for the asymmetric cases (case 3, 5), the corresponding values are plotted for both the upper and the lower sides.

It is important to mention that wall temperature fluctuations are not considered in our numerical simulations, as the wall temperature is fixed to a constant value by the

isothermal boundary condition, which applies to the experiments in hypersonic wind tunnels, where the short duration of the test does not cause significant changes in the wall temperature.

### 4.3.1 Structure of the disturbance field

The structure of the disturbance field behind the shock wave is first qualitatively analysed through plots of the density fluctuation field for two different Mach numbers, the highest (Mach 7.3) and the lowest (Mach 3) of those considered. Figures 4.5 and 4.6 show the density fluctuation field for the Mach 7.3 case (case 1) with fast and slow acoustic waves respectively, while figures 4.7 and 4.8 show the corresponding results for the Mach 3 case (case 6). While for case 6 the frequency range for fast and slow acoustic waves is the same (50-500 kHz), for case 1 the frequency ranges considered for fast and slow acoustic waves are different, being 50-500 kHz for fast waves, and 20-200 kHz for slow waves.

For case 1 and fast acoustic waves (figure 4.5), the waves downstream of the shock form with a lower wavelength (an effect of the higher frequency range), compared to the slow wave case (figure 4.6), and with a clear inclination angle of the wave fronts with respect to the $y$-axis, suggesting a delay of the waves that have crossed the shock with respect to the freestream wave fronts.

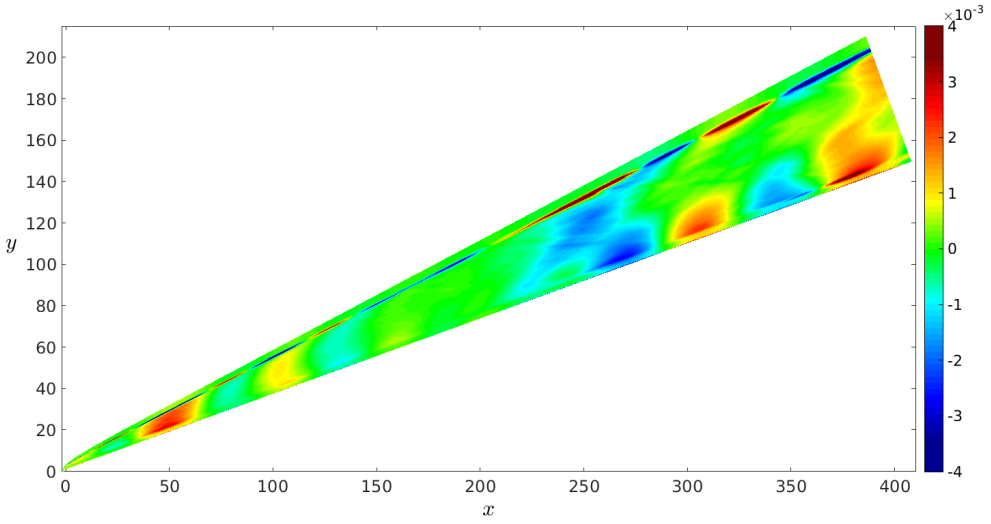


Figure 4.5: Density fluctuation field for fast acoustic waves. For the symmetry of the solution, only half the domain is shown. Case 1, Mach = 7.3

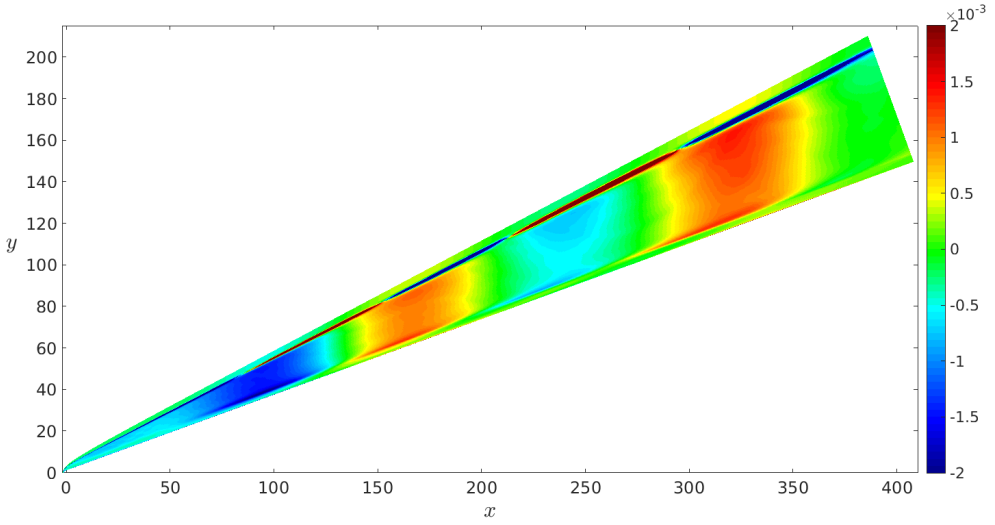


Figure 4.6: Density fluctuation field for slow acoustic waves. For the symmetry of the solution, only half the domain is shown. Case 1, Mach = 7.3

For slow acoustic waves, the post-shock wave fronts appear more compact and with a lower inclination angle, namely they are more aligned with the $y$-axis (and with the freestream wave fronts), suggesting in turn a more uniform propagation speed of the disturbances downstream of the shock. This difference between the fast and slow acoustic wave structure in the post-shock region is more evident in figures 4.7 and 4.8 for case 6 at Mach 3. In particular, the wave structure behind the shock appears to be more complex in the case of fast waves (figure 4.7), with a system of different waves with opposite inclination angles.

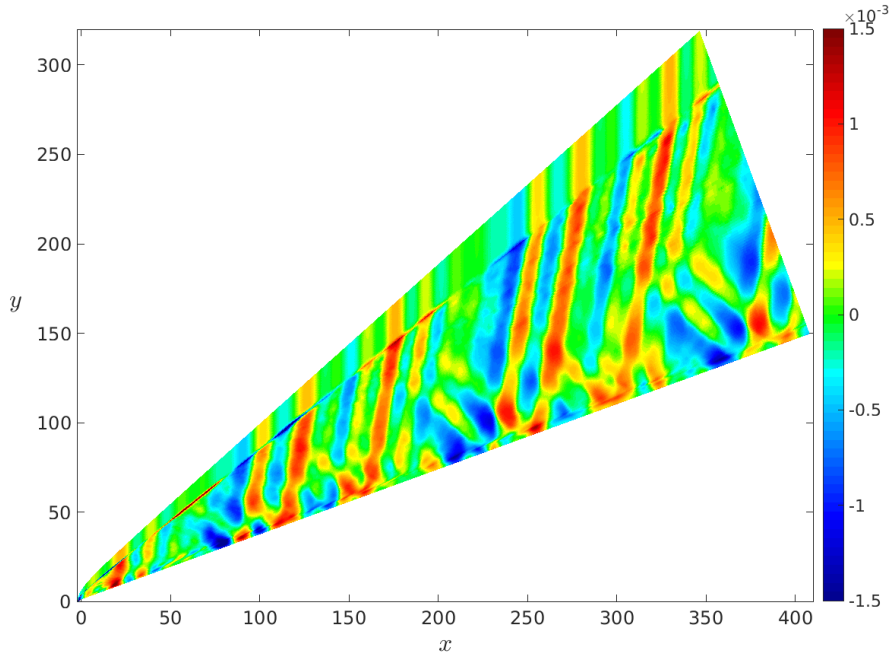


Figure 4.7: Density fluctuation field for fast acoustic waves. For the symmetry of the solution, only half the domain is shown. Case 6, Mach = 3

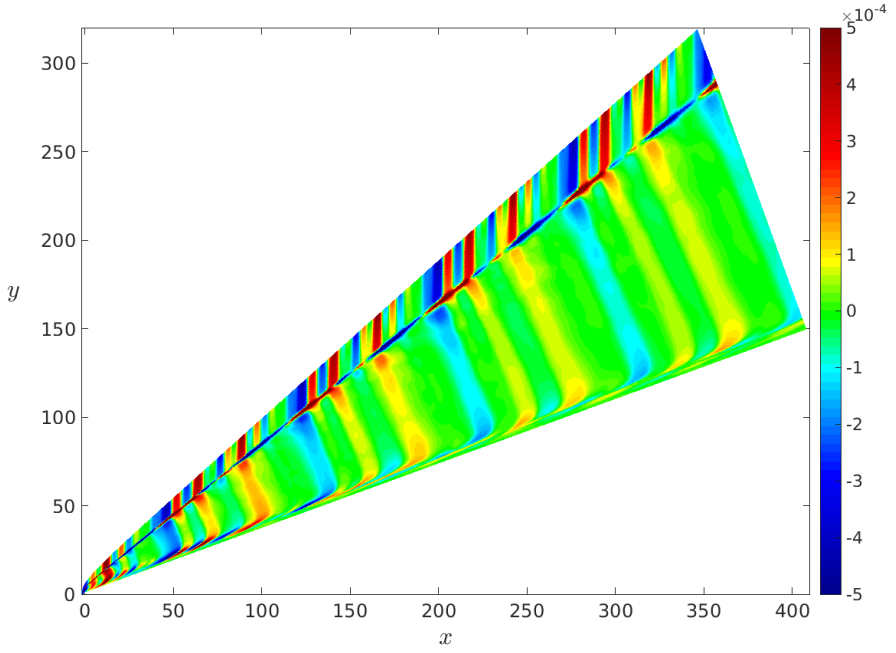


Figure 4.8: Density fluctuation field for slow acoustic waves. For the symmetry of the solution, only half the domain is shown. Case 6, Mach = 3

Figure 4.9 shows a sketch of the inclination angles and phase speeds of the wave fronts upstream and downstream of the shock, illustrating the characteristics of the propagation of the main waves in the post-shock region. A generic freestream wave front (depicted by a black dashed line aligned in the vertical direction) is labelled as $w_t$ and $w_{t+\delta t}$ at the

instants of time $t$ and $t+\delta t$ respectively. The blue oblique dot-dashed line along the shock indicates the shock direction, and $\sigma$ the angle of the oblique shock with respect to the $x$-axis. The angle $\beta$ represents the inclination angle of the wave front in the post-shock region with respect to the wall direction, and $\delta = 20°$ is the half-wedge angle. The vectors in the $x$-direction, denoted by $c_\infty$ and $c_{ps}$, represent respectively the freestream and the post-shock phase speed of the disturbances in the $x$-direction (the main propagation direction of the imposed waves), which for a time unit $\delta t = 1$ are coincident with the $x$-displacement vectors of two different points on the same wave front upstream and downstream of the shock. The lower length of the vector $c_{ps}$ indicates that the portion of the wave front that has crossed the shock is propagating with a lower streamwise phase speed, compared with the portion of the wave front still upstream of the shock, so that, after the time delay $\delta t$, the post-shock wave front reaches a point that is upstream of the point reached by the freestream wave front. These two points are located on the inclined black dashed line connecting the shock to the wall, which represents the deflected (or 'dragged') wave front due to the lower phase speed in the post-shock region. As the geometry is two-dimensional and the region of the computational domain considered in figure 4.9 is far enough away from the leading-edge (thus from the curvilinear part of the shock), the flowfield and the disturbance field behind the shock outside the boundary layer can be considered as approximately uniform, which explains why the post-shock dragged waves appear as oblique straight lines running from the shock to the boundary layer.

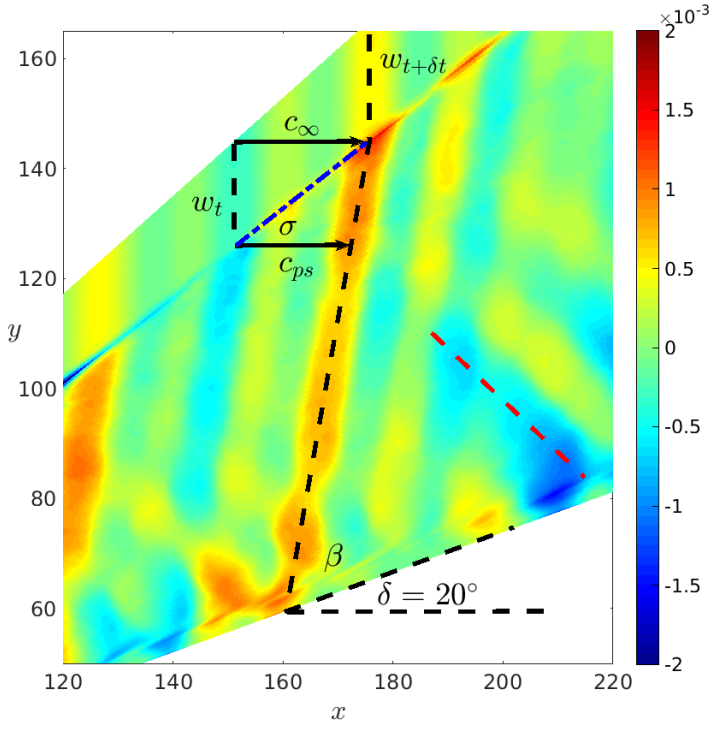


Figure 4.9: Expanded view of the density fluctuation field for fast acoustic waves, and sketch of the propagation features of the wave fronts upstream and downstream of the shock (Case 6, Mach = 3)

For the specific flow conditions of case 6 (Mach 3), the freestream phase speed is $c_\infty = u_\infty + a_\infty = 1 + 1/M = 1.33$. A theoretical estimation of the phase speed behind the shock, $c_{ps}$, can be made through the inviscid oblique shock theory, which links the $x$-convection velocity $u_{ps}$ and the local speed of sound $a_{ps}$ to the normal (to the shock) freestream Mach number through the normal shock jump relations. From the knowledge of the angle $\sigma$ of the oblique shock for a supersonic flow at Mach 3 over a wedge of $\delta = 20°$ half-wedge angle ($\sigma = 37.7°$), the normal freestream Mach number can be computed as $M_n = M \sin\sigma = 1.83$, and, by applying the shock jump relations, we compute a value for the post-shock $x$-wise phase speed equal to $c_{ps} = u_{ps} + a_{ps} = 1.195$. From the values of $c_\infty$ and $c_{ps}$, the inclination angle of the wave front in the post-shock region with respect to the $x$-axis ($\alpha_x$) can be computed through the relation

$$\alpha_x = \tan^{-1}\left(\frac{c_\infty \tan\sigma}{c_\infty - c_{ps}}\right), \tag{4.1}$$

which gives a theoretical estimation of the wave front inclination angle of $\alpha_x = 82.5°$. This angle represents the sum of the angle $\beta$ (see figure 4.9) and the half-wedge angle. The numerical value of $\alpha_x$ corresponding to the results shown in figure 4.9 (i.e. inclination of the wave front in the post-shock region) is $\alpha_x = \beta + \delta \approx 81°$, which is close to the theoretical estimation (with a relative error of 1.8% between the theoretical and the numerical results), indicating that the inclined wave fronts behind the shock in figure 4.9 are indeed dragged waves propagating with the velocity of the local fast acoustic waves behind the shock.

The presence of another type of wave with an opposite inclination can be noticed in figure 4.7 (whose direction is indicated by a red dashed line) close to the boundary layer. These waves can be considered as waves generated by the interaction of the main dragged waves with the surface and then reflected downstream. The fronts of these waves form an angle of about 135° with respect to the $x$-axis (considering angles starting from zero at the $x$-axis and increasing anticlockwise). This value corresponds in turn to an inclination of about 45° of the wave vector (normal to the wave fronts) of the reflected waves, which, subtracting the wall inclination angle ($\delta$), provides a propagation direction of approximately 25° with respect to the local flow direction. This value is slightly lower than the local Mach angle, which is equal to 30° at the boundary-layer edge. Hence, this second type of waves appear to be reflected fast waves propagating downstream with an angle close to the local Mach angle.

Case 6 with slow acoustic waves, depicted in figure 4.8, shows a significantly different structure of the waves behind the shock, made up of wave fronts deflected in an opposite angle compared to the fast-wave case. This indicates that the post-shock wave structure is dominated by transmitted waves travelling with a phase speed higher than the freestream phase speed of the slow acoustic waves. Applying the same method used for the fast acoustic wave case, the post-shock propagation speed of the wave fronts, $c_{ps}$,

can be evaluated from the numerical results, by the knowledge of the freestream phase speed of the slow acoustic waves ($c_\infty = 1 - 1/M = 0.66$), the numerical result for the oblique shock angle ($\sigma = 38.5°$, compared to the theoretical value of $\sigma = 37.7°$ given above), and the inclination angle of a generic wave front ($\alpha_x = 112°$, with respect to the $x$-axis), as $c_{ps} = c_\infty(1 + \tan\sigma/\tan(\alpha_x - 90)) = 0.87$. This value has been computed by assuming waves travelling in the $x$-direction, which is the preferential direction of the imposed acoustic waves. From the numerical results, the $x$-direction velocity just downstream of the shock is $u_{ps} = 0.774$ (computed at $x = 200$), and the speed of sound at the same point is $a_{ps} = 0.419$, which gives a value, for the local $x$-wise phase speed of fast acoustic waves, of $c_{Fps} = u_{ps} + a_{ps} = 1.193$, and, for slow acoustic waves, a value of $c_{Sps} = u_{ps} - a_{ps} = 0.355$. The disagreement of both the post-shock phase speeds of fast and slow acoustic waves with the estimated value of $c_{ps} = 0.87$ suggests that the transmitted waves are neither fast nor slow acoustic waves, but that they might represent convected waves travelling in the local flow direction (approximately tangential to the wall). By repeating the same procedure based on the inclination of the wave fronts, but assuming post-shock waves propagating in the local flow direction (namely with the wave vector inclined at 20° with respect to the $x$-axis), we obtain an estimated value for the x-component of the post-shock phase speed of $c_{ps} = 0.76$, which is much closer to the $x$-wise convection velocity component of 0.774. We have not considered the effect of the boundary-layer displacement thickness on the streamline direction, so the relative error of 1.8% between $c_{ps}$ and $u_{ps}$ is small enough to conclude that in this case the post-shock waves are convected waves (including vortical and entropy waves) travelling in the local flow direction, which are generated downstream of the shock through the interaction with the freestream disturbances.

Another feature of the post-shock generated disturbance field for our considered cases is that the slow waves induce a significantly lower amplitude response downstream of the shock than the fast waves, for both case 1 (figures 4.5 and 4.6) and case 6 (4.7 and 4.8). Again, this difference is more pronounced in the lower Mach number case (case 6).

Hence, a decreasing Mach number is seen to enhance the difference in the wave propagation features downstream of the shock between fast and slow acoustic waves. This is because the lower the Mach number, the higher is the difference in phase speed between fast and slow waves, due to the higher contribution of the sound speed on the propagation velocity, while for a theoretically infinite Mach number the phase speeds of the two wave types would collapse to the same value ($1 + 1/M = 1 - 1/M$, for $M = \infty$). This is one of the main Mach number effects on the boundary-layer receptivity characteristics, and explains why, at the high Mach numbers, the discrete internal modes (mode F and mode S) have similar values of the phase speed and are already synchronised with the continuous spectrum of external acoustic waves.

### 4.3.2 Validation of the numerical results through the linear interaction theory

The numerical results for the structure of the disturbance field in the post-shock region and the theoretical approach for the estimation of the transmitted wave class (illustrated in Section 4.3.1 for the Mach 3 case) can be compared with the interaction theory of linear freestream disturbances with oblique shock waves, described by McKenzie and Westphal [13]. They formulated Snell's laws of refraction for plane acoustic and nonacoustic waves striking an oblique shock, in the hypothesis of small disturbances. In particular, considering an incident wave striking the shock from ahead with a certain inclination angle and at a generic frequency, the inclination angle of the diverging wave generated behind the shock was obtained by imposing the continuity of the frequency ($\omega$) and of the component of the wave vector tangential to the shock ($k_\tau$) between the incident and the diverging wave, namely, $\omega_\infty = \omega_{ps}$ and $k_{\tau,\infty} = k_{\tau,ps}$, where the subscript '$\tau$' indicates the tangential-to-the-shock direction. Following this approach, McKenzie and Westphal [13] derived an equation giving the inclination angle of the diverging wave in the case of an incident acoustic wave generating an acoustic wave downstream of the shock as

$$\cos\lambda_{ps,ac} = \frac{-(a_{ps}/a_\infty)^2 \sin^2\lambda_\infty M_{n,ps} + \{\Theta[\Theta - (a_{ps}/a_\infty)^2 \sin^2\lambda_\infty (1 - M_{n,ps}^2)]\}^{1/2}}{(a_{ps}/a_\infty)^2 \sin^2\lambda_\infty M_{n,ps}^2 + \Theta} \,, \tag{4.2}$$

$$\Theta = (1 + M_{n,\infty}\cos\lambda_\infty)^2 \,, \tag{4.3}$$

and in the case of an acoustic wave generating an entropy/vorticity wave downstream of the shock as

$$\tan\lambda_{ps,ev} = \frac{(a_{ps}/a_\infty)^2 M_{n,ps}(\pm\sin\lambda_\infty)}{1 \pm M_{n,\infty}\cos\lambda_\infty} \,, \tag{4.4}$$

where $\lambda$ is the inclination angle of the wave vector ($\mathbf{k}$) with respect to the shock-normal direction, as illustrated in figure 4.10, the subscripts '$\infty$' and '$ps$' indicate quantities in the freestream and in the post-shock region respectively, $M_n$ is the Mach number in the shock normal direction, and the subscripts '$ac$' and '$ev$' refer respectively to acoustic and entropy/vorticity waves generated downstream of the shock. Equation 4.2 applies to an incident fast acoustic wave generating a fast wave behind the shock, while in equation 4.4 the $+(-)$ sign applies to fast (slow) incident waves. The refraction law for incident slow acoustic waves generating slow waves behind the shock is given by equation 4.2 provided the terms $\sin\lambda_\infty$ and $\cos\lambda_\infty$ are replaced by $-\sin\lambda_\infty$ and $-\cos\lambda_\infty$. In figure 4.10, $\mathbf{k}_\infty$ is the wave vector of the incident wave, which, for the considered case (Mach

3 case), is aligned with the flow direction, the versors $\hat{\tau}$ and $\hat{n}$ indicate the tangential and the normal directions to the oblique shock (inclined of the angle $\sigma$ with respect to the flow direction), while $\mathbf{k}_{ps}$ is the wave vector of the refracted wave behind the shock. From the numerical results for the considered case, the value of the oblique shock angle is $\sigma = 38.5°$, thus the value of the angle of the incident free-stream waves we use as input in equations 4.2, 4.3 and 4.4 (with reference to figure 4.10) is $\lambda_\infty = 90° - 38.5° = 51.5°$. Similarly, for the input terms $M_{n,ps}$ and $a_{ps}$, we use the numerically obtained values, while the terms $M_{n,\infty}$ and $a_\infty$ simply represent free-stream conditions of the considered numerical case.

By applying equations 4.2 and 4.3 for the Mach 3 case with fast acoustic waves, whose wave structure behind the shock is shown in figure 4.7, we obtain a refraction angle of the fast wave equal to $\lambda_{ps,ac} = 41.04°$, which is very close to the numerical refraction angle of $\lambda_{ps,ac} = \alpha_x - \sigma = 42.5°$ (with $\alpha_x = 81°$). This indicates that the transmitted waves behind the shock are indeed refracted fast acoustic waves, as was previously deducted from the theoretical estimation method based on the length of the streamwise phase speed vectors upstream and downstream of the shock.

In the same way, applying equation 4.4 to the Mach 3 incident slow-wave case gives a theoretical refraction angle for the generated entropy/vorticity waves of $\lambda_{ps,ev} = 74.53°$, corresponding to a wave vector pointing upstream, which shows again a very good agreement with the numerical result (shown in figure 4.8) of $\lambda_{ps,ev} = \alpha_x - \sigma = 73.5°$ (with $\alpha_x = 112°$). This confirms that the main waves generated behind the shock due to the interaction with incident freestream slow acoustic waves are indeed entropy/vorticity waves.

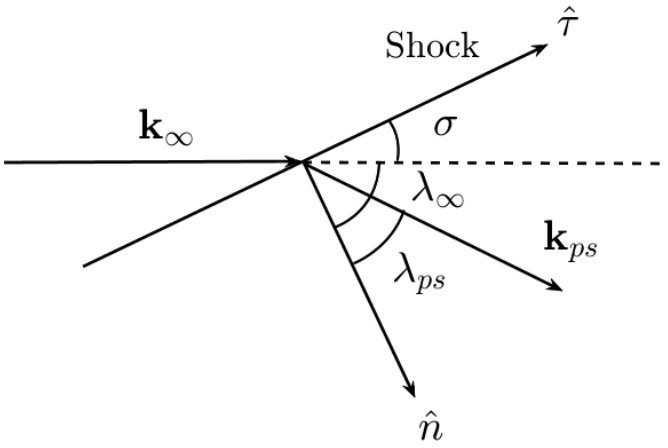


Figure 4.10: Sketch of the incidence and refraction wave angles in the shock-wave reference system

In summary, the application of the linear interaction theory to our considered case demonstrates the validity of our numerical results and, at the same time, of the theoretical method used to estimate the nature of the transmitted waves behind the shock, based on the relative length of the phase speed vectors upstream and downstream of the shock and on the inviscid oblique shock theory. The results obtained using the linear interaction theory described by McKenzie and Westphal [13] confirm that, for the considered Mach 3 case, the dominant waves transmitted behind the shock from incident fast acoustic waves are refracted (or dragged) fast acoustic waves, while the dominant waves generated behind the shock from incident slow acoustic waves are entropy/vorticity waves.

### 4.3.3 Response along the wall: resonance-modulation behaviour

In this Section the response along the wall for the pressure fluctuations is considered for cases 2, 4 and 6 (see Table 4.1), in order to study the main characteristics of the leading-edge receptivity mechanism, namely the generation, interaction and downstream evolution of the induced boundary-layer modes, for different Mach numbers.

Figures 4.11, 4.13 and 4.15 show the pressure fluctuation amplitudes along the wall at different frequencies respectively for cases 2, 4 and 6 with fast acoustic waves, while figures 4.12, 4.14 and 4.16 show the corresponding results for the same cases with slow acoustic waves. As can be seen, in case 2 the wall pressure fluctuation amplitude at each frequency gradually increases with the distance from the leading edge for fast acoustic waves (figure 4.11), while gradually decreasing for the slow wave cases (figure 4.12). The rates of growth and decay (respectively for the fast and slow wave cases) increase with the frequency, so that downstream along the wedge the higher frequencies reach higher response levels for fast waves, and lower levels for slow waves. This difference between fast and slow acoustic waves is the effect of a stronger resonance mechanism for fast waves, namely the synchronisation between the forcing mode of the fast acoustic waves and the internal boundary-layer fast mode (mode F, according to Fedorov [4]'s notation) that is generated at the leading edge. This leads to an initial amplification of mode F well upstream of the first neutral point of the second instability mode, which is not included in the computational domain, in contrast with a weaker resonance mechanism in the case of slow acoustic waves, leading to the generation and initial decay of the boundary-layer slow mode (mode S).

The difference in the resonance mechanisms is due to the characteristics of the wave transmission and propagation in the post-shock region, which determine the disturbance field forcing the boundary layer. As described in the previous Section, in the case of fast waves the transmission of the freestream acoustic waves across the shock appears to be more efficient, with the main freestream wave fronts being deflected as they cross the shock, due to the difference in phase speed upstream and downstream of the shock,

and amplified according to the pressure increase downstream of the shock wave. In the slow wave case, in contrast, the post-shock wave structure is dominated by lower amplitude convected waves travelling faster than the freestream waves. These waves are not synchronised with the slow mode generated at the leading edge. The interaction of the slow mode with the forcing waves of the post-shock region does not produce an efficient resonance mechanism, thus the response in the early nose region shows an initial decay.

Figures 4.13 and 4.14, for case 4 with fast and slow waves respectively, show a pronounced frequency-dependent oscillatory behaviour of the wall response for the fast wave case, and a substantially flat response (after an initial decay) for the slow-wave case. This is again due to the different interaction mechanism between the discrete boundary-layer modes and the forcing disturbance field for fast and slow waves. However, in this case, the wall response for both fast and slow waves appears as a continuation of the initial (growth/decay) response shown by 4.11 and 4.12 for case 2 for fast and slow waves respectively. This is essentially because, as $U_\infty$ decreases with decreasing Mach numbers (for the considered cases, see table 4.1), the nondimensional frequencies increase, for the same dimensional frequency range.

The large-wavelength oscillations shown in the fast-wave case are due to a modulation process between mode F and the forcing acoustic mode, since after the initial synchronisation the two are no longer coupled. Owing to the absence of a synchronisation with the forcing mode, mode F decays in this region, according to its stable nature. This region is known in the literature (e.g. Zhong and Ma[17]) to precede the region of synchronisation between mode F and mode S, and the consequent excitation of mode S (which is located downstream of our domain). We can describe the modulation mechanism with a simplified model involving two different modes, in which the distance ($\Delta x$) between two consecutive peaks of the oscillations, at a certain frequency $f$, is linked to the phase speeds of the two competing modes (modes $a$ and $b$) by the following relation (De Tullio and Sandham [85])

$$\Delta x = \frac{c_a c_b}{f|c_a - c_b|} \ , \tag{4.5}$$

where $c_a$ and $c_b$ are the phase speeds of the two modes. Considering the wall response at the frequency $f$=500 kHz in figure 4.13, the distance between two consecutive peaks downstream (located at $x = 262.5$ and $x = 372.5$) is $\Delta x = 110$. Assuming $c_a$ to be coincident with the phase speed of the fast acoustic waves computed in the post-shock region ($c_a = c_{ps} = 1.1$), the phase speed of mode $b$, by applying equation 4.5 is $c_b = 0.9179$. Hence, in the downstream region the fast acoustic wave mode is modulated by a mode whose phase speed is lower than the phase speed of the fast acoustic waves,

and higher than the phase speed of the slow acoustic waves in the freestream ($1-1/M = 0.83$). This is consistent with the downstream decay of mode F, whose phase speed is continuously decreasing from the leading edge, relative to the fast acoustic waves, until it approaches the value of the phase speed relative to mode S beyond the length of our computational domain. Hence the two competing modes in the modulation region can be attributed to the forcing fast acoustic wave mode and the desynchronised mode F.

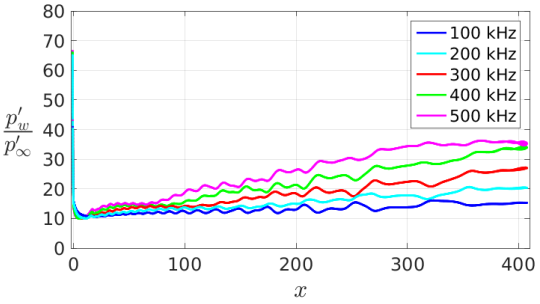


Figure 4.11: Wall response for case 2 (Mach 7.3) with fast waves

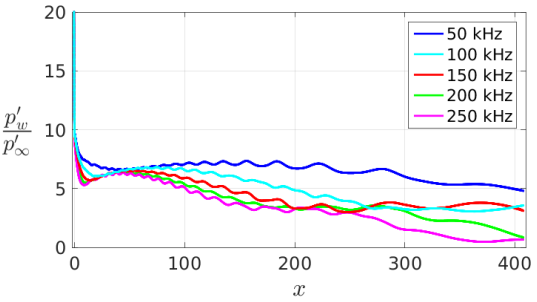


Figure 4.12: Wall response for case 2 (Mach 7.3) with slow waves

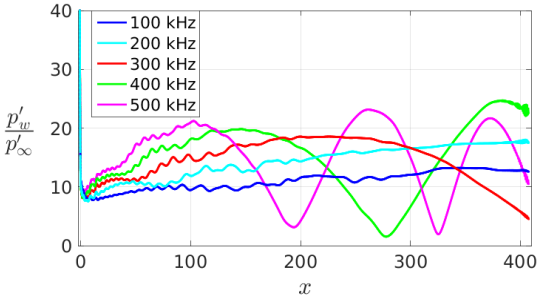


Figure 4.13: Wall response for case 4 (Mach 6) with fast waves

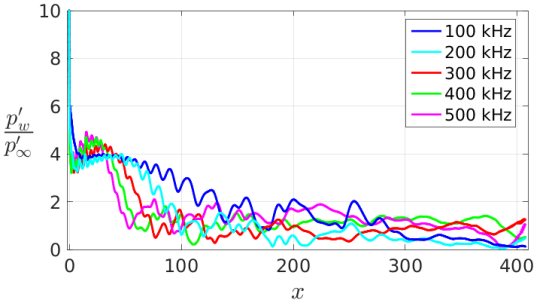


Figure 4.14: Wall response for case 4 (Mach 6) with slow waves

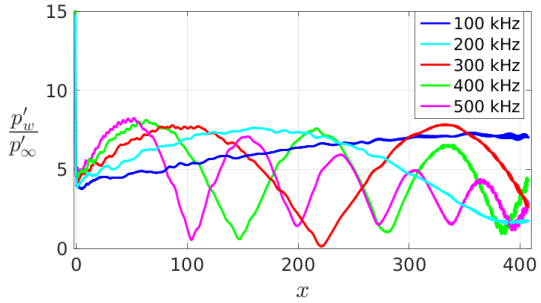


Figure 4.15: Wall response for case 6 (Mach 3) with fast waves

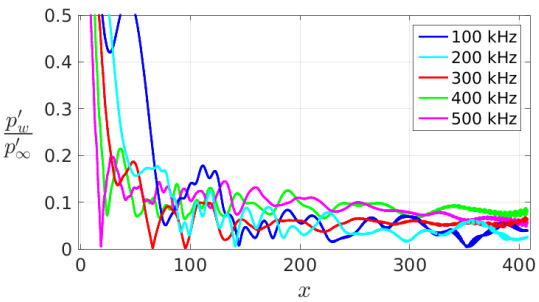


Figure 4.16: Wall response for case 6 (Mach 3) with slow waves

This modulation is even more evident in figure 4.15, for case 6 with fast acoustic waves. Here, the frequency of 500 kHz shows a prolonged region of oscillation cycles due to the

modulation process, downstream of the first peak (reached at about $x = 50$), with a gradual decay in amplitude, which is caused by mode F being no longer synchronised with the fast acoustic wave mode.

In contrast, figures 4.14 and 4.16, for cases 4 and 6 with slow acoustic waves, show a faster initial decay, and a flat overall response at each frequency, with a significantly lower amplitude compared to the fast wave cases. This suggests that mode S does not combine with the forcing waves in the same way as mode F, but maintains a low amplitude for an extended distance downstream, with a weaker modulation effect due to the weak forcing waves (with different phase speed) in the post-shock region, without becoming unstable within the computational domain. Due to the absence of a strong resonance mechanism, the receptivity to slow acoustic waves in the nose region is lower than to fast acoustic waves, and the difference in the amplitude level between the fast and slow mode response along the wall is seen to increase as the Mach number reduces.

Finally, it should be mentioned that for each case, as seen in all the figures above, the wall response starts from a high maximum value at the stagnation point, and decreases rapidly along the circle until approaching (at the circle-wedge junction) the level assumed along the wedge. This is due to the amplification of the waves when crossing the strong normal shock along the stagnation line. Figures 3.4 and 4.3 in Sections 3.1 and 4.1 respectively show a qualitative example of the wave patterns close to the nose. The freestream planar wave front is bent by the bow shock in front of the blunt leading edge, while the disturbance amplitude downstream of the shock varies along the curved wave front, assuming the highest values in the normal shock region. This produces significantly higher values of the wall response along the circle, compared to the values assumed by the response along the wedge, which is, in contrast, affected by the wave propagation patterns downstream of the oblique shock.

### 4.3.4 Effect of wave inclination angle and angle of attack

In this Section we present the results for cases 3 and 5, namely the asymmetric cases, which show the effect of the angle of incidence of the acoustic waves (case 3) and the angle of attack (case 5) on the receptivity characteristics of a hypersonic flow over a wedge. With reference to table 4.1 and to figure 2.1, in case 3 the fast and slow acoustic waves are introduced in the computational domain with an inclination angle $\theta$ (angle between the wave vector and the $x$-axis, taken in the anti-clockwise sense of rotation, starting from zero on the $x$-axis) of $10^\circ$ with respect to the freestream (which is aligned with the $x$-axis). In case 5, on the other hand, the wave vector of the acoustic waves is aligned with the freestream, which is at an angle of attack of $10^\circ$ (taken in the anti-clockwise sense of rotation) to the symmetric axis of the geometry (aligned with the $x$-axis). In both cases 3 and 5 the bottom side of the wedge is the windward side, and the top side is the leeward side. Since for case 5 the flowfield is asymmetric due to the

angle of attack, an asymmetric shock-adapted grid has been used, shaped in such a way to provide a good shock-grid alignment on both the sides of the wedge. In particular, the adapted grid has been obtained through the method based on the analytical hyperbola described in Section 3.3.

Figures 4.17 and 4.18 show the density fluctuation field for case 3 with fast and slow acoustic waves respectively, while figures 4.19 and 4.20 show the corresponding results for case 5. As can be seen, the results for case 3 (figures 4.17 and 4.18) show a slight difference between the post-shock wave structure on the windward side and the lee side with both fast and slow acoustic waves, which suggests a small effect of an incidence angle of 10° on the receptivity patterns. In contrast, figures 4.19 and 4.20 for case 5 reveal a significant effect of the angle of attack (10°) on the structure of the disturbance field downstream of the shock on the windward and the lee sides for both fast and slow waves.

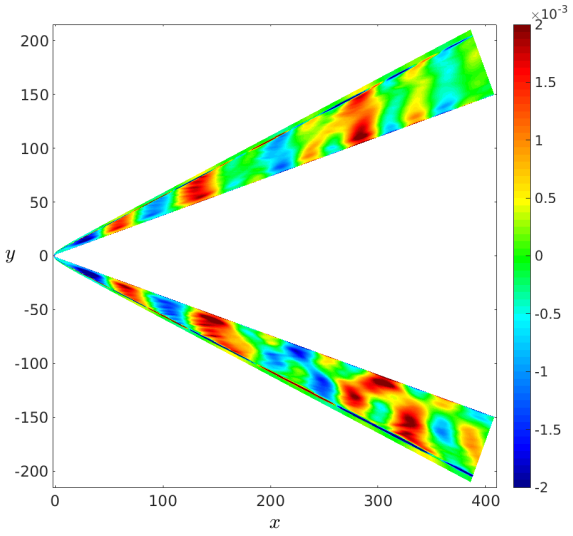


Figure 4.17: Density fluctuation field for case 3 (Mach 7.3) with fast waves

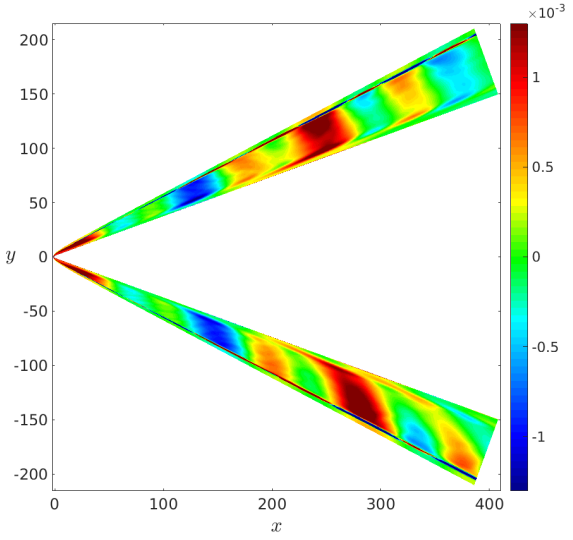


Figure 4.18: Density fluctuation field for case 3 (Mach 7.3) with slow waves

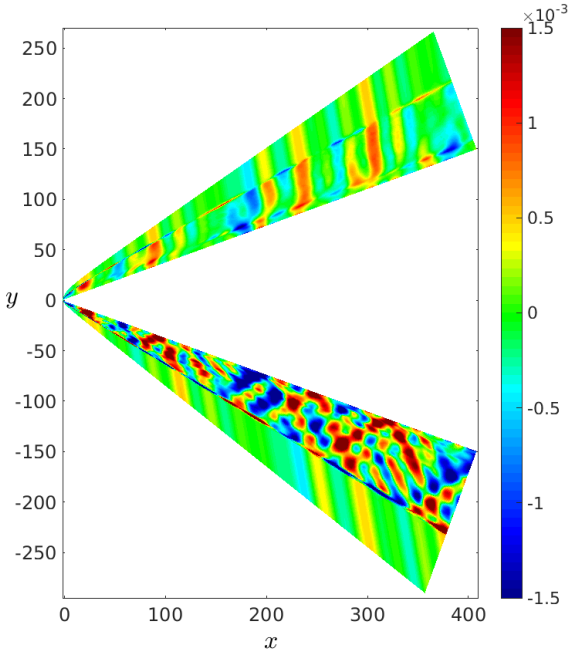


Figure 4.19: Density fluctuation field for case 5 (Mach 6) with fast waves

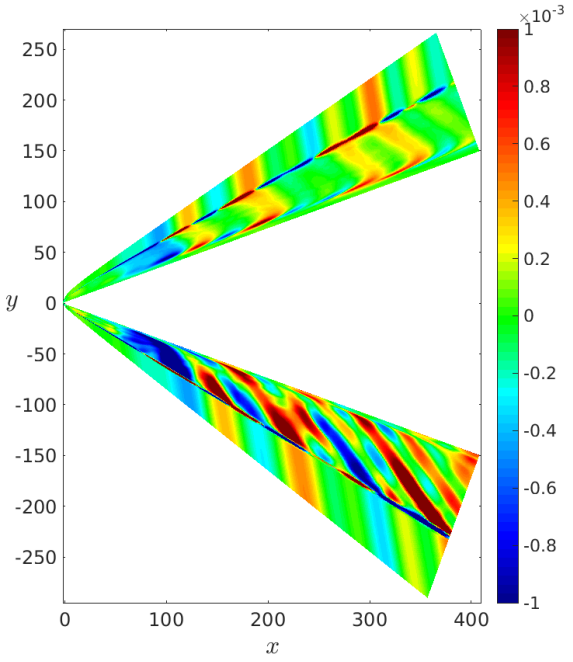


Figure 4.20: Density fluctuation field for case 5 (Mach 6) with slow waves

For non-zero angle of attack, the post-shock disturbances on the windward side (in figures 4.19 and 4.20) have a significantly higher amplitude than the waves crossing the shock on the lee side, which is due to the shock being stronger on the windward side and amplifying the waves in both the fast and the slow wave cases. The lee side shows the presence of dragged waves in the fast-wave case (figure 4.19) and low amplitude transmitted waves with higher phase speed than the freestream waves in the slow-wave case (figure 4.20), as discussed in Section 4.3.1. In contrast, the windward side shows a complex system of dragged and reflected waves between the shock wave and the boundary layer for the fast-wave case, and a reversal (with respect to the lee side) of the post-shock phase speed in the slow-wave case, with the presence of high amplitude dragged waves travelling with lower phase speed than the freestream waves.

The different wave structures between the lee and the windward side have a strong effect on the boundary-layer receptivity characteristics, as is shown in figures 4.21 and 4.22 for the wall pressure fluctuation amplitudes of case 3, with fast and slow waves respectively, and similarly in figures 4.23 and 4.22 for case 5. In each case, the results are shown at two different frequencies and on both the lee and the windward sides. For case 3 with fast acoustic waves (figure 4.21), the response at the lower frequency (100 kHz) is very similar between the two sides of the wedge, being slightly higher on the windward side. At the higher frequency (500 kHz), the response is higher on the windward side in the nose region up to the station $x = 250$, while downstream of this point a reversal is observed, as the response on the windward side starts decaying after the peak reached at about $x = 250$, and the response on the lee side continues growing along the wall,

reaching very high values close to the outer edge. Thus, at the higher frequencies the wave inclination angle appears to amplify the downstream response along the lee side for fast acoustic waves, which is in a good qualitative agreement with the results of Egorov *et al.* [41]. This behaviour suggests that the wave inclination angle enhances the resonance mechanism for mode F on the lee side at high frequencies.

An opposite trend is shown for the slow wave case, whose results are presented figure 4.22. Here, a higher response is observed on the lee side at the lower frequency (50 kHz), while a reversal is shown at the higher frequency (250 kHz), for which the response on the lee side is higher than on the windward side in a small region extending up to about $x = 100$. Further downstream the response on the windward side shows higher values than on the lee side, due to a higher decay rate shown by the wall pressure fluctuations on the lee side in the region $x = 100 - 200$.

The results for case 5, presented in figures 4.23 and 4.24 for fast and slow waves respectively, quantify the strong effect of the angle of attack on the receptivity. For both fast and slow acoustic waves, the response on the windward side is significantly higher than on the lee side, due to the stronger shock wave on the windward side and the consequently higher amplification of disturbances traversing the shock. In the fast-wave case at the highest frequency (500 kHz) the leading-edge resonance and downstream modulation mechanism discussed in Section 4.3.3 are seen. For slow acoustic waves, in contrast, a modulation behaviour is revealed by the long-wavelength oscillations shown at the lower frequency (20 kHz) on the windward side (red line in figure 4.24), which is probably due to the post-shock wave structure on the windward side (figure 4.20) being characterised by high amplitude dragged wave fronts, similarly to the case of fast acoustic waves.

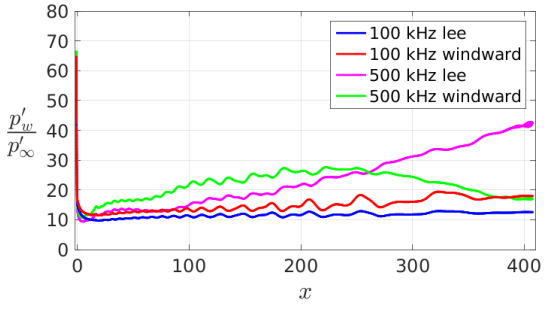


Figure 4.21: Wall response for case 3 (Mach 7.3) with fast waves

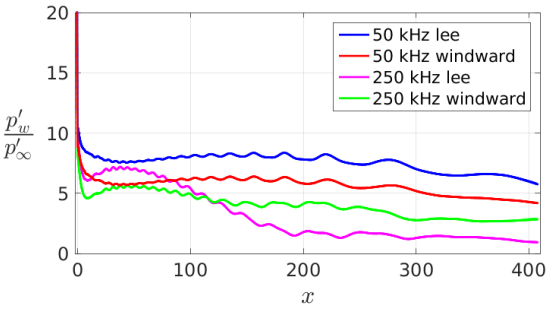


Figure 4.22: Wall response for case 3 (Mach 7.3) with slow waves

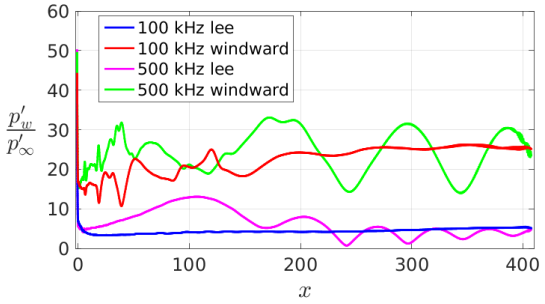


Figure 4.23: Wall response for case 5 (Mach 6) with fast waves

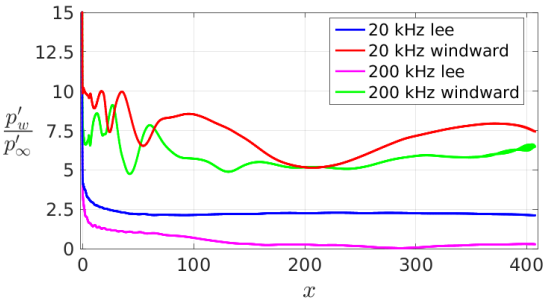


Figure 4.24: Wall response for case 5 (Mach 6) with slow waves

### 4.3.5 Estimation of the freestream noise levels

To help interpret the experimental results, we now focus on the behaviour at a transducer location ($x = 297.3$). Figure 4.25 shows frequency spectra of the wall pressure fluctuation amplitudes for Cases 1 to 3 (HEG), with fast and slow acoustic waves, in the frequency ranges described previously. This shows the effects of Reynolds number ($Re_m = 4.4\times10^6$ m$^{-1}$ for case 1, $Re_m = 1.4 \times 10^6$ m$^{-1}$ for cases 2 and 3) and angle of incidence of the acoustic waves ($\theta = 10°$ for case 3). For case 3 (Mach=7.3, $Re$=140, $\theta = 10°$) the results are shown on both the lee (upper) and the windward (lower) side. As can be seen, for all the cases considered in figure 4.25, the results show a significantly higher response for fast acoustic waves than for slow waves at all frequencies, which is due to the stronger resonance mechanism at the leading edge, characterising the receptivity to fast acoustic waves. The amplitude of the response to fast acoustic waves is seen to increase gradually with frequency, while the slow waves decrease in amplitude, with the minimum value being reached at the highest frequency. For fast acoustic waves, an angle of incidence of 10° (the dashed curves in figure 4.25) is seen to produce a slightly higher response on the windward side, and a slightly lower response on the leeward side, except for frequencies higher than 450 kHz. For slow acoustic waves, an opposite trend is observed, with the response on the lee side being higher, and the response on the windward side lower in the lower frequency range. However, as discussed in the previous Section, at higher frequencies (higher than 100 kHz), there is a reversal, so that the windward side shows higher amplitudes. The Reynolds number is seen to have only a slight effect on the amplitude of the wall response between cases 1 and 2 at all the frequencies.

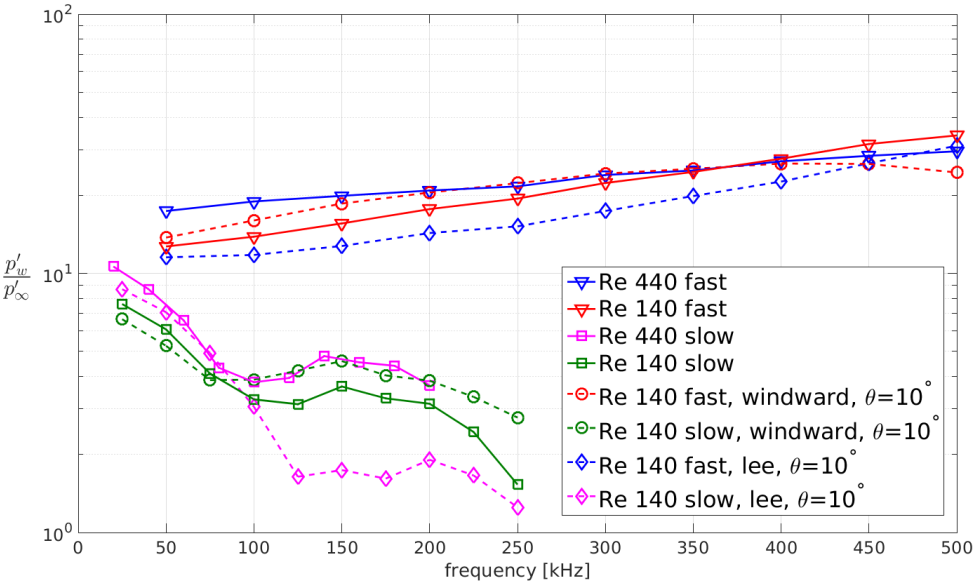


Figure 4.25: Frequency spectrum of the pressure fluctuation amplitudes at the transducer position ($x = 297.3$) for cases 1 to 3 (HEG) with both fast and slow acoustic waves. Mach=7.3, $Re_m = 4.4 \times 10^6$ m$^{-1}$ (case 1), Mach=7.3, $Re_m = 1.4 \times 10^6$ m$^{-1}$ (cases 2 and 3). For case 3, an inclination angle $\theta = 10°$ of the incident waves is considered

Figures 4.26, 4.27 and 4.28 show a comparison between the frequency spectra at the station $x = 297.3$ for case 1, 5 and 6 respectively. Since the modulation behaviour described earlier may lead to locally very low amplitudes at certain points on the surface, and these points would be expected to move around in experiments due to small variations in free stream conditions, the figures also include a spatial average over the region $x = 200 - 400$. The results for case 5 (Mach 6, $\alpha = 10°$) in figure 4.27 correspond to the wall response on the windward side, where the pressure transducers were located in the DLR experiments. Also, it should be noticed that the frequency spectra for case 4 (with reference to table 4.1) are not shown, as the measurements at Mach 6 were conducted only for the case with angle of attack (i.e. case 5). All the cases show a significantly higher-amplitude response for fast acoustic waves, compared to slow waves. Case 1, in figure 4.26, shows the features already discussed in connection with figure 4.25 and a very small effect of the space average on the frequency spectrum of the wall response.

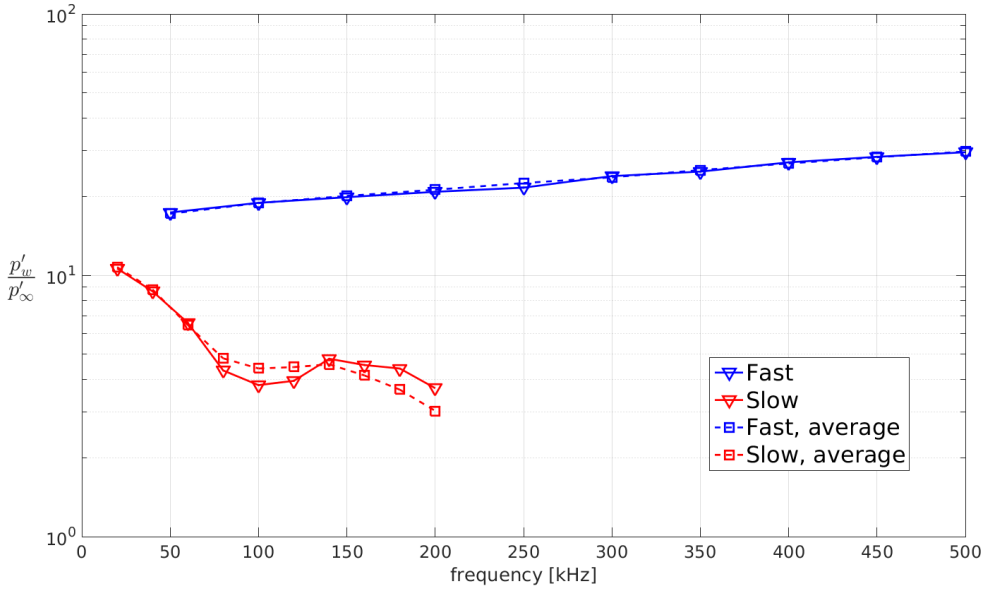


Figure 4.26: Frequency spectra for case 1 (HEG) with both fast and slow acoustic waves, with and without space average. Mach=7.3, $Re_m = 4.4 \times 10^6$ m$^{-1}$

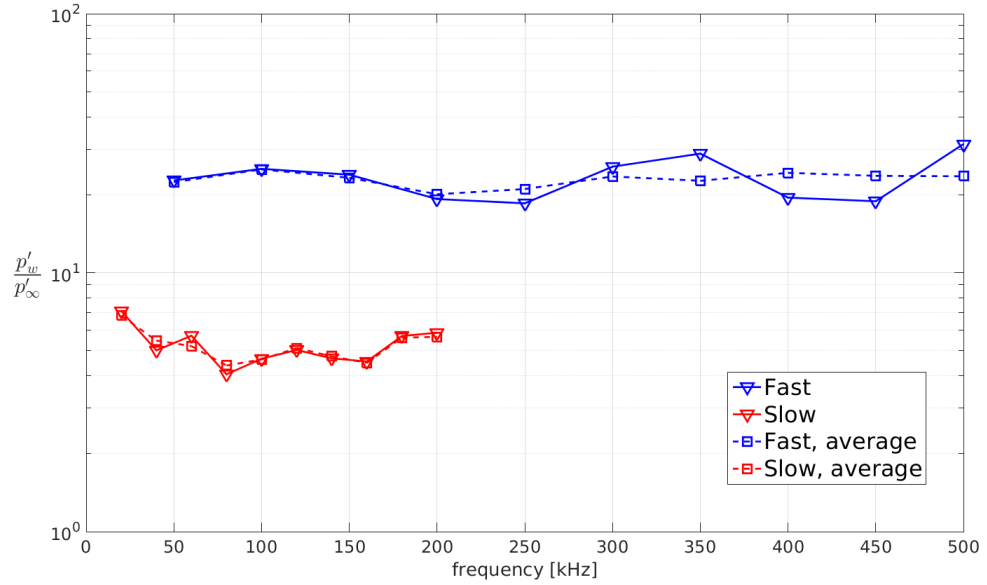


Figure 4.27: Frequency spectra for case 5 (RWG) with both fast and slow acoustic waves, with and without space average. Mach=6, $Re_m = 6.3 \times 10^6$ m$^{-1}$

For the RWG case at Mach 6 (case 5, in figure 4.27), the wall response shows a substantially flat trend with frequency for both the fast and the slow mode, as can be observed for the curves relative to the averaged spectra. In this case, the space average produces a slight change in the shape of the response for fast waves, and almost the same profile of the unaveraged spectrum for slow waves.

The response for case 6 (RWG, Mach 3, figure 4.28), for both fast and slow acoustic waves, is significantly lower than for the higher Mach number cases. Additionally, the discrepancy in the amplitude between the fast and the slow mode response is much higher compared to the other cases. This clearly indicates, as already said in Section 4.3.1, an important Mach number effect on the receptivity to acoustic waves in supersonic flows. Moreover, in contrast to the other cases, the non-averaged frequency spectra for the Mach 3 case (case 6) show a local minimum, at 250 kHz for fast waves, and at 200 kHz for slow waves, compared to the average value of the amplitude level at the other frequencies. As mentioned before, this is a consequence of the modulation mechanism of the pressure fluctuation response along the wall described in Section 4.3.3.

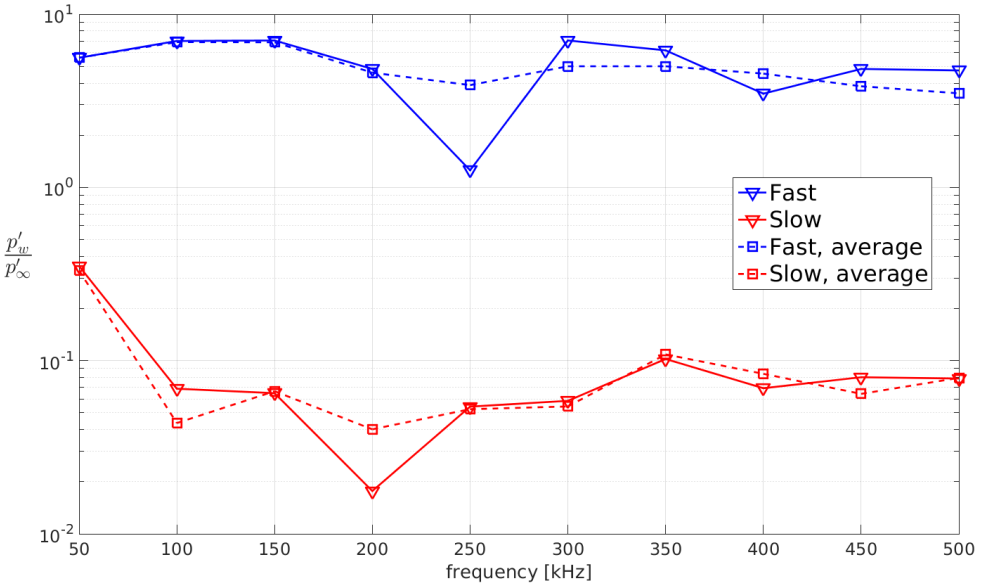


Figure 4.28: Frequency spectra for case 6 (RWG) with both fast and slow acoustic waves, with and without space average. Mach=3, $Re_m = 12 \times 10^6$ $\mathrm{m}^{-1}$

The effect of receptivity can now be assessed by combining the numerical transfer functions $(p'_\infty/p'_w)$, relating the freestream disturbance to the wall disturbance, with the wall pressure fluctuation data from the experiments. We do this in two stages, first by comparing the effect on the spectral shape, which turns out to be small, and then considering combinations of fast and slow modes.

Figures 4.29, 4.30 and 4.31 show the experimental frequency spectra of wall pressure fluctuation levels $(p'_w)$, integrated over a window of 50 kHz for each frequency, and the same frequency spectra projected to the freestream using the numerical transfer functions $(p'_\infty/p'_w)$, through the relation $p'_{\infty,est} = p'_{w,exp}(p'_\infty/p'_w)$, namely the estimated freestream noise levels, for case 1 (HEG Mach 7.3, $Re_m = 4.4 \times 10^6$ $\mathrm{m}^{-1}$), case 5 (RWG Mach 6) and case 6 (RWG Mach 3) respectively. The results are normalised with the values of the freestream mean pressure $(p^*_\infty)$ relative to each case, shown in Table 4.1.

For each case, the transfer functions used to obtain the estimated noise levels are the inverse functions of the corresponding wall-to-freestream pressure fluctuation frequency spectra relative to the averaged response, shown in figures 4.26, 4.27 and 4.28. To better compare the shapes of the spectra, each curve of the estimated noise levels, in figures 4.29, 4.30 and 4.31, is anchored to the curve of the wall values through multiplication by a scaling factor computed at 200 kHz. The corresponding scaling factors for fast and slow acoustic waves are indicated with the terms $a_F$ and $a_S$ respectively on the figures.

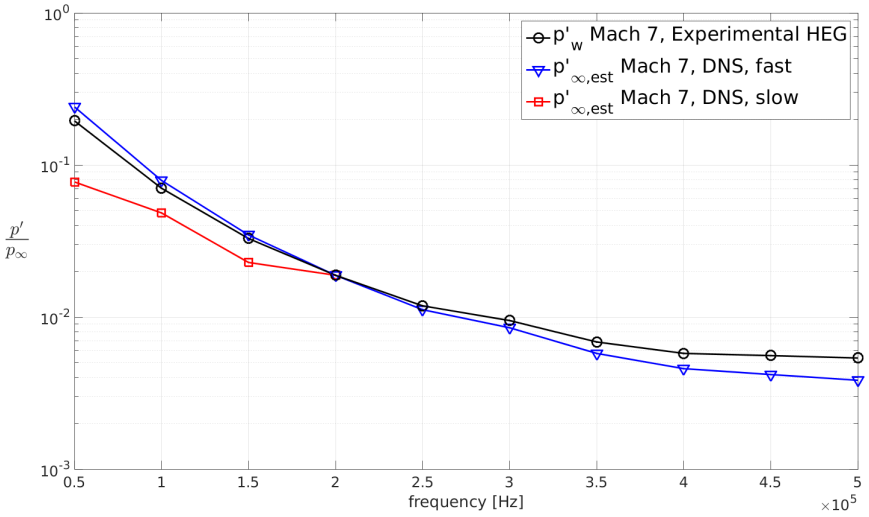


Figure 4.29: Experimental and numerical profiles of the wall response. Numerical profiles adjusted to the experimental data through the scaling factors $a_F = 6.3227$ (fast waves) and $a_S = 44.3943$ (slow waves). HEG, Mach 7.3.

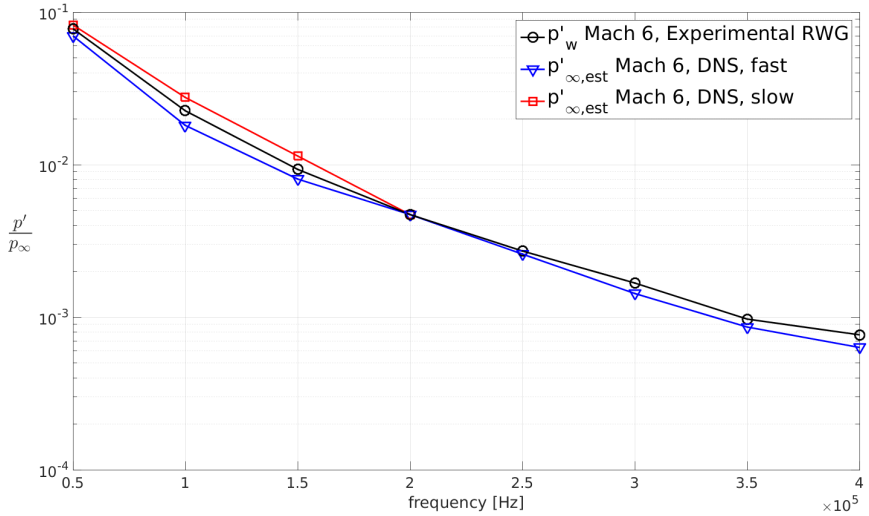


Figure 4.30: Experimental and numerical profiles of the wall response. Numerical profiles adjusted to the experimental data through the scaling factors $a_F = 1.6747$ (fast waves) and $a_S = 5.9515$ (slow waves). RWG, Mach 6.

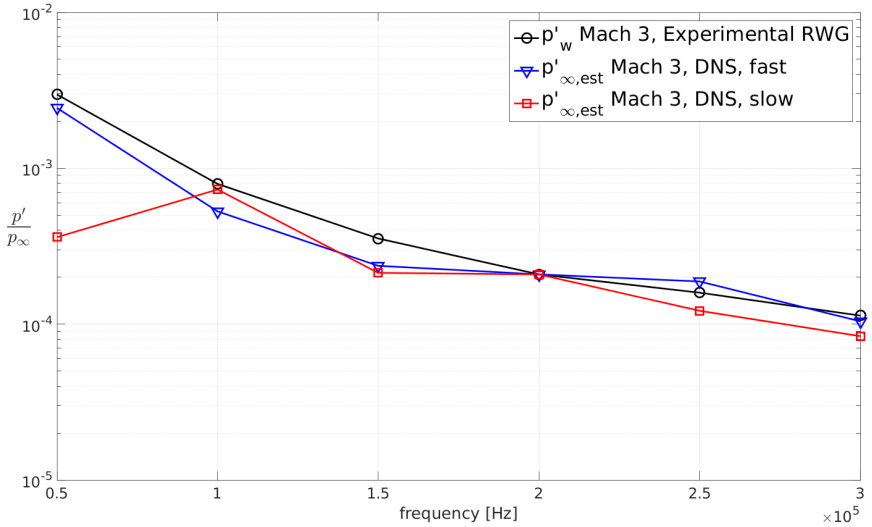


Figure 4.31: Experimental and numerical profiles of the wall response. Numerical profiles adjusted to the experimental data through the scaling factors $a_F = 0.3237$ (fast waves) and $a_S = 37.0909$ (slow waves). RWG, Mach 3.

As can be seen, for each case the shape of the estimated noise level curves is very similar to the shape of the experimental curve, for both fast and slow acoustic waves, due to the flatness of the frequency responses shown in figures 4.26, 4.27 and 4.28. Exceptions need to be made for the results observed for slow waves at the frequency 50 kHz in cases 1 and 6 (in figures 4.29 and 4.31 respectively). This suggests that the receptivity plays a marginal role in the shape of the spectra at the wall, which, then, represents approximately the spectral shape of the noise in the freestream.

The significantly higher scaling factors (given in figures 4.29, 4.30 and 4.31 for each case) for slow acoustic waves, compared to those for fast acoustic waves, indicate that a much higher freestream noise level would be needed, in the case of a freestream noise composed by only slow acoustic waves, to produce the same experimental wall response. Moreover, the difference in the scaling factors between fast and slow acoustic waves is distinctly higher for the Mach 3 case (figure 4.31), with $a_F$ being higher than $a_s$ by two orders of magnitude, which shows, again, that there are strong Mach number effects.

In practice we may consider the freestream acoustic disturbances to be a mixture of fast and slow acoustic waves. To investigate these effects, two arbitrary freestream wave combinations, namely 90% fast-10% slow and 10% fast-90% slow, are considered. Table 4.2 shows the estimated noise levels obtained at a frequency of 200 kHz for the different facilities (HEG and RWG) at the considered Mach numbers (Mach 7.3 for HEG, Mach 6 and 3 for RWG). The values for the different combinations were obtained by summing the numerical transfer functions $(p'_\infty/p'_w)$ relative to fast and slow acoustic waves, each one multiplied with a coefficient indicating the percentage contribution. The composite transfer functions are indicated in table 4.2 as $TF_{90F-10S}$ and $TF_{10F-90S}$, and the corresponding estimated noise levels, obtained through multiplication of the mixed

Table 4.2: Estimated free-stream noise levels for different combinations of the free-stream disturbances, at the reference frequency of 200 kHz.

| Facility | $(p'_w/p_\infty)_{Exp}$ | $TF_{90F,10S}$ | $TF_{10F,90S}$ | $(p'_\infty/p_\infty)_{90F,10S}$ | $(p'_\infty/p_\infty)_{10F,90S}$ |
|---|---|---|---|---|---|
| HEG $M7$ | 0.0188 | 0.0754 | 0.302 | 0.0014 | 0.0057 |
| RWG $M6$ | 0.0047 | 0.0625 | 0.1642 | 0.000294 | 0.000773 |
| RWG $M3$ | 0.000208 | 2.687 | 22.4435 | 0.00056 | 0.0047 |

transfer functions with the experimental pressure values, $(p'_w/p_\infty)_{Exp}$, are indicated as $(p'_\infty/p_\infty)_{90F-10S}$ and $(p'_\infty/p_\infty)_{10F-90S}$. The estimated noise levels range from $1.4\times10^{-3}$ to $5.7\times10^{-3}$ for the HEG facility at Mach 7.3, from $2.9\times10^{-4}$ to $7.7\times10^{-4}$ for the RWG at Mach 6, and from $5.6\times10^{-4}$ to $4.7\times10^{-3}$ for the RWG at Mach 3. Higher estimates are observed for the slow-mode dominated cases.

The higher noise levels estimated for a slow-wave-dominated freestream are due to the lower wall-response levels (resulting in the higher scaling factors in figures 4.29, 4.30 and 4.31) observed in general for slow acoustic waves in all the considered numerical cases, compared to the response to fast acoustic waves. The values listed in table 4.2 indicate higher freestream noise levels in the HEG facility at the highest Mach number (7.3), as was expected, but reveal also an unexpected increase of the noise levels (for both fast- and slow-wave-dominated freestreams) in the RWG wind tunnel when decreasing the Mach number from 6 to 3. This can be explained considering that the location of the measurement probe inside the wind tunnel can play an important role on the wall disturbance level as well, relative to the acoustic noise radiated by the nozzle walls and inclined of the Mach angle with respect to the local flow direction. In fact, for different Mach numbers, the value of the Mach angle will be different, thus the acoustic waves will, in general, impinge on the object at different longitudinal positions, as well as with a different inclination angle. This means that the wall response depends, in general, not only on the inclination angle of the incident acoustic waves, but also on the actual percentage of the total noise radiated by the nozzle walls (through the whole wall length) impinging on the object, which depends, in turn, on the Mach angle and the position of the probe.

Overall, the estimated noise levels in table 4.2 can be considered as realistic, as they are relatively close to the freestream pressure fluctuation level ($3.96\times10^{-3}$), normalised with the freestream mean value, computed by Duan *et al.*[12] in a DNS study on the acoustic noise generated by a turbulent boundary layer over a flat plate in a Mach 2.5 flow. Moreover, Duan *et al.*[12] found that the acoustic noise radiated by the turbulent boundary layer pertained to the class of slow acoustic waves. The freestream noise level we obtained for the Mach 3 case (which is the most comparable case with the study of Duan *et al.*[12] in terms of the Mach number) with dominant slow acoustic waves ($4.7\times10^{-3}$) is, then, very consistent with the results of Duan *et al.*[12], which suggests that slow acoustic waves were most likely the dominant disturbances in the

Mach 3 experiment. Furthermore, the work of Masutti *et al.*[11] indicates that freestream pressure disturbance levels (normalised with the time-averaged value) as high as 1% are usually observed in noisy hypersonic wind tunnels. The higher noise levels obtained, for each case, for the slow-wave-dominated freestream (see table 4.2) are closer to the typical experimental values, compared to the values relative to fast-wave-dominated freestream, which suggests that slow acoustic waves were most likely the dominant disturbances in all the DLR experiments, both in the HEG and RWG facilities.

## 4.4 Summary of the results

The receptivity to fast and slow freestream acoustic waves with multiple frequencies at supersonic/hypersonic speeds over a 2D cylinder-wedge geometry, for a set of six flow conditions with different Mach number, Reynolds number, angle of attack, and angle of incidence of the acoustic waves, has been studied through DNS. The present study has focused on the immediate leading-edge region (upstream of the region of second-mode instability), which is characterised by the generation and interaction of the induced boundary-layer modes. As a result, no second mode instability is observed along the wall for all the considered frequencies.

Three main aspects of the leading-edge receptivity to acoustic freestream disturbances in high speed flow have been analysed, namely a) the structure of the disturbance field in the post-shock region, b) the response along the wall, with emphasis on the resonance-modulation mechanism, and c) the effect of an inclination angle of the acoustic waves and an angle of attack. Preliminary simulations confirmed the linearity of the wall pressure perturbations at increasing freestream amplitudes of the acoustic waves, up to amplitudes as high as $10^{-1}$ for the freestream density.

The numerical results show that, when planar fast acoustic waves are inserted into the domain, the wave structure downstream of the shock is characterised by amplified 'dragged' waves, pertaining to the main forcing fast acoustic waves traversing the shock and being deflected due to the lower local phase speed in the post-shock region, plus reflected waves from the boundary-layer edge travelling downstream at the local Mach angle. For slow acoustic waves, in contrast, the disturbance field downstream of the shock is composed of transmitted waves with lower amplitude compared to the freestream amplitude, and travelling with a higher phase speed than the freestream slow waves. These waves have been shown to have the property of local convected waves (including entropy and vortical waves) generated downstream of the shock from the interaction with the freestream slow waves. A decreasing Mach number is seen to enhance the difference in the wave propagation features downstream of the shock between fast and slow acoustic waves, consistent with the higher gap in phase speed between fast and slow acoustic waves at the lower Mach numbers.

The fast acoustic waves produce a higher response along the wall than the slow waves, which is due to the different wave structure induced downstream of the shock and a stronger resonance mechanism at the leading edge. For each Mach number this mechanism produces an early amplification of mode F until a first peak is reached. A lower Mach number (for the same dimensional frequency range) and a higher frequency are seen to decrease the distance at which the first peak of Mode F is reached. For the Mach 3 and Mach 6 cases, the response further downstream is characterised by a frequency-dependent oscillatory behaviour, representing mode F (which is no longer synchronised with the forcing mode) being modulated by the forcing fast acoustic mode. The response to slow acoustic waves, in contrast, shows a frequency-dependent early decay, caused by the absence of a strong resonance mechanism, which is in turn due to the waves transmitted in the post-shock region and interacting with the boundary layer being desynchronised with the slow mode generated at the leading edge. Further downstream the slow mode is then seen to keep a substantially constant low amplitude.

An angle of incidence of the fast acoustic waves of 10° is seen to amplify the response along the lee side at the higher frequencies, thus suggesting an enhancement of the leading-edge resonance mechanism for mode F, whilst an opposite behaviour of the wall response is shown for slow acoustic waves, with a decaying amplitude downstream along the wall at all frequencies.

An angle of attack of 10° is shown to provide a significantly higher response along the windward side compared to the lee side, for both fast and slow acoustic waves, along with a substantially different post-shock wave structure between the two wedge sides. In particular, high-amplitude dragged waves downstream of the shock are observed for both fast and slow acoustic waves on the windward side, in contrast to the wave structure formed by the slow acoustic waves on the lee side, which consists of low-amplitude transmitted waves travelling with higher phase speed with respect to the freestream slow waves.

For all the Mach numbers, the numerical frequency spectra of the wall response showed a relatively flat profile compared to the decreasing trend of the experimental frequency spectra, for a constant amplitude of the freestream disturbances imposed at all the frequencies, which proves that, for the considered cases, the receptivity does not play a significant role in the shape of the frequency spectra of the wall response. As a result, the shape of the estimated freestream noise level spectra, obtained through a combination of the experimental wall pressure fluctuation levels and the numerical freestream-to-wall transfer functions, appeared substantially unaltered relative to the shape of the experimental wall pressure spectra.

Considering the freestream noise as a mixture of fast and slow acoustic waves, the estimated freestream noise levels corresponding to two arbitrary wave combinations (i.e. 90% fast-10% slow and 90% slow-10% fast) were obtained. The values were found in

the ranges: i) from $1.4 \times 10^{-3}$ to $5.7 \times 10^{-3}$ for the HEG facility at Mach 7.3, ii) from $2.9 \times 10^{-4}$ to $7.7 \times 10^{-4}$ for the RWG at Mach 6, and iii) from $5.6 \times 10^{-4}$ to $4.7 \times 10^{-3}$ for the RWG at Mach 3, as moving from a freestream dominated by fast acoustic waves to a freestream dominated by slow acoustic waves. These values agree reasonably well with other numerical and experimental values available in the literature, thus representing realistic noise levels in hypersonic wind tunnels, and indicate that the HEG wind tunnel is noisier, in general, than the RWG wind tunnel, and that the slow acoustic waves are dominant in the typical environment of a hypersonic wind tunnel.

# Chapter 5

# Results for the wedge with three-dimensional acoustic waves

In this Chapter we will present the results of the simulations for the planar span-periodic wedge geometry with 3D fast and slow acoustic waves. The receptivity mechanism at the leading edge for two different amplitude levels of the freestream disturbances is investigated, along with the effects on the downstream breakdown mechanism. The analysis of the receptivity-breakdown mechanism is performed for two different leading-edge configurations, namely an unswept and a swept (with 45° sweep angle) case. Moreover, a preliminary 2D numerical study, in conjunction with an LST analysis, is conducted, which provides an assessment of the relevance of previous theoretical studies available in the literature, concerning the receptivity process in hypersonic flows.

## 5.1 Flow conditions for the 3D numerical cases

A total of 10 numerical simulations have been carried out including two Reynolds numbers. For the lower Reynolds number, $Re = 1400$ (based on the nose radius), only the receptivity to fast acoustic waves has been investigated, for two different amplitudes, $5 \times 10^{-3}$ and $5 \times 10^{-2}$ at each frequency. For the higher Reynolds number, $Re = 5625$, which is in the range of the Reynolds numbers considered in the transition experiments of Durant *et al.* [89], the receptivity to both fast and slow acoustic waves has been studied, and for each case both higher amplitude and smaller amplitude freestream disturbances have been applied, so that 4 cases have been run overall at this Reynolds number in an unswept configuration. Finally, a further 4 cases, comprising fast and slow freestream acoustic waves at two different amplitudes, have been run at $Re = 5625$ in a swept configuration. The sweep angle (angle between the freestream direction and the $x$-axis of the body) has been set to 45°, corresponding to the sweep angle studied in some experimental and numerical cases for supersonic flow found in literature (Speer *et*

Table 5.1: Settings of the numerical simulations

| Case | $Re$ | $A_\infty$ | $\Lambda$ (°) | type |
|---|---|---|---|---|
| 1 | 1400 | $5\times10^{-3}$ | 0 | Fast |
| 2 | 1400 | $5\times10^{-2}$ | 0 | Fast |
| 3 | 5625 | $5\times10^{-3}$ | 0 | Fast |
| 4 | 5625 | $5\times10^{-2}$ | 0 | Fast |
| 5 | 5625 | $5\times10^{-3}$ | 0 | Slow |
| 6 | 5625 | $5\times10^{-2}$ | 0 | Slow |
| 7 | 5625 | $5\times10^{-3}$ | 45 | Fast |
| 8 | 5625 | $5\times10^{-2}$ | 45 | Fast |
| 9 | 5625 | $5\times10^{-3}$ | 45 | Slow |
| 10 | 5625 | $5\times10^{-2}$ | 45 | Slow |

*al.*[65], Creel *et al.* [57]). Table 5.1 shows the details of the 10 numerical cases just mentioned. For each case the Reynolds number based on the nose radius $Re$ is given along with the overall amplitude of the freestream disturbance $A_\infty$ (being $A_\infty = A_0 + A_1 + A_2$ the sum of the density fluctuation amplitudes of the 2D wave and the oblique waves for each frequency), the sweep angle $\Lambda$, and the type of acoustic wave used as freestream disturbance.

For each case the Mach number is $M = 6$, the freestream temperature is set to $T_\infty = 51.7$ K, and an isothermal boundary condition is used on the wall, with wall temperature fixed to the value $T_w = 300$ K. These conditions are intended to simulate the freestream conditions of a typical low enthalpy hypersonic wind tunnel. Ten different frequencies are inserted in the freestream forcing, each one an integer multiple of the base non-dimensional frequency $f_0 = 3.509 \times 10^{-3}$. Note that the non-dimensional frequency $f$ takes the form of a Strouhal number, $f = f^* R^*/U^*_\infty$, where $f^*$ is the dimensional frequency. In particular the spectrum of the 10 forced frequencies spans from $f_1 = 5f_0$ to $f_{10} = 14f_0$. The non-dimensional frequency in its standard definition, $F_s = 2\pi f^* \mu^*_\infty/(\rho^*_\infty U^{*2}_\infty)$, can be obtained from $F_s = 2\pi f/Re$. The frequency spectrum considered in the present computations is based on linear stability studies conducted by De Tullio and Sandham [85] for a flow at Mach 6 over a flat plate with a Reynolds number comparable with our $Re = 1400$ case. In particular, the frequencies from $f_5$ to $f_{10}$ covers the range of the most unstable second mode frequencies. The overall freestream amplitude levels for the density perturbation (rms of $\rho'_\infty$) of the multi-frequency 3D-wave inflow are 0.0064 and 0.064 for low and high amplitude disturbances respectively, and the corresponding levels for the $x$-wise velocity component $u'_\infty$ are 0.001 and 0.01 respectively. The rms levels of $v'_\infty$ and $w'_\infty$ are identically zero in the freestream, as the imposed acoustic waves propagate in the $xz$-plane with a 2D component (namely a wave oriented along the $x$-axis) and two pairs of oblique waves with the same amplitude and opposite angle (namely $\theta_{xz}$ and $-\theta_{xz}$).

The computational domain geometry, in a generic $xy$-plane is shown in figure 5.1, and consists of a cylinder-wedge shaped wall boundary, with non-dimensional nose radius $R = 1$ and half-wedge angle of 4°, an inlet boundary shaped in such a way to allow internal shock-grid alignment (by applying the spline-based method described in Section 3.3), an outlet boundary normal to the wall direction, and another boundary (not visible in the figure) going from the inlet to the stagnation point on the wall along the $x$-axis, where a symmetric boundary condition is applied due to the condition of zero angle of attack and with symmetric disturbances assumed.

Consistent with the boundary conditions described in Section 4.1 for the 2D cases, a fixed inflow boundary condition of a uniform freestream is imposed at each point on the inflow boundary surface for the 3D cases, in order to compute the baseflow first, then a time-periodic disturbance is added to the inflow (in the form shown in the Section 2.4) to carry out the unsteady simulations. On the wall the standard no-slip condition is applied, along with the isothermal condition described above. The isothermal wall boundary condition requires the effects of wall temperature fluctuations to be neglected, which applies to ground-test experiments of laminar-turbulent transition in hypersonic flows, where the short duration of the test does not cause significant changes in the wall temperature. The flow at the outlet is treated with a zero-gradient boundary condition. After the two-dimensional base flow has been computed on a single $xy$-plane, the computational domain in figure 5.1 is extruded in the $z$-direction in order to create a 3D cylinder-wedge geometry to study the three-dimensional effects of the system of forced acoustic waves on the flowfield. At the side boundaries of the domain a periodic boundary condition is applied, in order to simulate an object with an infinite length in the spanwise direction.

The main dimensions of the 3D computational domain are $L_x = 1000$ along the $x$-axis and $L_z = 55$ along the $z$-axis, and $L_y = 352$ along the $y$-axis (with all the lengths normalised with the nose radius). The grid contains 7920 points in the tangential-to-the-wall direction, 150 points in the normal-to-the-wall direction, and 100 points in the spanwise direction. The distribution of the grid points in the wall-normal direction is controlled through a function that provides clustering in the shock region and towards the wall in order to solve the captured shock wave and the boundary layer, as described in Chapter 3

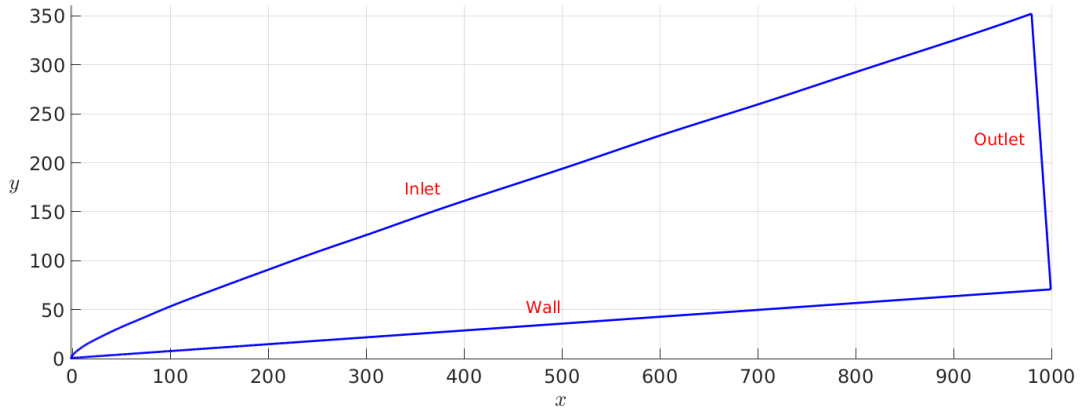


Figure 5.1: Computational domain geometry in the $xy$-plane

## 5.2 Preliminary two-dimensional results at $Re = 1400$: fast vs slow wave receptivity characteristics

### 5.2.1 Wave structure patterns behind the shock

For the case at $Re = 1400$ some preliminary two-dimensional unsteady simulations looking at the receptivity effects to fast and slow waves were performed first. These results served to verify the main differences in the propagation of fast and slow acoustic waves downstream of the shock and in their response on the wall, and can be used as reference 2D results when evaluating the effects of three-dimensional disturbances for the present case and for the next cases with higher $Re$. Figures 5.2 and 5.3 show the density fluctuation field of the flow downstream of the shock wave with freestream fast and slow acoustic waves respectively, for an amplitude of the disturbance equal to $5 \times 10^{-3}$ at each frequency.

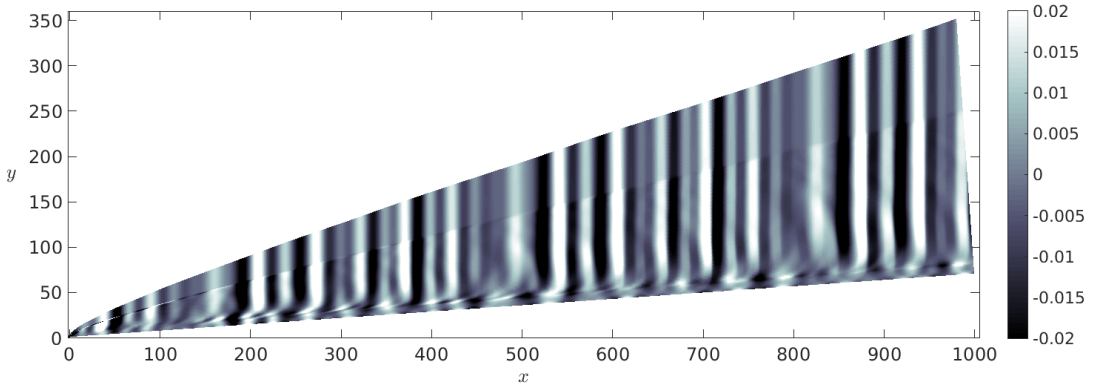


Figure 5.2: Density fluctuation field ($\rho'$) for the case of fast acoustic waves: 2D result, $A_\infty = 5 \times 10^{-3}$

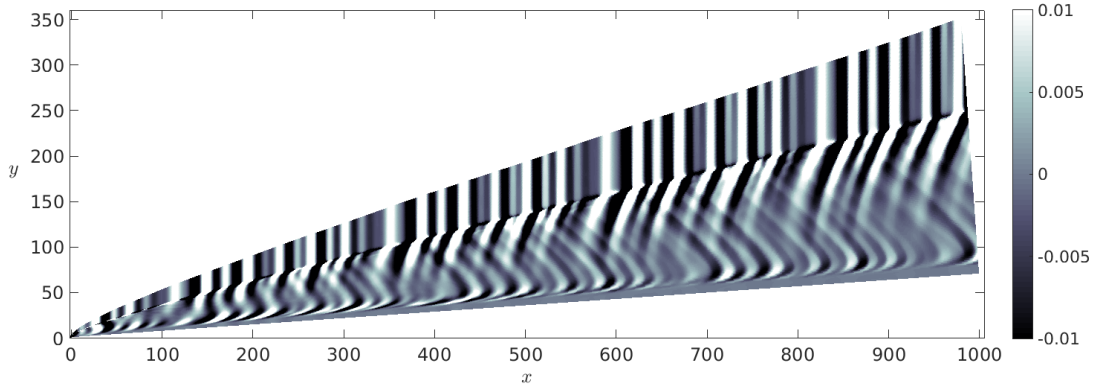


Figure 5.3: Density fluctuation field ($\rho'$) for the case of slow acoustic waves: 2D result, $A_\infty = 5 \times 10^{-3}$

The two figures highlight an important difference in the way in which fast and slow acoustic waves are transmitted through the shock wave and propagate downstream. In particular, it is evident that for the fast wave case the waves downstream of the shock are almost perfectly aligned with the freestream forcing waves, which indicates that the disturbance phase speed behind the shock is very similar to the phase speed in the freestream. This is reasonable for the present case with fast acoustic waves, for two main reasons: i) the Mach number is sufficiently high ($M = 6$) that the contribution of the streamwise convection speed ($u$) to the fast wave phase speed ($u + a$, with $a$ being the local speed of sound) is significantly more important than the contribution of the speed of sound, and ii) a small value of the half-wedge angle ($\delta = 4°$) causes the shock far enough from the nose region to be weak, with only a small decrease of the streamwise velocity downstream of the shock wave. The small decrease of the streamwise convection speed is partially balanced by the increase of the speed of sound downstream of the shock due to the temperature increase, which provides a minor difference in phase speed between the freestream and the post-shock flow.

This result can also be verified through the inviscid oblique shock wave theory for a shock formed on a sharp wedge of 4° inclination angle, which predicts a phase speed in the streamwise ($x$) direction for the fast waves in the post-shock region of $c_{ps} = u_{ps} + a_{ps} = 1.1661$ , a value that is very close to that of the freestream streamwise phase speed of the forced waves, $c_\infty = U_\infty + a_\infty = 1.1666$. From the computational results, by selecting a point just downstream of the shock far enough from the nose region (e.g. $x = 460$) we compute a $x$-phase speed of 1.1651, which proves the validity of the oblique shock theory for this case.

In contrast, in the case with slow waves, it appears that two different families of waves, not aligned with the freestream waves, are generated from the interaction with the shock: a first one, with wave fronts at an inclination angle $\alpha_x < 90°$ to the $x$-axis, which seems to be the dominant type of wave in the immediate post-shock region, and a second one, with an inclination angle $\alpha_x > 90°$ and a lower amplitude, which interacts with the boundary layer downstream. On the basis of the results shown in Section 4.3.1 for the characteristics of the post-shock wave structure, the former type of waves can be referred to as dragged waves, representing wave fronts of the main freestream forced waves crossing the shock and being deflected by the delay accumulated while travelling downstream with a phase speed lower than the freestream phase speed. This also explains the higher amplitude of these waves in the immediate post-shock region. The latter type of waves represents, instead, convected waves generated downstream of the shock from the interaction with the freestream slow waves. From the computational results at a point located just downstream of the shock at $x = 460$, the $x$-direction phase speed for slow acoustic waves is about $c_{ps} = 0.73$, while the phase speed of the slow waves in the freestream is $c_\infty = 0.83$. Evaluating the percentage difference between the freestream and the post-shock streamwise phase speeds ($\epsilon = |(c_\infty - c_{ps})/c_\infty|$) from the computed values given above for both the fast and slow wave cases, the value for the fast waves is $\epsilon_F = 4.28 \times 10^{-4}$, and for the slow waves $\epsilon_S = 0.12$, i.e. for the fast-wave case the post-shock phase speed is lower than the corresponding freestream value by about a 0.04%, while for the slow-wave case the difference is about the 12%, which is no longer a negligible value. This explains the pronounced deflection of the dragged wave fronts in the post-shock region for the slow-wave case.

As already seen in Chapter 4, the difference between fast and slow acoustic waves in the propagation downstream of the shock has strong effects on the boundary layer receptivity and the wall response. In particular, for fast acoustic waves, as the post-shock flowfield is dominated by a single wave mode consisting of the main forced fast waves crossing the shock, the dominant disturbances internalised in the boundary layer at the leading edge are synchronised with the post-shock disturbances. Hence, they undergo a strong resonance mechanism with the forcing waves, which in turn leads to a significant amplification of the fluctuations along the wall as long as the internal and external wave modes are synchronised. The internal mode amplified in the leading-edge region through

the resonance mechanism described above is known in the literature as Mode F (Fedorov [4]), or Mode I (Zhong and Ma [17]), and is predicted to be stable by LST, despite its strong initial growth.

### 5.2.2 Characteristics of the wall response

The effects on the wall response for fast acoustic waves are shown in figure 5.4, which depicts the distribution of the wall pressure fluctuation amplitudes along the wedge at all the considered frequencies, obtained through a Fast Fourier Transform (FFT) approach. As can be seen, the response to fast acoustic waves is characterised by an early strong amplification of mode F, due to the resonance mechanism discussed in Section 4.3.3, with a peak reached at a decreasing distance from the leading edge at increasing frequencies. The initial peak is then followed by a rapid decay, which is a result of the decrease of mode F phase speed along the wall (as shown in figure 5.5) and the consequent desynchronisation of mode F from the forcing fast acoustic waves. In particular, with reference to figure 5.5, at the leading edge, the phase speed (relative to the pressure fluctuation signal along the wall at the frequency $f_6$) assumes a value very close to the phase speed of the fast acoustic waves (thus indicating synchronisation of the internal mode, mode F, with the fast waves at the leading edge). Then, the phase speed reduces gradually until the internal mode (mode F) enters a modulation process with the forcing fast waves (as described in Section 4.3.3), which is shown by strong oscillations in the phase-speed curve, as well as in the corresponding curve of the wall-pressure fluctuation amplitude at the frequency $f_6$ (in figure 5.4). In the region $x = 600 - 700$, the phase speed has almost approached the value relative to the slow acoustic waves (synchronisation between mode F and mode S), which provides the excitation of mode S. In our case, mode S is still stable, as will be shown by an LST study presented in the next Section, so it does not show a strong growth, but a modulation, instead, with the forcing fast acoustic waves downstream of $x = 700$.

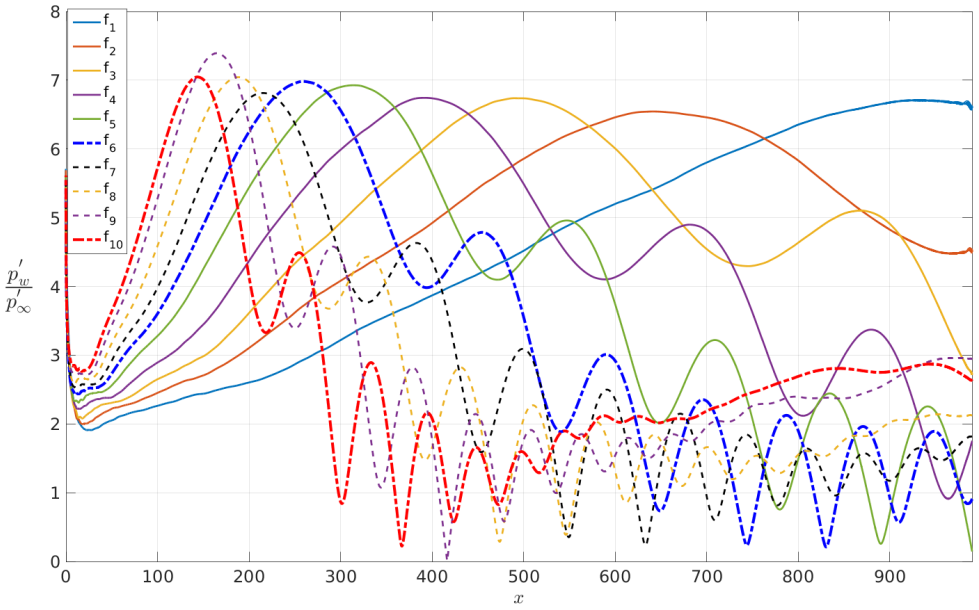


Figure 5.4: Wall pressure fluctuations for fast waves: 2D result, $A_\infty = 5 \times 10^{-3}$. The blue and red dash-dot curves, indicating frequencies $f_6$ and $f_{10}$ respectively, are the reference frequencies of the LST analysis in Section 5.2.3

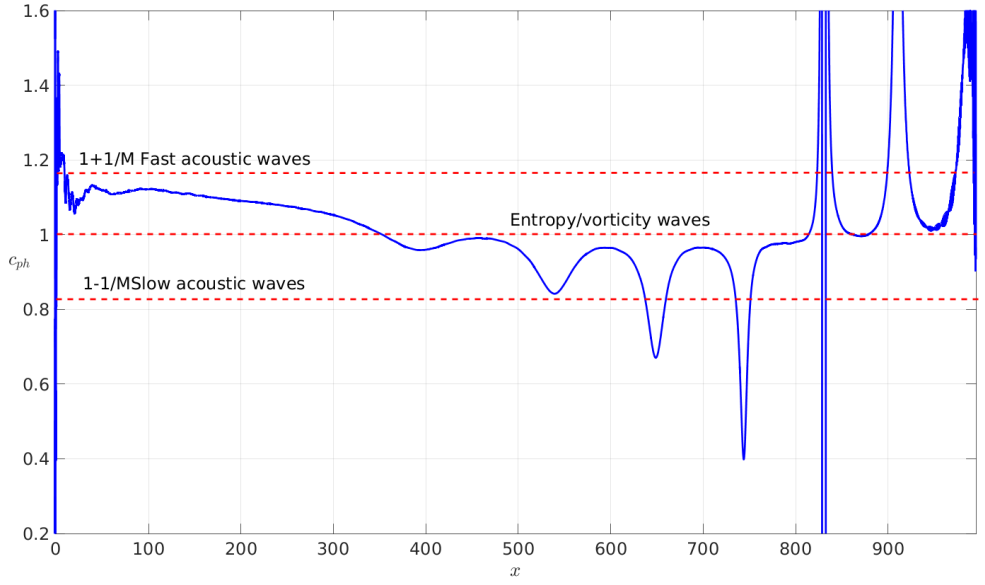


Figure 5.5: Phase-speed evolution of the pressure fluctuation signal along the wall at the frequency $f_6$: 2D result, $A_\infty = 5 \times 10^{-3}$. The red dashed lines represent the phase-speed values of fast and slow acoustic waves, and convected waves in the freestream

Downstream of $x = 800$, the phase speed suddenly increases and starts oscillating around the value relative to the fast acoustic waves, which represents a further synchronisation with the forcing fast acoustic waves, and provides the generation and downstream resonance-induced amplification of the second mode F (or mode II). This is observed

more clearly for frequency $f_{10}$ in figure 5.4, whose pronounced growth downstream of $x = 600$ represents the amplification of the second mode F (mode II) due to the second resonance mechanism with the fast acoustic waves. The smoothness of the curve (relative to frequency $f_{10}$ in figure 5.4) in the growth region of mode II indicates that mode II is the dominant mode in this region. These results are in a very good qualitative agreement with Fedorov's [4] theoretical predictions and with the numerical results of Zhong and Ma [17] and Zhong and Wang [23], and will be compared with the results of a linear stability analysis shown in Section 5.2.3.

In the case of slow acoustic waves (figure 5.6), in contrast, the trend of the pressure fluctuation amplitude appears to correspond to a modulation mechanism between different modes straight from the leading edge.

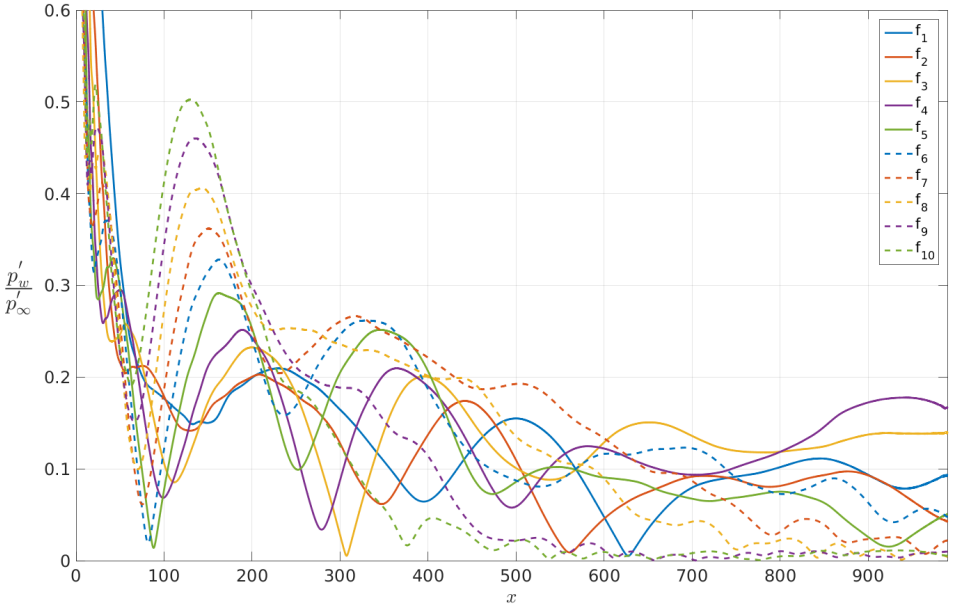


Figure 5.6: Wall pressure fluctuations for slow waves: 2D result, $A_\infty = 5 \times 10^{-3}$

The overall amplitude is lower by about an order of magnitude compared to fast acoustic waves for all the frequencies, due to the absence of a strong resonance mechanism at the leading edge (as discussed in Section 4.3.3), which is consistent with the energy of the freestream slow acoustic waves being transferred to a system of waves with different phase speeds after crossing the shock (namely 'dragged' and convected waves, as described in Section 5.2.1). Thus, in this case the slow mode (Mode S) is directly generated at the leading edge by means of the family of waves in the post-shock region with lower phase speed (pertaining to slow acoustic waves). However, as soon as it is generated, it undergoes a modulation process with the external waves of different phase speed and the other internalised boundary layer modes. This system of mixed forcing modes causes the response at the wall to be very similar for all the frequencies, with the positions of the first

peak at the different frequencies being located in a very narrow region ($x = 150 - 200$) close to the leading edge.

These 2D results show that in the early leading-edge region the receptivity to fast acoustic waves can lead to a much higher amplification of the internal boundary-layer modes, due to the resonance mechanism with the mode of the fast acoustic waves, compared to slow acoustic waves. In the following Sections we will study the effects of this behaviour on the receptivity and breakdown mechanisms in the presence of high-amplitude freestream disturbances and oblique acoustic forcing, for unswept and swept configurations.

### 5.2.3 Comparison with Linear Stability Theory

The numerical results previously described for the Fourier transformed wall pressure fluctuations and the phase speed of the signal along the wall are here compared with results obtained through a local temporal linear stability analysis, performed at several points along the wedge. The linear stability analysis was performed using the NoSTRANA (Nonlocal Stability and Transitional Analysis) code by Sansica[79].

#### 5.2.3.1 Method for the Local Linear Analysis

As a first step the governing equations 2.2 are rewritten in non-conservative form, with

$$\mathbf{q} = \begin{bmatrix} \rho \\ u \\ v \\ w \\ T \end{bmatrix} \tag{5.1}$$

as the vector of the primitive variables. The temperature ($T$) represents here the variable in the equation of the internal energy, which is in turn obtained subtracting the contribution of the mechanical energy, given by the scalar product between the momentum equation and the velocity vector ($\mathbf{u}$), from the total energy equation, in which the relation

$$E = \frac{T}{\gamma(\gamma - 1)M^2} + \frac{1}{2}\left(u^2 + v^2 + w^2\right) \tag{5.2}$$

is applied, where the first term represents the dimensionless internal energy. With this arrangement the governing equations assume the following form,

$$\frac{\partial \rho}{\partial t} + u_j \frac{\partial \rho}{\partial x_j} + \rho \frac{\partial u_j}{\partial x_j} = 0 \ , \tag{5.3}$$

$$\rho \frac{\partial u_i}{\partial t} + \rho u_j \frac{\partial u_i}{\partial x_j} + \frac{1}{\gamma M^2} \left( T \frac{\partial \rho}{\partial x_i} + \rho \frac{\partial T}{\partial x_i} \right) - \frac{1}{Re} \frac{\partial \tau_{ij}}{\partial x_j} = 0 \ , \tag{5.4}$$

$$\rho \frac{\partial T}{\partial t} + \rho u_j \frac{\partial T}{\partial x_j} + (\gamma - 1) \rho T \frac{\partial u_j}{\partial x_j} - \gamma(\gamma - 1) \frac{M^2}{Re} \tau_{ij} \frac{\partial u_i}{\partial x_j} + \frac{\gamma}{RePr} \frac{\partial}{\partial x_j} \left( \frac{\mu \partial T}{\partial x_j} \right) = 0 \ , \tag{5.5}$$

where the viscous stresses ($\tau_{ij}$) are linked to the spatial velocity derivatives through relation 2.5, and the pressure in both momentum and energy equations have been expressed in terms of the density and temperature through the equation of state 2.7.

The second step consists of superimposing small amplitude disturbances on the vector of the primitive variables, which will assume the form

$$\mathbf{q}(x, y, z, t) = \bar{\mathbf{q}}(x, y, z) + \mathbf{q}'(x, y, z, t) \ , \tag{5.6}$$

where $\bar{\mathbf{q}}(x, y, z)$ represents the boundary-layer solution vector in the unperturbed flow, while $\mathbf{q}'(x, y, z, t)$ is the disturbance vector. By applying this decomposition for the vector of the primitive variables the governing equations for the perturbed quantities can be obtained. Let us consider, for example, the continuity equation 5.7; by applying the relation 5.6 the resulting perturbed continuity equation is

$$\frac{\partial \bar{\rho}}{\partial t} + \bar{u_j} \frac{\partial \bar{\rho}}{\partial x_j} + \bar{\rho} \frac{\partial \bar{u_j}}{\partial x_j} + \frac{\partial \rho'}{\partial t} + \bar{u_j} \frac{\partial \rho'}{\partial x_j} + u'_j \frac{\partial \bar{\rho}}{\partial x_j} + \bar{\rho} \frac{\partial u'_j}{\partial x_j} + \rho' \frac{\partial \bar{u_j}}{\partial x_j} = -u'_j \frac{\partial \rho'}{\partial x_j} - \rho' \frac{\partial u'_j}{\partial x_j} \ , \tag{5.7}$$

in which the first three terms of the left hand side cancel out, as their sum represents the continuity equation for the unperturbed flow, while the two terms at the right hand side are nonlinear terms, which, in turn, are neglected for the assumption of small amplitude perturbations, namely the linearity assumption. So, the linear perturbed continuity equation is

$$\frac{\partial \rho'}{\partial t} + \bar{u_j} \frac{\partial \rho'}{\partial x_j} + u'_j \frac{\partial \bar{\rho}}{\partial x_j} + \bar{\rho} \frac{\partial u'_j}{\partial x_j} + \rho' \frac{\partial \bar{u_j}}{\partial x_j} = 0 \ , \tag{5.8}$$

At this point, another simplification assumption is made, namely the assumption of parallel flow, which states that the unperturbed flow does not vary along the streamwise direction. Hence, considering the streamwise direction coincident to the $x$-direction, the

adoption of the parallel flow assumption results in the unperturbed primitive variables being dependent on the $y$-direction only, namely

$$\bar{\rho} = \bar{\rho}(y), \bar{u} = \bar{u}(y), \bar{T} = \bar{T}(y), \bar{v} = \bar{w} = 0 \ . \tag{5.9}$$

Repeating the same procedure for all the other equations provides a linear system of equations in terms of the disturbance variables with coefficients depending on the independent variable $y$, known as linearised disturbance equations, or Orr-Sommerfeld equations. For the derivation of the full system of the linearised disturbance equations, which is beyond the purposes of the present study, the reader can refer to the work of Sansica [79].

The next step is to perform a separation of variables between the independent variable $y$ and the other independent variables $x$, $z$ and $t$, namely

$$\mathbf{q}'(x, y, z, t) = \hat{\mathbf{q}}(y) \cdot g(x, z, t) \ . \tag{5.10}$$

By introducing the variable separation 5.10 in the system of the linearised disturbance equations, and by imposing for the function $g(x, z, t)$ a periodic function in both the space variables and in time, corresponding to the wave solution

$$\mathbf{q}'(x, y, z, t) = \hat{\mathbf{q}}(y) \cdot e^{(i(\alpha x + \beta z - \omega t))} \ , \tag{5.11}$$

in which $\alpha$ represents the streamwise wavenumber in this Section (not to be confused with the symbol indicating the angle of attack in the other Sections), $\beta$ the spanwise wavenumber, and $\omega$ the angular frequency of the periodic wave perturbation, the linear system of partial differential equations reduces to a linear system of ordinary differential equations in the variable $y$, which can be expressed as

$$\mathbf{L}\hat{\mathbf{q}} = \omega \mathbf{K}\hat{\mathbf{q}} \ . \tag{5.12}$$

In equation 5.12, $\mathbf{L}$ is a matrix containing the $y$-dependent coefficients of the system, the wavenumbers $\alpha$, $\beta$, and the $y$-derivatives of the components of the variable vector $\hat{\mathbf{q}}$; while $\mathbf{K}$ is a diagonal matrix containing the terms multiplied by $\omega$, which come out from the time derivatives of the function $g(x, z, t)$ in all the equations.

System 5.12 represents an eigenvalue problem. The resolution of this eigenvalue problem, at a particular $x$-location along the wall, will provide a certain number of eigenvalues $\omega$, representing the frequencies of the different modes, and the corresponding eigenvectors $\hat{\mathbf{q}}(y)$, containing the eigenfunctions $\hat{\rho}(y)$, $\hat{u}(y)$, $\hat{v}(y)$, $\hat{w}(y)$, $\hat{T}(y)$, representing, in turn,

the shape of each mode inside the boundary layer at that particular $x$ location. The discretisation of the system in the wall-normal direction is made through a Chebyshev collocation method. Sansica [79] derives all the components of the matrices $\mathbf{L}$ and $\mathbf{K}$ in system 5.12, and gives a description of the Chebyshev discretisation method.

Two different approaches can be adopted for the local stability analysis, namely a temporal and a spatial approach. The temporal approach consists of imposing a certain real value for the streamwise wavenumber ($\alpha$) and for the spanwise wavenumber ($\beta$), which is set to zero for 2D waves, and performing the analysis described above to obtain as output the eigenvalues $\omega$ of the system, which have a real and an imaginary part. The real part ($\omega_r$) represents the angular frequency of a single mode, while the imaginary part ($\omega_i$) represents the temporal growth rate. A positive sign of $\omega_i$ indicates a stable mode, while a negative sign indicates an unstable mode. The spatial approach works the other way round, namely a real frequency $\omega$ is given as an input, along with an initial guess for $\alpha$ and $\beta$, and complex values of $\alpha$ and $\beta$ are obtained, for all the modes found at the given frequency $\omega$, with the real part indicating the corresponding wavenumber, and the imaginary part representing the spatial growth rate. In the present work only the temporal approach is considered, and the analysis is performed at several $x$ stations along the wedge, for different streamwise wavenumbers ($\alpha$) among the forcing wavenumbers of the freestream acoustic wave inflow in our unsteady numerical simulations. The spanwise wavenumber ($\beta$), in contrast, is set equal to zero, as we consider 2D waves. In order to perform the linear stability analysis, the boundary-layer solution vector of the baseflow ($\bar{q}$) is extracted from our numerical simulations at all the considered $x$ stations, and used as input in the temporal analysis. In order to guarantee a quicker convergence of the method, two bounds of the phase speed ($c_{ph}$) are imposed as input for the analysis, so that only complex eigenvalues $\omega$ within the specified range of phase speeds are returned, for each given value of $\alpha$, according to the relation $c_{ph} = \omega_r/\alpha$.

#### 5.2.3.2 LST results

The results of the local stability analysis, using the temporal approach, have been obtained at different points along the wedge for two different streamwise wavenumbers, corresponding to the forcing wavenumbers at the frequencies $f_6$ and $f_{10}$ for the case of fast acoustic waves. The wavenumbers were computed by considering the local value of the wall-tangential fast-wave phase speed at the boundary-layer edge resulting from the numerical solution for the baseflow, namely $c_{ph} = u_e + a_e$, where $u_e$ and $a_e$ are the velocity components in the wall-tangential direction and the speed of sound at the boundary-layer edge respectively. Thus, the wavenumber to be used as input in the temporal LST analysis is computed through the relation $\alpha = 2\pi f/c_{ph}$. Figure 5.7 shows the spectrum of the complex eigenvalues at different positions along the wedge for the frequency $f_{10}$. The analysis has been performed in a phase-speed range spanning from

the slow-wave to the fast-wave acoustic phase speed. Moving from low to high values of $\omega_r$ in the spectrum corresponds to moving from lower phase speeds to higher phase speeds. The two horizontal branches of modes at $\omega_i \approx 0$ positioned at the left and right extremes of the graph represent the slow and the fast acoustic wave continuous spectrum respectively. The branch of modes positioned in the middle of the graph, at approximately $\omega_r = 0.26$, represents the entropy/vorticity wave continuous spectrum.

As can be seen, performing the LST analysis at several $x$ positions is equivalent to tracking the movement of some discrete modes of interest in the spectrum. The evolution of the different discrete modes in the complex plane can, in turn, help understand the corresponding trend of the numerically obtained pressure fluctuation amplitude distribution along the wall shown in figure 5.4 at the frequency $f_{10}$. In particular, in the region of the first peak of wall response ($x \approx 150$), as seen in figure 5.4, figure 5.7 shows the presence of a discrete stable mode close to the continuous spectrum of the fast acoustic waves (blue star symbol, indicating the position $x = 143$, with $\omega_r = 0.294$). This mode corresponds to mode F, which is synchronised with the forcing fast acoustic waves in the leading-edge region, thus experiencing a resonance-induced strong amplification, as shown by the numerical results in figure 5.4. However, as is evident in figure 5.7, mode F gradually moves away from the fast acoustic wave continuous spectrum, corresponding to a desynchronisation, resulting in a downstream decay of the wall response, due to the decay of mode F, which decreases its phase speed (as it moves towards lower values of $\omega_r$) and becomes more stable (moving towards higher negative values of $\omega_i$).

In the region $x \approx 400 - 500$, characterised by a modulation behaviour shown by the oscillatory wall response in figure 5.4, mode F traverses the entropy/vorticity wave continuous spectrum, and, at the same time, another discrete mode, close to the slow acoustic wave continuous spectrum, starts moving rapidly from very low values of $\omega_i$ to higher values, thus becoming less stable, with increasing phase speed. This mode corresponds to mode S, which is excited due to a synchronisation with the decaying mode F, after crossing the convected wave continuous spectrum.

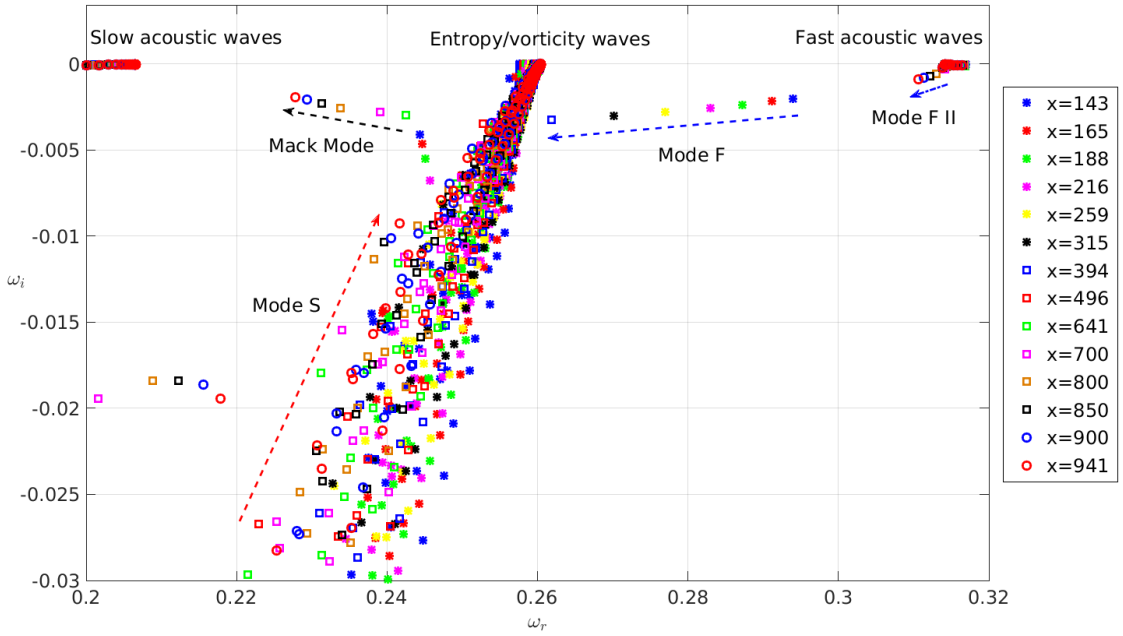


Figure 5.7: Spectrum of the eigenvalues at the frequency $f_{10}$

Between $x = 500$ and $x = 700$ the leftwards path of mode F in the eigenvalue spectrum is replaced by the leftwards path of a different discrete mode, namely a Mack mode, which first appears at $x = 641$ (indicated by a green square symbol) as a consequence of the previous wavelength exchange (or synchronisation) mechanism between mode F and mode S, and the progressive growth of mode S, moving towards the higher frequency ($\omega_r$) and the higher (closer to zero) growth rate ($\omega_i$) values. The Mack mode is generated at higher frequencies than mode S, however, as we move further downstream, it shows a decreasing frequency (and phase speed), and becomes progressively less stable. In this region, the continuous growth of mode S, due to the synchronisation with the decaying mode F, followed by the generation and progressive growth of the Mack mode, results in a growth of the wall response, as shown in figure 5.4, whose oscillatory behaviour indicates a modulation process between the forcing fast acoustic waves and the above mentioned internal competing modes.

Downstream of $x = 700$ figure 5.4 shows another growth of the wall response, which is now much smoother than the growth in the previous region, thus indicating that there is a dominant mode in this region. This mode is again mode F, which grows as a consequence of a second resonance-induced amplification cycle, due to the synchronisation with the fast acoustic waves. For this reason, we refer to this mode as the second fast mode, or mode F II. The downstream evolution of the second fast mode is represented by a short branch very close to the fast acoustic wave continuous spectrum in the top right corner of figure 5.7.

Similar characteristics to those described above for the eigenvalue spectrum at the frequency $f_{10}$ have been observed for the corresponding spectrum at the frequency $f_6$, with

the exception that the evolution path of the different modes along the wall extends up to approximately the position where mode F traverses the convected wave continuous spectrum. This means that the branches of the Mack mode and of the second fast mode are not present in the eigenvalue spectrum at the frequency $f_6$. In other words, the downstream generation-evolution path of the boundary-layer modes at the higher frequencies is quicker than at the lower frequencies, and results in the mode F - mode S wavelength exchange mechanism taking place closer to the leading edge. This effect can be observed in figure 5.8, which shows a comparison between the DNS and the LST results for the internal mode phase speed at both the frequencies $f_6$ and $f_{10}$ (the curve relative to the numerical result for the frequency $f_6$ is the same shown in figure 5.5). The phase speed from the DNS results has been computed through the fast Fourier transformed wall pressure fluctuations, using the relation for the streamwise wavenumber

$$\alpha(x,f) = \alpha_r + \alpha_i = \frac{1}{ip'_w(x,f)} \frac{\partial p'_w(x,f)}{\partial x} \ , \tag{5.13}$$

and then applying the relation $c_{ph} = 2\pi f/\alpha_r$. As can be seen, for both the frequencies, the numerical phase speed (represented by blue and red solid lines for the frequencies $f_6$ and $f_{10}$ respectively) starts at a value of about 1.12 in the early nose region ($x = 20-40$), which is slightly lower than the local fast acoustic wave phase speed of about 1.16. This may be due to non-parallel effects related to the presence of the strong bow shock, significantly affecting the flowfield and the wave propagation speed in the early leading-edge region. The LST analysis performed at the distance $x = 50$ from the leading edge provides, instead, phase speed values for mode F of about 1.165 for the frequency $f_6$ and 1.15 for the frequency $f_{10}$, which are much closer to the local fast acoustic wave phase speed. Thus, the internal mode generated at the leading edge is mode F. Overall, both DNS results and LST results for mode F show a good agreement in the decay part of the numerical phase speed, thus indicating that the internal mode decaying from the leading-edge towards downstream is indeed mode F. In particular, the numerical phase speed decreases up to about $x = 300$ at the frequency $f_{10}$, while it keeps decaying up to about $x = 750$ at the frequency $f_6$. Downstream of these two points mode F traverses the convected wave continuous spectrum, the numerical phase speed shows a rapid increase, and a second synchronisation with the local fast acoustic waves is reached (as already mentioned in Section 5.2.2). Downstream of this synchronisation point ($x = 370$ at the frequency $f_{10}$, and $x = 830$ at the frequency $f_6$), the numerical phase speed no longer follows the LST result for mode F, but, in contrast, agrees very well with the LST result for mode F II, as can be seen further downstream for the frequency $f_{10}$ (at the lower frequency, $f_6$, mode F II would be reached further downstream of the computational domain outer edge). During the decay of mode F, when the phase speed drops below the value of 0.9, strong oscillations of the numerical solution are observed, as a consequence of the mode F phase speed approaching the phase speed of mode S, which results in an initial growth of mode S, as is shown by the LST curves representing mode

S (blue and red dash-dot curves with square symbols). These oscillations represent, in fact, the modulation process between the forcing fast acoustic waves and the emerging mode S, which can be further validated, as described in Section 4.3.3, using relation 4.5. Assuming for the phase speed of the known mode ($c_a$) the value of the local fast-acoustic wall-tangential phase-speed at the location $x = 700$, namely 1.168, and taking the distance between the two consecutive peaks of the wall pressure response curve at $x = 696$ and $x = 787$ (within the modulation region), with reference to figure 5.4 for the frequency $f_6$, i.e. $\Delta x = 91$, the value of the second competing mode in the modulation process is $c_b = 0.855$, which is very close to the LST results for mode S phase speed shown in figure 5.8 in the considered region.

Strong oscillations are observed also further downstream, after the second synchronisation with the fast acoustic waves, representing a modulation between the growing mode S, with increasing phase speed, and the emerging mode F II. As shown by the frequency $f_{10}$, these oscillations reduce further downstream until disappearing when mode F II becomes the dominant mode inside the boundary layer. Furthermore, downstream of the intersection point between mode F and mode S LST phase speeds (i.e. the mode F - mode S synchronisation point) at the frequency $f_{10}$, the Mack mode is generated and develops downstream with an initial decrease of the phase speed, as a continuation of the mode F branch, but with increasing growth rate. These results are qualitatively in a very good agreement with the results of Zhong and Wang [23].

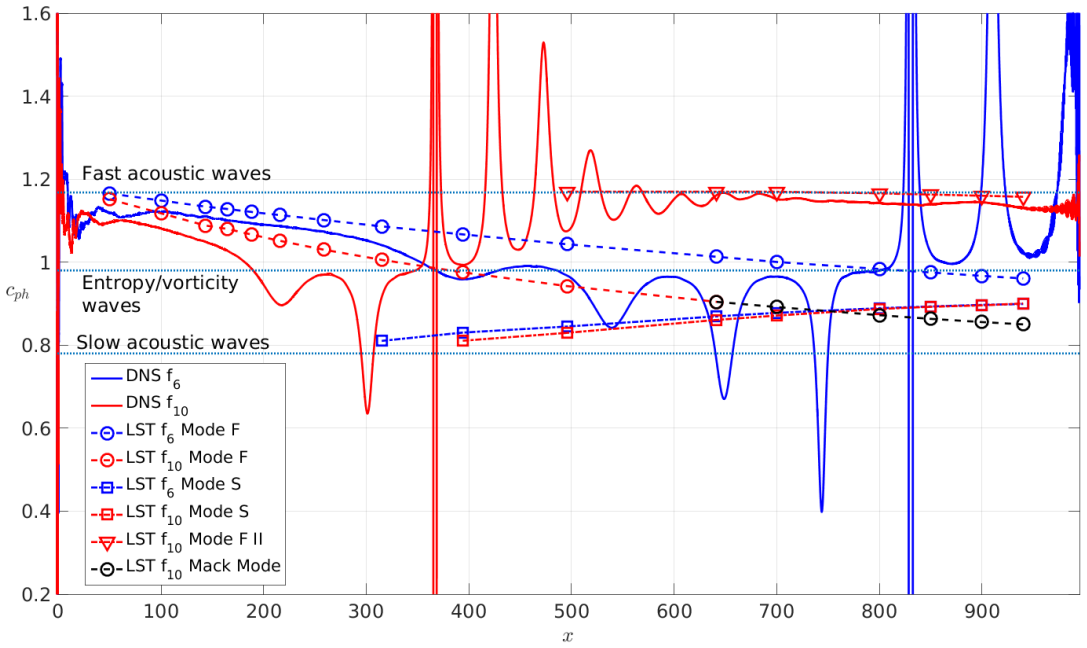


Figure 5.8: Phase speed of the boundary-layer modes along the wall for the frequencies $f_6$ and $f_{10}$. Comparison between DNS and LST results. The dotted horizontal blue lines indicate the local phase-speed values of the fast and slow acoustic waves, and the entropy/vorticity waves

Figure 5.9 shows the corresponding LST results for the growth rates of the internal modes at both the frequencies. As can be seen, all the fast modes, namely Mode F and Mode F II, have a decreasing growth rate, as they are damped modes. The slow modes, namely Mode S and the Mack mode (which can be considered as a second, or higher frequency, slow mode), show in contrast an increasing growth rate, as they represent the instability modes, although they are still stable (negative $\omega_i$) in this case. The arrow illustrates the exchange mechanism between the decaying fast mode (Mode F) and the Mack mode (or second instability mode) taking place at the synchronisation (or phase-speed intersection, as shown in figure 5.8) point between Mode F and Mode S. This mechanism is also evident in figure 5.7, where Mode F (blue) and Mode S (red) arrows illustrate the movement of either mode in frequency (hence in phase speed) towards each other, then, when their frequencies match, the Mack mode is excited and replaces Mode F in the path towards decreasing frequencies.

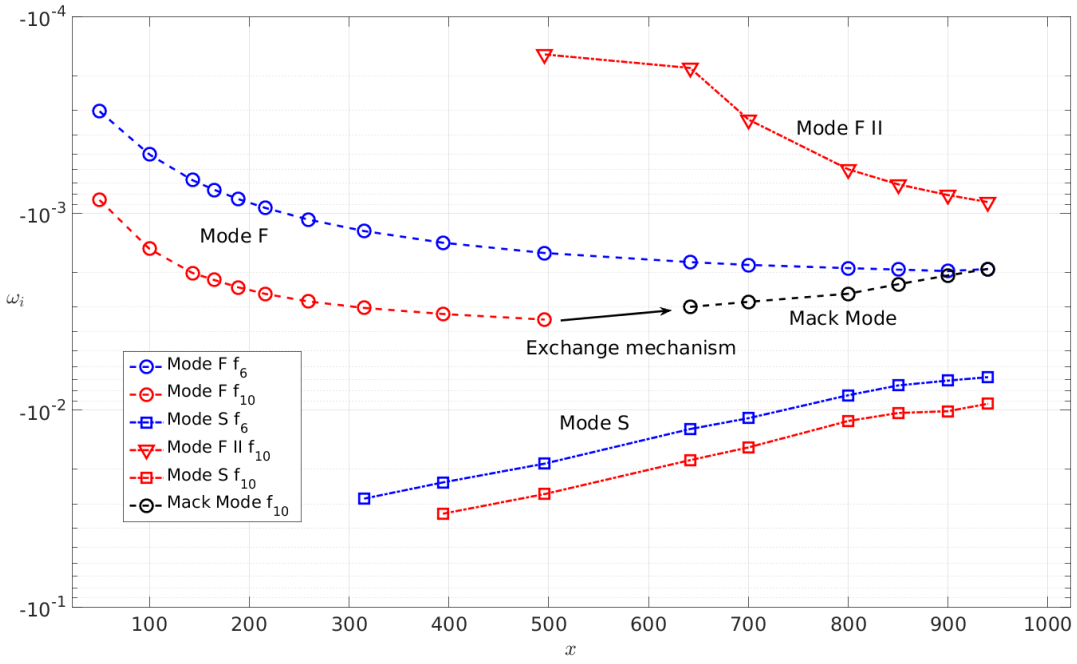


Figure 5.9: Growth rates of the boundary-layer modes along the wall for the frequencies $f_6$ and $f_{10}$, obtained through LST

A further comparison between the DNS and the LST results, as well as a more detailed identification of the internal modes, is made by considering the eigenfunctions of the different modes at several positions along the wall. Figure 5.10 shows the temperature and wall-tangential velocity eigenfunctions for the frequency $f_6$ at $x = 259$, which is the position where the first peak of the wall pressure fluctuation amplitude is reached due to the leading-edge fast-acoustic - mode F resonance mechanism (with reference to figure 5.4). At this position mode F is the dominant mode inside the boundary layer, which is proved by the good agreement between the DNS results for $\hat{T}$ and $\hat{u}$, namely the fast Fourier transformed temperature and wall-tangential velocity fluctuation amplitudes

along the wall-normal direction, and the LST eigenfunctions for mode F. As can be seen, the shape of mode F is characterised by a high peak near the wall. These results are also in a good qualitative agreement with the numerical and LST results of Zhong [86] for the eigenfunctions of mode F. It shall be noted that the fluctuation amplitudes are normalised with the maximum inside the boundary layer ($A/A_{max}$).

Figure 5.11 shows the corresponding eigenfunctions for the frequency $f_6$ at the position $x = 700$, which is within the modulation region, and in particular at about the location of a peak of the wall response. Here, the DNS results are compared with the LST results for Mode S at this position, which represents one the competing modes in the modulation region, as said above. As can be observed, the numerical eigenfunctions are characterised in general by the typical patterns of the fast acoustic wave mode, namely the maximum peak near the wall. However, the numerical temperature perturbation shows also a high peak close to the boundary-layer edge, which is a pattern of the eigenfunctions for mode S, as shown by the LST results. This is reasonable, as in the modulation region, as described above, the two competing modes are represented by the forcing fast acoustic waves and the growing mode S.

Finally, figures 5.12 and 5.13 show the eigenfunctions for the frequency $f_{10}$ at the positions $x = 641$ and $x = 940$ respectively. In figure 5.12 the LST eigenfunctions for the Mack mode are shown, which has been observed at the corresponding position ($x = 641$) in the eigenvalue spectrum in figure 5.7, while the LST results in figure 5.13 correspond to mode F II, which is the dominant mode in the downstream region. The numerical results at the position $x = 641$ show the strong influence of the external fast acoustic waves, which can be noticed also by the fact that both temperature and velocity perturbations do not approach zero outside the boundary layer ($y_n > 20$). This is due to the second synchronisation with the fast acoustic waves characterising this flow region, as shown by figure 5.8, which provides the second amplification of the fast mode. As the resonance mechanism with the fast acoustic waves leads again to a strong growth of the fast mode, the Mack mode, which is generated in this region, can be considered as covered by the fast mode. The fast mode, in turn, keeps growing further downstream forming mode F II, whose shape is shown in figure 5.13. Here a good agreement between the DNS results and the LST results for mode F II is observed, with mode F II being characterised by two consecutive peaks near the wall, as also shown in the work of Zhong [86]. This proves that mode F II, resulting from the second resonant interaction with the fast acoustic waves, has become the dominant mode in the downstream region.

In conclusion, the present numerical and theoretical results show the main characteristics of the leading-edge receptivity mechanism at hypersonic speeds, and are in qualitative agreement with other theoretical and numerical studies available in the literature, for different flow conditions.

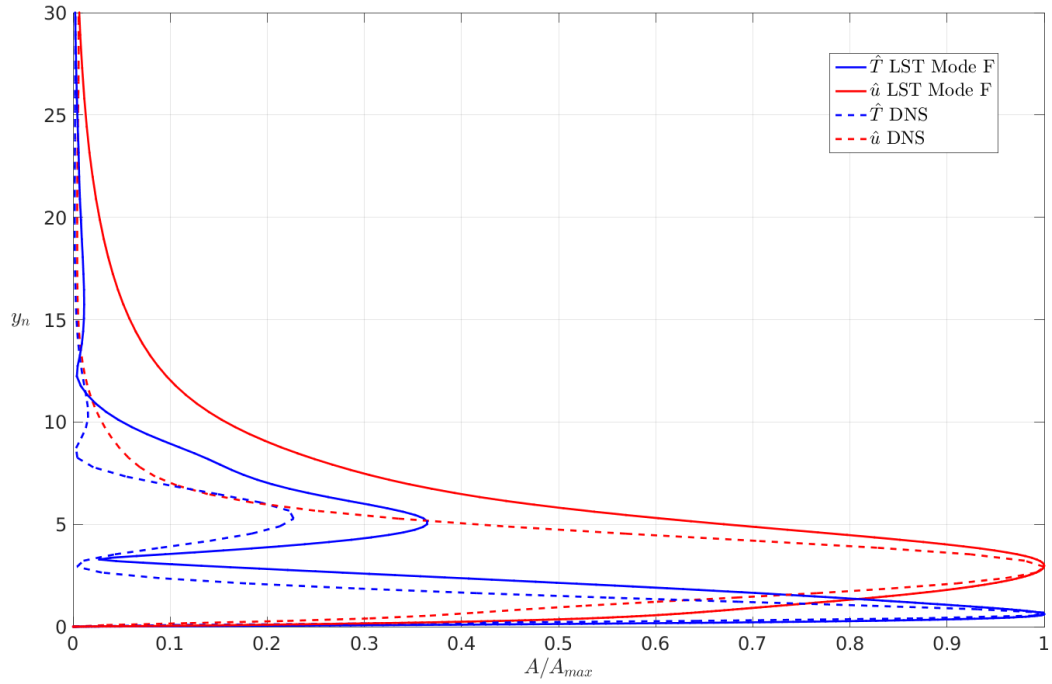


Figure 5.10: Temperature and wall-tangential velocity eigenfunctions for the frequencies $f_6$ at the position $x = 259$

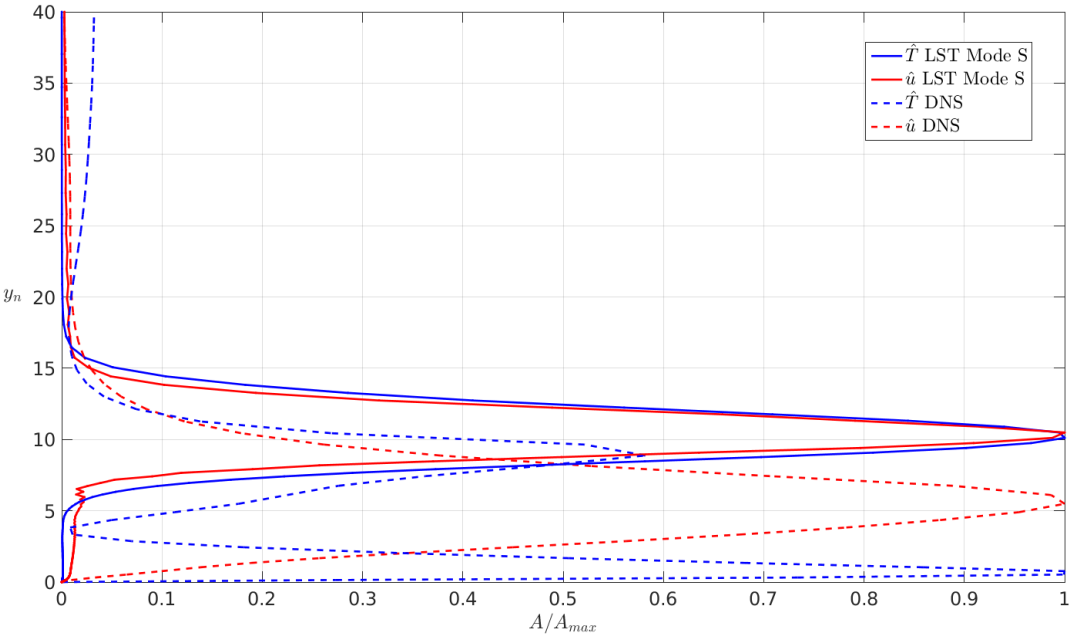


Figure 5.11: Temperature and wall-tangential velocity eigenfunctions for the frequencies $f_6$ at the position $x = 700$

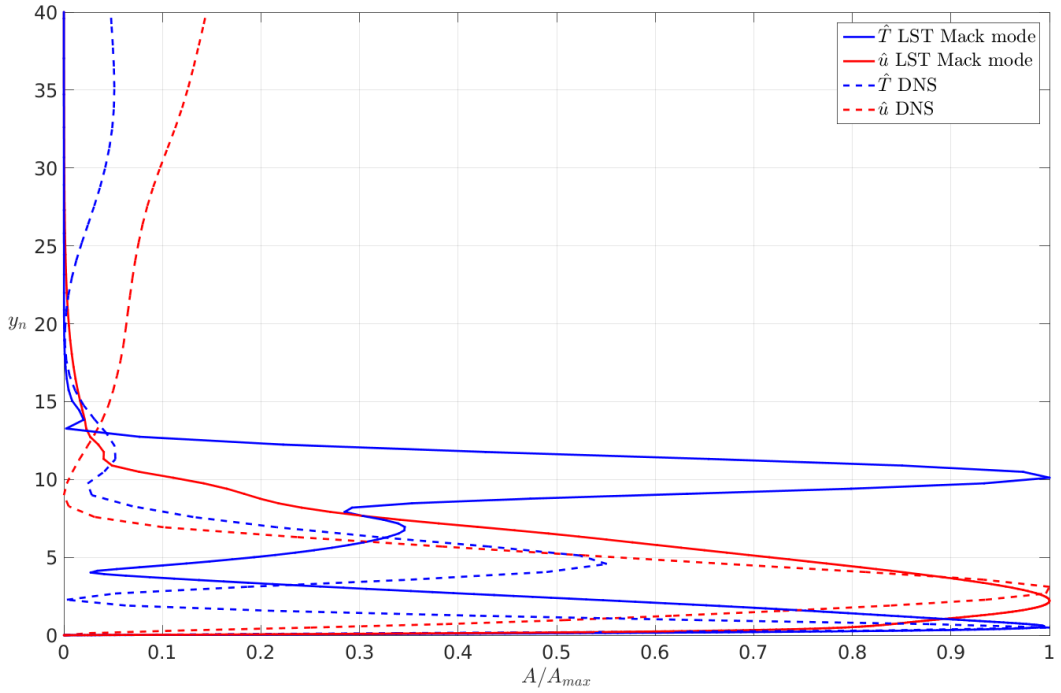


Figure 5.12: Temperature and wall-tangential velocity eigenfunctions for the frequencies $f_{10}$ at the position $x = 641$

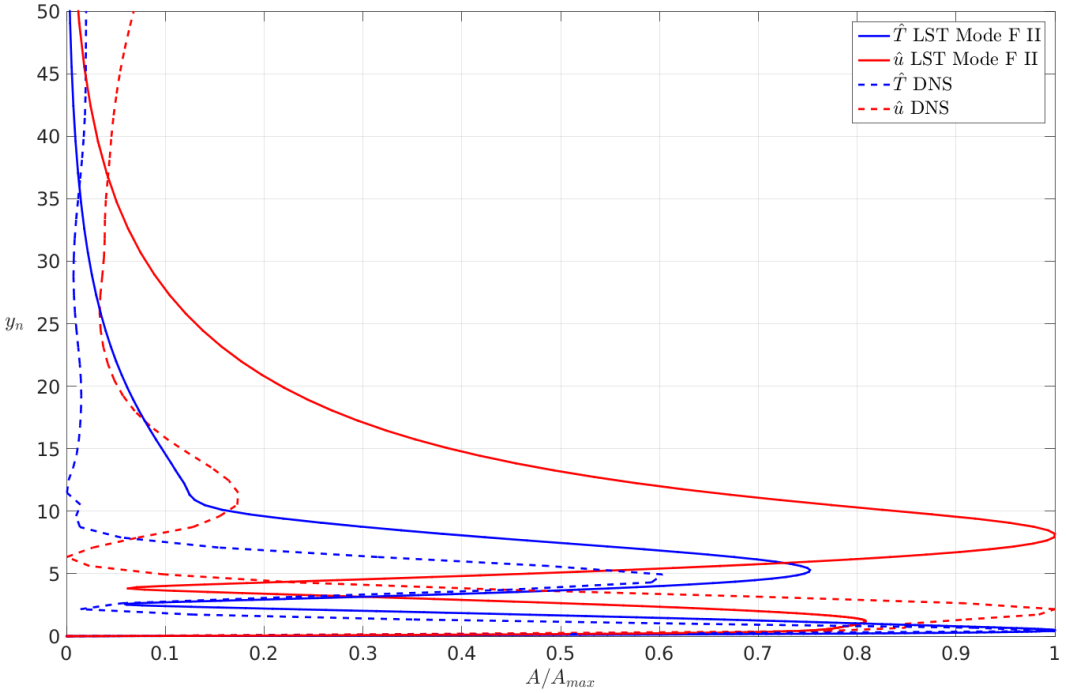


Figure 5.13: Temperature and wall-tangential velocity eigenfunctions for the frequencies $f_{10}$ at the position $x = 940$

## 5.3 Results for the unswept configuration

### 5.3.1 Cases 1-2, $Re = 1400$, fast waves: streak instability mode

We start to illustrate the results of the 3D simulations for the cases at lower Reynolds number with fast acoustic waves as freestream disturbances. Figures 5.14 and 5.15 show contours of the real part of the Fourier-transformed wall pressure fluctuations at all the considered frequencies (from $f_1$ at the top to $f_{10}$ at the bottom) for cases at lower and higher freestream disturbance amplitude respectively (cases 1 and 2 in table 5.1). Moving from top to bottom in both figures, the effect of frequency on the resonance mechanism can be seen, with the peak wall disturbance amplitude moving towards the leading edge as the frequency is increased. In the lower amplitude case (figure 5.14) the wall disturbances appear to be dominated by a 2D mode through the whole length of the computational domain; in contrast, in the higher amplitude case (figure 5.15) the 2D mode seems to be the most amplified mode only in the leading-edge region, namely in the early region of increasing amplitude, and, once the peak has been achieved, 3D modes (with non-zero spanwise wavenumber) emerge and become the dominant wave structures further downstream. The solution in the nose region ($x = 0 - 200$) is qualitatively very similar between the two different amplitude cases at all the frequencies, with the amplitude scaled by an order of magnitude as for the forcing, i.e. (unsurprisingly) the solution can be reasonably considered as linear in the early region of the computational domain. Further downstream, the solution becomes different between the cases at different amplitude, meaning that nonlinearities for the higher amplitude case are no longer negligible and become more and more important as going downstream.

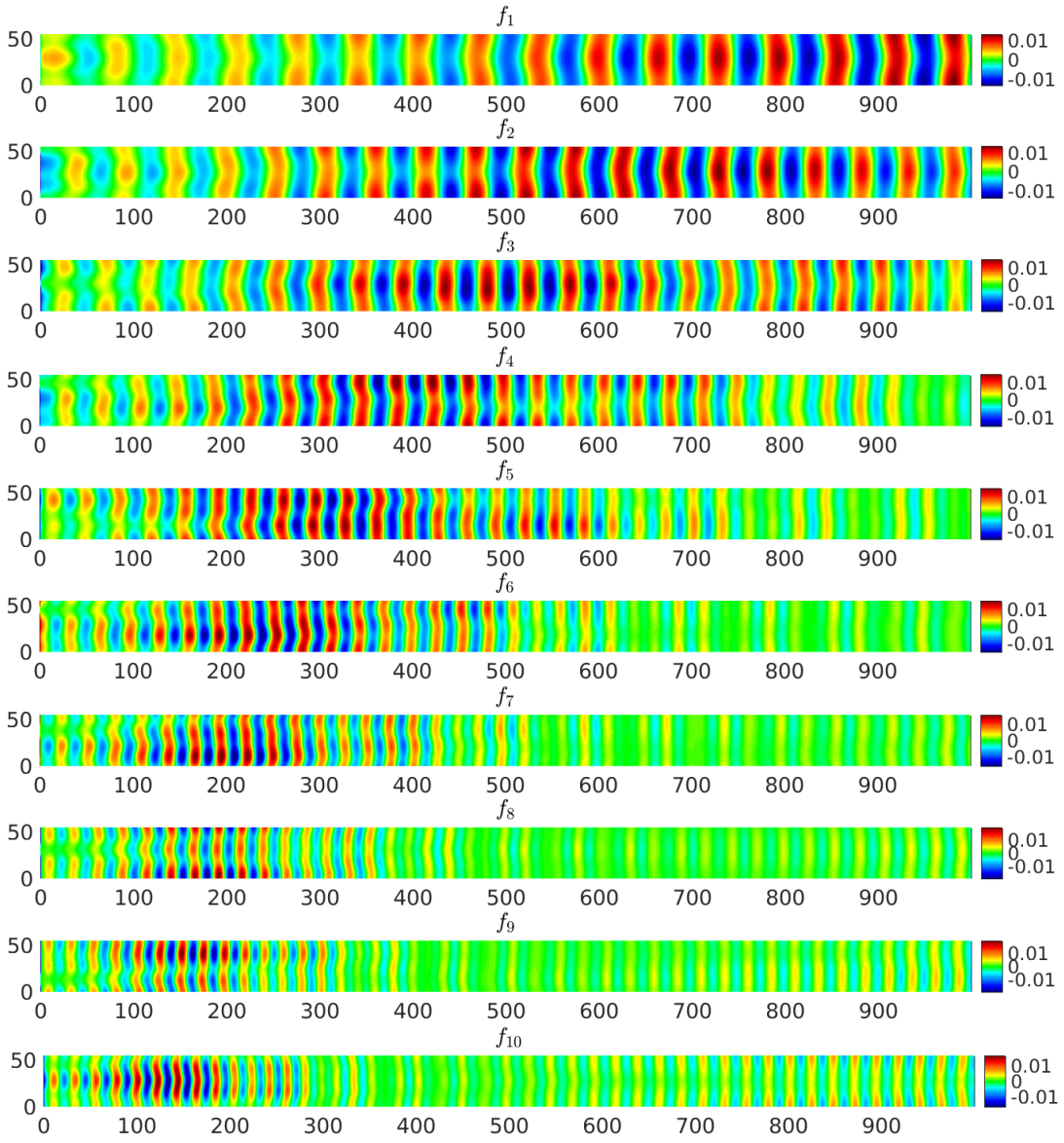


Figure 5.14: Real part of the Fourier transformed wall pressure fluctuations ($p'_w$) at the different forced frequencies. Case 1, $A_\infty = 5 \times 10^{-3}$. The labels of the vertical ($z$) and horizontal ($x$) axis have been purposely omitted

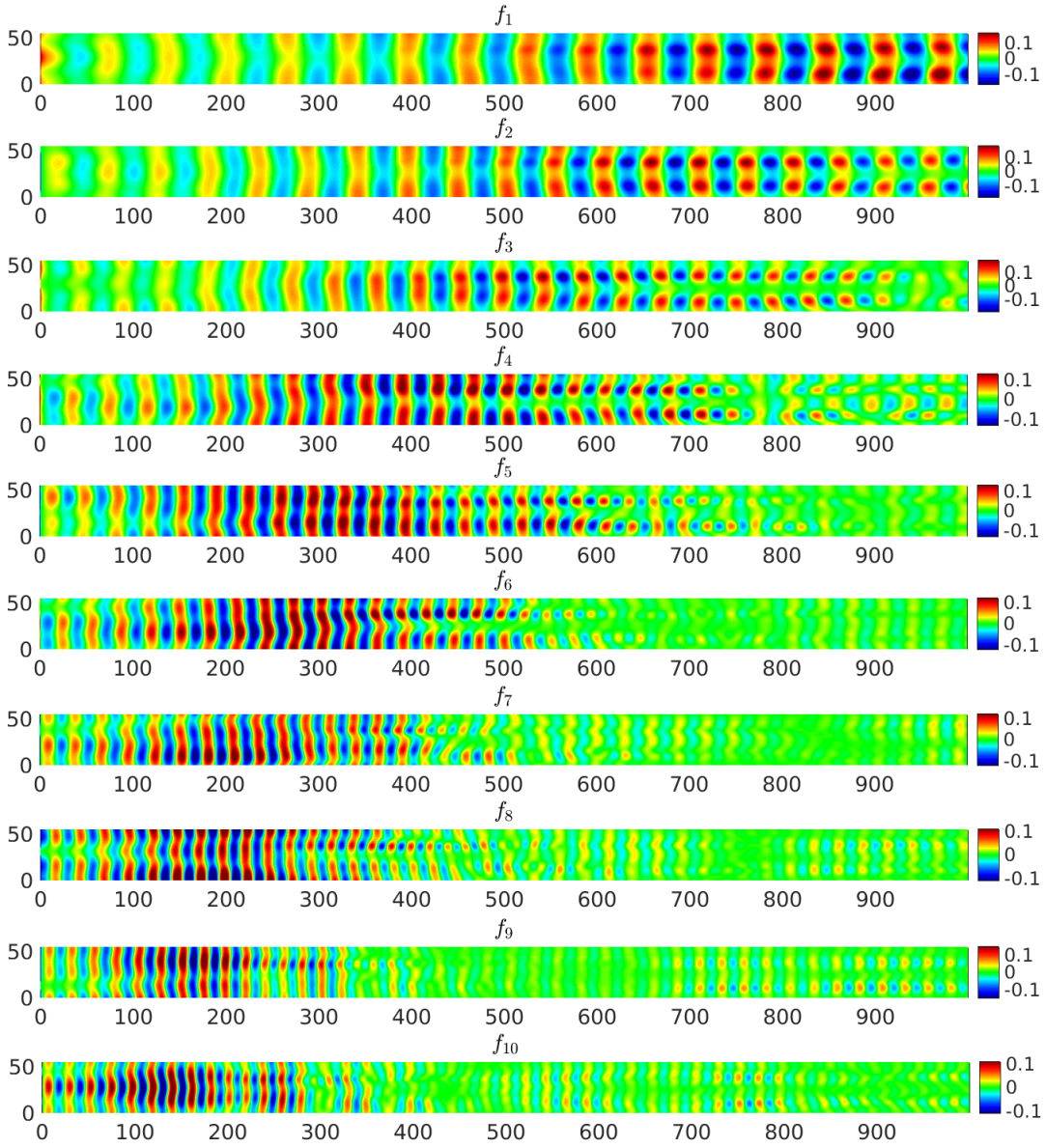


Figure 5.15: Real part of the Fourier transformed wall pressure fluctuations ($p'_w$) at the different forced frequencies. Case 1, $A_\infty = 5 \times 10^{-2}$. The labels of the vertical ($z$) and horizontal ($x$) axis have been purposely omitted

Figure 5.16 shows the trend of the wall pressure fluctuation amplitudes along the wedge for the modes $\beta = 0, 1, 2$ at the frequency $f_2$ for both high and low amplitude cases, obtained through a FFT in time and in the spanwise direction. The wall pressure fluctuation amplitudes for each mode are normalised with the value of the freestream pressure fluctuation amplitude (i.e. as $p'_w/p'_\infty$) pertaining to the specific mode (e.g., the wall perturbation relative to the 2D mode is divided by the imposed freestream perturbation amplitude for the 2D mode). As can be seen, the wall response very close to the leading edge does not show a significant disagreement between case 1 and case 2 , due to the nonlinear effects being relatively small in this region. In the second

half of the computational domain, in contrast, the high nonlinear effects in the case of higher freestream disturbance amplitude (case 2) provide markedly different behaviours between cases 1 and 2. In particular, the $\beta = 2$ mode decays to very low values in case 1, whilst, in case 2, is strongly excited in the second half of the domain. Also, it is evident that the rapid growth of the $\beta = 2$ mode starts at a position very close to the point where the peak of the 2D mode F is reached, thus suggesting that the resonance mechanism at the leading edge might play an important role in the excitation of 3D boundary-layer instabilities.

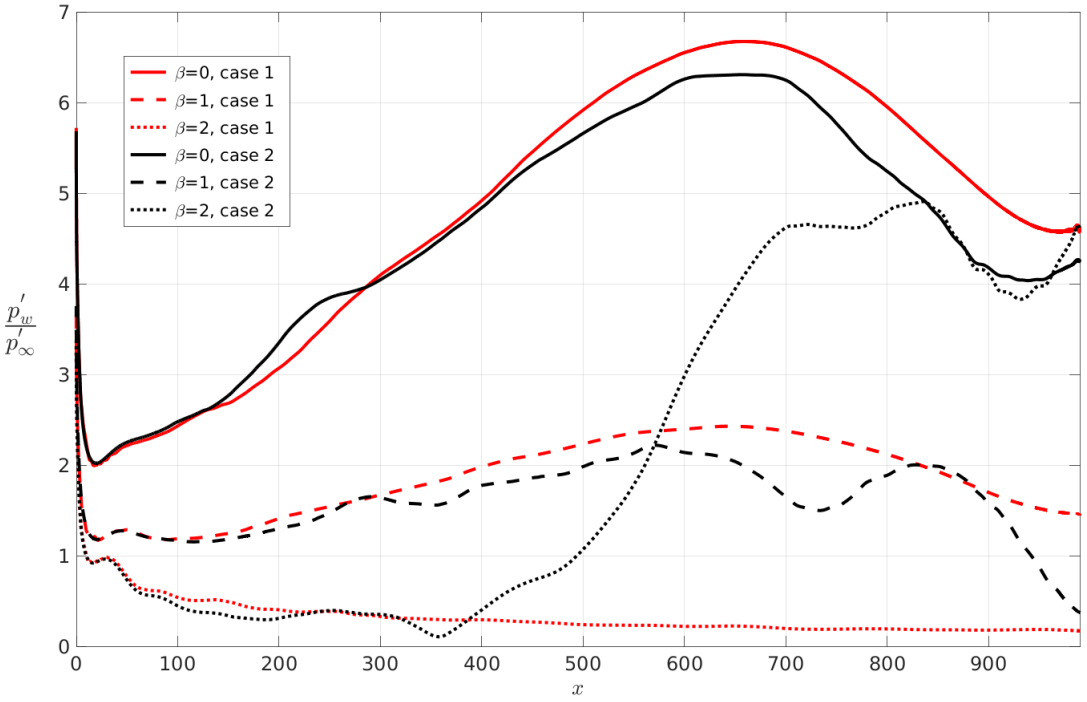


Figure 5.16: Extracted modes ($\beta = 0, 1, 2$) of the wall pressure fluctuation amplitudes at the frequency $f_2$, for case 1 and case 2

By looking at figure 5.17, which shows an instantaneous contour of the streamwise (tangential to the wall) velocity component ($u_t$) along the $j = 10$ grid line inside the boundary layer, it is evident that the excitation of the $\beta = 2$ mode at the different forcing frequencies corresponds to the generation and downstream development of streaks in the streamwise direction inside the boundary layer. In particular, the figure reveals the presence of two low velocity streaks generated approximately in the region $x = 400 - 500$ and growing downstream, which correspond to the pair of high temperature streaks shown in figure 5.18, depicting the temperature contour along the same grid line $j = 10$. Figure 5.19 shows a cross-section of the streamwise velocity in the $zy_n$-plane (where $y_n$ represents the normal distance from the wall) at the position $x = 940$, that highlights the boundary layer distortion at the location of the streaks. In between the low-velocity streaks (namely at about $z = 25$) the streamwise velocity assumes higher values, compared to those assumed inside the streaks, which is consistent with

the streaks being formed by a pair of counter-rotating vortices that take high-speed cold fluid from the upper layers towards the wall. The streaks represent a stationary instability, which can be referred to as the (0,2) mode (indicating with 0 the frequency, as they are stationary, and with 2 the spanwise wavenumber $\beta$).

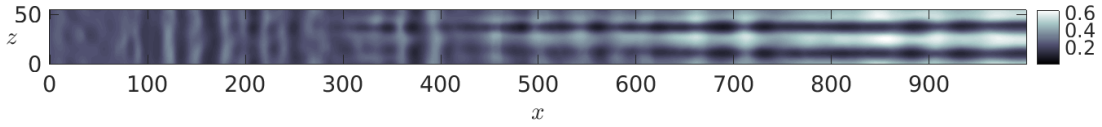


Figure 5.17: Instantaneous contour of the streamwise (tangential to the wall) velocity component ($u_t$) along the grid line $j = 10$ inside the boundary layer. Case 2, $A_\infty = 5 \times 10^{-2}$

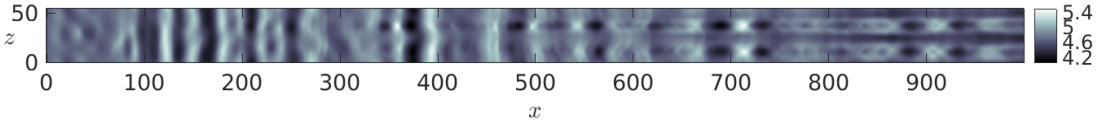


Figure 5.18: Instantaneous temperature contour ($T$) along the grid line $j = 10$ inside the boundary layer. Case 2, $A_\infty = 5 \times 10^{-2}$

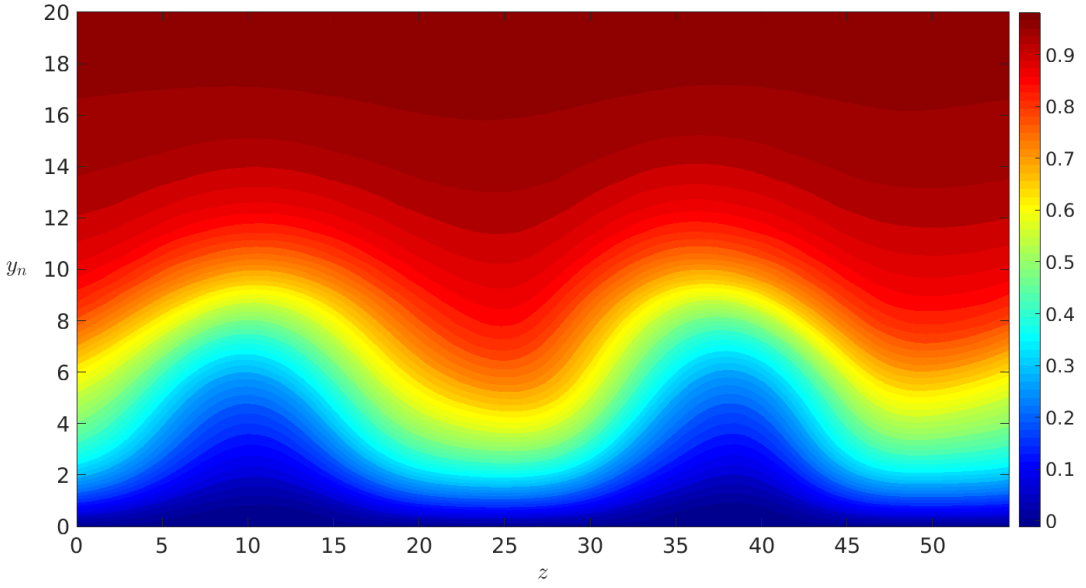


Figure 5.19: Instantaneous contour of the streamwise velocity component ($u_t$) on the $zy_n$-plane at the position $x = 940$. $y_n$ is the distance from the wall along the local normal direction. Case 2, $A_\infty = 5 \times 10^{-2}$

### 5.3.2 Cases 3-4, $Re = 5625$, fast waves: streak breakdown mechanism

Cases 3 and 4 pertain to the higher $Re = 5625$ and freestream fast acoustic waves in the unswept configuration. For the case of higher freestream disturbance amplitude (case 4), due to numerical instability issues, the computation has been performed through DNS up to the station $x = 400$, and then continued from this point up to $x = 750$ through a Large Eddy Simulation (LES), using the Mixed-Time Scale approach (described in Section 2.7). For case 3, the results in terms of the main wave structures forming in the boundary layer are similar to the corresponding low freestream amplitude case at lower Reynolds number (case 1), as the wall response is mainly dominated by the 2D fast mode. Figure 5.20 shows the real part of the Fourier-transformed wall pressure fluctuations at the frequency $f_8$ for case 3. The figure reveals a superposition along the whole length of the computational domain between the 2D mode and the oblique $\beta = 1, 2$ modes, which are all evolving from the resonance mechanism in the nose region and the modulation mechanism further downstream, with the 2D mode being dominant. A similar trend is shown for all the other frequencies (which are not shown for reasons of brevity). For this case (case 3) at lower amplitude, as also for the corresponding case at lower Reynolds number (case 1), there is no streak formation due to negligible nonlinearity effects. Figure 5.21 shows the wall pressure fluctuation field at the same frequency $f_8$ for case 4. Here, the 2D mode is shown to be dominant in the region $200 \leq x \leq 300$, while downstream of $x = 400$ the response is characterised by streaks, which in this case are seen to start breaking down for $x > 500$.

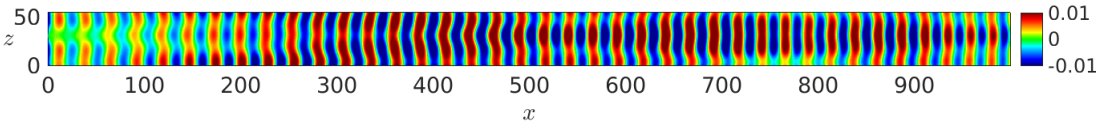


Figure 5.20: Real part of the Fourier transformed wall pressure fluctuations ($p'_w$) at the frequency $f_8$. Case 3, $A_\infty = 5 \times 10^{-3}$

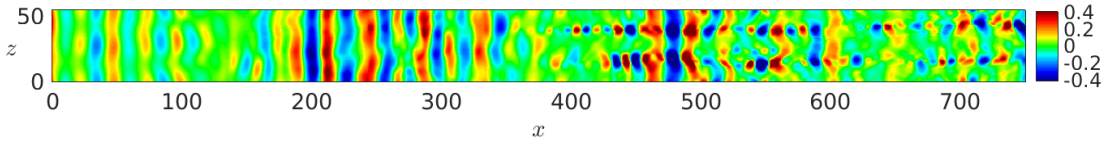


Figure 5.21: Real part of the Fourier transformed wall pressure fluctuations ($p'_w$) at the frequency $f_8$. Case 4, $A_\infty = 5 \times 10^{-2}$

Evidence of the breakdown mechanism can be found in figures 5.22 and 5.23, showing the instantaneous streamwise velocity and temperature contours along the $j = 10$ grid line inside the boundary layer. In these figures, two low velocity streaks are clearly seen to form around $x = 350$. These streaks grow further downstream remaining laminar up to about $x = 500$, and finally break down in the region $500 \leq x \leq 550$. Moreover, in the

region $400 \leq x \leq 500$ the streak structures appear strongly distorted by the interaction with the wave fronts of the 2D mode, which seems to cause oscillations of the streak, streak bending and even bifurcation. The streak located at $0 \leq z \leq 25$ appears to develop a curvature along its longitudinal path in the region $450 \leq x \leq 500$, while, at the same position (around $x = 450$), another thinner (secondary) streak (located at about $z = 25$) seems to detach from the main streak. This then develops downstream with an inclination angle with respect to the main streak oriented along the $x$-axis. At the same time, the second main streak ($25 \leq z \leq 55$) deviates from the original $x$-oriented path at about $x = 500$ and continues downstream with a slight inclination angle. These phenomena that modify the streak structures are coincident with a superposition of the streaks and highly amplified 2D modes, as seen in figure 5.21 in the region $450 \leq x \leq 500$. Namely, the interaction between the amplified 2D modes in the leading-edge region and the streak mode leads rapidly to the streak breakdown. Figure 5.24 shows a cross section of the streamwise velocity ($u_t$) in the boundary layer at $x = 500$. It is evident that the streak structure consists of two main low velocity streaks, with cores located at $z = 15$ and $z = 40$, and a secondary smaller streak located at $z = 22$ that is detaching from the first main streak ($z = 15$). As in the lower Reynolds number case (case 2), the intermediate regions between two adjacent streaks are characterised by much higher values of the streamwise velocity, corresponding to areas where the cold high speed fluid of the upper layers is brought towards the wall by means of a pair of counter-rotating streamwise vortices.

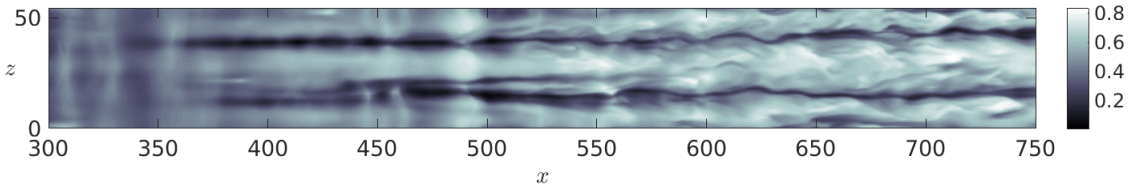


Figure 5.22: Instantaneous contour of the streamwise (tangential to the wall) velocity component ($u_t$) along the grid line $j = 10$ inside the boundary layer. Close-up in the region $300 \leq x \leq 750$ to highlight the streak evolution. Case 4, $A_\infty = 5 \times 10^{-2}$

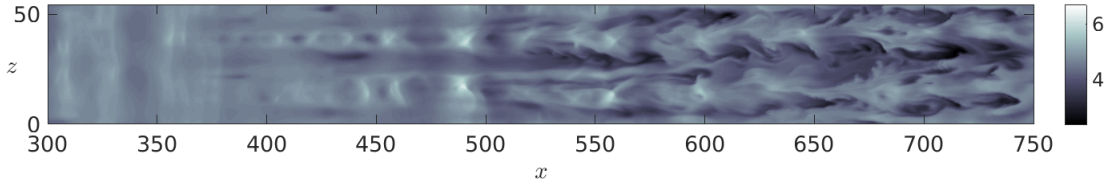


Figure 5.23: Instantaneous temperature contour ($T$) along the grid line $j = 10$ inside the boundary layer. Close-up in the region $300 \leq x \leq 750$ to highlight the streak evolution. Case 4, $A_\infty = 5 \times 10^{-2}$

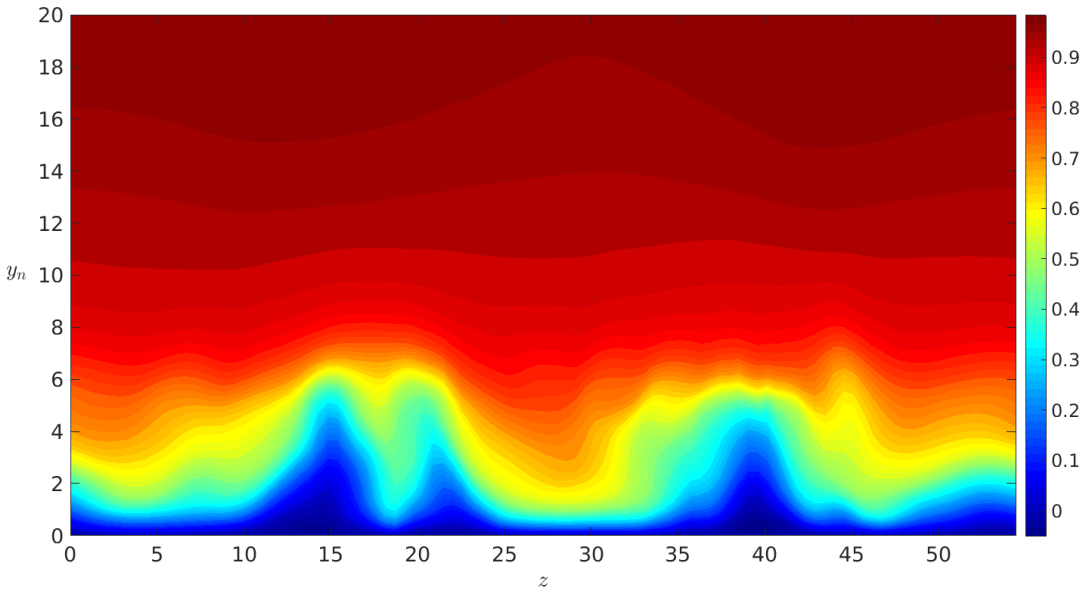


Figure 5.24: Instantaneous contour of the streamwise velocity component ($u_t$) on the $zy_n$-plane at the position $x = 500$. $y_n$ is the distance from the wall along the local normal direction. Case 4, $A_\infty = 5 \times 10^{-2}$

The particularly rapid generation and growth of the streak mode observed in figures 5.16, 5.17 and 5.18, for the lower Reynolds number case, and the corresponding rapid breakdown observed in figures 5.22 and 5.23, for the higher Reynolds number case, suggest that in the presence of high-amplitude freestream disturbances nonlinear effects may become dominant already in the early leading-edge region, thus leading to a violent fully-nonlinear transition process further downstream. However, previous studies (e.g. Andersson *et al.*[87] and Brandt and Hennigson [88] for the case of an incompressible flow over a flat plate) showed that the physical mechanism behind the generation, growth and breakdown of streamwise streaks, can be associated to a transient growth of the streak instability mode. In particular, based on these studies, a lift-up effect associated to vortices in the streamwise direction (representing the initial disturbances in the leading-edge region) is at the basis of the generation and non-modal growth of elongated streaks, whose early breakdown is induced by secondary instabilities that take place once the amplitude of the streaks grows up to a sufficiently large value.

The present numerical results have shown that the resonance mechanism of the 2D fast mode at the leading edge can enhance the mechanism of generation, growth and breakdown of the streaks, however the question relative to whether this is associated to a fully nonlinear process or to a transient growth mechanism is still open and requires a more in-depth analysis, which we address to a future investigation.

### 5.3.3 Cases 5-6, $Re = 5625$, slow waves

For the slow wave cases at $Re = 5625$ in the unswept configuration (cases 5 and 6), we show representative results at two different frequencies ($f_4$ and $f_{10}$). Figures 5.25 and 5.26 show the wall pressure fluctuation field for case 5 (lower freestream amplitude) at frequencies $f_4$ and $f_{10}$ respectively, while figures 5.27 and 5.28 show the corresponding results for case 6 (higher freestream amplitude) at the same frequencies. It can be seen that the change in freestream disturbance amplitude level does not produce significant changes in the wave structure of the wall response, due to the weaker amplification rates shown by the response to slow acoustic waves in the leading-edge region compared to fast acoustic waves, which has been previously discussed, thus proving a much lower degree of nonlinearity in the receptivity to slow acoustic waves compared to the receptivity to fast acoustic waves. At all the frequencies the wall response consists of three-dimensional wave structures over the whole domain length, which means that in the case of slow acoustic waves there is no clearly dominant mode among the forced $\beta = 0, 1, 2$ modes.

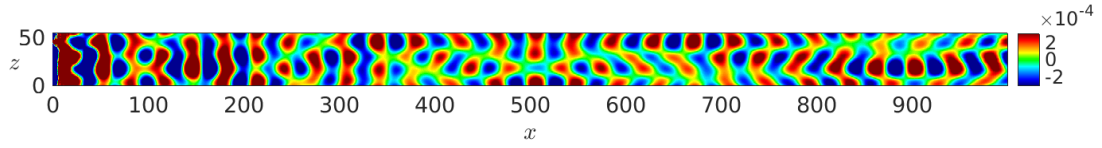


Figure 5.25: Real part of the Fourier transformed wall pressure fluctuations ($p'_w$) at the frequency $f_4$. Case 5, $A_\infty = 5 \times 10^{-3}$

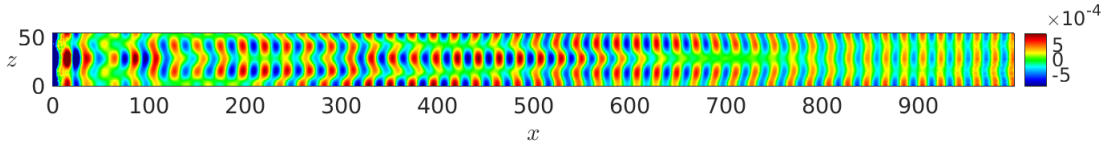


Figure 5.26: Real part of the Fourier transformed wall pressure fluctuations ($p'_w$) at the frequency $f_{10}$. Case 5, $A_\infty = 5 \times 10^{-3}$

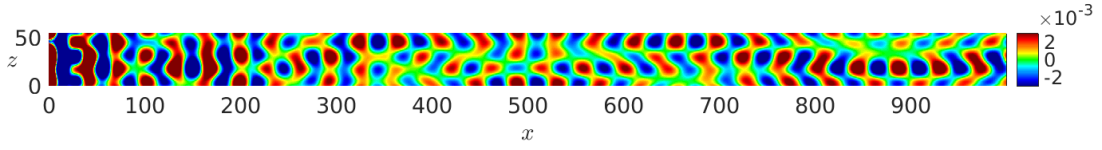


Figure 5.27: Real part of the Fourier transformed wall pressure fluctuations ($p'_w$) at the frequency $f_4$. Case 6, $A_\infty = 5 \times 10^{-2}$

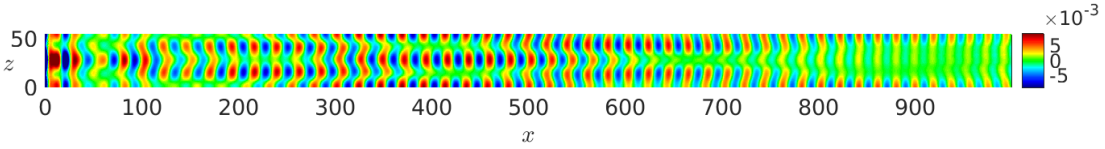


Figure 5.28: Real part of the Fourier transformed wall pressure fluctuations ($p'_w$) at the frequency $f_{10}$. Case 6, $A_\infty = 5 \times 10^{-2}$

Figures 5.29 and 5.30 show the distribution of the pressure fluctuation amplitude along the wall for the modes $\beta = 0, 1, 2$ at the frequencies $f_4$ and $f_{10}$, for cases 5 and 6 respectively. In both cases the oblique modes ($\beta = 1, 2$) show a higher amplification than the 2D mode at both the considered frequencies. In particular, at the higher frequency ($f_{10}$), for which all the modes show a considerably higher amplitude than the corresponding modes for the $f_4$ frequency in the leading-edge region, the oblique mode $\beta = 2$ is the most amplified mode, with an amplitude ($p'_w/p'_\infty$) of about twice the amplitude of the 2D mode and 1.4 times the amplitude of the $\beta = 1$ mode at the position of its maximum ($x = 350$). This proves that, in contrast to the fast waves, in the case of slow acoustic waves the absence of a strong resonance mechanism at the leading edge causes the 2D mode not to be the dominant mode in the nose region, and the oblique modes, on the contrary, are eventually more amplified, dependent on the frequency, than the 2D mode, such that the overall response along the wall surface consists of a mix of 2D and 3D competing modes.

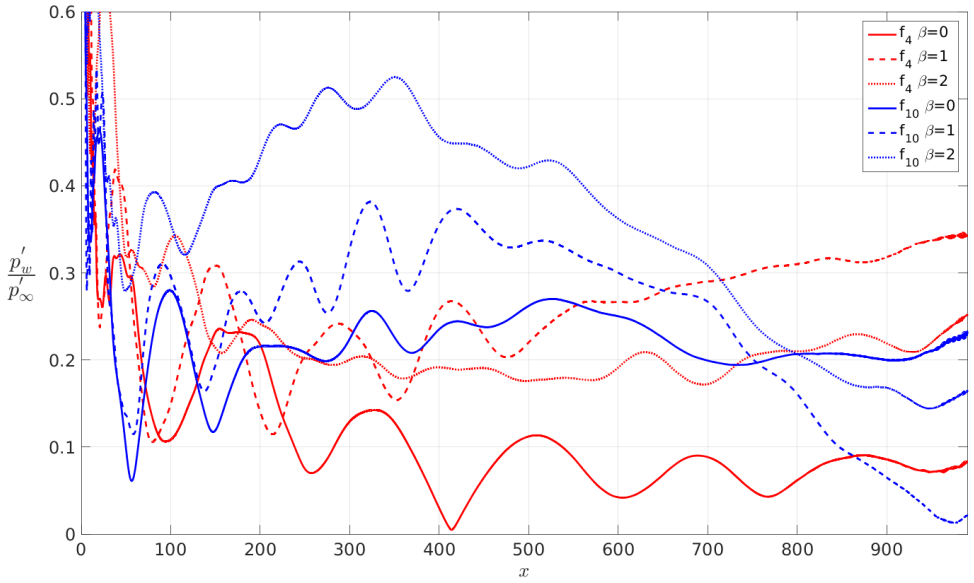


Figure 5.29: Extracted modes ($\beta = 0, 1, 2$) of the wall pressure fluctuation amplitudes at two forced frequencies ($f_4$ and $f_{10}$). Red and blue colours are used to indicate the $f_4$ and $f_{10}$ frequencies respectively. Solid, dashed and dotted lines are used for the $\beta = 0$ (i.e. 2D), $\beta = 1$ and $\beta = 2$ modes respectively. Case 5, $A_\infty = 5 \times 10^{-3}$

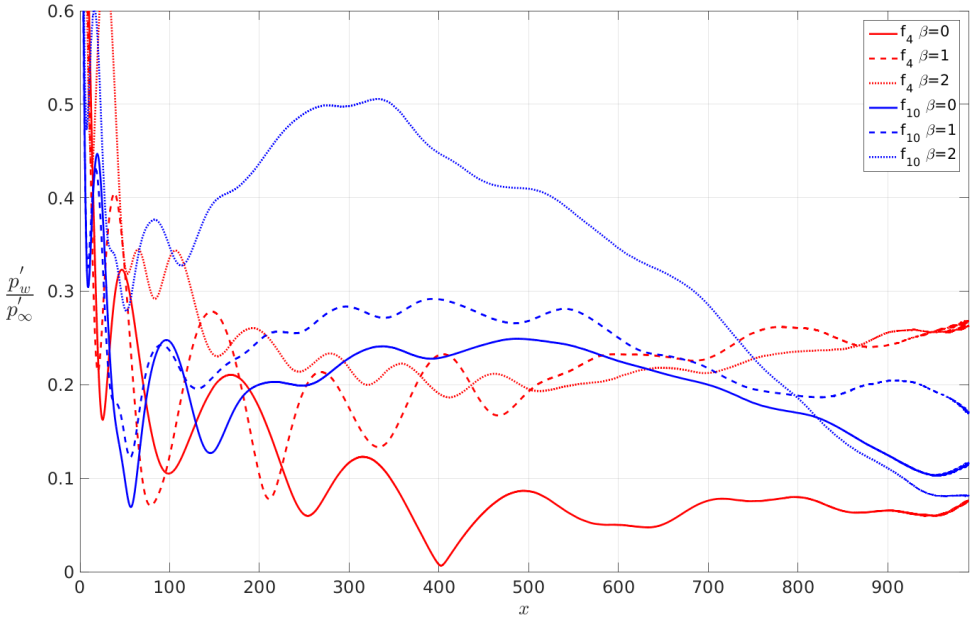


Figure 5.30: Extracted modes ($\beta = 0, 1, 2$) of the wall pressure fluctuation amplitudes at two forced frequencies ($f_4$ and $f_{10}$). Red and blue colours are used to indicate the $f_4$ and $f_{10}$ frequencies respectively. Solid, dashed and dotted lines are used for the $\beta = 0$ (i.e. 2D), $\beta = 1$ and $\beta = 2$ modes respectively. Case 6, $A_\infty = 5 \times 10^{-2}$

Moreover, the growth of the wall fluctuations (at both low and high freestream amplitude, in figures 5.29 and 5.30 respectively) for the $\beta = 1$ mode at the frequency $f_4$ through the whole domain length, and for the $\beta = 2$ mode at the higher frequency $f_{10}$ in the first half of the domain, might be connected to oblique first mode linear instabilities present in particular regions of the domain, in the considered range of frequencies. However, in contrast to the fast wave case, the receptivity to slow waves is seen not to produce streak instability. This is due to the absence, for slow waves, of a strong resonance mechanism between the external forcing mode and the internal boundary layer modes. Thus, in the presence of high freestream noise levels, the fast acoustic waves can be more dangerous than the slow waves, as they appear to be more efficient in the generation of streaks in the leading-edge region and in leading the boundary layer to transition.

## 5.4 Results for the infinitely swept configuration ($\Lambda = 45°$)

### 5.4.1 Crossflow instability in the mean flow

For the swept case, with reference to the sketch in figure 5.31 and the illustration given in figure 2.2, a sweep angle of $\Lambda = 45°$, between the streamwise direction of the flow and the leading edge, was considered. At the side boundaries of the computational domain a periodic boundary condition is applied, in order to simulate an infinitely swept leading edge.

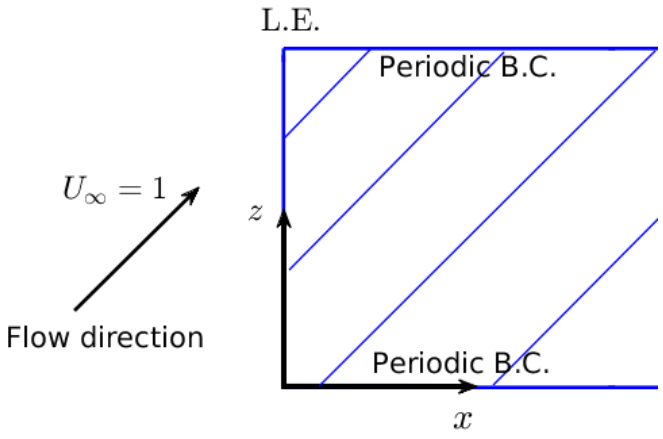


Figure 5.31: Sketch of a swept leading edge

Before showing the results for our unsteady simulations, we present some numerical results for the mean flow, which show the presence of a crossflow inflection point in the swept configuration. Figure 5.32 shows the mean pressure trend along the wall, showing a streamwise gradient that is still present up to high distances downstream along the wedge. Indeed, figure 5.33, depicting the crossflow boundary-layer profiles at different distances from the leading edge along the wall, shows that the crossflow boundary-layer profile is characterised by inflectional profiles from the leading-edge region, where it assumes higher values due to the higher pressure gradient, up to high distances downstream. This proves that in the swept configuration the boundary layer is likely to be subjected to a crossflow instability along the whole length of the wedge.

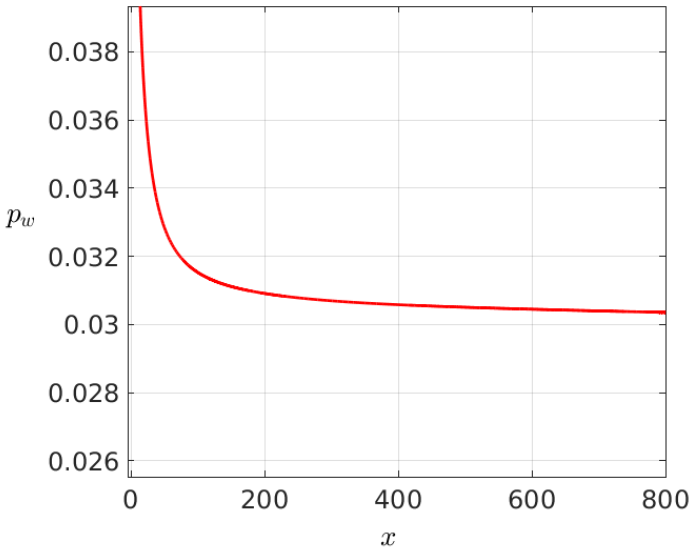


Figure 5.32: Mean pressure trend along the wall

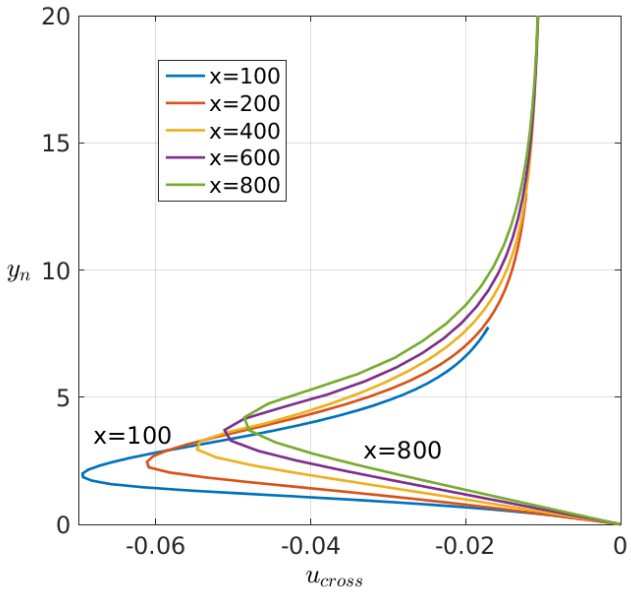


Figure 5.33: Mean crossflow boundary-layer profiles at several distances from the leading edge

### 5.4.2 Cases 7-8, $Re = 5625$, fast waves: fast-mode breakdown mechanisms

For the infinite swept case we show results at representative frequencies $f_2$ and $f_{10}$, based on the general physical aspects we want to highlight. In particular, $f_2$ is representative

of a lower frequency range (from $f_1$ to $f_5$), as the results reached at this frequency are quite similar to those of the other low frequencies, whilst, for the same reason, $f_{10}$ is to be considered as representative of a higher frequency range (from $f_6$ to $f_{10}$). As in case 4, the results of case 8 (fast waves, high disturbance amplitude) have been achieved through a mixed DNS/LES approach, with DNS up to $x = 550$, then from this station up to the domain outer edge the computation has been continued by means of an LES, using the Mixed-Time Scale approach (described in Section 2.7).

#### 5.4.2.1 Crossflow-instability-related breakdown mechanism

Figures 5.34 and 5.35 depict the wall pressure fluctuation field for case 7 (low freestream amplitude) at the frequencies $f_2$ and $f_{10}$ respectively. At both the frequencies, the $\beta = 0$ waves are dominant close to the leading edge, namely in the region of early growth of mode F. For the swept case the $\beta = 0$ mode (whose wave vector is aligned with the $x$-axis) has to be considered carefully, as the streamwise direction is now inclined of 45° with respect to the $x$-axis, pointing towards the increasing values of $x$ and $z$. Thus, the $\beta = 0$ mode represents actually an oblique mode with respect to the freestream direction. At both the frequencies, the $\beta = 0$ fast mode appears to be modulated by wave fronts (more visible at the higher frequency, $f_{10}$) approximately aligned in the streamwise direction (thus with a wave vector in the crossflow direction), which pertain to a weak crossflow mode superimposed onto the forced $\beta = 0$ mode.

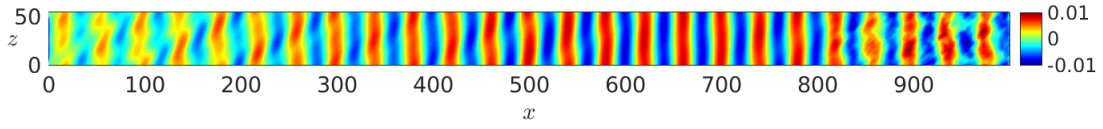


Figure 5.34: Real part of the Fourier transformed wall pressure fluctuations ($p'_w$) at the frequency $f_2$. Case 7, $A_\infty = 5 \times 10^{-3}$

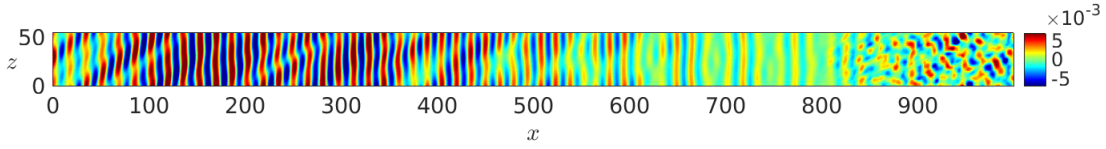


Figure 5.35: Real part of the Fourier transformed wall pressure fluctuations ($p'_w$) at the frequency $f_{10}$. Case 7, $A_\infty = 5 \times 10^{-3}$

An interesting result is observed in figures 5.36 and 5.37 for the streamwise velocity and temperature contours along the $j = 10$ grid line inside the boundary layer for case 7 (lower disturbance amplitude), which show that in the swept configuration fast acoustic waves with low freestream amplitude level are able to lead the flow to early breakdown very close to the domain outer edge. In this case, the mechanism leading to breakdown

seems to originate from high-wavenumber oscillations (representing secondary instabilities of the crossflow mode), as is evident from the thin streamwise oriented wavy structures forming at about $x = 750$ and growing downstream until starting breaking down at about $x = 850$. In the last section of the domain, downstream of $x = 900$, the wavy structures appear to lose their regular structure, being slightly thicker and more oscillatory along the streamwise direction (i.e. they appear to be destabilised), but do not show a high degree of fragmentation, which may indicate that the flow has reached the early stage of a gradual breakdown process, which would develop further downstream of the domain edge. The early breakdown stage reached in the low amplitude case proves that the boundary layer in the swept configuration is much more unstable than in the unswept configuration, where the breakdown was reached only at the high amplitude level of the freestream disturbances.

The mesh resolution in the downstream region (where the grid is coarser along the wall-normal and wall-tangential directions, compared to the nose region) consists of about 30 points inside the boundary layer (e.g. at the position $x = 900$) in the wall-normal direction, a $x$-wise spacing in the wall-tangential direction of approximately 0.3, and a (constant) spanwise spacing of 0.55. Considering that the smallest dimensionless disturbance wavelengths relative to the freestream forcing are about 24 and 17 for fast and slow acoustic waves respectively in the $x$-wise direction, and 27.5 in the spanwise direction, the present downstream grid resolution can be considered as suitable to capture the initial breakdown-transition process (consistent with the quality of the solution shown in figures 5.36 and 5.37). However it is believed that a grid refinement would be needed for fully turbulent simulations (which are not the purpose of the present study).

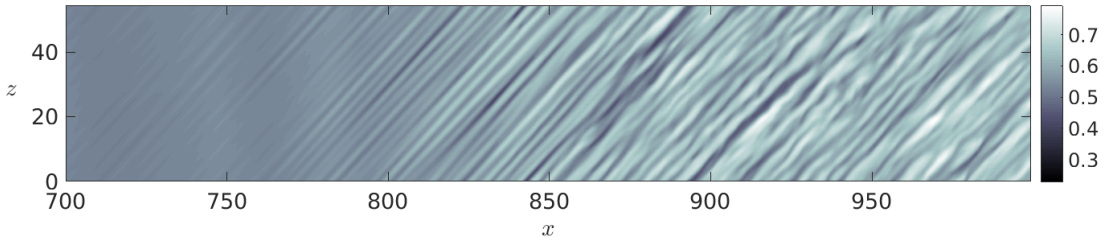


Figure 5.36: Instantaneous contour of the streamwise (tangential to the wall) velocity component ($u_t$) along the grid line $j = 10$ inside the boundary layer. Contour region starting from $x = 700$. Case 7, $A_\infty = 5 \times 10^{-3}$

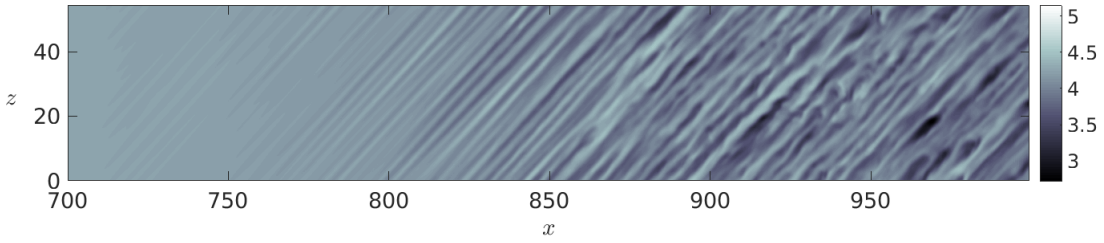


Figure 5.37: Instantaneous temperature ($T$) contour along the grid line $j = 10$ inside the boundary layer. Contour region starting from $x = 700$. Case 7, $A_\infty = 5 \times 10^{-3}$

An evidence that the breakdown mechanism observed in figures 5.36 and 5.37 is induced by crossflow instabilities is given in figure 5.38, which shows the boundary-layer profiles of mean crossflow velocity ($u_{cross}$), wall-normal velocity fluctuation ($v'$), first and second derivatives of the mean crossflow velocity ($\partial u_{cross}/\partial y_n$, $\partial^2 u_{cross}/\partial y_n^2$), at $z = 27$ and $x = 500$. It should be mentioned that all the quantities plotted along the horizontal axis are normalised with their corresponding maximum value inside the boundary layer. As can be seen, the peak of the wall-normal velocity fluctuation is reached at the distance from the wall $y_n = 2$, which is approximately the same position along the wall-normal direction of an inflection point, namely a point where the second derivative of $u_{cross}$ is zero. Thus, this inflection point (corresponding to a change in concavity happening between the wall and the peak of $u_{cross}$) represents an inviscid instability of the crossflow, which grows downstream leading to breakdown. This is further confirmed by considering that the profile of $u_{cross}$, between the wall and the negative peak, satisfies both Rayleigh's and Fjortoft's necessary conditions for instability. Rayleigh's condition requires the presence of an inflection point for a boundary layer to be considered as potentially unstable, which is satisfied in our case by $\partial^2 u_{cross}/\partial y_n^2 = 0$ at $y_n = 2$, which is corresponding to a peak in the first derivative ($\partial u_{cross}/\partial y_n$, namely the spanwise vorticity). Fjortoft's criterion adds a further constrain to Rayleigh's condition, namely, if $u_{cross}(y_n)$ is a monotonic function with an inflection point (considering, for example, the curve of $u_{cross}$ from the wall to the negative peak), a necessary condition for instability is that $(\partial^2 u_{cross}/\partial y_n^2)(u_{cross} - u_I) < 0$ inside the boundary layer, in which $u_I$ is the crossflow velocity at the inflection point. The validity of this criterion, applied to our case, is shown by the dashed curve in 5.38, which assumes negative values above $y_n = 2$.

Hence, the boundary layer contains a crossflow instability, which induces secondary instabilities downstream leading to nonlinear breakdown.

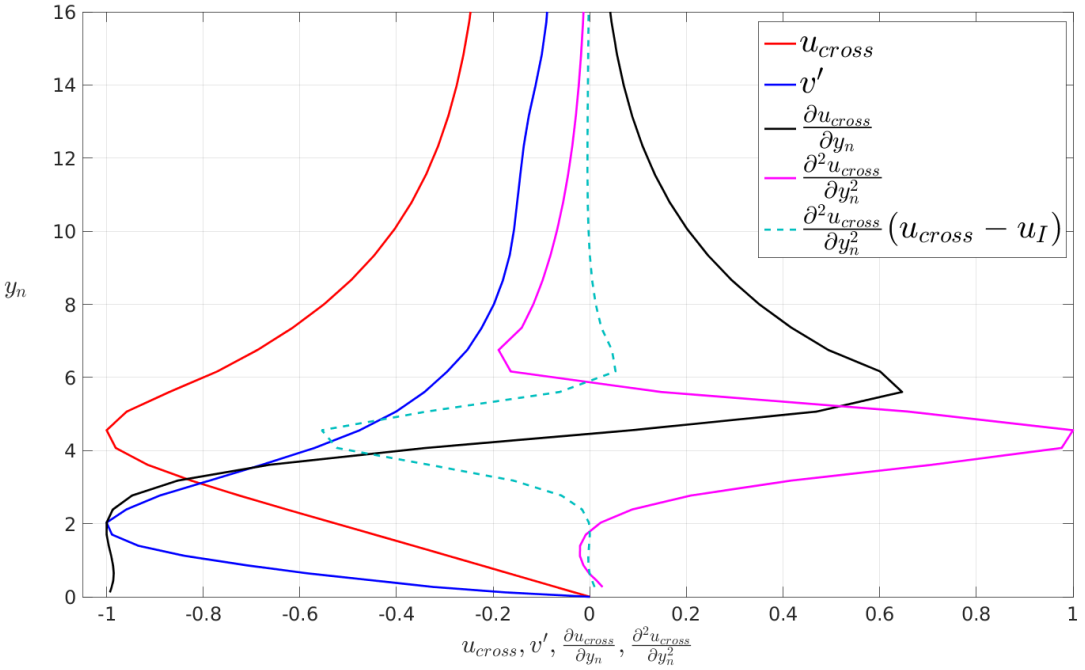


Figure 5.38: Profiles, along the wall-normal direction, of mean crossflow velocity ($u_{cross}$), wall-normal velocity fluctuation ($v'$), first and second derivatives of the mean crossflow velocity ($\partial u_{cross}/\partial y_n$, $\partial^2 u_{cross}/\partial y_n^2$), and Fjortoft's stability condition, at $z = 27$ and $x = 500$. Case 7, $A_\infty = 5 \times 10^{-3}$

#### 5.4.2.2 Resonance-related by-pass mechanism

Figures 5.39 and 5.40 show the wall pressure fluctuation results for case 8 (high freestream amplitude) at the same frequencies. In particular, in case 8, at the higher frequency ($f_{10}$), the crossflow mode appears strongly amplified in the region $400 \leq x \leq 650$ and competes with the $\beta = 0$ mode, with marked high wavelength oscillations in the spanwise direction perpendicular to the freestream flow.

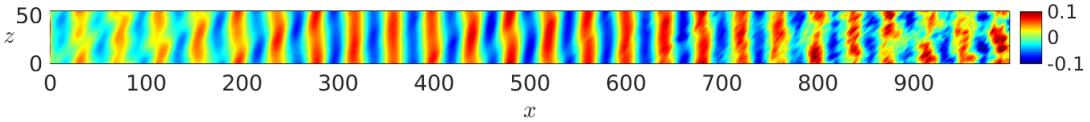


Figure 5.39: Real part of the Fourier transformed wall pressure fluctuations ($p'_w$) at the frequency $f_2$. Case 8, $A_\infty = 5 \times 10^{-2}$

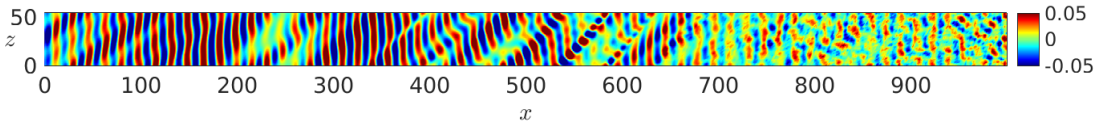


Figure 5.40: Real part of the Fourier transformed wall pressure fluctuations ($p'_w$) at the frequency $f_{10}$. Case 8, $A_\infty = 5 \times 10^{-2}$

This interaction between the crossflow mode and the highly amplified $\beta = 0$ mode (the dominant forced mode), due to the leading-edge resonance mechanism, leads to a by-pass-type early breakdown mechanism starting at about $x = 650$, which is possible to see in figures 5.41 and 5.42, showing the contours of the streamwise velocity (inclined of the sweep angle with respect to the $x$-axis) and of the temperature along the grid line $j = 10$ in the boundary layer.

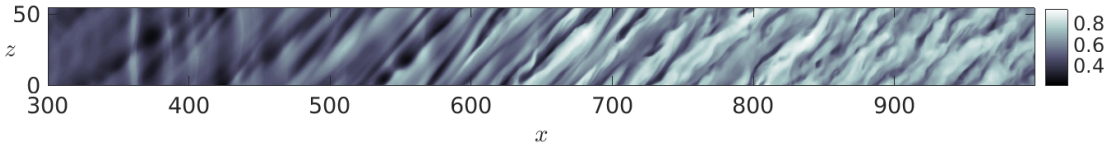


Figure 5.41: Instantaneous contour of the streamwise (tangential to the wall) velocity component ($u_t$) along the grid line $j = 10$ inside the boundary layer. Contour region starting from $x = 300$. Case 8, $A_\infty = 5 \times 10^{-2}$

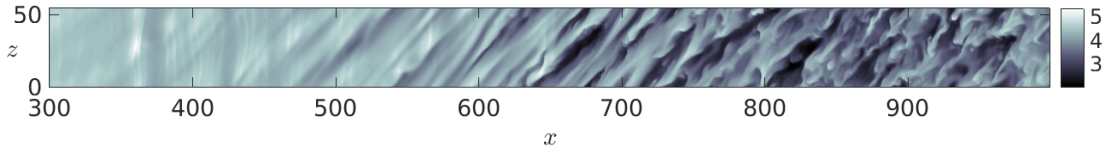


Figure 5.42: Instantaneous temperature ($T$) contour along the grid line $j = 10$ inside the boundary layer. Contour region starting from $x = 300$. Case 8, $A_\infty = 5 \times 10^{-2}$

As can be seen, low-velocity high-wavelength streaks oriented in the streamwise direction are observed in the early leading edge region. These streaks are related to a crossflow instability mode, as seen for the previous low-amplitude case, and undertake a rapid nonlinear growth in the region of interaction with the resonance-amplified $\beta = 0$ waves, until starting breaking down at around $x = 650$. In this case the breakdown is much more rapid than in case 7 (at the low freestream disturbance amplitude), and leads the boundary layer into fully turbulent flow downstream. As in case 4 (unswept case), freestream high amplitude fast acoustic waves are efficient in leading the boundary layer to an earlier transition in the nose region.

Figures 5.43 and 5.44 show results of case 8 for the $zy_n$-plane cross-sections of the streamwise velocity inside the boundary layer at two different positions along the wall, $x = 500$, and $x = 800$.

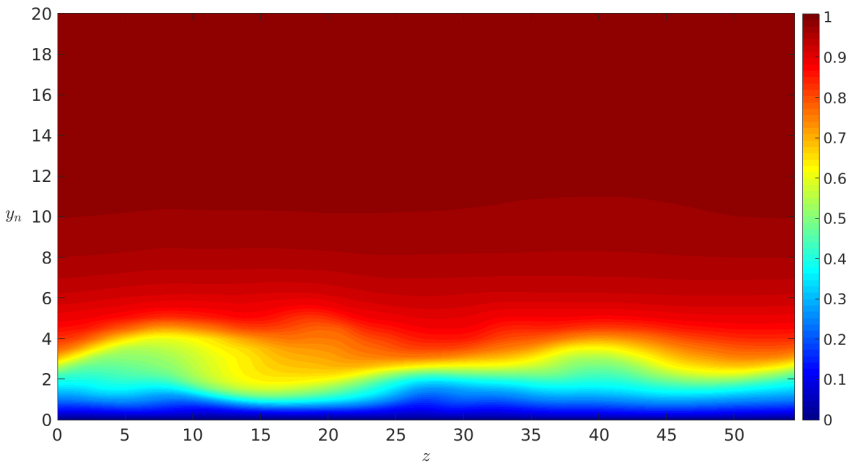


Figure 5.43: Instantaneous contour of the streamwise velocity component ($u_t$) on the $zy_n$-plane at the position $x = 500$. $y_n$ is the distance from the wall along the local normal direction. Case 8, $A_\infty = 5 \times 10^{-2}$

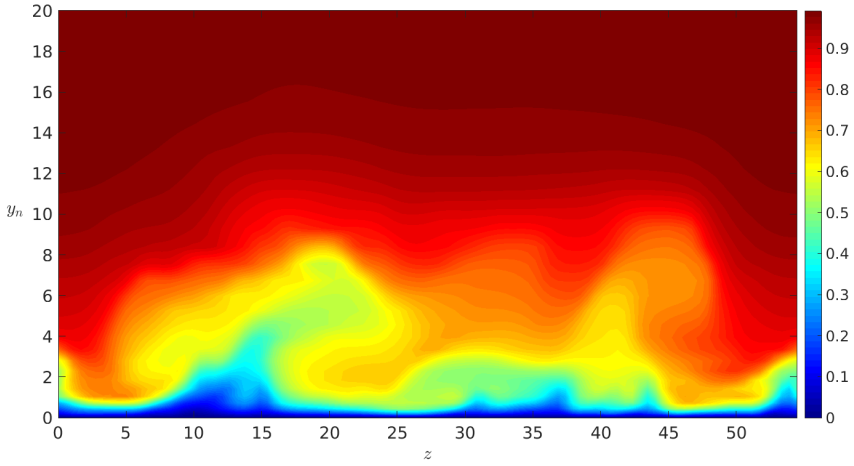


Figure 5.44: Instantaneous contour of the streamwise velocity component ($u_t$) on the $zy_n$-plane at the position $x = 800$. $y_n$ is the distance from the wall along the local normal direction. Case 8, $A_\infty = 5 \times 10^{-2}$

At $x = 500$, spanwise oscillations with a certain orientation, consistent with the presence of streamwise low-velocity streaks, are observed. Then, at $x = 800$, where the flow is in the later stages of transition, the boundary layer streaks still appear, but are much more fragmented and with other secondary streaks forming at different spanwise positions.

An illustration of the time evolution of the high-wavelength streamwise streaks observed in figures 5.41 and 5.42 is given in figure 5.45, in which the temperature contours along the $j = 10$ grid line inside the boundary layer are plotted consecutively for different instants of time ($t$=0, 1/4T, 1/2T, 3/4T, T) over the base period T of the freestream acoustic waves. In particular, figure 5.45 reveals that these streaks remain in the same position for different time instants, thus suggesting that they are stationary streaks.

Also, it is possible to notice the growth in time of the streaks along their relative direction, which gives a clearer representation of the transition process over an infinite swept wedge.

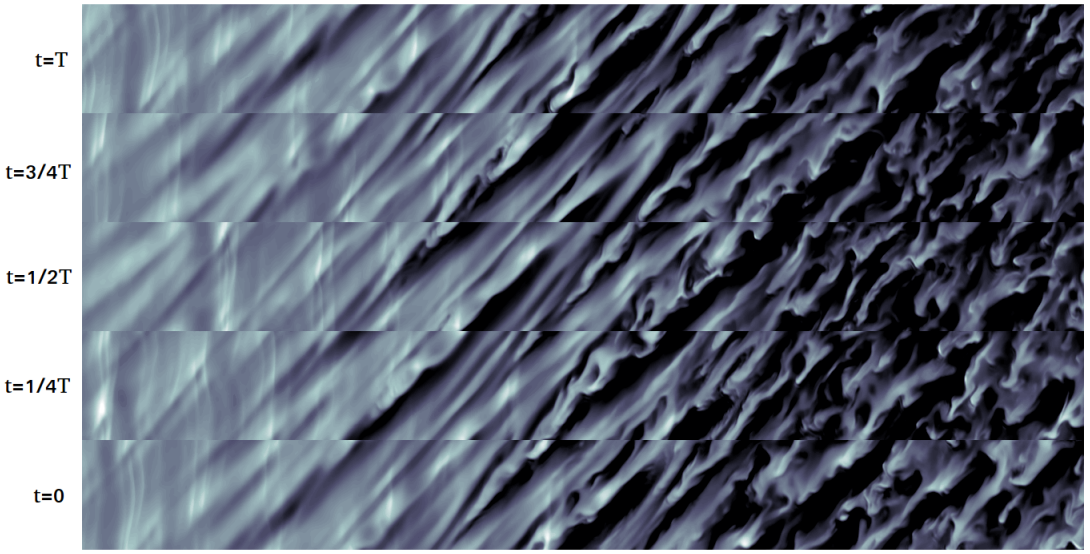


Figure 5.45: Evolution of the temperature ($T$) streaks at different instants of time ($t$=0, 1/4T, 1/2T, 3/4T, T) over the base period T of the freestream acoustic waves. The solution is relative to the region $x = 400 - 900$ of the computational domain. Time increasing upwards. Case 8, $A_\infty = 5 \times 10^{-2}$

### 5.4.3 Cases 9-10, $Re = 5625$, slow waves: slow-mode breakdown mechanisms

Figures 5.46 and 5.47 show the wall pressure fluctuation field for case 9 (low freestream amplitude) at the frequencies $f_2$ and $f_{10}$ respectively, while figures 5.48 and 5.49 show the corresponding results for case 10 (high freestream amplitude) at the same frequencies. Here, it is evident how, in contrast with the fast wave cases (7 and 8), the $\beta = 0$ mode is not the only mode to be excited in the early nose region at each frequency, and the solution is seen to be much more frequency dependent and diverse in terms of wave structure, with different modes excited at different frequencies and in different regions of the flow. At the lower frequency ($f_2$), the response of the early nose region is dominated by wave fronts approximately perpendicular to the flow direction. Downstream of $x = 200$, the wave structure changes and gradually modifies the incidence angle until the structures develop a streamwise orientation. Figure 5.50 shows a close up of this wave structure in the region $400 \leq x \leq 700$ for case 10 (and frequency $f_2$). This wave structure seems to indicate a crossflow instability mode excited in the boundary layer, which leads the flow to transition further downstream ($x = 800$ for the low amplitude, case 9, and $x = 700$ for the high amplitude, case 10).

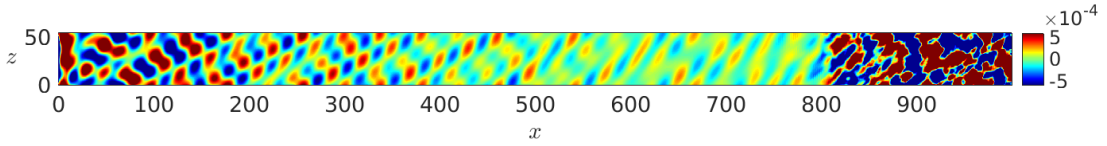


Figure 5.46: Real part of the Fourier transformed wall pressure fluctuations ($p'_w$) at the frequency $f_2$. Case 9, $A_\infty = 5 \times 10^{-3}$

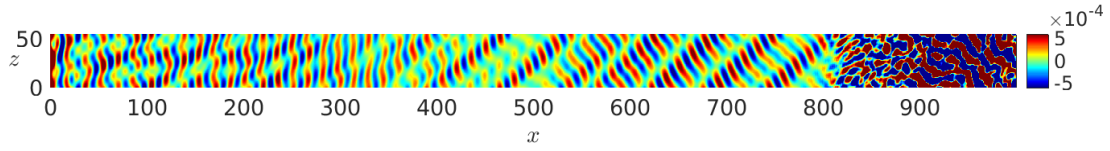


Figure 5.47: Real part of the Fourier transformed wall pressure fluctuations ($p'_w$) at the frequency $f_{10}$. Case 9, $A_\infty = 5 \times 10^{-3}$

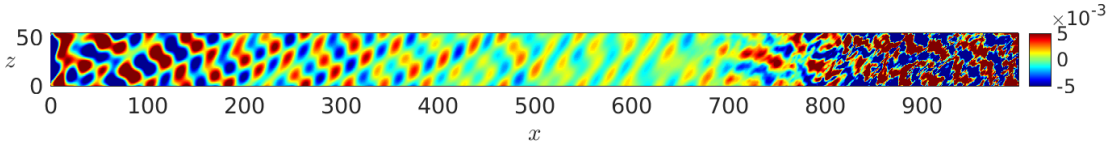


Figure 5.48: Real part of the Fourier transformed wall pressure fluctuations ($p'_w$) at the frequency $f_2$. Case 10, $A_\infty = 5 \times 10^{-2}$

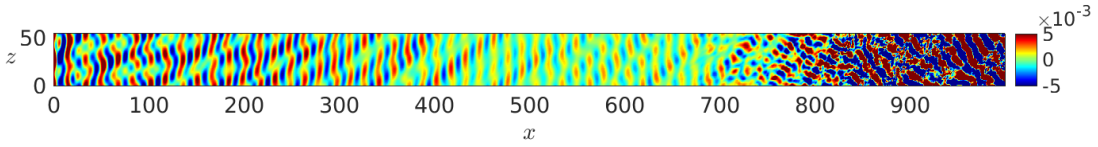


Figure 5.49: Real part of the Fourier transformed wall pressure fluctuations ($p'_w$) at the frequency $f_{10}$. Case 10, $A_\infty = 5 \times 10^{-2}$

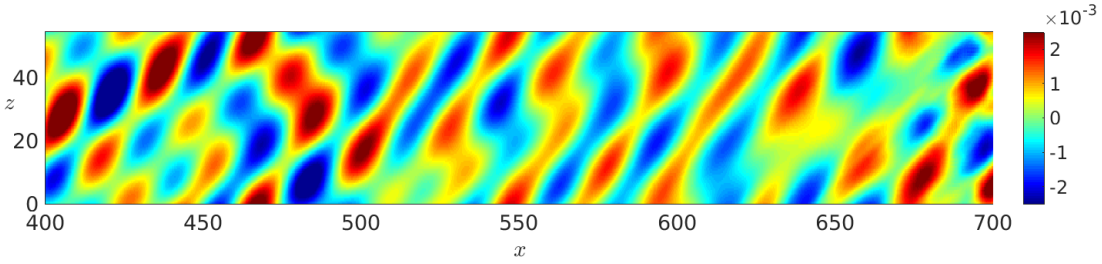


Figure 5.50: Real part of the Fourier transformed wall pressure fluctuations ($p'_w$) at the frequency $f_2$. Close up in the region $400 \leq x \leq 700$. Case 10, $A_\infty = 5 \times 10^{-2}$

At the higher frequency ($f_{10}$), in figures 5.47 and 5.49, the $\beta = 0$ mode appears to be the dominant mode in the nose region up to about $x = 400$ for both case 9 and 10, but, at the same time, it is seen to be significantly disturbed by the crossflow mode immediately after the leading edge. Downstream of $x = 400$ the $\beta = 0$ mode seems to decay, while traces of the streamwise oriented oscillations are still visible until the final transition. However, at this frequency, a significant difference can be noticed between case 9 and case 10, namely in the low-amplitude case (case 9), in figure 5.47, there is a strong excitation, in the region $550 \leq x \leq 750$, of a mode with wave fronts approximately aligned with the crossflow direction (namely a 2D mode, relative to the flow direction), which is actually not present in the case of higher freestream noise level due to nonlinear effects. In fact, in case 10 the response in this region seems to be characterised by the crossflow mode superimposed onto a decaying $\beta = 0$ mode. Figures 5.51 and 5.52 highlight the thin streamwise oriented wave structures in the streamwise velocity and temperature fields respectively, for case 9. These structures are generated in the region $700 \leq x \leq 750$ and appear as narrow streaks aligned with the streamwise direction. These streaks then grow between $x = 800$ and $x = 875$, where they finally enter an early breakdown stage, leading to the generation of streamwise-oscillating higher-wavelength structures still oriented in the streamwise direction further downstream. Thus, the crossflow instabilities lead to an early breakdown stage, as it was shown for the swept fast-wave case with low freestream disturbance amplitude (case 7).

Figures 5.53 and 5.54 show the corresponding results for case 10 (higher freestream amplitude). In this case the mechanism leading to breakdown seems to be the same of case 9 (and of case 7, with fast acoustic waves). However, due to the higher amplitude, the breakdown of the narrow streamwise streaky structures is reached at an earlier

location ($x = 750$), and there is a rapid breakdown of fragmented larger-scale structures, which leads the boundary layer to a final transition stage.

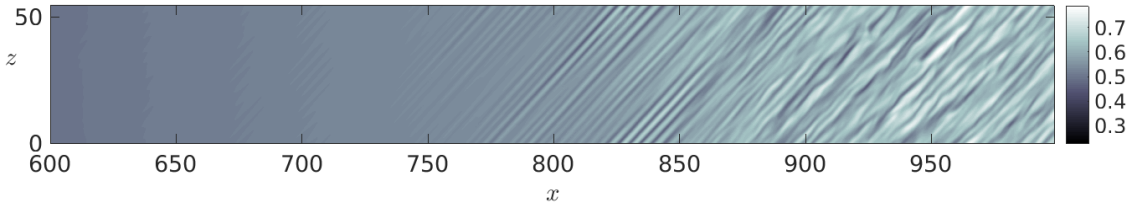


Figure 5.51: Instantaneous contour of the streamwise (tangential to the wall) velocity component ($u_t$) along the grid line $j = 10$ inside the boundary layer. Contour region starting from $x = 600$. Case 9, $A_\infty = 5 \times 10^{-3}$

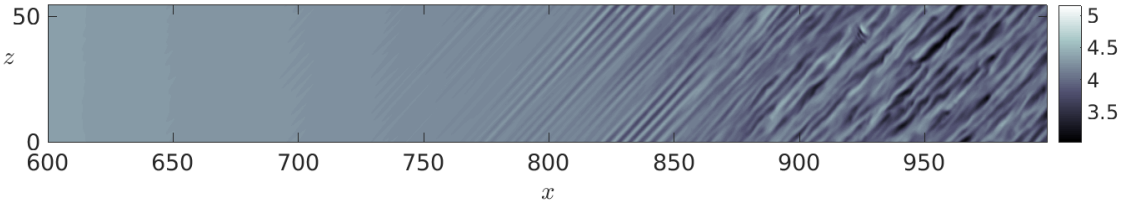


Figure 5.52: Instantaneous temperature ($T$) contour along the grid line $j = 10$ inside the boundary layer. Contour region starting from $x = 600$. Case 9, $A_\infty = 5 \times 10^{-3}$

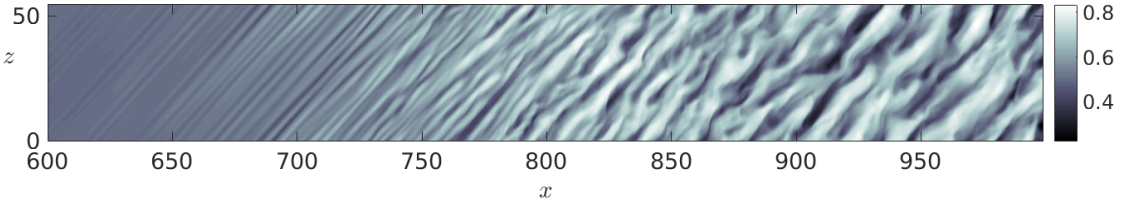


Figure 5.53: Instantaneous contour of the streamwise (tangential to the wall) velocity component ($u_t$) along the grid line $j = 10$ inside the boundary layer. Contour region starting from $x = 600$. Case 10, $A_\infty = 5 \times 10^{-2}$

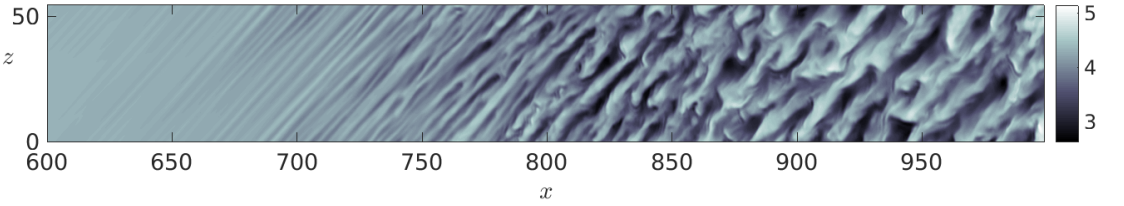


Figure 5.54: Instantaneous temperature ($T$) contour along the grid line $j = 10$ inside the boundary layer. Contour region starting from $x = 600$. Case 10, $A_\infty = 5 \times 10^{-2}$

Figure 5.55 shows the boundary-layer profiles of mean crossflow velocity ($u_{cross}$), wall-normal velocity fluctuation ($v'$) relative to case 10, first and second derivatives of the mean crossflow velocity ($\partial u_{cross}/\partial y_n$, $\partial^2 u_{cross}/\partial y_n^2$), normalised with their corresponding maximum value inside the boundary layer, at $z = 27$ and $x = 280$. Through the same approach used in Section 5.4.2.1 for the fast-wave low-amplitude case, we find that the mean crossflow boundary layer at this position on the wedge presents, at about $y_n = 2$, an inflection point satisfying Fjortoft's stronger condition for instability, as shown by the negative values assumed by the dashed curve. Moreover, as can be seen, the maximum absolute value of the wall-normal velocity perturbation inside the boundary layer is reached at a wall distance close to this inflection point. This again indicates that the flow is dominated by crossflow instabilities, whose growth induces secondary instabilities (represented by the narrow streamwise-oriented streaky structures observed in the downstream region) and final breakdown.

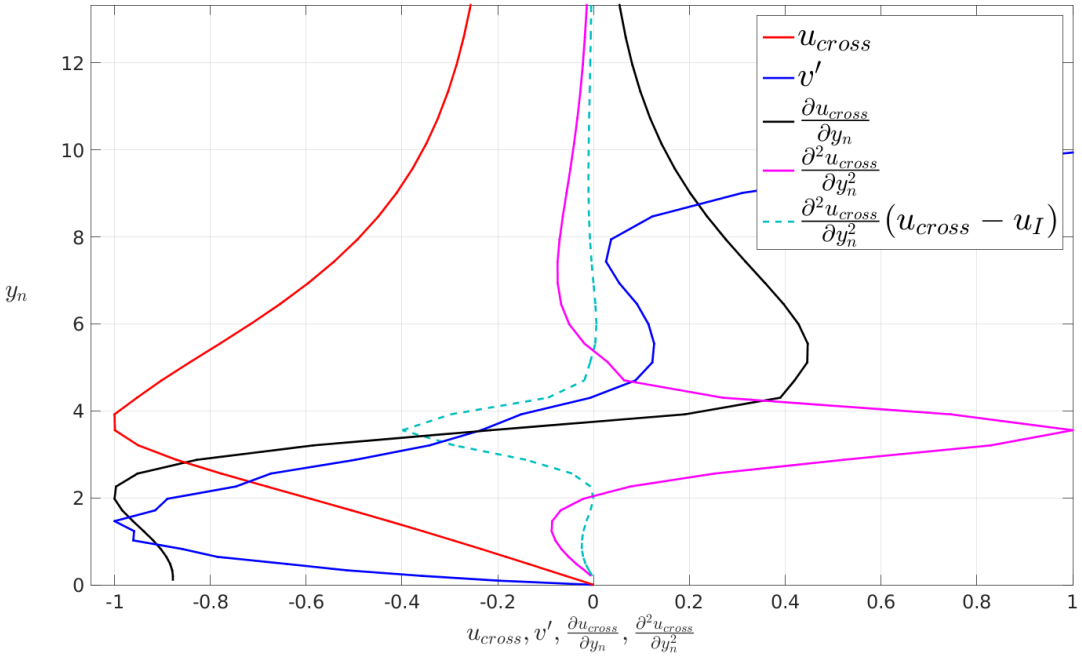


Figure 5.55: Profiles, along the wall-normal direction, of mean crossflow velocity ($u_{cross}$), wall-normal velocity fluctuation ($v'$), first and second derivatives of the mean crossflow velocity ($\partial u_{cross}/\partial y_n$, $\partial^2 u_{cross}/\partial y_n^2$), and Fjortoft's stability condition, at $z = 27$ and $x = 280$. Case 10, $A_\infty = 5 \times 10^{-2}$

The process leading from small-wavelength oscillations to the formation of more fragmented large-wavelength structures is also visible in the streamwise velocity cross-section contours at the positions $x = 700$ (shown in figure 5.56) and $x = 800$ (shown in figure 5.57) for case 10.

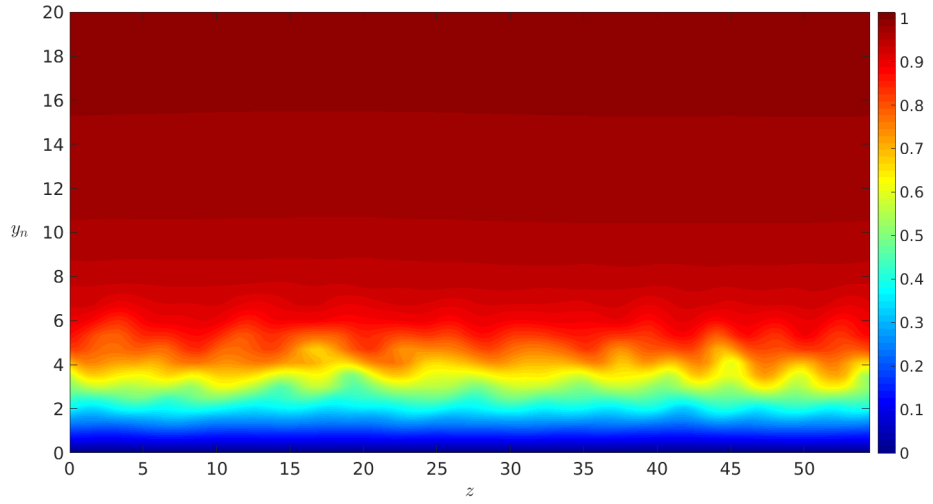


Figure 5.56: Instantaneous contour of the streamwise velocity component ($u_t$) on the $zy_n$-plane at the position $x = 700$. $y_n$ is the distance from the wall along the local normal direction. Case 10, $A_\infty = 5 \times 10^{-2}$

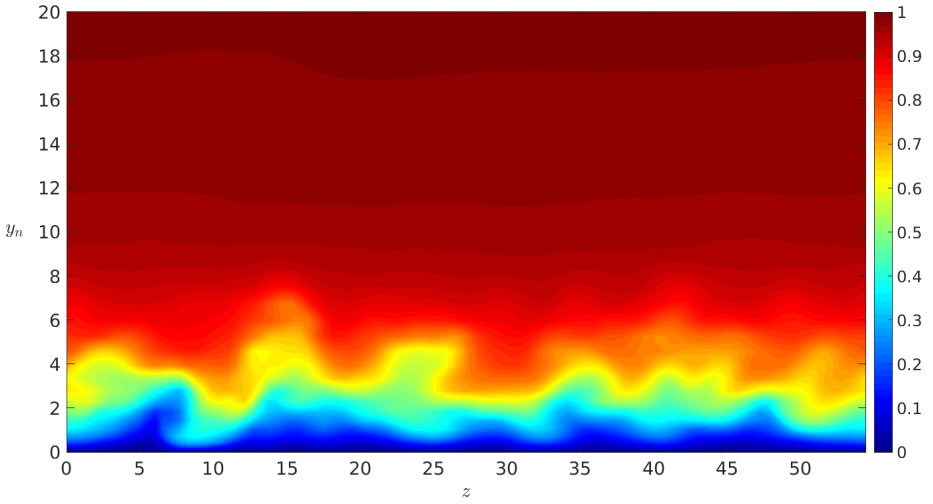


Figure 5.57: Instantaneous contour of the streamwise velocity component ($u_t$) on the $zy_n$-plane at the position $x = 800$. $y_n$ is the distance from the wall along the local normal direction. Case 10, $A_\infty = 5 \times 10^{-2}$

Hence, for the cases of slow acoustic waves, only one type of breakdown mechanism is observed for both the amplitude levels, namely a breakdown initiated by secondary instabilities of the crossflow mode, which grow very rapidly in the downstream region leading to the fragmentation process of the boundary-layer structures. This mechanism is the same that was observed for the fast-wave case at the low disturbance amplitude (case 7), and indicates that for the slow-wave case there is no by-pass mechanism even for the high amplitude level of the freestream disturbances. However, in the slow-wave case at the high amplitude level, the breakdown process is more rapid and leads to a fully transitional stage close to the domain outflow boundary.

### 5.4.4 Skin friction profiles for the breakdown/transitional cases

Finally, figure 5.58 shows the trend of the span-averaged skin friction coefficient from the station $x = 300$ downstream for all the swept cases (cases 7,8,9,10) and for the transitional unswept case (case 4). For each case, the profile of the skin-friction coefficient was obtained through a time average (over the base period T) based on a limited number of samples, which explains the oscillations observed in each curve. The cases with high freestream disturbance amplitude (cases 4, 8, 10) show an evident transition process, with the skin friction increasing by almost a factor of 3 for the two swept cases (cases 8 and 10) and a factor of 2 for the unswept case (case 4). The unswept case (represented by a black dashed line) shows earlier transition compared to the swept cases, while, among the swept cases with high amplitude, the case with fast waves (case 8, blue solid line) shows boundary-layer transition further upstream (by a distance of about 200) compared to the corresponding case with slow waves (case 10, red solid line).

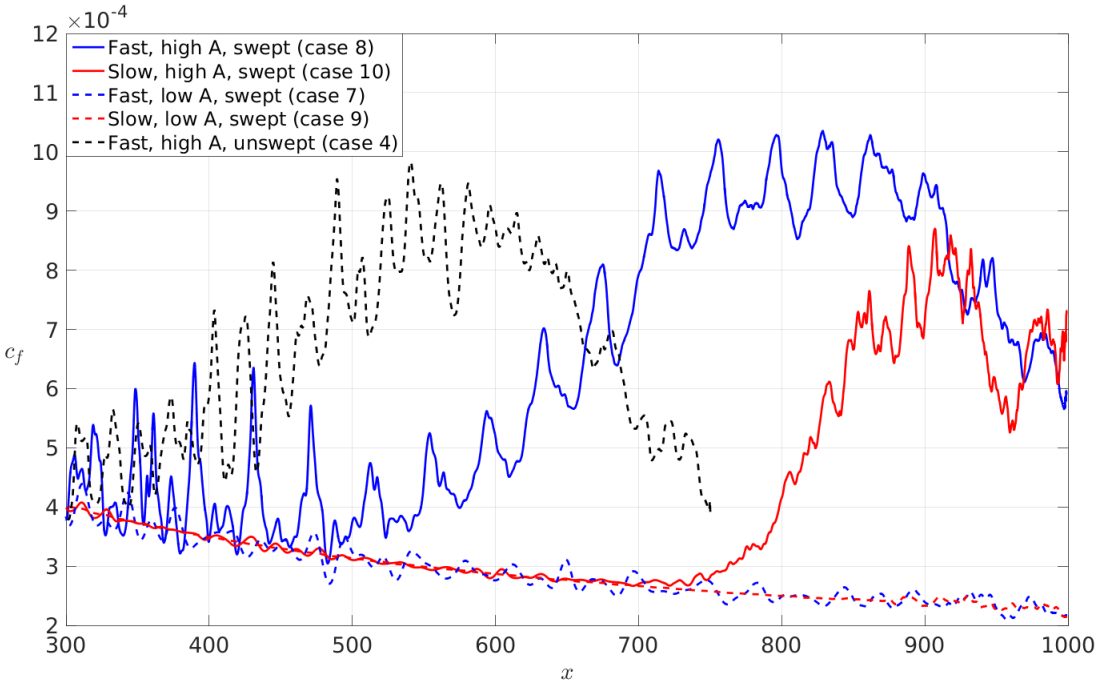


Figure 5.58: Span averaged skin friction coefficient downstream of $x = 300$ for all the swept cases (7, 8, 9, 10) and the transitional unswept case (case 4). For case 4 (black dashed line) the curve reaches $x = 750$, as this is the outer edge in the mixed DNS/LES approach for this case

The case with slow waves and high amplitude (case 10) shows a faster increase in the skin friction coefficient, thus proving that the breakdown mechanism for this case is very rapid. For the two swept cases at low freestream amplitude (cases 7 and 9, the blue and red dashed lines respectively in figure 5.58) the skin friction follows the laminar trend through all the domain length, thus proving that the boundary layer has not yet reached a transition stage. However, figures 5.36, 5.37, 5.51 and 5.52, shown previously

for the streamwise velocity and temperature contours along the $j = 10$ grid line in the boundary layer for the swept fast wave and slow wave cases respectively with low freestream amplitude, clearly show the initial stage of a breakdown process starting downstream of $x = 850$. This breakdown mechanism, at the low amplitudes, is not as strong as the breakdown at the higher amplitudes, that would lead to boundary-layer transition downstream of the domain outflow boundary.

## 5.5 Summary of the results

A set of ten simulations have been carried out for a blunt cylinder-wedge geometry in a hypersonic flow at Mach 6, for unswept and swept configurations. The main objective of this study was to investigate the effect of three-dimensional disturbances on the leading-edge receptivity to fast and slow acoustic waves at different amplitude levels, and on the induced breakdown mechanism in an unswept configuration and in the presence of a sweep angle.

Preliminary 2D simulations have shown the effects on the wall response of the frequency-dependent resonance-modulation mechanism associated with the generation and downstream evolution of the fast mode (mode F) in the case of fast acoustic waves. A set of temporal linear stability analyses, carried out at different points along the wall and for two different frequencies, have provided results in very good quantitative agreement with the numerical results, illustrating and supporting Fedorov's theory about the resonance-induced leading-edge generation and amplification of mode F, the wavelength-exchange mechanism between mode F and mode S in the synchronisation region, as well as the second resonant-interaction cycle leading to mode F II at the higher frequencies. The results are also in a very good qualitative agreement with several of Zhong's numerical results.

In the unswept configuration and at a low freestream amplitude level, fast acoustic waves have been found to induce a response substantially dominated by a 2D mode pertaining to mode F through all the domain length, due to the strong amplification of the main (two-dimensional) boundary layer fast mode (mode F), which is generated by the resonance mechanism with the forcing fast acoustic wave mode at the leading edge. On the contrary, at the higher freestream disturbance amplitudes, the response includes low-velocity streamwise streaks, which produce a significant distortion of the boundary layer causing transport of high-velocity cold fluid (in between the streaks) from the upper layers towards the wall, due to the local action of two counter-rotating vortices. While at the lower Reynolds number the streaks remain laminar, in the higher Reynolds number case they start breaking down. In the case of slow acoustic waves, no streaks are formed, and no boundary layer breakdown is reached; which is probably due to the lower amplification rates of the wall response in the leading-edge region. This is

in turn caused by the absence of a strong resonance mechanism between internal and external modes at the leading edge. The effect of this different receptivity characteristic for slow waves is the generation of a more complex three-dimensional wave structure straight from the leading edge, consisting of a mix of different 2D and 3D competing modes, but without any evident early amplification mechanism for each one of them. Hence, our results for the unswept case show that a freestream disturbance characterised by fast acoustic waves and high amplitude levels can be more dangerous (depending on the disturbance environment) than slow acoustic waves, as it can easily lead to streak formation and early breakdown in the leading-edge region.

In the case of a sweep angle of $\Lambda = 45°$, both fast and slow acoustic waves, even with low freestream disturbance amplitudes, lead to breakdown downstream along the wedge. In the cases with high freestream amplitudes a final transition stage is reached, while in the cases with low amplitudes the flow is shown to reach an early breakdown stage close to the outflow boundary. The cases of slow acoustic waves with high and low freestream amplitude and the case of fast waves with low freestream amplitude seem to have in common the same kind of breakdown mechanism, being characterised by the generation of small-wavelength elongated streaks oriented in the streamwise direction, which are due to a crossflow instability originating in the nose region and growing downstream, thus destabilising the boundary layer. The case of fast acoustic waves with high freestream amplitudes is significantly different. For this case, the wall response is dominated in the nose region by the forced $\beta = 0$ mode due to the resonance mechanism, which appears to be strongly disturbed further downstream by a growing crossflow mode coming from the leading edge. The interaction of the amplified $\beta = 0$ mode and the crossflow mode leads to the direct generation and rapid growth of long-wavelength streamwise streaks (with approximately the same wavelength of the crossflow waves) in the middle of the domain. These streaks then break down to an earlier position with respect to the other swept cases, leading quickly to boundary-layer transition.

# Chapter 6

# Results for the 3D forebody model

## 6.1 Geometry and mesh

As a final application of our receptivity-to-breakdown approach, we consider now the three-dimensional geometry of a generic forebody model, proposed by MBDA, for which transition experiments were performed recently in the Mach 6 hypersonic wind tunnel of the Purdue University (Durant *et al.* [89]). Figure 6.1 shows different views of the geometry. It consists essentially of a wedge with a rounded leading-edge shape, a nose radius of 1.25 mm (in the $xy$-plane), a length of 340 mm, a maximum width along the $z$-axis of 120 mm, a maximum height along the $y$-axis of 50 mm, and a half-wedge angle (in the $xy$-plane, with reference to the side view in 6.1) of 4°.

In our numerical simulations we consider a case with zero angle of attack and zero yaw angle, namely the flow direction is aligned with the $x$-axis of the body, and symmetry with respect to both the $xy$ and $xz$ planes (considering the origin of the reference system on the tip of the body) is assumed, including the upstream disturbances. Figures 6.2 and 6.3 show respectively the section of the body that we consider and an example of a coarse mesh for the surface. To simplify the mesh generation, the side boundary of the computational domain is obtained by cutting the geometry along the longitudinal direction at a particular spanwise distance from the symmetry axis. Figure 6.4 shows the mesh details, in the $xz$-plane, on the surface in the leading-edge region. As can be seen, the point distribution is denser near the leading-edge, in order to resolve the high gradients characterising this zone of the flowfield, and gets coarser downstream. The internal grid lines are wrapped to the leading-edge in such a way to follow the shape of three-dimensional shock. None of the shock-grid alignment methods described in Chapter 3 was used, as they were not extended to the general 3D case. However, as noted in Section 3.3, the results for this case have not been observed to be affected

by numerical noise (as will be shown later in the present Chapter), due both to the relatively weak shock wave (as a result of the small half-wedge angle and the large local sweep angles along the leading edge) and to the fact that only high-amplitude acoustic waves have been considered as freestream disturbance in the numerical simulations.

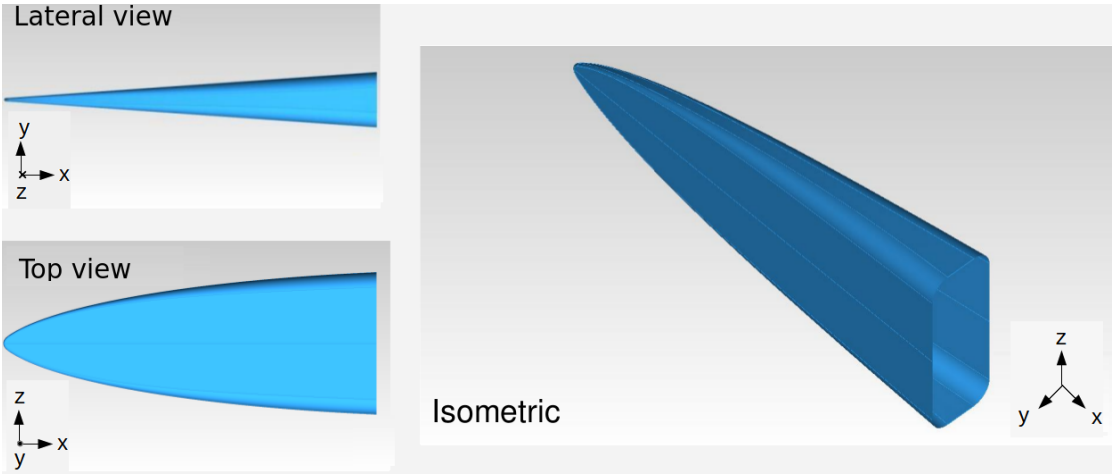


Figure 6.1: Lateral view, isometric view and lower surface view on the $xz$-plane of the MBDA forebody geometry.

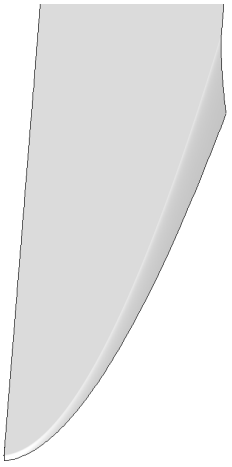

Figure 6.2: Wall shape of the computational domain in the nose region. Due to the symmetry of the body on the $xy$ and $xz$ planes, considering a flow aligned in the longitudinal ($x$) axis of the body, only one quarter of the full geometry is studied in our numerical simulations

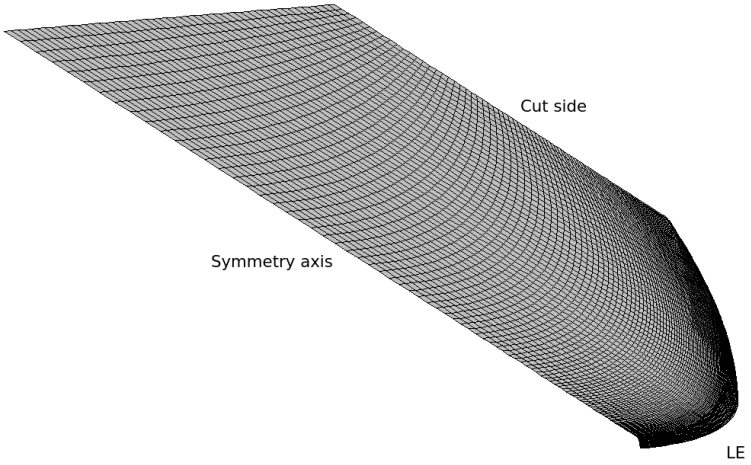


Figure 6.3: Example of a coarse mesh on the surface. Note that the side has been obtained by cutting the geometry along the longitudinal ($x$-axis, that is the symmetry axis) direction

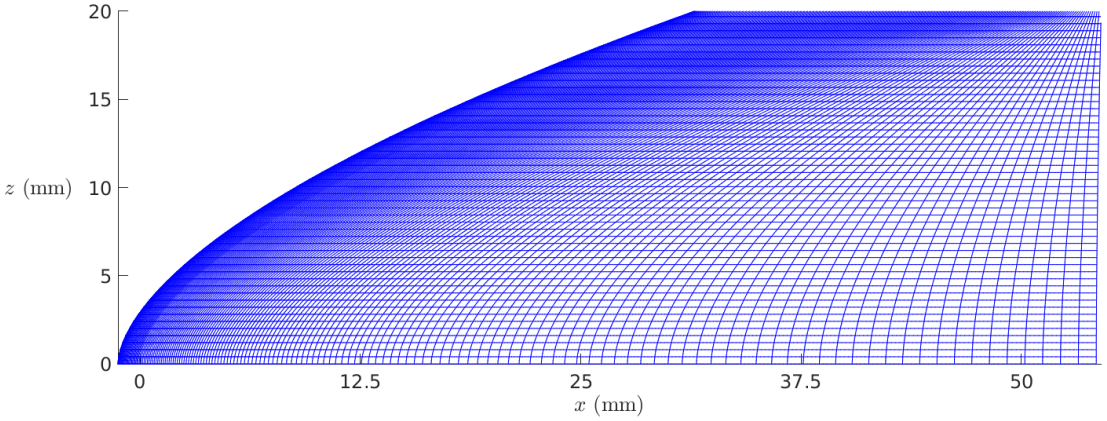


Figure 6.4: Example of a coarse mesh in the leading-edge region of the computational domain

As mentioned above, the computational domain in the width dimension is obtained by truncating the domain along the $x$-direction at a certain $z$-distance from the body $xy$-symmetry plane. The side boundary condition consists of a zero-gradient condition, which sets the gradients of each quantity along the grid lines to zero, namely $\frac{\partial()}{\partial\tau} = 0$, with $\tau$ indicating the direction tangential to the $k$-grid lines. The use of the zero-gradient boundary condition is motivated by the assumption that at sufficiently high distances from the centerline ($z = 0$) the gradients of the physical quantities in the tangential direction are small enough to be neglected. Figures 6.5 and 6.6 show the surface density field for a body with a width of 40 mm. In both figures the minimum density value is 0.23, however in figure 6.5 the maximum magnitude has been set to 1, while in figure 6.6 it has been restricted to 0.4, in order to allow the reader to distinguish between the

high-gradient and the small-gradient regions along the wall surface. As expected, the high gradients are confined in the near-centerline region, while the off-centerline region is characterised by much smaller gradients.

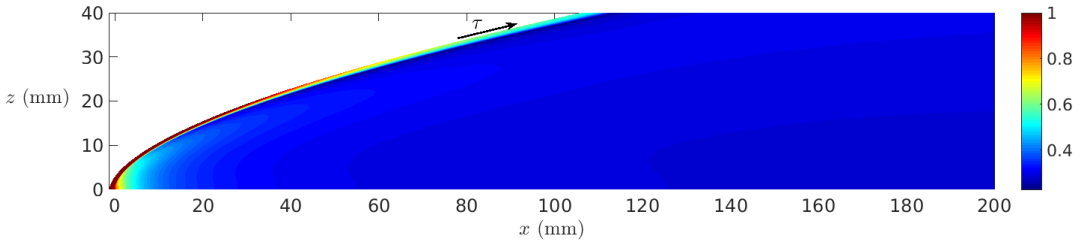


Figure 6.5: Density field on the wall surface. Magnitude range: $0.23 - 1$

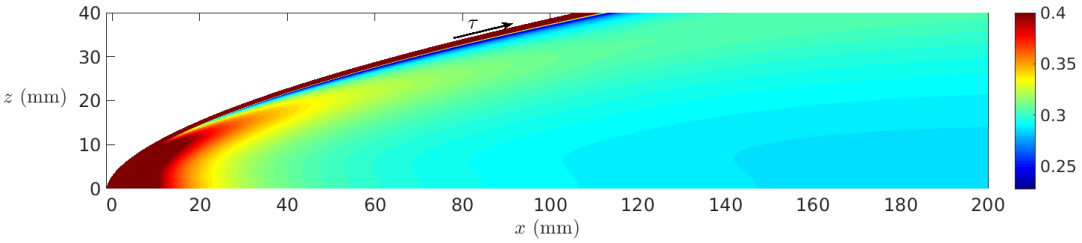


Figure 6.6: Density field on the wall surface. Magnitude range: $0.23 - 0.4$

The above described approach to obtain the computational domain presents the following advantages,

- it provides a uniform spanwise resolution everywhere, so that both the leading-edge region, which is crucial for the receptivity mechanism, and the downstream region, zone of nonlinearities and boundary-layer breakdown, are treated with the same spanwise resolution;
- it increases the computational time efficiency, by limiting the number of points in the required leading-edge region, and avoiding at the same time a too small (thus CFL constraining) $z$-spacing downstream, which would be the main issue of a grid built through grid lines following the radial (normal to the leading edge) direction.

The disadvantage of this domain configuration is the presence of a side boundary effect on the internal solution, which needs to be quantified (as will be shown in Section 6.5) in order to guarantee reliable results for the leading-edge receptivity and breakdown mechanisms.

## 6.2 Flow conditions and settings of the numerical simulations

The flow conditions of the present numerical case reproduce the freestream of the Mach 6 low-enthalpy wind tunnel of the Purdue University. The experiments were carried out for different values of the unit Reynolds number ($Re_m$), ranging from $2.3 \times 10^6$ to $13 \times 10^6$. In our numerical study a unit Reynolds number of $4.6 \times 10^6$ is considered, corresponding to one of the transitional cases in the experiments. The flow conditions are listed as follows,

- freestream Mach number: $M = 6$,
- unit Reynolds number: $Re_m = 4.6 \times 10^6$,
- freestream temperature: $T^*_\infty = 51.7K$,
- stagnation temperature: $T_0 = 424K$,
- wall temperature ratio: $T^*_w/T^*_\infty = 5.8$ (corresponding to an isothermal condition with wall temperature assumed equal to $300K$).

On the $xy$ and $xz$ symmetric planes a symmetric boundary condition is adopted. A fixed uniform inflow boundary condition (corresponding to the freestream conditions for the baseflow computation) is set on the inlet boundary, and a zero-gradient boundary condition is used on both the side and the outlet boundaries. When unsteady simulations are performed, the three-dimensional acoustic-wave model described in Section 2.4 is used as inflow on the inlet boundary. Thus, in our numerical study, the disturbance field is also assumed to be symmetric with respect to both the $xy$ and $xz$ symmetry planes of the body. Two unsteady numerical simulations have been run for each domain width, one with fast acoustic waves, and the other with slow acoustic waves as freestream disturbances, with a freestream disturbance amplitude of $10^{-2}$ (for the density fluctuation), corresponding to the high-amplitude level considered in the three-dimensional numerical cases of Chapter 5. For both the cases, the transition patterns are analysed and compared with the available experimental data (Durant *et al.* [89]).

## 6.3 Laminar base flow in the leading-edge region

In this Section we present preliminary numerical results obtained for the mean flow on a narrow ($L_z^* = 20$ mm) and short ($L_x^* = 53.75$ mm) domain, showing the main characteristics of the baseflow in the leading-edge region. The grid size is $620 \times 300 \times 200$ (in the $x$, $y$ and $z$ direction respectively, with indices $i$, $j$ and $k$). The preliminary simulations for this domain size represent the first step of a process in which the domain is gradually extended and the grid size gradually increased both in the $x$ and $z$ directions, in order to increase numerical stability and steady-state convergence rate for the solution of a higher domain size by starting from the converged solution of a smaller domain. At the same time, this process allowed us to perform a sensitivity study of the solution relative to the effect of the side boundary condition (zero gradient), by comparing the solutions of domains with different width, with results presented later in this Chapter.

Figure 6.7 shows the density field on the surface in the leading-edge region. Here, a significant decrease of the density along the leading edge is observed towards the side boundary, which indicates that the region close to the tip of the body is characterised by higher gradients compared to the side region. The shape of the bow shock in the symmetry plane can be seen in figure 6.8, showing the pressure field in a $xy$-slice at the symmetry plane. Figures 6.9, 6.10 and 6.11 show cross-sections in the $yz$-plane of temperature, streamwise velocity component ($u$) and spanwise velocity component ($w$) respectively, at a longitudinal distance of $x = 45$ mm from the tip. In particular, the left boundary of the figures ($z = 0$ mm) corresponds to the symmetry plane, while the right boundary corresponds to the side of the domain ($z = 20$ mm). As can be seen, the boundary layer is thicker at the symmetry plane, and gets thinner moving towards the side. The figures show also the curvilinear edge of the shock, with a stand-off distance decreasing along the spanwise direction.

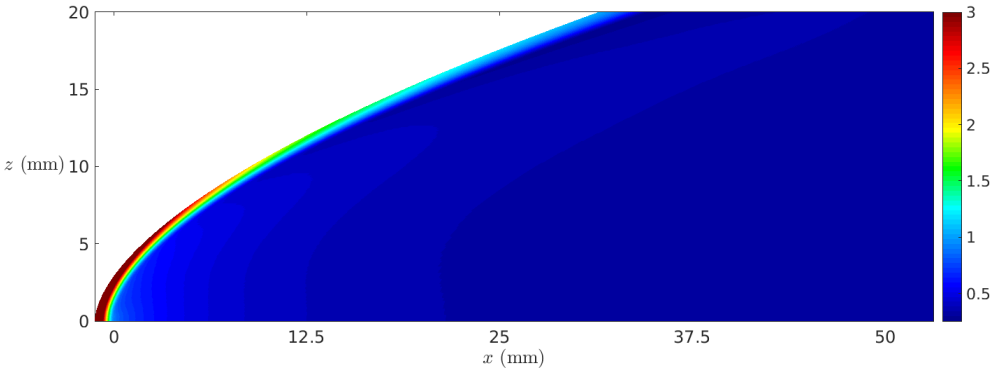


Figure 6.7: Density mean field on the surface in the leading-edge region

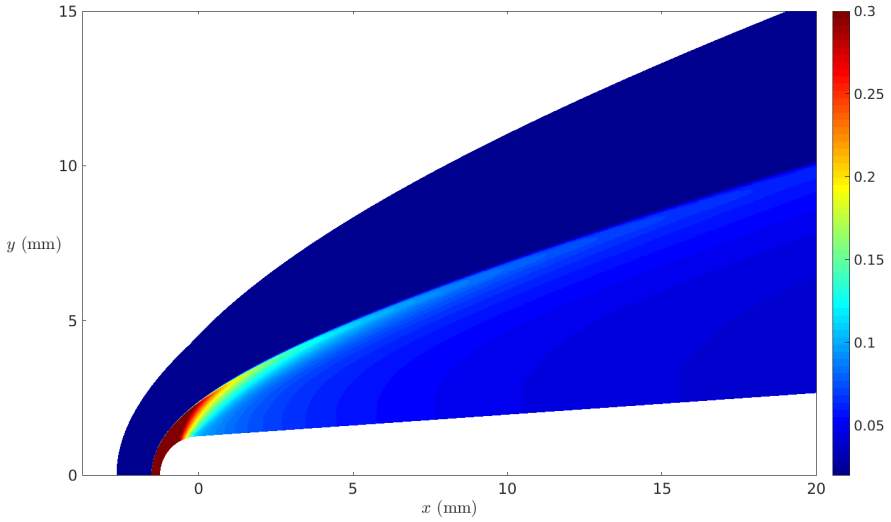


Figure 6.8: Pressure mean field in the symmetry plane of the body

The result for the spanwise velocity in figure 6.11 is particularly important, as it shows that negative values of the spanwise velocity are obtained inside the boundary layer close to the wall, while positive values are reached at the boundary-layer edge and outside the boundary layer (note that positive values indicate flow in the direction away from the centerline). This means that the flow in the leading-edge zone is characterised by a region of inflectional crossflow boundary-layer profiles, extending from the side up to a small distance from the symmetry plane (where the spanwise velocity is uniformly zero). This was expected, due to the high values of the local leading-edge sweep angle close to the side boundary.

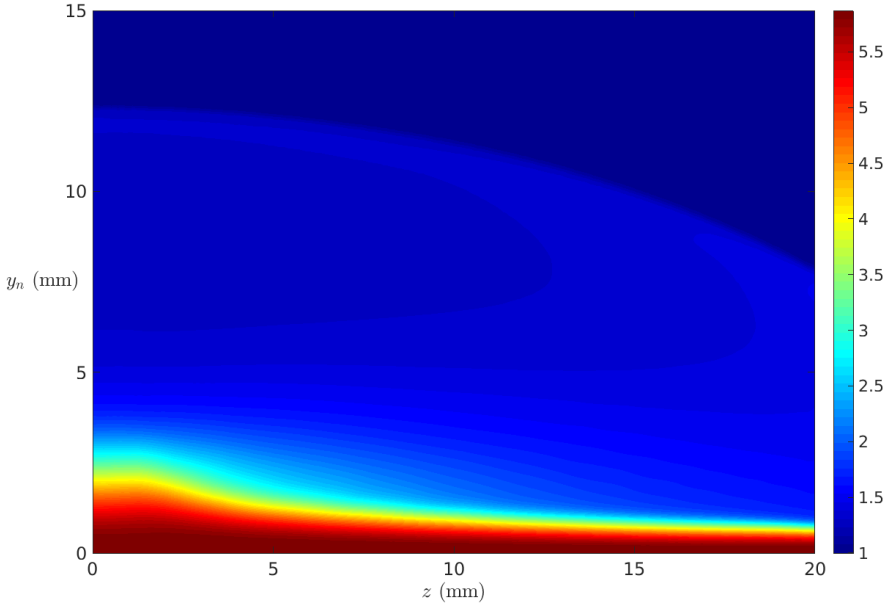


Figure 6.9: Temperature mean field on a cross-section in the $yz$-plane at the distance $x = 45$ mm from the leading edge

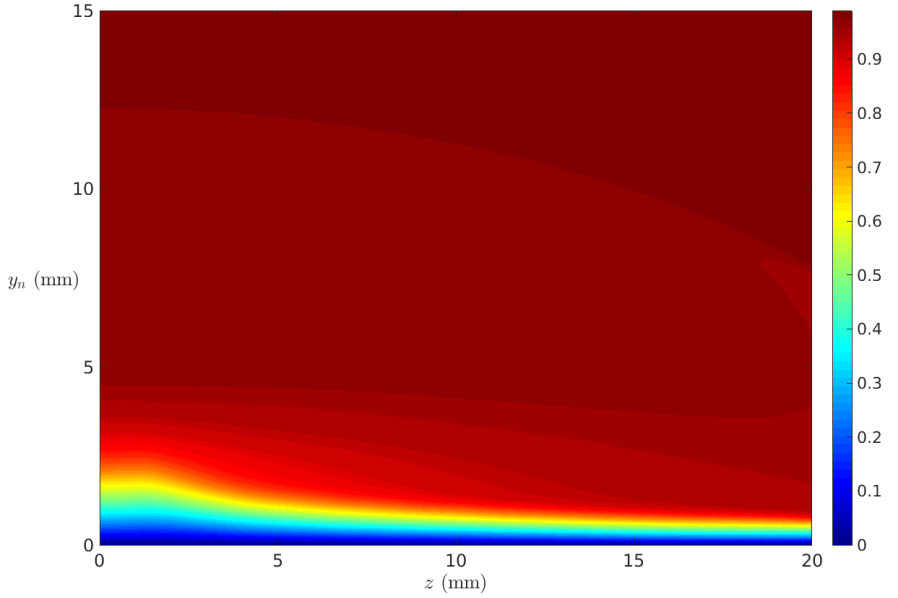


Figure 6.10: Streamwise velocity ($u$) mean field on a cross-section in the $yz$-plane at the distance $x = 45$ mm from the leading edge

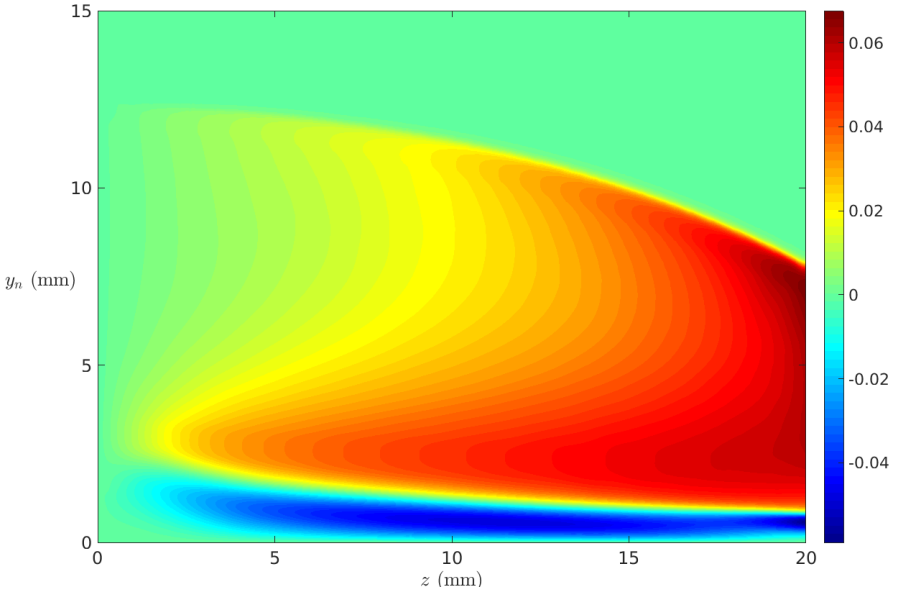


Figure 6.11: Spanwise velocity ($w$) mean field on a cross-section in the $yz$-plane at the distance $x = 45$ mm from the leading edge

## 6.4 Experimental observations and domain sizing

The observation of the experimental results of Durant *et al.* [89], at the target unit Reynolds number ($Re_m = 4.6 \times 10^6$), allows us to set the minimum required size of the computational domain (in both the $x$ and $z$ directions) in order to solve the most relevant flow regions for the receptivity-breakdown mechanism as well as to be able to capture the main transition patterns obtained in the experiments. In figure 6.12 the dimensional wall heat flux (kW/m$^2$) obtained in the transition experiments of Durant *et al.* [89], for the unit Reynolds number $Re_m = 4.6 \times 10^6$, is shown. This experimental case was performed under noisy wind tunnel conditions. As can be seen, the highest heat-flux values are reached in the front leading-edge region, as is expected from the high temperature values characterising the flow inside the shock layer in the nose region (note that in the experimental reference system the body tip, which is not shown, is located at the position $x = -100$ mm). In the downstream region, the wall heat flux assumes low values at the centerline, thus suggesting that the boundary layer near the symmetry plane is laminar through the whole domain length; however, the off-centerline region is characterised by high heat flux values, starting from about $x = 50$ mm, which suggests, in contrast, that the boundary layer here undergoes transition to turbulence.

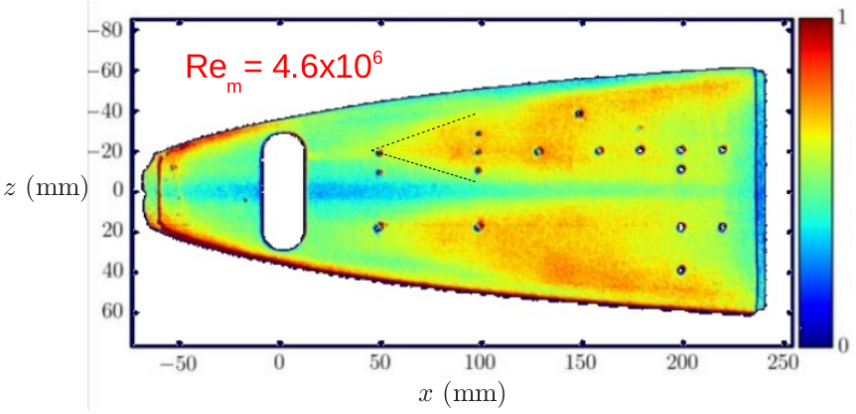


Figure 6.12: Experimental result for the wall heat flux (kW/m$^2$) shown in the work of Durant *et al.* [89]. $Re_m = 4.6 \times 10^6$

From the wall heat-flux experimental results the following observations can be made,

- transition appears to start at a streamwise distance from the tip between about 140 mm and 150 mm, and at a distance approximately of 20 mm from the centerline;
- the transition front spreads downstream forming a wedge initially symmetric with respect to the $x$-axis, as indicated by the black dashed lines drawn along the edges of the early transition front;

- thus, transition might be induced downstream by disturbances coming from the early leading-edge region and developing downstream at a distance from the centerline of approximately one-third of the maximum half-body width ($L_z^*/2 = 60$ mm).

These considerations allow us to shape the computational domain in such a way to be suitable for solving the main mechanism inducing transition. Figure 6.13 shows the edges of two additional computational domains we chose to perform our numerical simulations, drawn over the contour plot of the experimental wall heat flux. The red lines indicate the lateral and backwards edges of a domain with a spanwise width of 30 mm and a longitudinal length of about 200 mm (which, from now on, we shall refer to as the small domain), while the black lines represent the corresponding edges of a 40 mm wide and 250 mm long domain (representing the large domain).

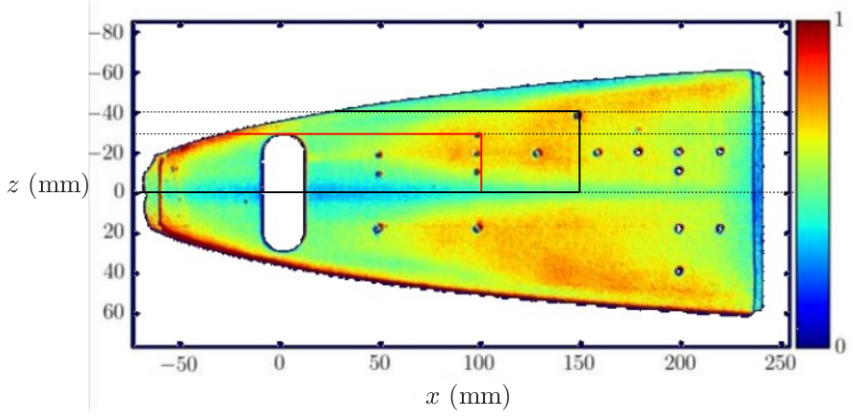


Figure 6.13: Edges of two different computational domains superimposed on the experimental result for the wall heat flux (kW/m$^2$) shown in the work of Durant *et al.* [89]. $Re_m = 4.6 \times 10^6$

## 6.5 Baseflow solution sensitivity to the side boundary effect

The computational domains described in Section 6.4 allow us to perform sensitivity study to quantify the effect of the zero-gradient lateral boundary condition on the internal solution. Numerical simulations of the mean flow have been carried out for both the computational domains. The mesh size of the small domain (30 mm width) is $2120 \times 300 \times 300$ (corresponding to the $x$, $y$ and $z$ direction number of points respectively), while the mesh size for the large domain (40 mm width) is $2120 \times 300 \times 400$. Note that the same uniform spanwise resolution is used in both the domains.

Figures 6.14 and 6.15 show the surface heat flux for the 30 mm and the 40 mm wide domains respectively. A very good agreement is observed between the two results, with the exception of a small region adjacent to the lateral boundary, corresponding to the region beyond the horizontal dashed line in figure 6.14, where the heat-flux contours differ from the result for the wider domain in figure 6.15. This effect can be seen more clearly in figure 6.16, showing a zoomed view of the heat-flux contours. The edge of the affected region (dashed line in figure 6.14) is located at about $z = 28.3$ mm, meaning that the internal solution is influenced by the boundary condition within about a 5.6% of the domain width (for the 30 mm wide domain). For comparison, the zoomed view of the same region for the 40 mm wide domain is shown in figure 6.17. Here, the heat-flux contour lines show a monotonic profile near the position $z = 30$ mm, in contrast with the result shown for the 30 mm wide domain in figure 6.14, in which the contour line profiles reach a peak near the side, and then approach the boundary with a reverse trend.

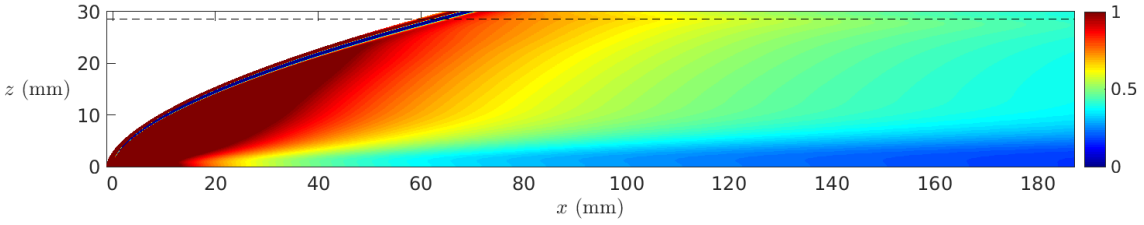


Figure 6.14: Surface heat-flux (kW/m$^2$) contours for the 30 mm wide domain

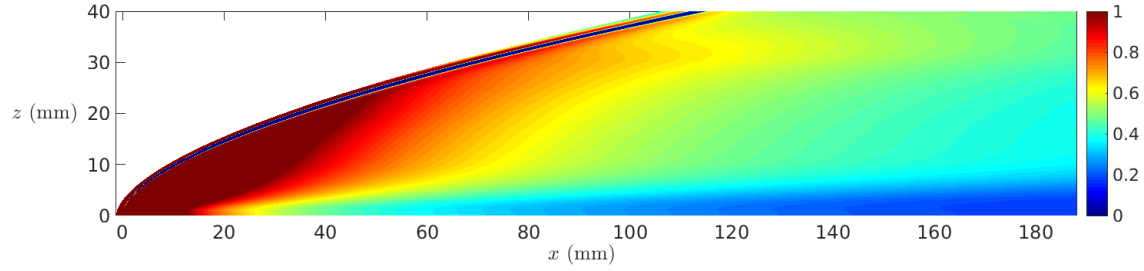


Figure 6.15: Surface heat-flux (kW/m$^2$) contours for the 40 mm wide domain

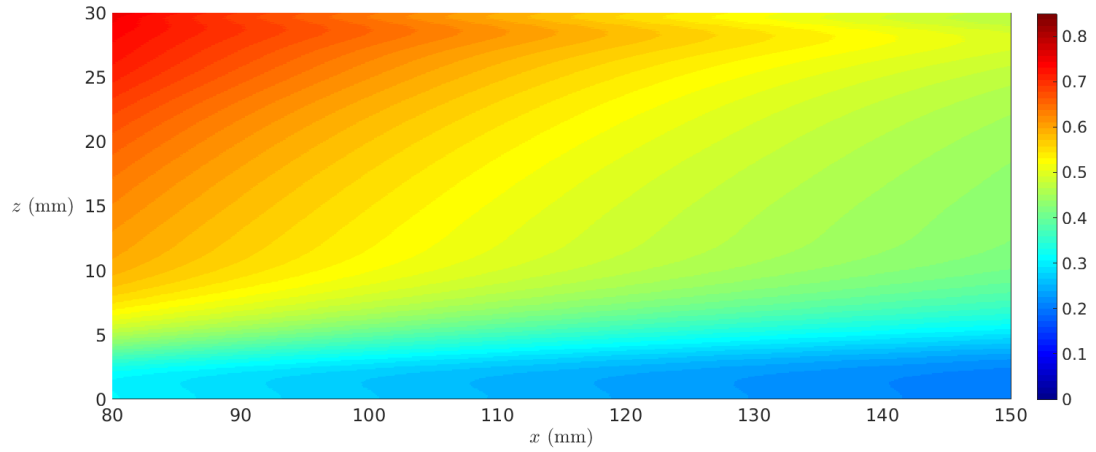


Figure 6.16: Surface heat-flux (kW/m$^2$) contours for the 30 mm wide domain. Zoom on the lateral boundary to highlight the boundary condition effect

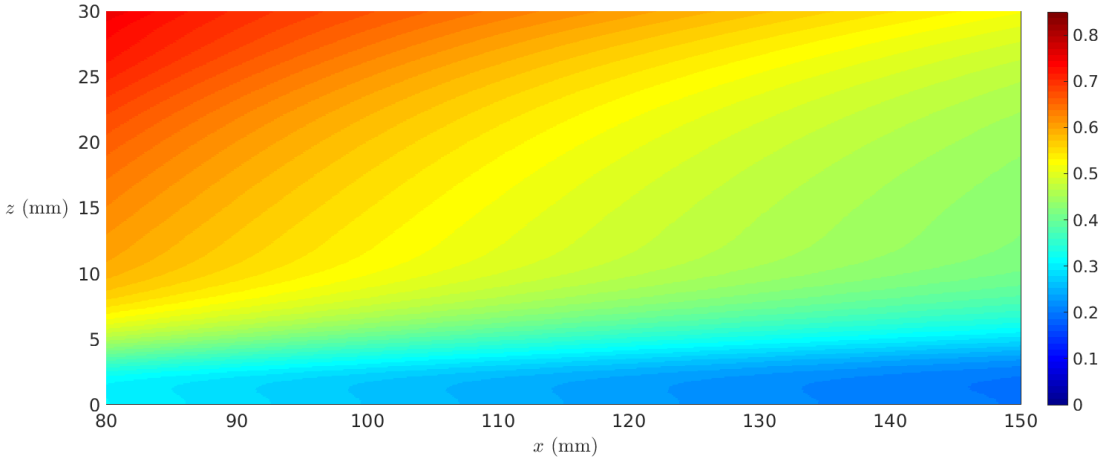


Figure 6.17: Surface heat-flux (kW/m$^2$) contours for the 40 mm wide domain. Zoom near the position $z = 30$ mm

These results show that only a limited portion of the domain is affected by the side boundary condition, which suggests that the zero-gradient boundary condition, based on the assumption of small gradients along the $k$-grid line tangential direction (described in Section 6.1), is suitable for the present simulations. As shown in the preliminary results for the cross-section contours of the spanwise velocity in figure 6.11 of Section 6.3, the off-centerline flowfield is characterised by a region of negative (namely inwards) spanwise velocity inside the boundary layer, and a region of positive (namely outwards) spanwise velocity outside the boundary layer. The inwards flow, in particular, may be critical for the accuracy and reliability of the internal solution. For this reason, it is necessary to evaluate the region adjacent to the lateral boundary which would be influenced by the flow entering the domain from the side.

Figure 6.18 shows the streamlines computed on the $j = 3$ grid line inside the boundary layer, for the small domain. As can be seen, the streamlines coming from the leading edge are inclined towards the centerline by a variable angle along the leading edge. This is an effect of the local sweep angle and the high pressure gradients of the leading edge region, which cause the curvilinear motion of the boundary-layer streamlines around the leading edge. The boundary-layer flow going around the leading edge gets deflected, with a small radius of curvature, towards the centerline, as can be seen in more detail in figure 6.19, showing a close-up of the streamlines (along with the relative vectors) on the leading edge in the near centerline region. Consequently, the region adjacent to the side boundary which is not traversed by the streamlines originating from the leading edge (with reference to figure 6.18) represents the region affected by the presence of the side boundary.

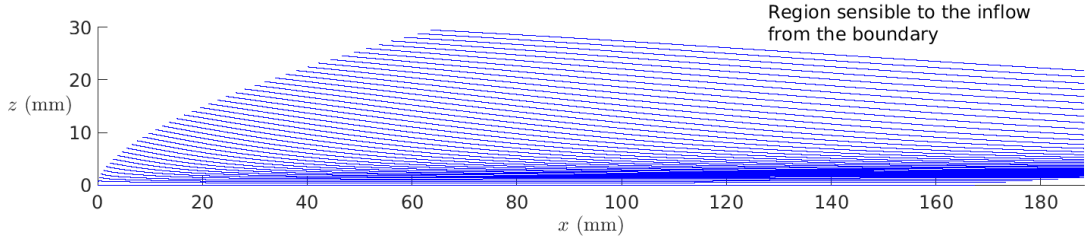


Figure 6.18: Streamlines on the $j = 3$ grid lines for the 30 mm wide domain

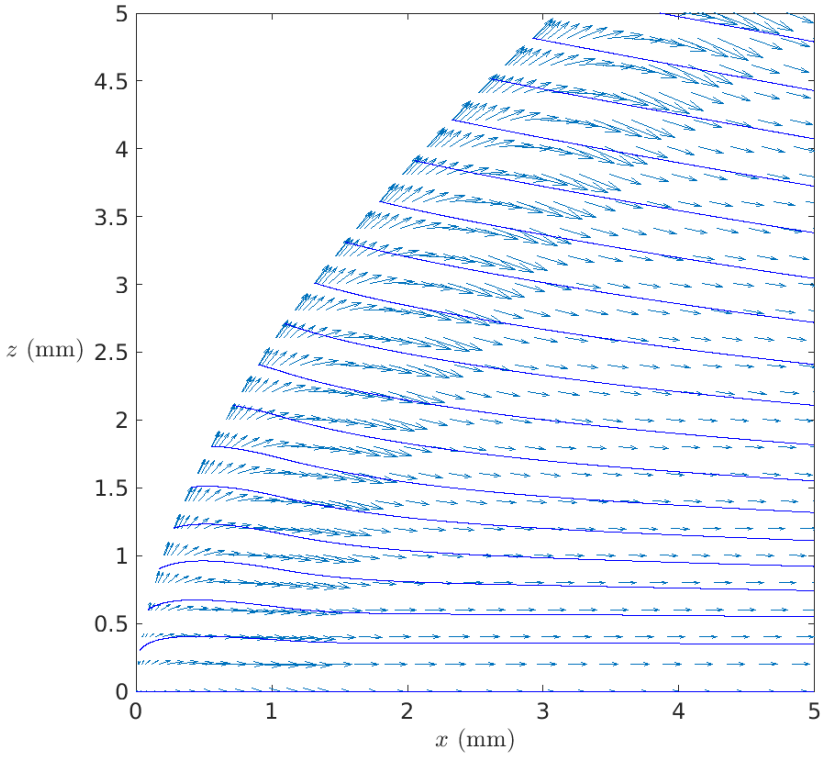


Figure 6.19: Streamlines on the $j = 3$ grid lines for the 30 mm wide domain. Close-up on the leading edge near the symmetry plane

Figures 6.20 and 6.21 show the streamlines for the 40 mm wide domain computed inside the boundary layer on the $j = 3$ and $j = 16$ grid lines respectively. As can be seen in figure 6.20, for the large domain the inclination angle of the streamline originating at $z = 40$ mm is higher than the corresponding lateral streamline of the small domain, originating at $z = 30$ mm, shown in figure 6.18, thus proving that away from the centerline the inwards deflection of the streamlines increases with the local sweep angle. However, the transition point, which appears to be located approximately at the position indicated by a red circle in figure 6.20, as observed in the experimental results shown in figure 6.12, is well inside the zone not affected by the presence of the side boundary, suggesting that the large domain should capture the main physical mechanism leading to transition, as well as the early stage of the transition process. Furthermore, as seen in figure 6.21, the streamlines at a higher distance from the wall inside the boundary layer show a smaller inwards deflection angle at $z = 40$ mm, suggesting that the inwards deflection angle decreases as we move away from the wall until it becomes negative (i.e. outwards flowing) outside of the boundary layer. This is consistent with the results presented in figure 6.11 for the cross-section contours of the $w$ velocity component at a certain $x$ location, showing that the flow entering the domain from the side boundary is confined in a near-wall region inside the boundary layer, while outside the boundary layer the flow is in the outwards direction.

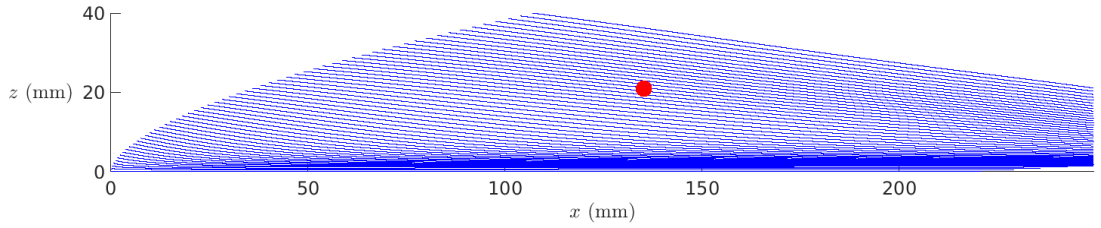


Figure 6.20: Streamlines on the $j = 3$ grid lines for the 40 mm wide domain. The red circle indicates approximately the point where transition appears to start in the experimental results

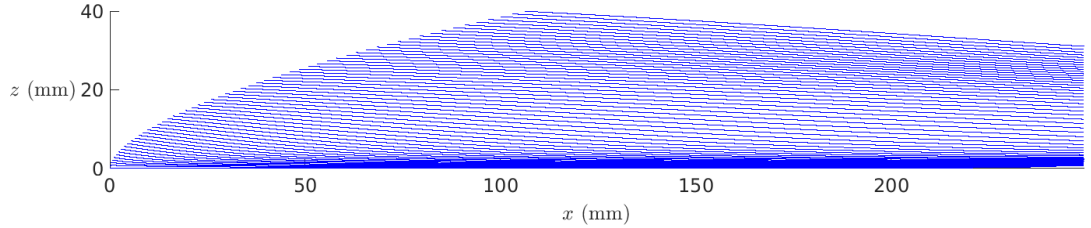


Figure 6.21: Streamlines on the $j = 16$ grid lines for the 40 mm wide domain

## 6.6 Wedge-junction effect: crossflow inflectional profiles and reverse heat flux

The wedge junction to the circular leading edge is a critical zone determining the general characteristics of the flowfield over the entire wedge (e.g. the streamline orientation), and in particular the boundary-layer stability properties. This is due to the strong expansion taking place at the wedge junction and to the associated streamline deflection. In fact, the near-wall flow entering the wedge with an inwards (towards the centerline) orientation, in combination with the outwards orientation of the outer boundary-layer flow, generates inflectional crossflow boundary-layer profiles in the zone of the wedge junction, as can be observed in figures 6.22 and 6.23, showing respectively the crossflow boundary-layer profiles at several $x$ positions within the circle-wedge junction zone and the contours of the crossflow velocity ($w$) on the $xy$-plane, at $z = 30$ mm. The crossflow boundary-layer profiles show the presence of an inflectional profile due to the inwards (i.e negative $w$) flow direction near the wall, corresponding to the blue region located at the wedge junction shown in the $w$ contour plot. The flow inside the shock layer downstream of the bow shock shows, in contrast, a high positive $w$ velocity, namely oriented towards the positive values of $z$, which is due to the inclination of the shock with respect to the $xy$-plane and the resulting deflection of the flow crossing the shock. This is also the reason why the crossflow profiles in figure 6.22 do not approach zero outside the boundary layer, but a positive value instead.

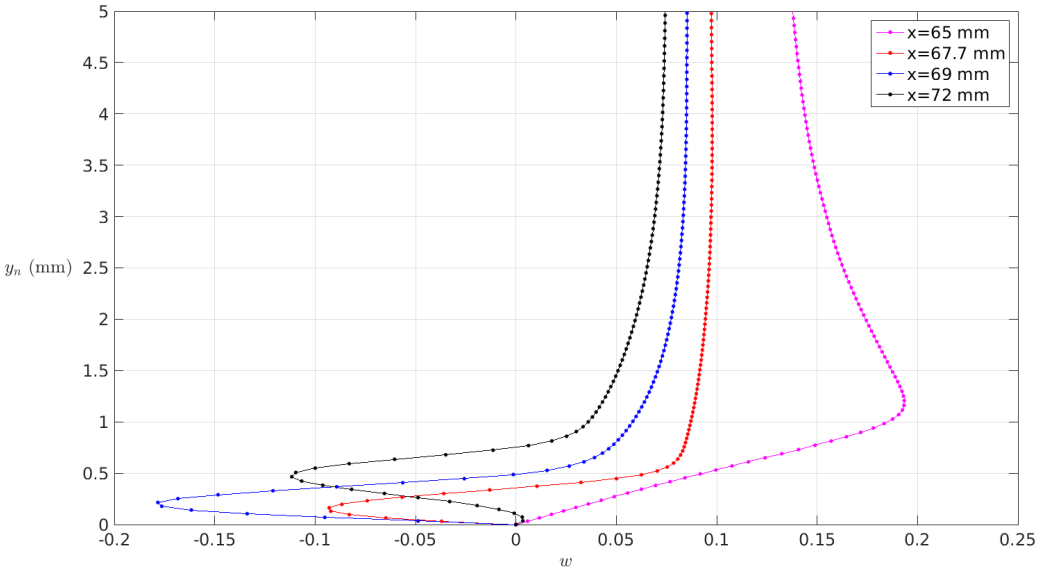


Figure 6.22: Crossflow boundary-layer profiles at different streamwise locations and at the spanwise position $z = 30$ mm

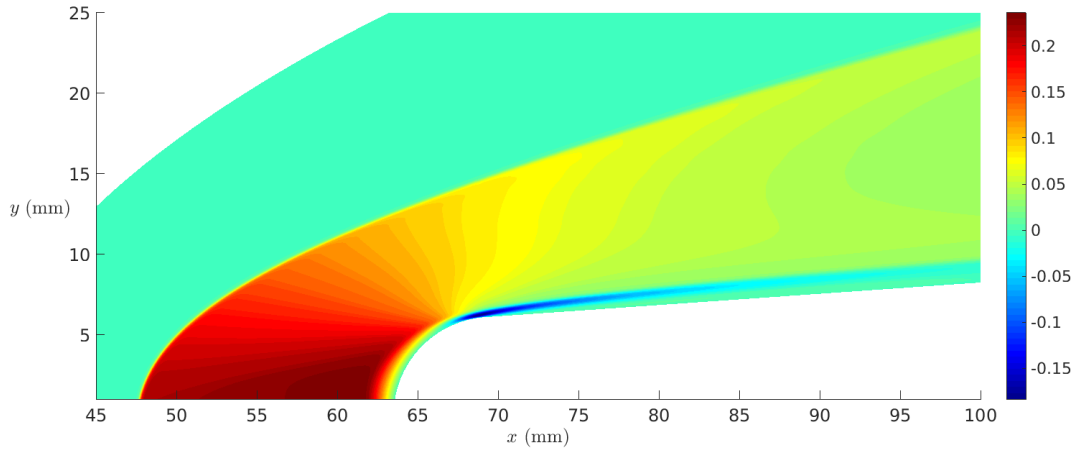


Figure 6.23: Crossflow ($w$) contours in the $xy$-plane at the spanwise position $z = 30$ mm

The inflectional profiles of the crossflow boundary layer have, of course, an impact on the boundary-layer stability characteristics downstream. However, there is another important effect of the wedge junction, which is a direct consequence of the crossflow inside the boundary layer and plays a significant role on the local wall heat flux. This effect consists of the boundary layer being very thin at the wedge junction, as a result of the mass conservation equation in conjunction with the strong localised 3D flow effects in the high crossflow region (the dark blue zone in figure 6.23), as can be seen in the contour plot of temperature in the $xy$-plane at $z = 30$ mm shown in figure 6.24. As a result, the cold fluid flow outside the boundary layer gets very close to the wall, so that the constant temperature at the wall (where an isothermal boundary condition is applied) is higher than the temperature values reached at every point inside the boundary layer. This produces, in turn, a reverse of the wall heat flux, such that the fluid is heated by the wall in this region.

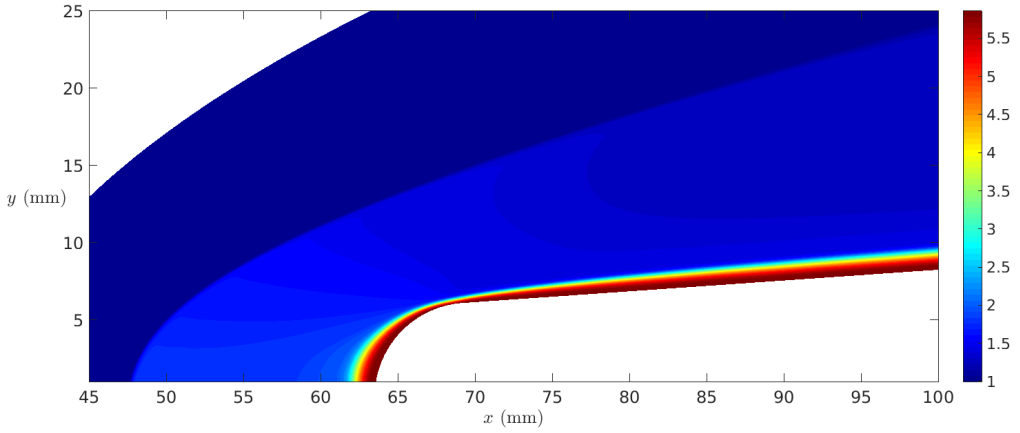


Figure 6.24: Temperature ($T$) contours in the $xy$-plane at the spanwise position $z = 30$ mm. Note the very thin boundary layer at the circle-wedge junction

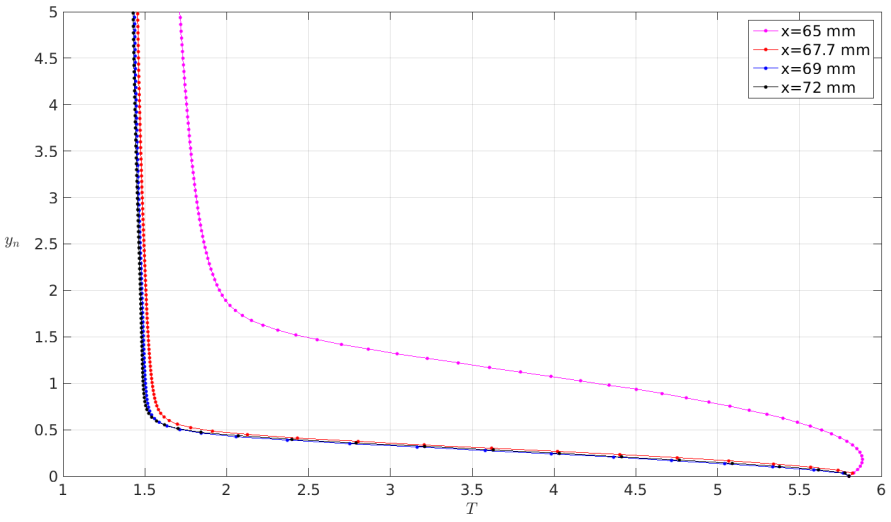


Figure 6.25: Temperature ($T$) boundary-layer profiles at different streamwise locations and at the spanwise position $z = 30$ mm

Figure 6.25 shows the temperature boundary-layer profiles at the same points of the crossflow profiles as figure 6.22. At $x = 65$ mm, which is still in the circle behind the wedge junction, the maximum temperature is reached at a certain normal distance ($y_n$) from the wall, but as soon as the wedge junction is approached and the negative crossflow originates, the boundary-layer thickness decreases dramatically and the temperature gradient at the wall becomes negative. In figure 6.26, showing a close-up of the wall heat flux at the leading edge, a narrow region of high negative (blue) heat-flux values, corresponding to the wedge-junction zone, is observed.

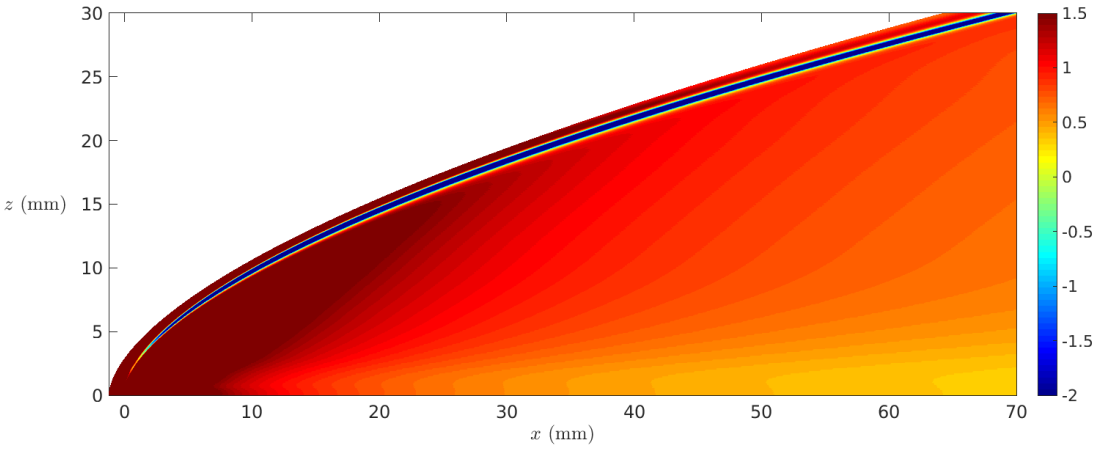


Figure 6.26: Close-up of the wall heat flux (kW/m$^2$) in the leading-edge region. The blue stripe of high negative values corresponds to the wedge junction.

Figures 6.27 and 6.28 show the temperature and crossflow velocity ($w$) cross sections (in the $zy_n$-plane) respectively, at the streamwise position $x = 40$ mm. The right edge of the plots corresponds to the wedge-junction $z$ position, where the minimum boundary-layer thickness is observed. The figures highlight how the boundary layer gets rapidly thinner along the spanwise direction as the wedge junction is approached. The result shown in figure 6.28 is particularly interesting, as it shows the high inwards crossflow velocity magnitudes reached at the wedge junction, which indicate that a stream coming from the leading edge and flowing towards the centerline is released by the wedge junction into the flowfield over the wedge surface.

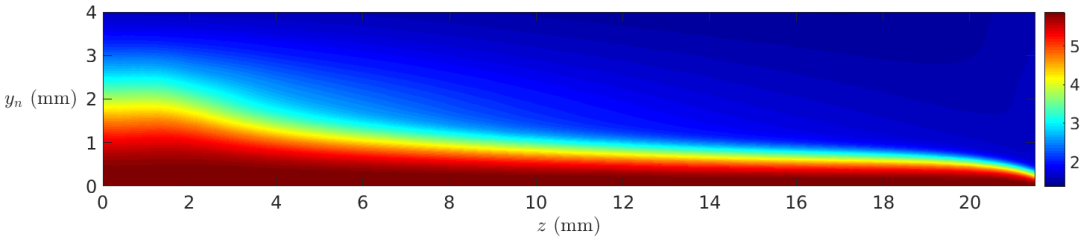


Figure 6.27: Temperature ($T$) contours in the $zy_n$-plane at the streamwise position $x = 40$ mm

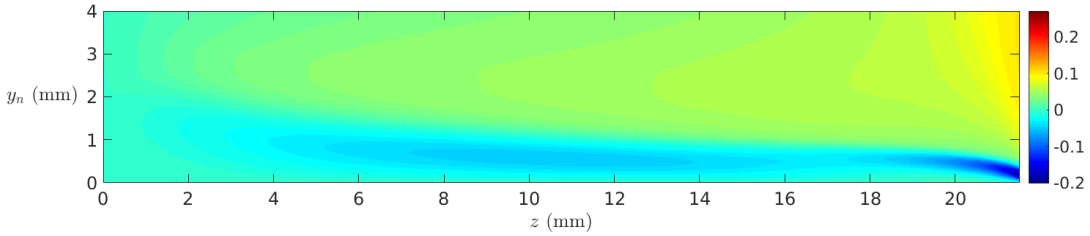


Figure 6.28: Crossflow ($w$) contours in the $zy_n$-plane at the streamwise position $x = 40$ mm

The reversal of the surface heat flux at the wedge junction can significantly affect the aerodynamic and thermal-protection performances of a hypersonic vehicle, thus it has to be taken into consideration in the aero-thermal design process.

## 6.7 Results for the unsteady simulations

### 6.7.1 transition patterns with 3D fast and slow acoustic waves

We now present numerical results for the unsteady simulations with three-dimensional fast and slow acoustic waves as freestream disturbances. The aim of these simulations is to understand the physical mechanism leading to transition downstream, starting from

the internalisation of the freestream disturbances and the generation of boundary-layer instabilities at the leading edge. The numerical results will then be compared with the experimental results.

The acoustic model used to carry out the unsteady simulations is the 3D model described in Section 2.4, consisting of a 2D wave plus two pairs of opposite angle oblique waves with multiple spanwise wavenumbers. In particular, the considered spanwise wavenumbers in this case are $\beta_2 = 2 \cdot \frac{2\pi}{L_z}$ and $\beta_4 = 4 \cdot \frac{2\pi}{L_z}$, with $L_z = 32$ (corresponding to 40 mm in dimensional scale). The corresponding spanwise wavelengths of the oblique waves are one-half and one-quarter of the domain width. This particular choice of the spanwise wavenumbers has been made in order to provide a disturbance wavelength across the span comparable with the spanwise off-centerline distance within which transition is expected to take place (approximately 20 mm, namely half the domain width), on the basis of the experimental observations in Section 6.4. The choice of the wavenumbers $\beta_2$ and $\beta_4$ is consistent with the corresponding spanwise wavenumbers used in the 3D simulations for the extruded cylinder-wedge geometry in unswept and swept configurations described in Chapter 5 (namely $\beta_1$ and $\beta_2$). However, while for the 3D wedge simulations the oblique waves were introduced with a random phase in the spanwise direction, in this case a fixed phase, $\phi_m = 0$, is used for each $m^{th}$ spanwise wavenumber ($\beta_m$), with reference to equation 2.26, so that to guarantee the symmetry of the freestream disturbance field with respect to the body symmetry plane ($z = 0$) at each $x$ position along the domain length.

Furthermore, in order to reduce disturbance reflection effects from the side boundary into the internal flowfield, a $z$-dependent hyperbolic-tangent based damping function ($h(z)$) has been applied over the 3D wave model 2.26 which gradually damps out the amplitude of all the imposed freestream disturbance waves (both 2D and oblique) along the $z$-direction from a certain position ($z_0$) to the side boundary. The 3D wave model used in this case is expressed by,

$$\rho'(x,z,t) = \sum_{m=0}^{M} \sum_{n=1}^{N} A_m h(z) \cos\left(\beta_m z + \phi_m\right) \cos\left(\alpha_n x - \omega_n t + \psi_n\right) \ , \tag{6.1}$$

$$h(z) = 1 - \frac{1}{2}\left(\tanh\left(\frac{S(z - z_0)}{L_z^* - z_0}\right) + 1\right) \tag{6.2}$$

in which $S = 10$, and $z_0 = 26.5$ mm. This value of $z_0$ guarantees the resulting signal to be coincident to the corresponding non-damped signal (given by equation 2.26) for $z = 0 - 20$ mm.

This set-up of the 3D wave model is the final result of a series of preliminary tests aimed at verifying that the boundary-layer solution in the internal domain region where

the early transition process is expected to be located (as well as the whole corresponding upstream region, location of the receptivity process) is not affected by reflections of disturbances (reaching the lateral edge within a certain $x$ distance) from the side boundary.

The overall freestream amplitude of the wave system (the sum between the amplitudes of the 2D and oblique waves) is set to $A_\infty = 5 \times 10^{-2}$, as in the high-amplitude 3D wedge cases of Chapter 5, in order to simulate noisy conditions and capture nonlinear effects. A set of 10 multiple frequencies were introduced, ranging from $f_1 = 0.0105$ to $f_{10} = 0.105$, which correspond to the dimensional values of $f_1^* = 7.3$ kHz and $f_{10}^* = 73$ kHz. This frequency range has been chosen in order to adapt the streamwise wavelength scale of the disturbances at the higher frequencies to the boundary-layer thickness in the region that is susceptible to the crossflow inflectional instabilities, as shown in Section 6.6. In particular, the minimum streamwise wavelength, corresponding to the highest frequency ($f_{10}$), of the 3D wave inflow is about $\lambda_{min} = 10$ mm for slow acoustic waves, and about $\lambda_{min} = 13.75$ mm for fast acoustic waves. The boundary-layer thickness near $z = 20$ mm, at a streamwise distance of $x = 50$ mm from the nose tip, is $\delta \approx 1.6$ mm, thus the smallest streamwise wavelength of the inflow 3D wave for both slow and fast acoustic waves is about 6.25 times higher than the reference boundary-layer thickness over the wedge near the nose region. This is also the smallest scale we can afford in our numerical simulations, namely the lowest wavelength we can resolve accurately (considering a minimum of about 60 points per wavelength) based on the restrictions imposed by the mesh resolution in the downstream (coarser) region of the domain. Any smaller wavelength (namely higher frequency) would have required a further increase of the mesh resolution and of the computational cost.

Figure 6.29 shows the overall amplitude levels (rms of $\rho'_\infty$ and $u'_\infty$) of the multi-frequency signal imposed in the freestream along the spanwise direction. As can be seen, due to the fixed value of the phase ($\phi_m = 0$) for each spanwise wavenumber, the imposed noise level in the freestream is $z$ dependent, with the maxima located at $z = 0$ and $z = 20$ mm. As mentioned in Section 5.1, the freestream fluctuations of the vertical and spanwise velocity components, $v'_\infty$ and $w'_\infty$, are identically zero.

Figures 6.30 and 6.31 show the time-averaged surface heat flux (in kW/m$^2$) for fast and slow acoustic waves respectively. As can be seen, the surface heat-flux structure in the case of fast acoustic waves show the presence of wavefronts nearly perpendicular to the flow direction, which is consistent, as discussed in Chapter 5, with the 2D fast mode being the dominant mode in the nose region, due to the powerful resonance mechanism, and leading to a modulated response further downstream. The case of slow acoustic waves (figure 6.31) shows, in contrast, a fundamentally different structure, which is characterised by the presence of elongated streamwise-oriented streaks generated in the early leading-edge region. In particular, three streaky structures can be distinguished (whose position and direction is indicated by arrows in figure 6.31) : i) one close to the

centerline, near $z = 10$ mm, which forms between $x = 50$ mm and $x = 100$ mm, and then decays rapidly downstream; ii) another, with higher spanwise size, located near the side boundary at about $z = 35$ mm, forming just downstream of the leading edge and gradually decaying downstream; iii) and a third one, originating in the leading-edge zone at about $z = 20$ mm, which grows until it undergoes breakdown after $x = 200$ mm.

Another noticeable difference between the fast-wave and slow-wave results is observed for the solution in the near-centerline region, which, in the slow-wave case, suggests that the boundary layer along the symmetry plane is laminar through the whole domain length, while showing, in the fast-wave case, a highly perturbed boundary layer which reaches a transitional stage within the region $x = 70$ mm $-150$ mm. This is due to the amplification of the 2D fast mode in the upstream nose region, leading to earlier generation of nonlinear effects, compared to the slow-wave case, and consequent destabilisation of the boundary layer in the near symmetry-plane zone, which is, in turn, the most susceptible zone to the 2D modes (in fact, the baseflow here is essentially two-dimensional, due to the very low sweep angles of the leading edge near the centerline and the symmetry boundary condition).

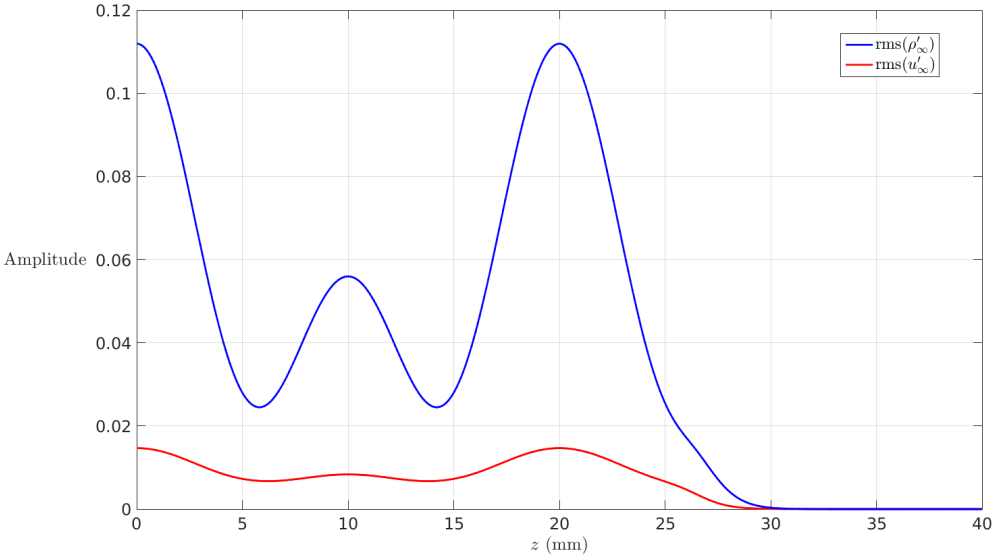


Figure 6.29: Amplitude levels (rms of $\rho'_\infty$ and $u'_\infty$) of the imposed freestream signal along the spanwise direction

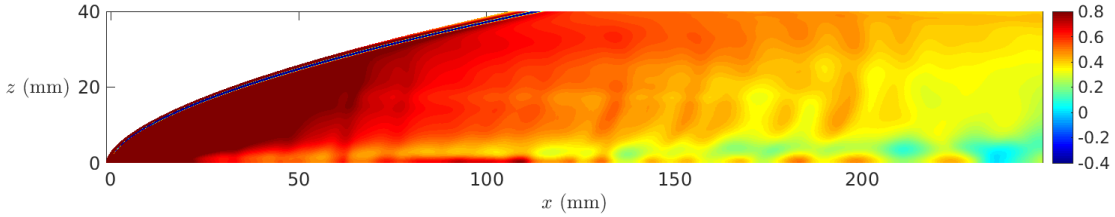


Figure 6.30: Time-averaged surface heat flux (kW/m$^2$) for fast acoustic waves

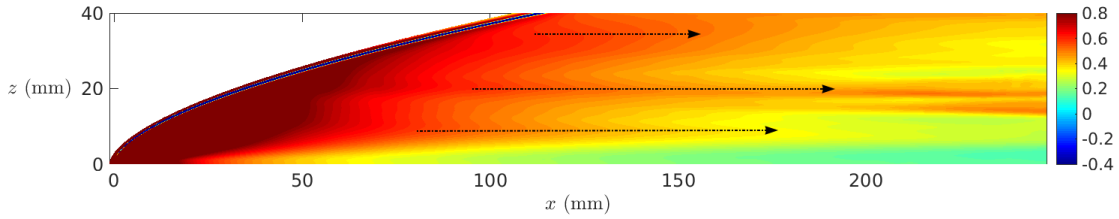


Figure 6.31: Time-averaged surface heat flux (kW/m$^2$) for slow acoustic waves. The arrows indicate the path of the streamwise streaks

In figure 6.32 a zoomed view of the heat flux for the slow-wave case in the downstream region is shown, which provides more details of the nonlinear growth of the streamwise streak located at $z = 20$ mm. The main streak coming from the leading edge grows in amplitude and spanwise size, also forming a secondary streak adjacent to the main one at about $x = 200$ mm. This new streak grows very quickly in amplitude, reaching the same values of the main streak within a distance of about 30 mm, and starts spreading downstream, assuming a deflected path oriented towards the centerline.

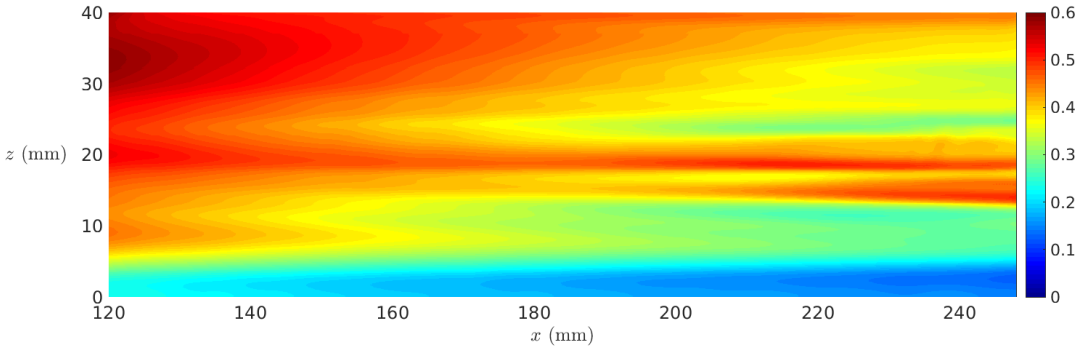


Figure 6.32: Time-averaged surface heat flux (kW/m$^2$) for slow acoustic waves. Close-up in the downstream region

The results for the surface heat flux indicate that the solution obtained with slow acoustic waves is closer to the experimental results observed in figure 6.12, which showed an off-centerline transition core and a laminar boundary layer near the centerline. A direct comparison between numerical and experimental results for the slow-wave solution is shown in figure 6.33, where the experimental figure has been adapted to match the scale of the numerical plot. Also, the same colorbar range of the experimental result has been used for the numerical result. The comparison shows qualitatively similar high heat-flux values reached along the leading edge and in the early nose region of the wedge, and decreasing values towards the centerline, where the blue values indicate a laminar boundary layer. However, the high (red) heat-flux zone near the leading edge appears to cover a larger area in the numerical result, which might be due to calibration effects of the experimental apparatus used to compute the heat flux, as well as to uncertainties in the flow direction inside the wind tunnel test section which might

have affected the freestream creating regions of slightly non-uniform flow. The main difference between the numerical prediction and the experimental results is observed downstream of $x = 150$ mm, where, in the experimental case, a wedge-shaped transition front is seen to develop and spread symmetrically downstream, affecting also the near-centerline region at long downstream distances. In contrast, in the numerical case, the heat flux near the symmetry plane keeps decreasing through all the domain length and no transition front is observed until the distance of about $x = 230$ mm is reached, where the streamwise streak located at $z = 20$ mm begins the nonlinear breakdown process, as discussed earlier, and starts spreading towards the centerline close to the outer boundary.

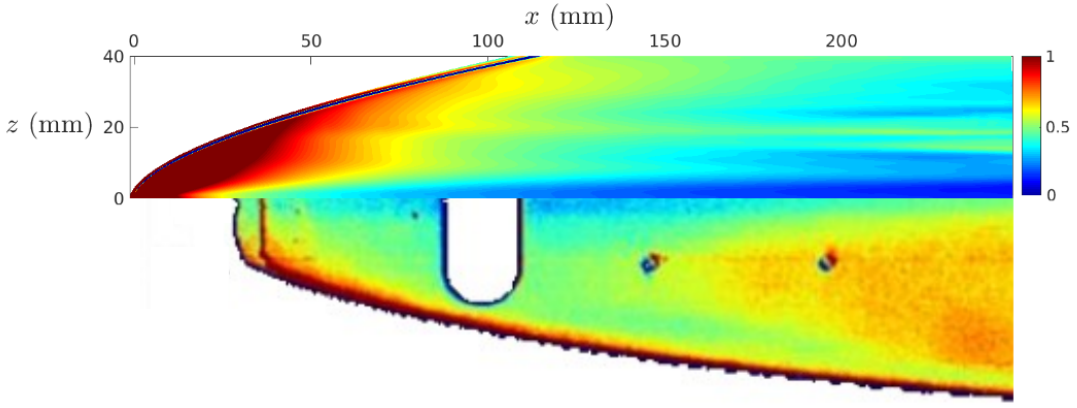


Figure 6.33: Numerical time-averaged surface heat flux (kW/m$^2$) obtained for slow acoustic waves (top half) compared to the corresponding experimental results (bottom half). Both heat-flux magnitude and length scales have been adapted in order to guarantee the matching between the numerical and the experimental case

Hence, the experimental results show a more rapid transition process, which is most likely due to a higher noise level of the wind tunnel, with respect to the freestream disturbance amplitude used in the numerical simulations. In addition, the pressure transducer placed upstream of the position $x = 150$ mm, and at approximately $z = 20$ mm, as figure 6.33 clearly shows, might have worked as a roughness element during the experimental tests, thus enhancing the transition process downstream.

In order to see in more details the breakdown process taking place in the downstream region in the numerical solution, we show in figure 6.34 the instantaneous contours of the wall-tangential velocity component ($u_t$) in the $xy$-plane along the $j = 15$ grid lines inside the boundary layer. Here the main disturbances coming from the leading edge near the $z = 20$ mm position and growing downstream, which are most probably correlated to the crossflow inflectional instabilities shown in Section 6.6, are seen to reach very high values just upstream of $x = 150$ mm, and to induce a transition process. This transition process, in turn, is observed to spread downstream forming a series of strong velocity spikes propagating towards the centerline with an inclination angle (indicated by the

dashed line in the figure) close to the wedge-shaped transition front angle shown by the experimental results.

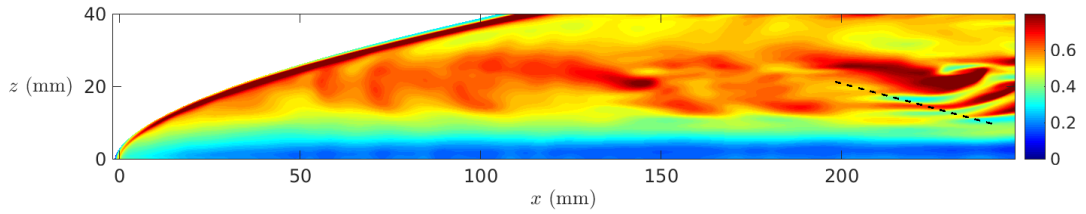


Figure 6.34: Wall-tangential velocity ($u_t$) on the $j = 15$ grid lines inside the boundary layer, for slow acoustic waves.

Hence, contrary to the surface heat-flux results, the numerical results inside the boundary layer show transition patterns more similar to those observed in the experimental results. The numerical results show the transition process starting away from the wall, and at about the same streamwise and spanwise positions over the wedge surface as in the experimental case. This suggests that the perturbations related to the nonlinear breakdown process, coming from the boundary-layer edge, have not yet approached the wall.

Finally, the difference observed in the transition patterns between the cases of fast and slow acoustic waves, namely the destabilisation of the boundary layer in the region of the symmetry plane due to the highly amplified 2D fast mode in the fast-wave case, is a further confirmation that the resonance mechanism at the leading edge for the fast mode at the higher amplitude levels can strongly affect the transition mechanism, enhancing the probability of by-pass transition, as was previously seen for the three-dimensional cases in Chapter 5. For the specific case of the three-dimensional forebody geometry, this difference between fast and slow acoustic waves can have significant effects on the transition process to a final turbulent state further downstream of our computational domain outflow boundary.

### 6.7.2 Slow-mode receptivity and streak evolution

As shown in Section 6.7.1, the numerical solution with slow acoustic waves is closer to the experimental results in terms of transition patterns, so, in this Section, we focus on the results for the slow-wave case. The receptivity process is studied through contours of the Fourier transformed wall pressure fluctuations (real part) at different frequencies, from $f_3$ to $f_8$, shown in figure 6.35. Both lower and higher frequencies show fluctuations in the early nose region (e.g. see the first positive-negative-positive peaks just downstream of the tip at the frequencies $f_3$ and $f_4$), corresponding to waves travelling in the direction of the flow along the attachment line. Then, as soon as the position $z = 20$ mm is approached, or, in other words, when a certain high-enough value of the sweep angle

($\Lambda = 70°$ at $z = 20$ mm) is reached, the disturbances detach from the leading edge, and propagate downstream towards the $x$-direction in the internal part of the wedge (this path is illustrated by the dashed black line in figure 6.35 for the frequency $f_4$). The amplitude of the disturbances, as soon as they are released by the leading edge into the internal domain near the $z = 20$ mm position, assumes very high values in the early internal region, namely between $x = 40$ mm and $x = 100$ mm, which is a region characterised by high crossflow inflectional profiles. Then, dependent on the frequencies, the amplitude either decays downstream, or increases leading to the nonlinear growth of a streamwise streak downstream of $x = 200$ mm.

Figures 6.36 and 6.37 show profiles of mean crossflow velocity ($w$), wall-normal velocity fluctuation ($v'$), first and second derivatives of the mean crossflow velocity ($\partial w/\partial y_n$, $\partial^2 w/\partial y_n^2$), at $z = 20$ mm, and at the positions $x = 50$ mm and $x = 60$ mm respectively. As seen in Chapter 4 for the 3D wedge in the swept configuration, also in this case the peak of $v'$ (note that the quantities plotted on the $x$-axis are normalised with their maximum value assumed in the wall-normal profile) inside the boundary layer is close to an inflection point of the mean crossflow velocity profile. This is more evident in figure 6.37, in which the peak of $v'$ is almost coincident with the peak of $\partial w/\partial y_n$. However, while in the swept wedge case the maximum absolute value of $v'$ was reached for the first inflection point near the wall (with a negative value of the crossflow velocity first derivative), in this case the peak of $v'$ is located (at both the $x$ positions) at the inflection point corresponding to a positive peak of $\partial w/\partial y_n$. In both figures the curve representing Fjortoft's stability condition is plotted as well, whose negative values indicate that the boundary layer is potentially unstable at both the considered positions. Thus, we deduce that crossflow instabilities are indeed responsible for the generation and downstream evolution of the streamwise streaks.

Figure 6.38 shows the maximum absolute values at the inflection points (inside the boundary layer) of the mean crossflow derivative ($\partial w/\partial y_n$) in the leading-edge region, which gives an indication of the strength of the crossflow on the body surface. As can be seen, the highest values are reached near the wedge junction, as expected due to the effect of the streamline deflection around the leading edge discussed in Section 6.6. Downstream of the wedge junction, the crossflow derivative in the region $z = 10$ mm - 20 mm maintains high values up to longer $x$-wise distances compared to different spanwise regions. The zone near the side boundary ($z = 30$ mm - 40 mm), which is the most similar to the case of a swept wedge (with straight leading edge), due to very small variations of the local sweep angle along the leading edge, as observed from the quasi-2D trend of the crossflow derivative contours, shows, in contrast, a rapid decrease of the wall-normal crossflow derivative downstream. This is an indication that the middle region across the span (near $z = 20$ mm) is indeed the most susceptible to the crossflow instability effects.

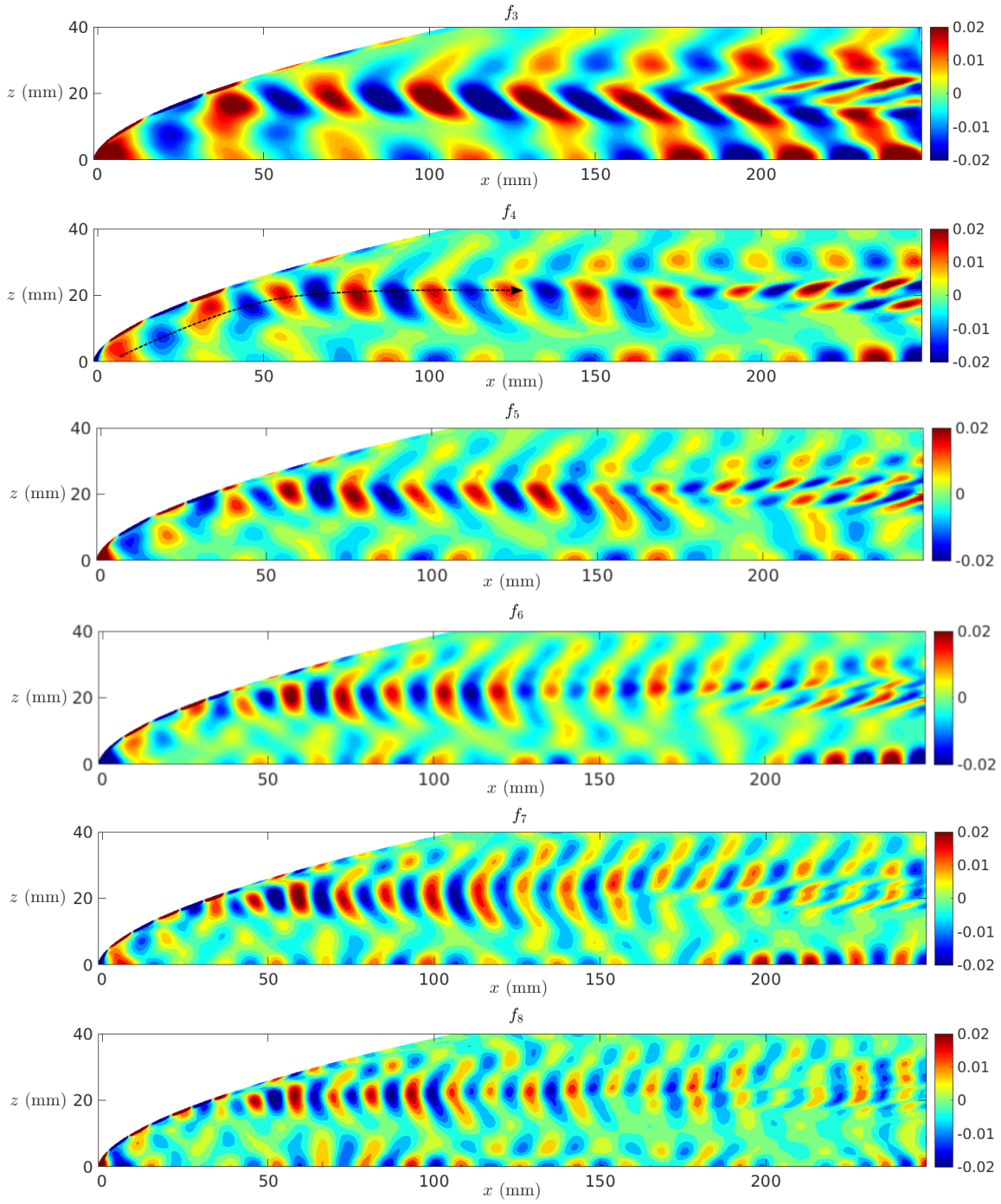


Figure 6.35: Real part of the Fourier transformed wall pressure fluctuations ($p'_w$) at different forcing frequencies.

As shown in figure 6.35, the lower frequencies are characterised by the higher amplitude levels, and are responsible for the nonlinear growth and bifurcation of the streamwise streak downstream. Moreover, in the region downstream of $x = 200$ mm there is also a strong increase in amplitude of the disturbances along the symmetry plane, which is

consistent, as seen in Section 6.7.1, with the spreading towards the centerline of the early nonlinear breakdown process.

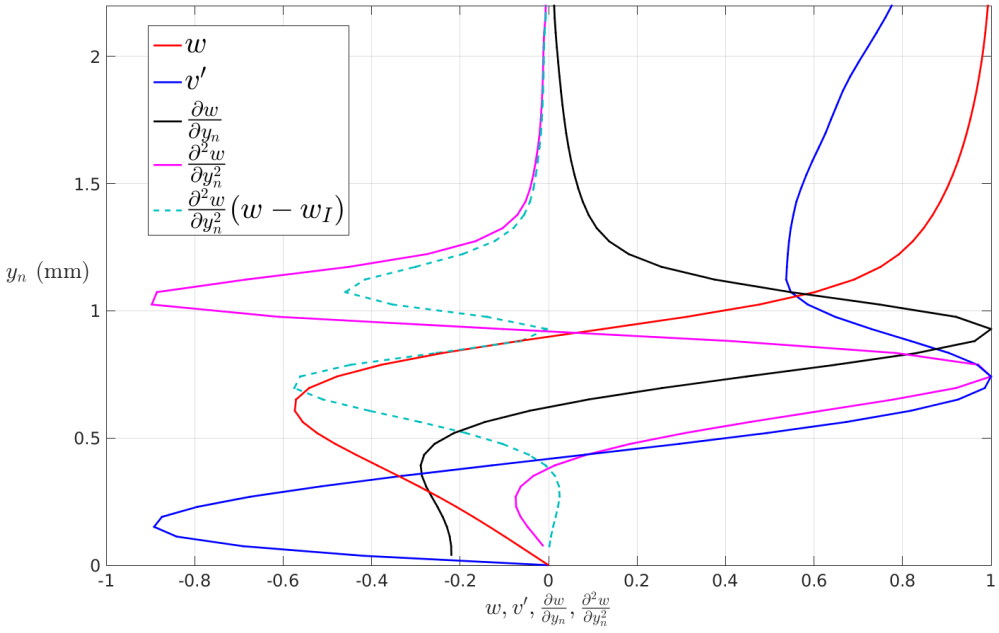


Figure 6.36: Profiles, along the wall-normal direction, of mean crossflow velocity ($w$), wall-normal velocity fluctuation ($v'$), first and second derivatives of the mean crossflow velocity ($\partial w/\partial y_n$, $\partial^2 w/\partial y_n^2$), and Fjortoft's stability condition, at $z = 20$ mm and $x = 50$ mm

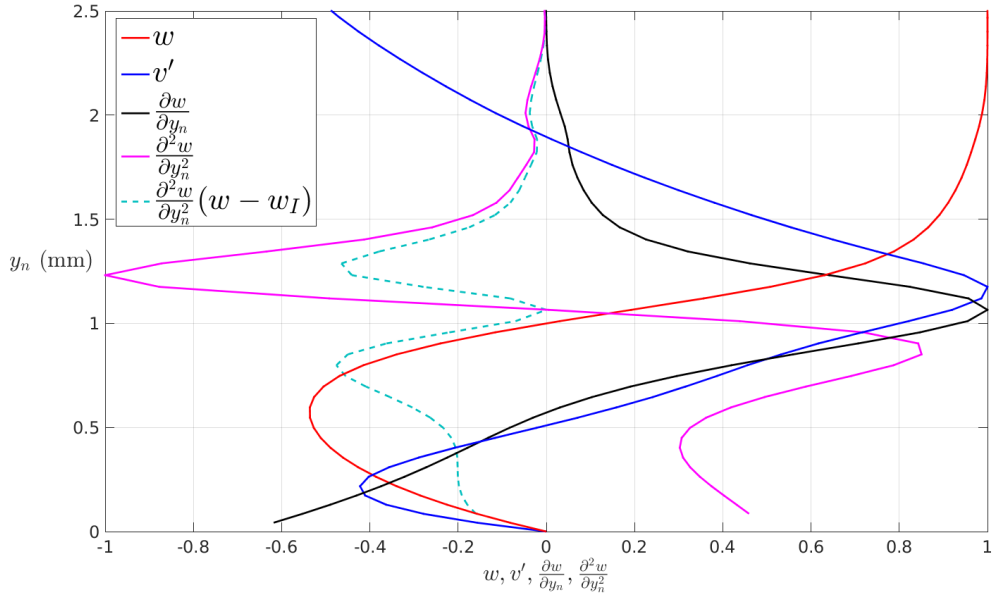


Figure 6.37: Profiles, along the wall-normal direction, of mean crossflow velocity ($w$), wall-normal velocity fluctuation ($v'$), first and second derivatives of the mean crossflow velocity ($\partial w/\partial y_n$, $\partial^2 w/\partial y_n^2$), and Fjortoft's stability condition, at $z = 20$ mm and $x = 60$ mm

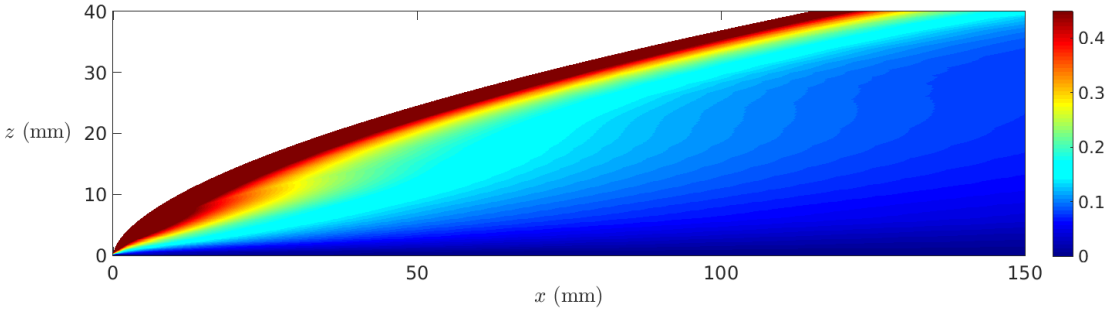


Figure 6.38: Contours of the maximum absolute values of the mean crossflow derivative ($\partial w/\partial y_n$) on the wedge in the leading-edge region

The streamwise-oriented streaks seen in figure 6.31 appear in a good qualitative agreement with some numerical studies available in the literature, e.g. the work of Bartkowicz *et al.* [90], showing the presence of crossflow-instability related streaks in a Mach 8 flow over an elliptic cone in low-enthalpy wind tunnel conditions. Hence the crossflow instability mode represents the most likely source of generation and downstream development of the streamwise streaks in our numerical solution.

Further evidence of the streamwise streaks belonging to a crossflow instability can be observed in figures 6.39 and 6.40, which show the temperature and wall-tangential streamwise vorticity ($\omega_x = 1/2[\partial w/\partial y_n - \partial v_n/\partial z]$, where $v_n$ is the wall-normal velocity component) cross-sections in the $zy_n$-plane at the streamwise positions $x = 220$ mm, $x = 230$ mm, $x = 240$ mm, namely in the region corresponding to the nonlinear growth and bifurcation process of the streamwise-oriented streak. The temperature contours near $z = 20$ mm have a similar orientation (i.e. a certain inclination of the oscillations with respect to the $y_n$-axis) at all the different streamwise locations, which is a common aspect of crossflow-instability-induced streaks (shown also in the results of Bartkowicz *et al.* [90]).

The main streak is initially located at about $z = 20$ mm, as evident also in figure 6.32. As it moves downstream, it spreads across the span and increases rapidly in amplitude. This is shown more clearly in figure 6.40, where two zones of opposite vorticity are observed across the boundary-layer thickness at $x = 20$ mm, both centred near $z = 20$ mm, representing two indistinct vortices at this streamwise position. Further downstream ($x = 230$ mm) two distinct co-rotating (negative vorticity) vortices appear, a weaker (secondary) one located inside the region $z = 15$ mm $-20$ mm, and a stronger one, with increased amplitude with respect to the upstream position, located in the region $z = 20$ mm $-25$ mm, and consistent with the main streamwise streak. Finally, at the position $x = 240$ mm, both the vortices show a higher amplitude, and appear shifted to increasing $z$ locations. The main vortex is also shifted upwards, providing the pronounced deformation of the boundary-layer edge seen in figure 6.39. The formation of another pair of counter-rotating secondary vortices is observed at about $z = 13$

mm, corresponding to the streak deflection towards the centerline shown in figure 6.32. Another much weaker secondary vortex (with negative sign) is seen to start forming at the boundary layer edge alongside the main vortex, at about the position $z = 27.5$ mm. This fragmentation of the boundary-layer structure corresponds to a breakdown process, which started further upstream ($x \approx 140$ mm), as seen in figure 6.34, where it involved only the upper region of the boundary layer.

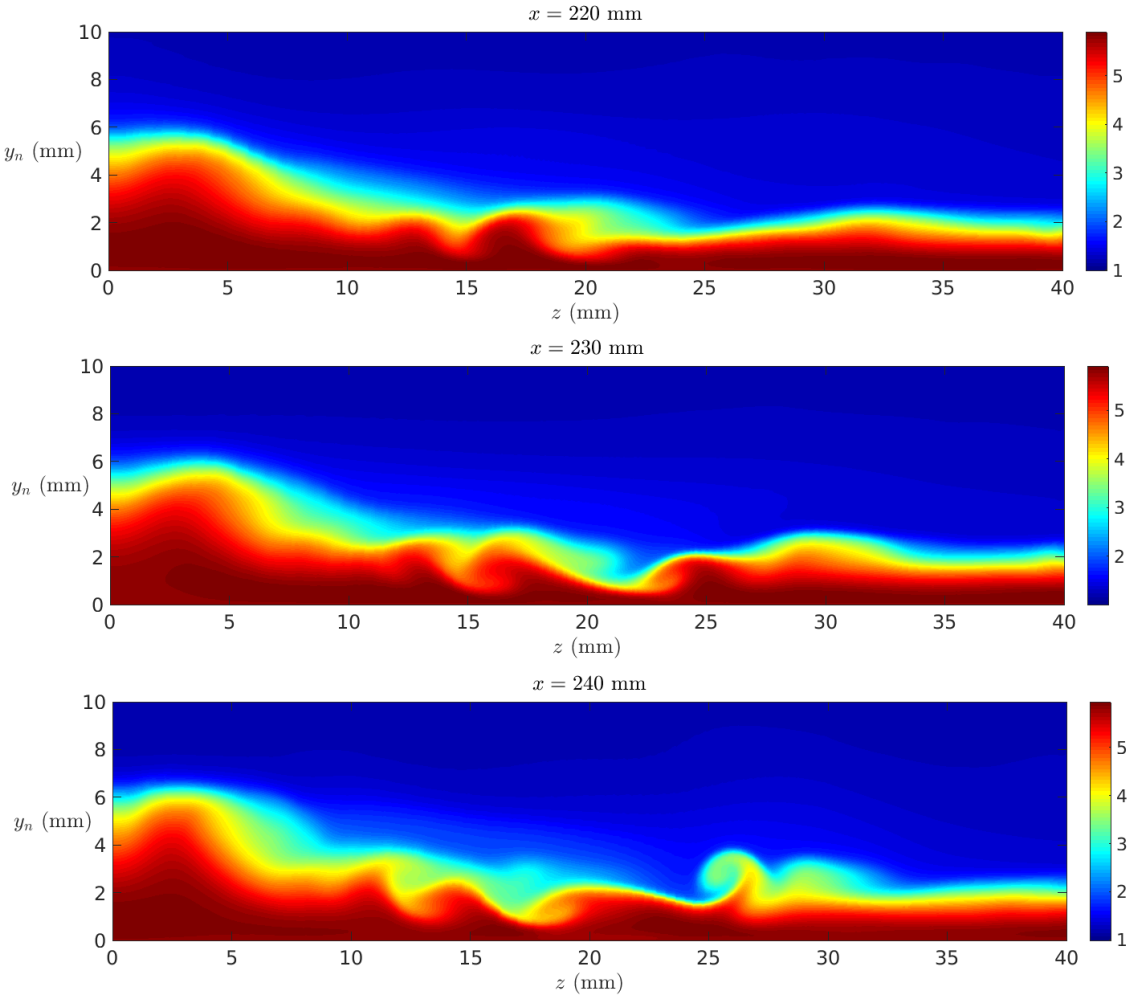


Figure 6.39: Temperature contours cross-sections in the $zy_n$-plane at different $x$ positions.

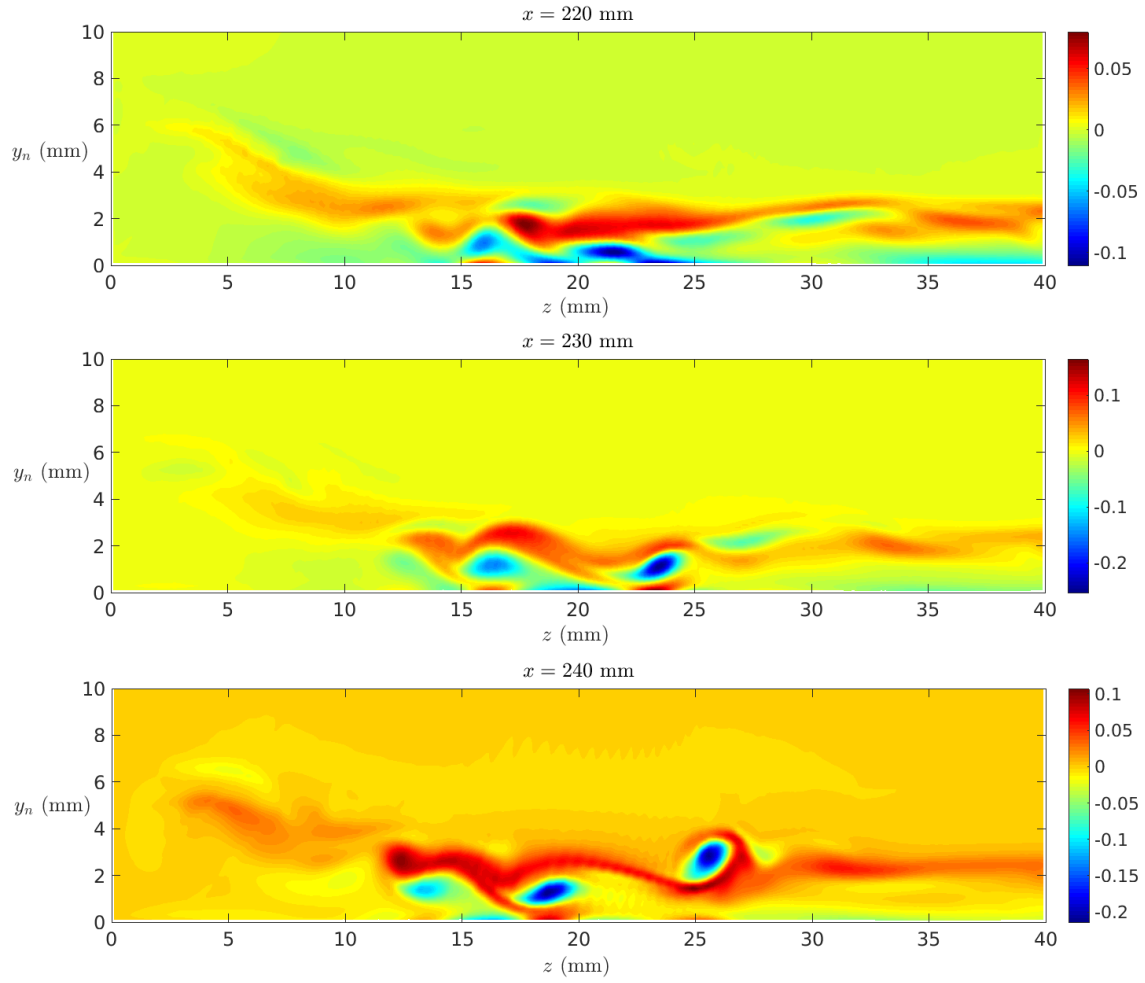


Figure 6.40: Streamwise vorticity contours cross-sections in the $zy_n$-plane at different $x$ positions.

Finally, the results for the wall heat flux in the case of fast acoustic waves seen in figure 6.30, showing earlier transition induced along the centerline, appear in a good conceptual agreement with the BiGlobal linear instability analysis results of the works of Paredes *et al.* [62], and Paredes and Theofilis [61], in which it was found that, in hypersonic flow over an elliptic cone, the centerline is sensitive to instability modes (centerline modes) driven by the high shear-layer associated to a low-velocity streak away from the wall (mushroom-like structure) formed at the centerline. These centerline instabilities can be even more amplified than the crossflow instabilities, thus playing a more relevant role in the transition process. Hence, our results for the fast waves suggest that the resonance mechanism relative to the fast mode at the leading edge can efficiently contribute to the generation and rapid growth of centerline instabilities leading to earlier transition.

In the case of slow acoustic waves, in contrast, the absence of a strong resonance mechanism leads to a laminar solution at the centerline, thus suggesting a much weaker

interaction between slow modes and centerline instabilities. This can also be explained considering that in our geometrical configuration the curvature effect of the elliptic cone surface is not present. Hence, the thicker boundary layer formed at the centerline, as an effect of the streamlines coming from the leading edge and converging on the centerline (as seen in figures 6.20 and 6.21), does not form a pronounced mushroom-like structure within the considered $x$-wise domain length (as seen in figure 6.39).

## 6.8 Summary of the results

Numerical simulations have been run in order to study transition scenarios for 3D fast and slow acoustic freestream wave disturbances, for the MBDA 3D forebody model tested in the Purdue Mach 6 hypersonic wind tunnel.

The mean flow in the leading-edge zone is found to be characterised by a region of inflectional crossflow boundary-layer profiles, extending from the side up to a small distance from the symmetry plane (where the spanwise velocity is uniformly zero). This was expected, due to the high values of the local leading-edge sweep angle.

The wedge junction represents a critical zone affecting the characteristics of the internal flowfield, due to the flow coming from near the leading-edge tip (along the attachment line) going around the leading-edge curvature and being deflected, as a result of the high centripetal acceleration, towards the centerline. This creates a stream inside the near-wall boundary layer, released into the internal nose region through the wedge junction, which flows towards the symmetry plane (thus with negative values of the spanwise velocity). The main consequences of this physical behaviour are i) the generation of inflectional crossflow boundary-layer profiles near the wedge junction, consistent with the positive values of the spanwise velocity reached outside of the boundary layer (for the flow in the shock layer being directed towards the side boundary), and ii) a strong 3D-flow effect in the wedge junction zone, causing a pronounced thinning of the boundary layer, with the external cold flow getting very close to the wall and producing a narrow zone of reverse wall heat flux (i.e. the wall releases heat into the fluid).

The side boundary effect on the internal solution has been assessed, showing that only a limited-size region adjacent to the lateral edge of the computational domain is affected by the presence of the side boundary, which does not include the zone where transition is seen to start in the experimental results. The 40 mm wide domain (in the spanwise direction) has been proved to be suitable for obtaining reliable receptivity-transition results in the flow region of interest.

The unsteady numerical simulations with fast and slow acoustic waves have been performed at a high freestream amplitude level, in order to simulate the noisy wind tunnel

conditions of the considered experimental case, and to trigger transition through rapid generation and growth of nonlinearities. Two important differences are observed between the transition patterns in the fast and the slow acoustic wave cases. First, in the fast-wave case the surface heat-flux structure shows signs of 2D oscillations, consistent with the 2D fast mode being the dominant mode inside the boundary layer due to the resonance mechanism at the leading edge; in the slow-wave case, instead, the heat-flux structure is characterised by streamwise-oriented streaks. Moreover, in the fast-wave case, the boundary layer adjacent to the symmetry plane is shown to be highly destabilised by the forced disturbances and to undertake earlier transition at about a distance of 70 mm from the nose tip; while, on the contrary, in the slow-wave case the near-centerline boundary layer is substantially laminar through the whole length of the domain. This difference is again due to the resonance-induced amplification of the 2D fast mode, which plays a major role in the region near the symmetry plane, where the mean flow is more two-dimensional. This is a further confirmation that the resonance mechanism at the leading edge for the fast mode, at the higher amplitude levels, can strongly affects the transition mechanism, enhancing the possibility of by-pass transition.

The results with slow acoustic waves provide a better correlation with the experiments, which suggests that the wind tunnel noise was characterised mostly by slow acoustic disturbances during the experimental tests. In particular, transition is induced by the nonlinear growth of streamwise-oriented streaks generated in the nose region, at a certain spanwise distance from the centerline (about 20 mm) corresponding to high local sweep angles and strong local inflectional crossflow profiles. The receptivity study has shown that disturbances coming from the nose tip, and initially following the flow path along the attachment line, are released through the wedge junction inside the internal wedge surface 20 mm off the centerline, and then propagate downstream leading to the generation of a main streamwise-oriented streak. The boundary-layer edge distortion is consistent with a crossflow-instability related streak. Further downstream, due to the high amplitudes, the streak undergoes nonlinear growth with bifurcation and generation of secondary vortices which spread towards the centerline, thus initiating the breakdown process. The initial stage of the nonlinear growth leading to transition is actually observed inside the boundary layer further upstream ($x \approx 140$ mm). However, at this streamwise location, the nonlinear process is confined to the upper part of the boundary layer, thus not involving yet the flow near the wall and the surface heat flux.

The disagreement between the numerical and experimental results in terms of the exact location of the transition point is most probably related to a difference in the freestream noise level inside the hypersonic wind tunnel, compared to the fixed disturbance amplitude used in the numerical simulations, which would indicate that higher noise levels were reached in the wind tunnel runs. However, the presence of the pressure transducers over the wedge surface, which might have worked as roughness elements leading to a more rapid transition process, may have been a contributing factor.

# Chapter 7

# Conclusions and future work

The present work has elaborated, through direct numerical simulations, details of the receptivity and breakdown mechanisms for hypersonic flow over blunt leading-edge configurations with imposed freestream acoustic disturbances. A two-dimensional and a three-dimensional model of the freestream acoustic waves have been developed and used in the numerical simulations. The former has been adopted in 2D simulations over the geometry of a blunt-nose wedge probe designed by DLR to measure the freestream noise level in hypersonic wind tunnels; the latter has been used to perform 3D simulations for a blunt wedge in an unswept and a swept configuration, and for the full three-dimensional geometry of a generic forebody model developed and tested by MBDA in the Purdue hypersonic wind tunnel.

## 7.1 2D wedge probe

In the 2D simulations for the DLR wedge probe, performed for both fast and slow acoustic waves as freestream disturbances, the wave structure behind the shock, resulting from the shock-disturbance interaction, and the characteristics of the wall response, related to the boundary-layer receptivity mechanisms for the fast and the slow mode, have been analysed and validated through theoretical estimations and other numerical results available in the literature. Furthermore, the sensitivity to different flow conditions, including an angle of attack and an angle of incidence of the acoustic waves, has been assessed. The set of two-dimensional simulations for the wedge probe has also provided the numerical freestream-to-wall transfer functions for the pressure disturbances, that have been used, in conjunction with the experimental data for the wall disturbance levels, to estimate the freestream noise levels in the DLR high-enthalpy (HEG) and low-enthalpy (RWG) hypersonic wind tunnels.

The objectives of these 2D simulations, which were stated in Section 1.7, are rewritten below:

- to determine the characteristics of the transmitted waves behind of the shock,
- to determine the characteristics of the response along the wall,
- to assess the sensitivity of the leading-edge receptivity to the angle of attack and the angle of incidence of the acoustic waves,
- to estimate the freestream noise levels in the DLR wind tunnels.

The results obtained for the 2D numerical simulations, described in Section 4.3, allow us to give the following conclusions:

- fast acoustic waves are efficiently transmitted across the shock as refracted waves, while slow acoustic waves generate entropy/vorticity waves in the post-shock region;
- the receptivity to fast acoustic waves is characterised by a strong resonance mechanism at the leading edge, producing a significant amplification of the fast mode, and a modulation further downstream between the decaying mode F and the external forcing; while in the slow-wave case, a much weaker response is observed, which decays in the nose region and assumes a substantially constant amplitude further downstream;
- a wave incidence angle of 10° amplifies the response along the lee side at the higher frequencies for fast acoustic waves, while providing an opposite behaviour for slow acoustic waves; in contrast, an angle of attack of 10° provides a significantly higher response along the windward side, compared to the lee side, and a pronounced difference in the post-shock wave structure between lee and windward sides, for both fast and slow acoustic waves;
- the estimated freestream noise levels indicate higher levels in the HEG wind tunnel at the higher Mach numbers, compared to the RWG wind tunnel, a higher contribution of slow acoustic waves in the wind-tunnel freestream disturbance field (in agreement with the results of Duan *et al.*[12]), and a marginal role of the leading-edge receptivity in the frequency-spectra shape at the wall, which is mainly dependent on the shape of the spectra in the freestream.

## 7.2 3D wedge swept and unswept

The 3D simulations for the span-periodic wedge geometry with oblique acoustic disturbances, performed for a flow at Mach 6 and for two different Reynolds numbers, have focused on the characteristics of the receptivity-breakdown mechanism associated with fast and slow acoustic waves, in a linear and a nonlinear regime (namely for two different

freestream disturbance amplitude levels), and for an unswept and a swept configuration. These numerical simulations have assessed the role played by the fast-mode resonance mechanism at the leading edge on the breakdown mechanism, and the effect of the crossflow instabilities generated at the leading edge in the presence of a sweep angle. Different transition scenarios have been observed, each one resulting from a specific linear/nonlinear receptivity mechanism to fast/slow acoustic waves in an unswept/swept leading-edge configuration. Moreover, results of an LST analysis have been compared with numerical results for the receptivity to 2D fast acoustic waves over the same wedge geometry, showing a very good agreement, consistent with results present in the literature. In particular, the objectives we addressed to this set of 3D simulations in Section 1.7 were the following:

- to deduce the different receptivity mechanisms to freestream fast and slow acoustic waves, with and without nonlinearities,
- to determine the resonance mechanism at the leading edge between the internal modes and the external forcing, including an assessment of the relevance of previous theoretical approaches (Fedorov and Khokhlov[32]),
- to determine the extent of influence of crossflow instabilities generated at the leading edge due to the presence of a sweep angle.

From the results discussed in Sections 5.3 and 5.4, the following conclusions can be drawn:

- the fast-wave receptivity is characterised by a dominant 2D fast mode in the leading-edge region (due to the resonance mechanism with the incident fast acoustic waves), which, further downstream, remains the dominant mode inside the boundary layer at the lower freestream disturbance amplitudes, while leading to the generation and growth of streamwise streaks at the higher amplitudes. The slow-wave receptivity is, in contrast, characterised, for both low and high freestream disturbance amplitudes, by a combination of 2D and 3D modes (with no one dominant mode), and a lower response (compared to the fast-wave case), as a consequence of a mixed wave structure propagating in the post-shock region and interacting with the boundary layer;
- the resonance mechanism between the incident fast waves and the boundary-layer fast mode leads to subsequent amplification cycles of the fast mode, which hence becomes the dominant mode in different regions of the flow (starting from the leading edge). The intermediate regions are, in contrast, characterised by a decay of the fast mode, and by a modulation between the forcing waves and the other internal competing modes, including the fast mode itself and the slow mode (mode

S). The latter grows when mode F - mode S synchronisation is reached, and leads to the generation of a Mack mode. This mechanism was shown by previous theoretical (Fedorov and Khokhlov[32], Fedorov's [4]) and numerical (Zhong and Ma [17], Zhong and Wang [23]) studies. Our results are consistent with those of the above mentioned studies, and, in addition, have found that the resonance mechanism for the fast mode at the leading edge is efficient in triggering, at the higher amplitudes, the generation and rapid growth of instability modes (streaks) which lead quickly to transition (in both the unswept and the swept configuration);

- the effect of a sweep angle is a more unstable boundary layer, which is subject to crossflow instabilities originating in the leading-edge region. In both fast and slow wave cases, the crossflow instability produces narrow streamwise streaks in the downstream region, whose rapid nonlinear growth leads to final breakdown. The fast-wave case at high amplitudes represents an exception, in which earlier transition is induced through a by-pass mechanism related to the interaction, in the leading-edge region, between the crossflow modes and the resonance-induced $\beta = 0$ fast modes.

## 7.3 Generic forebody

The numerical simulations performed for the MBDA 3D forebody geometry have investigated the transition patterns for the cases of three-dimensional fast and slow acoustic waves, serving as a validation of the transition experiments carried out for the forebody model in the Mach 6 Purdue hypersonic wind tunnel, and have represented, relative to the previous 3D numerical cases for the span-periodic wedge, an extension to a case with a different leading-edge shape along the spanwise direction. The role of the receptivity to fast and slow acoustic waves on the transition patterns has been analysed, and the corresponding numerical results for the surface heat flux have been compared with the experimental data.

The objectives of these 3D simulations were the following, as stated in Section 1.7:

- to compare the simulations with the experimental results, thus assessing the suitability of the acoustic-wave model, and the dominant disturbances in the Purdue hypersonic wind tunnel,
- to determine the main transition mechanism on the geometry of a generic forebody.

On the basis of the results discussed in Chapter 6, the main conclusions can be summarised as follows:

- the numerical results with slow acoustic waves provide similar transition patterns to the experimental case, indicating that the wind tunnel noise was characterised mostly by slow acoustic disturbances during the experimental tests, and, at the same time, that the 3D acoustic-wave model described in Section 2.4 is suitable to reproduce the main characteristics of the real disturbance field in hypersonic wind tunnels. The more rapid transition observed in the experiments is most likely due to a slightly higher freestream disturbance amplitude in the hypersonic wind tunnel, and to the presence of the pressure transducers on the surface of the body, which might have worked as roughness elements, thus inducing earlier transition;

- the main mechanism leading to transition consists of high-amplitude disturbances released by the leading edge into the internal wedge surface near a particular off-centerline position where a local sweep angle of about 70° is reached. These disturbances trigger crossflow instability modes near the leading edge with the generation of streamwise streaks, which grow downstream until nonlinear breakdown is reached. In particular, the lower frequencies (7.3 kHz - 36.5 kHz) have been found to be responsible for the streak nonlinear growth.

## 7.4 Key contributions and future work

This work has identified the main mechanisms and parametric dependence of the leading-edge receptivity to acoustic disturbances in several high-speed flow conditions, and has shed light on the complex relations between types of acoustic disturbance, amplitude level in the freestream, and receptivity/breakdown mechanism on the wall in a hypersonic flow for different blunt leading-edge configurations. Hence, it represents a fundamental basis for the future development of transition-predictor methods aimed at i) correlating the physical mechanism of the breakdown to the characteristics of the leading-edge receptivity mechanism, and at ii) modelling the disturbance environment of a conventional hypersonic wind tunnel through the computation of the receptivity/breakdown mechanism, in conjunction with the data of transition experiments in the noisy environment of a generic hypersonic wind tunnel.

In particular, the main contributions of this research work to the advancement of the knowledge in the hypersonic-transition field can be summarised in the following points:

- the combined experimental-numerical approach for the estimation of the noise levels in the DLR experiments, as well as the comparison between our numerical results and the transition experiments in the Purdue Mach 6 hypersonic wind tunnel, have provided evidence of the relevance of slow acoustic waves in the real disturbance field of hypersonic wind tunnels, thus confirming the purely numerical predictions of Duan *et al.*[12].

- In addition to the assessment of the resonance mechanism at the leading edge, which was shown by previous theoretical (Fedorov and Khokhlov[32], Fedorov's [4]) and numerical (e.g. Zhong and Ma [17]) studies, the present research work has demonstrated the link between the receptivity mechanism at the leading edge and the characteristics of the wave structure propagating behind the shock, and its fundamental implications on the transition mechanism. In particular, our study has shown that fast acoustic waves are efficiently transmitted and amplified through the shock, thus triggering a strong resonance mechanism (involving the internal fast mode) when interacting with the boundary layer at the leading edge, and that slow acoustic waves, in contrast, are in part transmitted with a lower amplitude (compared to the freestream waves) and in part converted into a different type of waves (convected waves) downstream of the shock, thus producing a weaker and mixed (i.e. a combination of 2D and 3D modes) response on the wall. This difference in the wall response has been shown, in turn, to provide significant differences in the transition process downstream. Moreover, our study has shown that the post-shock wave structure is strongly dependent on the angle of attack, for both fast and slow acoustic waves, resulting in different propagation patterns between the lee and the windward sides.

- In the literature, slow acoustic waves are known to be more dangerous than fast waves, as previous studies (e.g. Kara *et al.*[39], Malik and Balakumar[29]) showed that slow waves induce second instability modes of higher amplitude, compared to the fast waves. However, this may only be true when considering linear instabilities (which is the case of the above mentioned studies). The present numerical study has demonstrated that in nonlinear cases (for high freestream disturbance levels), in contrast, the fast-mode-induced transition is significantly more powerful than the slow-mode-induced transition. The key mechanism of the fast-mode transition is the leading-edge resonance mechanism, which triggers the generation and rapid growth of streak instability modes, leading to earlier transition both in the unswept and swept configurations. This represents important progress in the understanding of the relative role played by fast and slow acoustic waves in the transition process for different freestream disturbance levels, and can have important implications in any (ground-test or in flight) conditions where fast acoustic waves may represent a relevant contribution to the disturbance field (e.g. in the case of entropy waves generating fast acoustic waves behind the shock).

These findings highlight the importance of a numerical approach aimed at simulating the full transition process from freestream disturbances, in contrast with the traditional approaches based on inserting prescribed disturbances into the boundary layer, for future transition-prediction studies.

The most important studies yet to be addressed, on the basis of the computational results, concern further theoretical analyses for the span-periodic wedge flow and the flow

over the 3D generic forebody. For the span-periodic wedge in the unswept configuration, the physical mechanism of the generation, growth and breakdown of the streamwise streaks needs to be assessed through a more detailed analysis aimed at understanding whether the streak breakdown can be associated to a purely nonlinear process or to a transient-growth mechanism. In the cases of the swept span-periodic wedge and the 3D generic forebody, the role of the crossflow inflectional instabilities, located in the near leading-edge region, on the transition mechanism downstream, for both fast and slow acoustic waves, needs to be assessed through an appropriate linear stability analysis. In order to achieve this, an improvement of the existing version of the LST code needs to be performed first, which takes into account also the crossflow modes. The new version of the code will then need to be validated through validation test cases available in the literature.

Moreover, as seen in Chapter 6, for the generic forebody geometry, the role of the pressure transducers on the body surface on the transition mechanism, during the experimental tests in the hypersonic wind tunnel, is not yet understood, and needs to be studied, in order to shed light on the possible causes of the disagreement between the numerical and the experimental results concerning the exact location of the transition point. This will need a set of new numerical simulations, eventually more expensive in terms of computational time, in which an isolated roughness element has to be located, and opportunely discretised, in correspondence of the nearest position to the transition point observed in the experimental results (i.e $x \approx 150$ mm). The shape and size of the pressure transducer will have to be provided by the experimentalists in order to appropriately model the roughness element.

Finally, a list of other possible future applications and developments of our work is as follows,

- study of the sensitivity of the receptivity mechanism, and the characteristics of the full transition mechanism, in the presence of nonequilibrium chemical effects, e.g. the dissociation and exchange reactions in the shock layer and the recombination reactions in the boundary layer, for high Mach number flows (e.g. by developing a nonequilibrium chemical effects version of the SBLI code);
- study of the receptivity-breakdown mechanism in the presence of wall blowing of the gas species (with appropriate blowing profiles) produced by the ablation (surface chemical reactions and/or internal pyrolysis) of the TPS (Thermal-Protection-System) material, e.g. for the heat shield of a reentry probe, or the TPS of the nozzle wall of a rocket;
- development of a theoretical predictor method of the receptivity-breakdown mechanism over blunt leading-edge configurations, on the basis of the results from the direct numerical simulations and LST/PSE studies;

- extension of the shock-grid alignment method, described in Section 3.3, to a generic 3D grid.

# References


[1] Anderson, J. D. *Hypersonic and High Temperature Gas Dynamics*, AIAA Education Series, 2000

[2] Schneider, S. P. *Hypersonic Laminar-Turbulent Transition on Circular Cones and Scramjet Forebodies*, Progress in Aerospace Sciences 40 (1-2), pp. 1-50, 2004

[3] Park, C. Nonequilibrium hypersonic aerothermodynamics, NASA Ames Research Center, Moffett Field, CA, United States, John Wiley and Sons, 1989

[4] Fedorov, A. V. *Transition and Stability of High-Speed Boundary Layers*, Annual Review of Fluid Mechanics 43 (1), pp. 79-95, 2011

[5] Balakumar, P., and Owens, L. R. *Stability of Hypersonic Boundary Layers on a Cone at an Angle of Attack*, AIAA Paper 2010-4718, 40th AIAA Fluid Dynamics Conference, Chicago, Illinois, 2010

[6] Ma, Y., and Zhong, X. *Receptivity of a supersonic boundary layer over a flat plate. Part 1: Wave structures and interactions* Journal of Fluid Mechanics 488, pp. 31-78, 2003

[7] Ma, Y. and Zhong, X. *Receptivity of a supersonic boundary layer over a flat plate. Part 2: Receptivity to free-stream sound*, Journal of Fluid Mechanics 488, pp. 79-121, 2003

[8] Schneider, S. P. *Developing mechanism-based methods for estimating hypersonic boundary-layer transition in flight: The role of quiet tunnels.* Progress in Aerospace Sciences 72, pp. 17-29, 2015

[9] Schneider, S. P. *Development of hypersonic quiet tunnels.* Journal of Spacecraft and Rockets, 45 (4), pp. 641-664, 2008

[10] Schneider, S. P. *Effects of high-speed tunnel noise on laminar-turbulent transition.* Journal of Spacecraft and Rockets, 38 (3), pp. 323-333, 2001

[11] Masutti, D., Spinosa, E., Chazot, O., and Carbonaro, M. *Disturbance level characterization of a hypersonic blowdown facility.* AIAA Journal 50 (12), pp. 2720-2730, 2012

[12] Duan, L., Choudhari, M. M., and Wu, M. *Numerical study of acoustic radiation due to a supersonic turbulent boundary layer.* Journal of Fluid Mechanics 746, pp. 165-192, 2014

[13] McKenzie, J. F., and Westphal, K. O. *Interaction of linear waves with oblique shock waves.* Physics of Fluids 11 (11), pp. 2350-2362, 1968

[14] Duck, P. W., Lasseigne, D. G., and Hussaini, M. Y. *On the interaction between the shock wave attached to a wedge and freestream disturbances.* Theoretical and Computational Fluid Dynamics, 7 (2), pp. 119-139, 1995

[15] Duck, P. W., Lasseigne, D. G., and Hussaini, M. Y. *The effect of three-dimensional freestream disturbances on the supersonic flow past a wedge.* Physics of Fluids, 9 (2), pp. 456-467, 1997

[16] Ma, Y., and Zhong, X. *Receptivity of a supersonic boundary layer over a flat plate. Part 3: Effects of different types of free-stream disturbances*, Journal of Fluid Mechanics 532, pp. 63-109, 2005

[17] Zhong, X., and Ma, Y. *Boundary-layer receptivity of Mach 7.99 flow over a blunt cone to free-stream acoustic waves*, Journal of Fluid Mechanics, 556, pp. 55-103, 2006

[18] Balakumar, P. and Kegerise, M. A. *Receptivity of Hypersonic Boundary Layers over Straight and Flared Cones*, AIAA Journal 53 (8), pp. 2097-2109, 2015

[19] Schneider, S. P. *Flight Data for Boundary-Layer Transition at Hypersonic and Supersonic Speeds*, Journal of Spacecraft and Rockets 36 (1), pp. 8-20, 1999

[20] Schneider, S. P. *Effects of High-Speed Tunnel Noise on Laminar-Turbulent Transition*, Journal of Spacecraft and Rockets, 38 (3), pp. 323-333, 2001

[21] Schneider, S. P. *Developing mechanism-based methods for estimating hypersonic boundary-layer transition in flight: The role of quiet tunnels*, Progress in Aerospace Sciences 72, pp. 17-29, 2015.

[22] Kachanov, Y. S. *Physical Mechanisms of Laminar Boundary-Layer Transition*, Annual Review of Fluid Mechanics 26 (1), pp. 411-482, 1994

[23] Zhong, X., and Wang, X. *Direct Numerical Simulation on the Receptivity, Instability, and Transition of Hypersonic Boundary Layers*, Annual Review of Fluid Mechanics 44, pp. 527-561, 2012

[24] Saric, W. S., Reed, H., and Kerschen, E. *Boundary-layer receptivity to freestream disturbances*, Annual Review of Fluid Mechanics 34, pp. 291-319, 2002

[25] Goldstein, M. *Scattering of acoustic waves into Tollmien-Schlichting waves by small streamwise variations in surface geometry*, Journal of Fluid Mechanics 154, pp. 509-529, 1985

[26] Lin, N., Reed, H. L., and Saric, W. S. *Effect of leading-edge geometry on boundary-layer receptivity to freestream sound.* In Instability, Transition, and Turbulence, pp. 421-440, Springer New York, 1992

[27] Schrader, L. U., Brandt, L., Mavriplis, C., and Henningson, D. S. *Receptivity to free-stream vorticity of flow past a flat plate with elliptic leading edge.* Journal of Fluid Mechanics, 653, pp. 245-271, 2010

[28] Nagarajan, S., Lele, S. K., and Ferziger, J. H. *Leading-edge effects in bypass transition.* Journal of Fluid Mechanics, 572, pp. 471-504, 2007

[29] Malik, M. R., and Balakumar, P. *Acoustic receptivity of Mach 4.5 boundary layer with leading-edge bluntness*, Theoretical and Computational Fluid Dynamics, 21 (5), 2007, pp. 323-342

[30] Mack, L. M. *Boundary-layer linear stability theory*, Tech. Rep. ADP004046, California Inst. of Technology, Pasadena JPL, 1984

[31] Fasel, H. and Konzelmann, U. *Non-parallel stability of a flat plate boundary layer using the complete Navier-Stokes equations*, Journal of Fluid Mechanics 221, pp. 311-347, 1990

[32] Fedorov, A. V., and Khokhlov, A. P. *Prehistory of Instability in a Hypersonic Boundary Layer*, Theoretical and Computational Fluid Dynamics 14 (6), pp 359-375, 2001

[33] Klebanoff, P. S., Tidstrom, K. D., and Sargent, L. M. *The three-dimensional nature of boundary-layer instability*, Journal of Fluid Mechanics 12, pp. 1-34, 1962

[34] Kachanov, Y. S., Kozlov, V. V., and Levchenko, V. Y. *Nonlinear development of a wave in a boundary layer*, Fluid Dynamics 12 (3), pp. 383-390, 1977

[35] Emmons, H. W. *The laminar-turbulent transition in a boundary layer-Part I*, Journal of the Aeronautical Sciences 18 (7), pp. 490-498, 1951

[36] Redford, J. A., Sandham, N. D., and Roberts, G.T. *Numerical simulations of turbulent spots in supersonic boundary layers: Effects of Mach number and wall temperature*, Progress in Aerospace Sciences 52, pp. 67-79, 2012

[37] Stetson, K. F., Thompson, E. R., Donaldson, J. C., and Siler, L. G. *Laminar boundary layer stability experiments on a cone at Mach 8. ii- blunt cone*, AIAA Aerospace Sciences Meeting 22nd, Reno, Nevada, 1984

[38] Balakumar, P. *Receptivity of a supersonic boundary layer to acoustic disturbances*, AIAA Journal 47 (5), pp. 1069-1078, 2009

[39] Kara, K., Balakumar, P., and Kandil, O. A. *Receptivity of Hypersonic Boundary Layers Due to Acoustic Disturbances over Blunt Cone*, AIAA Paper 2007-945, 45th AIAA Aerospace Sciences Meeting and Exhibit, Reno, Nevada, 2007

[40] Tumin, A., Wang, X., and Zhong, X. *Direct numerical simulation and the theory of receptivity in a hypersonic boundary layer.* Physics of fluids, 19 (1), 2007

[41] Egorov, I. V., Sudakov, V. G., and Fedorov, A. V. *Numerical modeling of the receptivity of a supersonic boundary layer to acoustic disturbances*, Fluid Dynamics 41 (1), 2006

[42] Kara, K., Balakumar, P. and Kandil, O. A. *Effects of Wall Cooling on Hypersonic Boundary Layer Receptivity over a Cone*, AIAA Paper 2008-3734, 38th Fluid Dynamics Conference and Exhibit, Seattle, Washington, 2008

[43] Hornung, H. G., Adam, P. H., Germain, P., Fujii, K. and Rasheed, A. *On transition and transition control in hypervelocity Flow*, Proceedings of the 9th Asian Congress of Fluid Mechanics, Isfahan, Iran, May 27-31, 2002

[44] Stuckert, G., and Reed, H. L. *Linear disturbances in hypersonic, chemically reacting shock layers.* AIAA Journal, 32 (7), pp. 1384-1393, 1994

[45] Ma, Y., and Zhong, X. *Receptivity to freestream disturbances of a Mach 10 nonequilibrium reacting oxygen flow over a flat plate.* AIAA Paper 2004-256, 42nd AIAA Aerospace Sciences Meeting and Exhibit, Reno, Nevada, 2004

[46] Stemmer, C. *Transition Investigation on Hypersonic Flat-Plate Boundary Layers Flows with Chemical and Thermal Non-Equilibrium.* Proc. 6th IUTAM Symposium on Laminar-Turbulent Transition, ed. R Govindarajan. Fluid Mechanics and Its Applications, 78, Springer, Dordrecht, 2006

[47] Parsons, N., Zhong, X., Kim, J. and Eldredge, J. *Numerical Study of Hypersonic Receptivity with Thermochemical Non-Equilibrium on a Blunt Cone*, AIAA Paper 2010-4446, 40th AIAA Fluid Dynamics Conference, Chicago, Illinois, 2010

[48] Jewell, J., Wagnild, R., Leyva, I., Candler, G., and Shepherd, J. *Transition within a hypervelocity boundary layer on a 5-degree half-angle cone in air/CO2 mixtures.* AIAA Paper 2013-523, 51st AIAA Aerospace Sciences Meeting including the New Horizons Forum and Aerospace Exposition, Grapevine, Dallas/Ft. Worth Region, Texas, 2013

[49] Mortensen, C. H., and Zhong, X. *Real-Gas and Surface-Ablation Effects on Hypersonic Boundary-Layer Instability over a Blunt Cone.* AIAA Journal, 54 (3), pp. 980-998, 2016

[50] Fasel, H., Thumm, A. and Bestek, H. *Direct numerical simulation of transition in supersonic boundary layers: oblique breakdown.* ASME-PUBLICATIONS-FED 151, 1993

[51] Berlin, S., Lundbladh, A., and Henningson, D. *Spatial simulations of oblique transition in a boundary layer.* Physics of Fluids 6 (6), pp. 1949-1951, 1994

[52] Berlin, S., and Henningson, D. S. *A nonlinear mechanism for receptivity of free-stream disturbances.* Physics of Fluids 11 (12), pp. 3749-3760, 1999

[53] Saric, W. S., Reed, H. R., and White, E. B. *Stability and transition of three-dimensional boundary layers.* Annual Review of Fluid Mechanics 35 (1), pp. 413-440, 2003

[54] White, E. B., and Saric, W. S. *Secondary instability of crossflow vortices.* Journal of Fluid Mechanics 525, pp. 275-308, 2005

[55] Bippes, H. *Basic experiments on transition in three-dimensional boundary layers dominated by crossflow instability.* Progress in Aerospace Sciences 35 (4), pp. 363-412, 1999

[56] Cattafesta, III, L. N., Iyer, V., Masad, J. A., King, R. A., and Dagenhart, J. R. *Three-dimensional boundary-layer transition on a swept wing at Mach 3.5.* AIAA Journal 33 (11), pp. 2032-2037, 1995

[57] Creel Jr., T. R, Beckwith, I. E., and Chen, F. J. *Transition on swept leading edges at Mach 3.5.* Journal of Aircraft 24 (10), pp. 710-717, 1987

[58] Tokugawa, N., Sugiura, H., and Ueda, Y. *Boundary-layer transition on an axisymmetric body at incidence at Mach 1.2.* AIAA Journal 44 (5), pp. 973-980, 2006

[59] Li, F., and Choudhari, M. M. *Spatially developing secondary instabilities in compressible swept airfoil boundary layers.* Theoretical and Computational Fluid Dynamics 25 (1-4), pp. 65-84, 2011

[60] Nomura, T. *Stability of Supersonic Swept-Wing Boundary Layers with or without Crossflow.* Transactions of the Japan Society for Aeronautical and Space Sciences 48 (162), pp. 193-198, 2006

[61] Paredes, P., and Theofilis, V. *Centerline instabilities on the hypersonic international flight research experimentation HIFiRE-5 elliptic cone model.* Journal of Fluids and Structures 53, pp. 36-49, 2015

[62] Paredes, P., Grosse R., Theofilis, V., Kimmel, R. *Linear modal instabilities of hypersonic flow over an elliptic cone.* Journal of Fluid Mechanics 804, pp. 442-466, 2016

[63] Balakumar, P., and King, R. A. *Receptivity and stability of supersonic swept flows.* AIAA Journal 50 (7), pp. 1476-1489, 2012

[64] Pruett, C. D., Chang, C., and Streett, C. L. *Simulation of crossflow instability on a supersonic highly swept wing.* Computers and Fluids 29 (1), pp. 33-62, 2000

[65] Speer, S. E., Zhong, X., Gong, L., Quinn, R. *DNS of Attachment-line/Crossflow Boundary Layer Instability in Supersonic Swept Wing Flows.* AIAA Paper 2004-252, 42nd AIAA Aerospace Sciences Meeting and Exhibit, Reno, Nevada, 2004.

[66] Yee, H. C., Vinokur, M., and Djomehri, M. J. *Entropy splitting and numerical dissipation*, Journal of Computational Physics 162 (1), pp. 33-81, 2000

[67] Carpenter, M. H., Nordstrom, J., and Gottlieb, D. *A Stable and Conservative Interface Treatment of Arbitrary Spatial Accuracy*, NASA/CR, 206921, ICASE Report No. 98−12, 1998

[68] Yee, H. C., Sandham, N. D., and Djomehri, M. J. *Low-dissipative high-order shock-capturing methods using characteristic-based filters*, Journal of Computational Physics 150 (1), pp. 199-238, 1999

[69] Ducros, F., Ferrand, V., Nicoud, F., Weber, C., Darracq, D., Gacherieu, C., and Poinsot, T. *Large-Eddy Simulation of the Shock/Turbulence Interaction*, Journal of Computational Physics 152 (2), pp. 517-549, 1999

[70] Roe, P. L. *Approximate Riemann solvers, parameter vectors, and difference schemes*, Journal of Computational Physics 43 (2), pp. 357-372, 1981

[71] Yee, H. C., Klopfer, G. H., and Montagne J-L. *High-resolution shock-capturing schemes for inviscid and viscous hypersonic flows*, Journal of Computational Physics 88 (1), pp. 31-61, 1990

[72] Piperno, S., and Depeyre S. *Criteria for the design of limiters yielding efficient high resolution TVD schemes*, Computers and Fluids 27 (2), pp. 183-197, 1998

[73] Toro, E. F., and Billett S. J. *Centred TVD schemes for hyperbolic conservation laws* IMA Journal of Numerical Analysis 20 (1), pp. 47-79, 2000

[74] Lee, T. K., and Zhong, X. *Spurious numerical oscillations in simulation of supersonic flows using shock-capturing schemes*, AIAA Journal 37 (3), pp. 313-319, 1999

[75] Arora, M., and Roe, P. L. *On postshock oscillations due to shock capturing schemes in unsteady flows*, Journal of Computational Physics 130 (1), pp. 25-40, 1997

[76] Zaide, D. W., and Roe, P. L. *Flux functions for reducing numerical shockwave anomalies*, 7th International Conference on Computational Fluid Dynamics (ICCFD7), Big Island, Hawaii, 2012

[77] Van den Eynde, J. *Stability and transition of the flow behind isolated roughness elements in hypersonic boundary layers.* Doctoral Thesis, University of Southampton Research Repository, 2015

[78] Sagaut, P. *Large eddy simulations for incompressible flows.* Springer-Verlag, NY, 3rd Edition, 2006

[79] Sansica A. *Stability and Unsteadiness of Transitional Shock-Wave/Boundary-Layer Interactions in Supersonic Flows*. Doctoral Thesis, University of Southampton Research Repository, 2015

[80] Touber, E., and Sandham, N. D. *Oblique Shock Impinging on a Turbulent Boundary Layer: Low-Frequency Mechanisms*. AIAA Paper 2008-4170, 38th Fluid Dynamics Conference and Exhibit, Seattle, Washington, 2008

[81] Inagiki, M., Kondoh, T., and Nagano, Y. *A mixed-time-scale SGS model with fixed model-parameters for practical LES*. Journal of Fluids Engineering, 127, pp. 1-13, 2005

[82] De Tullio, N., Paredes, P., Sandham, N. D., and Theofilis, V. *Laminar-turbulent transition induced by a discrete roughness element in a supersonic boundary layer*. Journal of Fluid Mechanics 735, pp. 613-646, 2013

[83] Bianchi, D., Nasuti, F., and Martelli, E. *Navier-Stokes simulations of hypersonic flows with coupled graphite ablation*, Journal of Spacecraft and Rockets 47 (4), pp. 554-562, 2010

[84] Wagner, A., Schuelein, E., and Hannemann, K. *High Frequency Free-Stream Disturbance Measurements in Hypersonic Wind Tunnels by Means of a Slender Wedge Probe*. AIAA Paper 2016-3192, 46th AIAA Fluid Dynamics Conference, Washington D.C., 2016

[85] De Tullio, N., and Sandham, N. D. *Influence of boundary-layer disturbances on the instability of a roughness wake in a high-speed boundary layer*. Journal of Fluid Mechanics 763, pp. 136-165, 2015

[86] Zhong, X. *Leading-edge receptivity to free-stream disturbance waves for hypersonic flow over a parabola*. Journal of Fluid Mechanics 441, pp. 315-367, 2001

[87] Andersson, P., Brandt, L., Bottaro, A., and Henningson, D. S. *On the breakdown of boundary layer streaks*. Journal of Fluid Mechanics, 428, pp. 29-60, 2001

[88] Brandt, L., and Henningson, D. S. *Transition of streamwise streaks in zero-pressure-gradient boundary layers*. Journal of Fluid Mechanics, 472, pp. 229-261, 2002

[89] Durant, A., André, T., Edelman, J. B., Chynoweth B. C., and Schneider, S. P. *Mach 6 Quiet Tunnel Laminar to Turbulent Investigation of a Generic Hypersonic Forebody*, AIAA Paper 2015-3575, 20th AIAA International Space Planes and Hypersonic Systems and Technologies Conference, Glasgow, Scotland, 2015

[90] Bartkowicz, M. D., Subbareddy, P. K., and Candler, G. V. *Simulation of boundary layer transition on elliptic cones in hypersonic flow*. AIAA Paper 2010-1064, 48th AIAA Aerospace Sciences Meeting Including the New Horizons Forum and Aerospace Exposition, Orlando, Florida, 2010